博士論文
Doctoral Thesis

Modification of Kinetics and Thermodynamics by Various Oxides Addition and Composite Formation for Magnesium-Hydrogen System

マグネシウム-水素系における酸化触媒添加及び複合体形成による動力学及び熱力学制御

SINGH PANKAJ KUMAR

広島大学大学院先端物質科学研究科
Graduate School of Advanced Sciences of Matter
Hiroshima University

2022 年 3 月
(March 2022)

Contents

1. Introduction 1
1.1 Fossil Fuels and Renewable Energy 1
1.2 Hydrogen 4
1.3 Hydrogen Isotopes 5
1.4 Hydrogen Storage 5
1.4.1 Compressed Hydrogen Storage 7
1.4.2 Liquid State Hydrogen Storage 8
1.4.3 Solid State Hydrogen Storage 9
1.5 Hydrogen Storage Materials 10
1.5.1 Challenges of using Hydrogen as an Energy Carrier 11
1.6 Kinetics of Metal Hydrogen-System 12
1.6.1 Role of Catalysts 17
1.7 Thermodynamics of Metal-Hydrogen System 17
1.8 Magnesium and Magnesium Hydride 20
1.8.1 Magnesium as an important Hydrogen Storage Materials 20
1.8.2 Magnesium Hydride Polymorph and its Phase diagram 23
1.8.3 Thermodynamic of MgH_2 25
1.8.4 Kinetic of MgH_2 26
1.8.5 Other important properties of MgH_2 27
1.9 Thermodynamic modification of Magnesium-Hydrogen System 29
1.10 Kinetic modification of Magnesium-Hydrogen System using various catalysts 30
1.10.1 Transition Metal 31
1.10.2 The Oxidation States 33
1.11 References 36
2. Purpose of this thesis 42
3. Experimental Procedures 46
3.1 Materials 46
3.2 Synthesis of Ternary Oxide 46
3.3 Mechanical Ball Milling Method 49
3.4 Scanning Electron Microscope (SEM) 52
3.5 Energy Dispersive Spectroscopy (EDS) 57

3.6 X-Ray diffraction (XRD) 61
3.7 Thermal Analysis Technique 70
3.7.1 Enthalpy Change 71
3.7.2 Thermogravimetry (TG) 72
3.7.3 Differential Thermal Analysis (DTA) 75
3.8 X-Ray Photoelectron Spectroscopy (XPS) 78
3.9 References 86
4. Result and Discussion 88
4.1. Study on effective factors of oxide catalysts for the Mg-H system 88
4.1.1 Structural properties of MgH_2 with oxides 89
4.1.2 Hydrogen desorption properties of MgH_2 with oxides 103
4.1.3 Instability for catalytic activity of the various catalyzed samples 108
4.1.4 Thermodynamic estimation on reduction routes of oxides 118
4.1.5 The Chemical States of oxides 123
4.1.6 Estimation of effective factors on oxide catalysts 136
4.2 Study on the catalytic tuning of Mg-H system using ternary oxide 140
4.2.1 Synthesis of $TaVO_5$ 140
4.2.2 Structural and hydrogen sorption properties of MgH_2 with $TaVO_5$ 143
4.2.3 Synthesis of Nb_9VO_{25} 149
4.2.4 Structural and hydrogen sorption properties of MgH_2 with Nb_9VO_{25} 151
4.2.5 Synthesis of $Nb_{0.6}Cr_{0.4}O_2$ 158
4.2.6 Structural and hydrogen sorption properties of MgH_2 with $Nb_{0.6}Cr_{0.4}O_2$ 163
4.3 Study on synthesis technique of highly activated Mg 166
4.3.1 Structural properties of gel oxides with MgH_2 166
4.3.2 Hydrogen desorption properties of MgH_2 with gel oxides 169
4.3.3 Chemical states of gel oxides 176
4.3.4 H_2O desorption analysis of gel oxides 177
4.3.5 Stability of gel oxides compared with ternary oxide 178
4.4 Study on thermodynamic modification of MgH_2 using CaH_2 179
4.4.1 Structural properties of MgH_2-CaH_2 composite 179
4.4.2 Hydrogen sorption properties of MgH_2-CaH_2 composite 183
4.4.3 Thermogravimetric analysis of MgH_2-CaH_2 composite 185
4.4.4 Hydrogen desorption kinetics of MgH_2-CaH_2 composite 186

4.4.5 PCI analysis of MgH_2-CaH_2 composite 190
4.5 References 193
5. Conclusion 195

主 論 文
(Main Thesis）

Abstract

Magnesium has always been the center of extensive investigations for its potential use as a medium for storing hydrogen as a basic technology for next-generation hydrogen transportation and increasing the amount of hydrogen flow because it can store up to 7.6 mass % of hydrogen. However, sluggish kinetics and high-temperature desorption for thermodynamics is the key issue with it when it comes to releasing or absorbing hydrogen. In this thesis Modification of Kinetics and Thermodynamics by Various Oxides and Composites for the Magnesium Hydrogen System has been explored. Four different approaches have been made to modify the kinetics of MgH_2.

Owing to the above-mentioned complicated process, it is difficult to define and compare the essential catalytic properties of oxides. A systematic catalytic behavior of a single phase of TiO_2, ZrO_2, HfO_2, V_2O_5, Nb_2O_5, Ta_2O_5, CrO_3, MoO_3, and WO_3 (Nb_2O_5 and its neighboring oxide) with Mg-MgH_2 system were investigated. Each oxide was taken in its maximum oxidation state followed by a possibility to reduce in several lower oxidation states causes catalysis. A highly dispersed state of Mg was found in the case of TiO_2, ZrO_2, V_2O_5, Nb_2O_5, and CrO_3 followed by a reduction in the peak temperature around 200 °C, categorized as group A. On the other hand, MgH_2 + Ta_2O_5, MgH_2 + HfO_2, MgH_2 + WO_3, and MgH_2 + MoO_3 show the hydrogen desorption peak temperature about 285, 303, 310, and 324°C, respectively, categorized as group B. The XPS analysis was performed to determine the reduction state of each oxide with MgH_2. Using the NIST data base we assigned the peak and found that MgH_2 + TiO_2 and MgH_2 + V_2O_5 have a low-intensity spectrum which is difficult to analyze. ZrO_2 slightly reduced to Mg surface with the probability of around +2 chemical state. On the other hand, HfO_2 is completely consistent with thermodynamic estimation and no reduction was found in the sample. Reduction of Nb_2O_5 on Mg surface found in +4, +2, and 0 chemical states. In case of MgH_2+Ta_2O_5, Ta_2O_5 was reduced in Ta metal with 0 chemical state.

Reduction of CrO_3 took place in +3, +2, and 0 oxidation states. In the same way, MoO_3 reduced on Mg surface in 0 chemical states. Whereas WO_3 reduced in +4 and 0 followed by remaining small amount of +6 oxidation state. The dispersion state expected from the XRD patterns is an important factor because almost all the samples with no diffraction peaks of oxides showed high catalysis. From the thermodynamic estimation and XPS analyses, it was clarified that the high catalytic activity was obtained when the intermediate oxidation states such as +2 and +3 can be formed.

In many cases, we need intermediate catalysis along with the search of newest and best catalysts, not only low catalysis but also extremely high catalysis (few cases) was not suitable for practical applications because the former requires excess energy input and later is dangerous due to the high activity. Thus, I tried to tune the catalysis by exchanging/replacing the element by combining the catalytic active elements and inactive elements (formation of ternary oxides $A_xB_yO_z$) with single phase and vice versa for the Mg-H system. The purpose is to control or tune catalysis same as the alloy studies for hydrogen storage, as in the case of alloy systems with the search of best and newest catalysis.

$TaVO_5$, Nb_9VO_{25} and $Nb_{0.6}Cr_{0.4}O_2$ ternary oxide (single phase) was synthesized using longer milling followed by heat treatment respectively. The hydrogen desorption peak temperature for MgH_2 with synthesized $TaVO_5$ oxide was evaluated and found to be 250 °C which is in the middle of MgH_2+V_2O_5 peak temperature 213 °C and Ta_2O_5 peak temperature 288 °C respectively, yields tuning of catalysis. On the other hand, the dehydrogenation peak temperature for MgH_2 with Nb_9VO_{25} oxide was found to be 250 °C which is comparatively higher compared to MgH_2+V_2O_5 (220 °C) and MgH_2+ Nb_2O_5 (225 °C) respectively, yields tuning of catalysis. Similarly, for $Nb_{0.6}Cr_{0.4}O_2$ ternary oxide, the hydrogen desorption peak temperature for MgH_2 with synthesized $Nb_{0.6}Cr_{0.4}O_2$ oxide was found around 303 °C which is comparatively higher compared to MgH_2+Nb_2O_5 peak temperature 222 °C and MgH_2+CrO_3 peak temperature 206 °C respectively.

Simple and easy synthesis of Nb and Ta gel oxide using solution gel method compared to complicated time taking process as explained above, milling followed by higher temperature heating for long duration. The dispersion of Nb and Ta gel oxide on Mg to create highly activated Mg by ball milling for ten times shorter than conventional processes. Each oxide shows the catalytic effect for hydrogen desorption and absorption on the Mg surface. Magnesium absorbed the hydrogen even around 40°C, proposing that highly activated Mg was synthesized for 2h ball milling. The Nb_2O_5 gel and heat-treated shows the highest catalytic effect among all. It is indicated that the mixed oxide state such as solid solution or ternary oxide (Nb-Ta-O) synthesized by the sol-gel methods shows characteristic catalytic effects differently from that of each oxide. The Nb_2O_5 gel with higher catalysis is further reduced compared to the heat-treated one because the gel oxide is more unstable owing to the lesser network between Nb and O atoms due to the existence of OH groups. By using gel oxides, highly activated Mg can be synthesized under milder conditions compared with previous cases.

Both CaH_2 and MgH_2 are good candidates for the development of hydrogen storage materials because of their high hydrogen storage capacity. However, both the hydrides are quite stable thermodynamically and required high temperatures for the hydrogen sorption process. The MgH_2-CaH_2 composite could show a favorable hydrogen sorption reaction because of $CaMg_2$ intermetallic formation. The present study indicated that the CaH_2-MgH_2 -$ZrCl_4$ could be a potential candidate for the mobile hydrogen storage system.

1. Introduction

1.1 Fossil Fuels and Renewable Energy

Renewable energy is crucial for being able to reduce the amount of CO_2, which is emitted by the combustion of fossil fuels, pumping into the atmosphere and oceans to be able to mitigate dangerous levels of climate change. Climate change mitigation is a huge concern for governments around the world and with ever-increasing energy demand, especially in newly industrialized countries, we need to look for different ways of producing energy that is sustainable for future generations. The Earth's average temperature has risen by 1.1°C since the late 19th century caused by global warming. Mostly the rise in temperature has occurred in the last 35 years at the fastest rate in documented history. A worldwide temperature alteration happens in last decades, Global warming occurs when carbon dioxide and other greenhouse gases collect in the atmosphere and absorb sunlight and solar radiation that have bounced off the Earth's surface. Naturally, this radiation would escape into space, but these pollutants, which can last for years to centuries in the atmosphere, trap the heat and cause the planet to get hotter called the greenhouse effect. [1-1] Due to global warming, there is a continuous rise in the water level of the sea, 3.2 mm each year due to melting ice sheets and thermal expansion of water. Greenland and Antarctic ice sheets decrease by 413 gigatons each year. Arctic ice, decreasing by 13% each decade. Regularly, glaciers are retreating around the world, particularly in the Alps, Himalayas, Andes, Rockies, Alaska, and Africa.

Another effect is the ocean system, carbon dioxide reacts with ocean water to produce acid is known as Ocean acidification.

$$H_2O + CO_2 \longrightarrow H_2CO_3 \quad \text{(carbonic acid)} \qquad (1)$$

The lowering of the pH value of the ocean makes it more acidic. When conditions are too acidic corals cannot absorb the calcium carbonate, they need to maintain their skeletons and they dissolve. This is known as coral bleaching and results in the loss of vital reef habitats home to thousands of species of marine life. Carbon absorbed by ocean surface layers is increasing by 2 billion tonnes every year and coral reefs are suffering ever-increasing levels of bleaching. There were several reasons exist for pollution and increase in temperature to harm our environment and habitates. Based on the above-mentioned problems, we need to develop alternative energy resources, apart from carbon-based fuels . The energy crisis has been one of the most prevalent issues in the 21st century, and many research and development activities are ongoing to develop new, clean, reliable, flexible, cost-efficient, and CO_2-free energy resources. Various kinds of natural sources, such as sunlight, wind, biomass, water, wave, tide, and geothermal heat, are green energy sources. Unlike fossil fuels, these energy sources are renewable, infinite, and naturally replenished. [1-2]

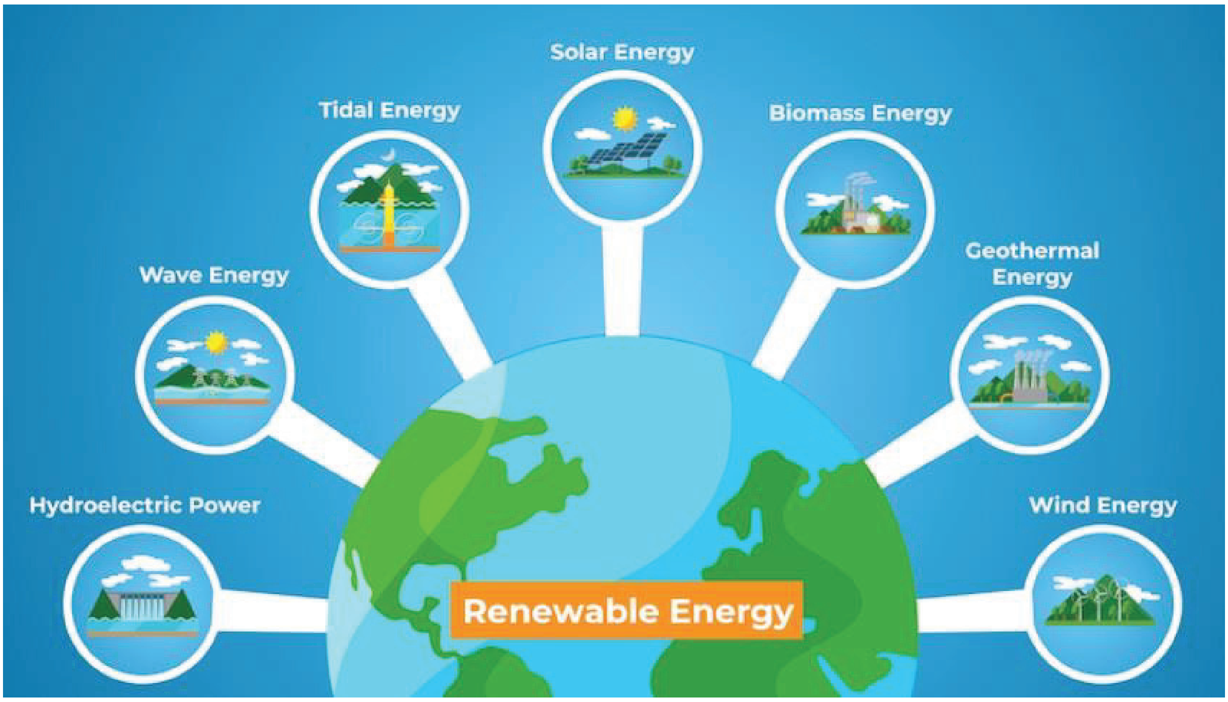

Figure 1.1 Renewable Energy: Sources and types [1-1]

A global trend of searching for renewable energy as the primary energy source has become a growing concern to mitigate the several issues and threats of non-renewable resources. The negative consequences of green energy are significantly less, and their direct contribution to greenhouse gas emissions is almost negligible. Therefore, developing renewables as a critical player in the global energy sector is essential to promote an environmentally friendly and sustainable energy future. In the future, the integration of the technological development made in the ongoing fourth industrial revolution may establish the sustainable green energy industry as a thriving global industry. However, many factors played a quite crucial role in the development, such as environmental, social, economic, technical, plan and policy, subsidy, geographical, and market availability, for an energy sector. [1-3,4]

Hydrogen is a promising energy carrier that has been highly regarded because of its advantages, such as high energy density (142 MJ/kg), great variety of potential sources, lightweight, and environmental friendliness. Hydrogen is not a primary energy source; it stores, transports, and delivers energy. An efficient and effective hydrogen storage method must be developed to realize a hydrogen-based energy system. Researchers trying to use hydrogen as a energy carrier because it burns cleanly and give H_2O as a by product makes it environmental friendly in nature. In connection to it hydrogen is also fuel efficient as it has highest energy density compared to other available fuels. There are various types of hydrogen storage materials, such as conventional metal, complex, and chemical hydrides, as well as liquid organic materials. Various types of intermetallic compounds have been developed for stationary applications. However, low hydrogen storage capacity, high material cost, and heavy weight prohibit the mobile application of intermetallic compounds. Light s- and p-block elements, such as lithium (Li), sodium (Na), magnesium (Mg), calcium (Ca), and their compounds, are promising candidates for storing massive amounts of hydrogen for stationary and onboard applications.

Table 1.1 Energy density value per unit mass of any fuel

	Energy Source	Energy Density per unit mass
i	Hydrogen	142.0 MJ/kg
ii	Methane	55.5 MJ/kg
iii	Gasoline	45.8 MJ/kg
iv	Diesel	45.0 MJ/kg
v	Biodiesel	38.0 MJ/kg
vi	Ethanol	29.7 MJ/kg
vii	Coal	24.0 MJ/kg
viii	Methanol	22.7 MJ/kg
ix	Ammonia	17.0 MJ/kg
x	Wood	16.0 MJ/kg

Among all the light element-based materials, magnesium hydride (MgH_2) has been considered as an attractive candidate in terms of its gravimetric hydrogen storage capacity (7.7 wt.%) as per the United States Department of Energy, natural abundance, cost-effectiveness, and user safety. Additionally, MgH_2 has the highest energy density (9 MJ/kg Mg) of all reversible hydrides applicable for hydrogen storage. There is various kind of research and development is going on to develop hydrogen storage materials for mobile applications. [1-5]

1.2 Hydrogen

“Hydrogen”, which provides clean energy without greenhouse gas emissions, is widely regarded as the promising alternative to carbon-based fuels. However, the transition from fossil fuel economy to hydrogen economy is very challenging. The hydrogen storage technology, the ability to transport enough hydrogen safely, compactly, and economically, is one of the most important approaches to the success of this transition. As hydrogen is a gaseous state under ambient condition so volumetric energy density is low around 0.09 kg/m^3. Therefore, advanced hydrogen storage materials with high hydrogen density, moderate reaction temperature, and high reaction rate are expected to be developed urgently. [1-6]

1.3 Hydrogen Isotopes

Hydrogen has 3 kinds of isotopes, ordinary isotope known as protium, ${}^{1}_{1}H$ (1 proton and 1 electron). 2nd stable isotope is known as deuterium, ${}^{2}_{1}H$ or D with an atomic weight of 2 (1 proton and 1 neutron plus 1 electron). Later after 2 years a 3rd isotope was also discovered named Tritium ${}^{3}_{1}H$ or T, with an atomic weight of 3 (1 proton and 2 neutrons plus 1 electron). Hydrogen isotope had desirable behavior, all isotopes of hydrogen react together and form covalent molecules like H_2, D_2, and T_2 respectively due to the presence of a single electron in the atom. Hydrogen easily converts itself as an anion (H^-) or cation (H^+) in ionic compounds, on other hand, it easily forms the covalent bond by sharing its valence electron. In the year 1934, an American scientist, Harold C. Urey, got a Nobel Prize for separating hydrogen isotope of mass number 2 by physical methods. [1-7,8]

1.4 Hydrogen Storage

For successful application of hydrogen as an energy carrier for mobile application, hydrogen demands to be stored safely for the variable period as efficiently as gasoline. The energy density of hydrogen [120(LHV) -142(HHV) MJ/kg (net calorific value)] is almost more than 2 times of conventional fuels (natural gas: 43 MJ/kg and gasoline 44.4 MJ/kg). To store the hydrogen for mobile applications volumetric density is the important parameter as it is low around 0.09 kg/m^3.

At ambient conditions, 1 liter of hydrogen contains only 10.7 kJ of energy, which is less than other conventional fuels in practice.

Table 1.2 Atomic and physical properties of hydrogen [1-8]

Property	Hydrogen	Deuterium	Tritium
Relative abundance (%)	99.985	0.0156	10^{-15}
Relative atomic mass (g mol^{-1})	1.008	2.014	3.016
Melting point / K	13.96	18.73	20.62
Boiling point / K	20.39	23.67	25.0
Density /gL^{-1}	0.09	0.18	0.27
Enthalpy of fusion /kJ mol^{-1}	0.117	0.197	-
Enthalpy of vaporization /kJ mol^{-1}	0.904	1.226	-
Enthalpy of bond dissociation /kJ mol^{-1} at 298.2K	435.88	443.35	-
Intermolecular distance / pm	74.14	74.14	-
Ionization Enthalpy / kJ mol^{-1}	1312	-	-
Electron gain enthalpy / kJ mol^{-1}	-73	-	-
Covalent radius / pm	37	-	-
Ionic radius (H^-) / pm	208	-	-

Even in a liquid state, the volumetric energy density of liquid hydrogen (8.4 MJ/L) is less than half that of the other conventional fuels (natural gas 17.8 MJ/L, gasoline 31.1 MJ/L), which is a major drawback with it. To accumulate enough hydrogen for the mobile application we need a large volume of the storage system. [1-9-19] Therefore, to make it practical, various types of research and development are going on by using compressed hydrogen storage, liquid state hydrogen storage, and solid-state hydrogen storage.

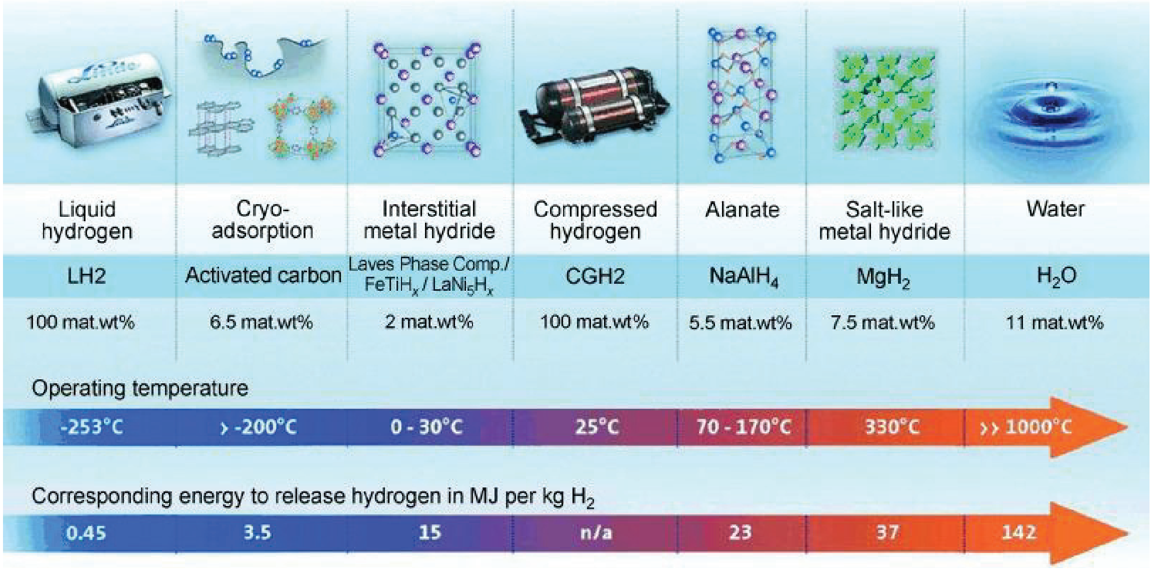

Figure 1.2 Several hydrogen storage technologies and their operating conditions [1-19]

1.4.1 Compressed Hydrogen Storage

In the case of fuel cell vehicle (FCV) rapid supply of compressed hydrogen is made using oxygen from the air, that emit only water and heat classified as zero emissions vehicle. On the other hand in case of internal combustion engine direct burning of hydrogen have been made from compressed hydrogen cylinder. On comparing internal combustion vehicles with fuel cell vehicle, fuel cell vehicles centralize pollutants at the site of hydrogen production, where hydrogen is typically derived from reformed natural gas. A gaseous hydrogen storage system needs a high-pressure gas cylinder that has high tensile and compressive strength to sustain the hydrogen gas pressure with high gravimetric and volumetric density. The recent target of the cylinder, set by the global industry is 70 MPa with a mass of 110 kg, resulting in a gravimetric density of 6.0 mass% and volume density of 30 kg m^{-3}. A lot of energy is lost during compression step of hydrogen in compressed hydrogen storage. Another issue is the relatively large contribution from the content material to the overall weight of the storage system which reduces the gravimetric storage density. This means cylinder materials are the most important parameter for the design of it, if cylinder thickness increases, the gravimetric density of hydrogen including the cylinder decreases. [1-20] New cylinders were developed using a new lightweight composite, which can sustain a pressure up to 80 MPa, and therefore the hydrogen can reach a volume density of 36 kg m^{-3}. Hydrogen compression can be done using a mechanical type piston-cylinder arrangement. The theoretical work ΔG at the isothermal compression for the hydrogen can be calculated using the following equation,

$$\Delta G = \mathrm{R}\, T \ln \left(\frac{p}{p_0}\right), \qquad (2)$$

where R = Avogadro gas constant = 8.314 $\mathrm{jmol^{-1}K^{-1}}$, T is absolute temperature, p_0 and p defines the initial pressure vs end pressure respectively. [1-13-20]

1.4.2 Liquid State Hydrogen Storage

Another potential hydrogen storage method is in the liquid form using the cryogenic vessel. It has an advantage of high hydrogen density which is suitable for large distance transportation. Liquid hydrogen is usually stored at -253 °C at ambient pressure in open systems to prevent pressure build-up. The volumetric density of liquid hydrogen possesses a higher value around 71 $\mathrm{kgm^{-3}}$ than that of hydrogen gas. For liquid hydrogen storage systems, a large amount of energy is required during a liquefaction process. During liquefaction of hydrogen, the conversion from ortho hydrogen to para-hydrogen by an exothermic process is considered to form the stable liquid hydrogen. Normal hydrogen contains 25% of parahydrogen with 75% of ortho hydrogen at room temperature. When we need to store it around -253 °C, the composition of ortho hydrogen is completely converted to para-hydrogen (75% to almost 0%). On the other hand, heat flowing from the environment into the vessel leads to the evaporation of hydrogen. Therefore, the pressure inside the vessel increases, and after a certain maximum pressure it reached (in the order of 1 MPa), hydrogen has to be vented. [1-9-20]

1.4.3 Solid State Hydrogen Storage

Storage of hydrogen in solid-state form is more feasible compared to liquid or gaseous form. This storage method is known for large volumetric capacities which do not suffer from the drawbacks of compressed and liquid hydrogen. Hydrogenation and dehydrogenation are ideally controlled at ambient temperature and pressure conditions especially for utilization as fuels of mobile application, widely explored these days due to safety concerns. Recently various research and development were performed by various scientists on solid-state hydrogen storage materials, and they proposed the following properties are important in optimized hydrogen storage materials. [1-9-20]

① Materials should contain high gravimetric as well as volumetric density of hydrogen

② Appropriate thermodynamic properties: reversible hydrogen absorption/desorption at moderate temperature and pressure

③ Appropriate kinetic properties: quick hydrogen absorption/desorption in a short time

④ The material should be active for H_2 but inactive for O_2, H_2O, moisture, and other impurities

⑤ Easily available at low cost with long cyclic durability

⑥ Easy with safe handling

1.5 Hydrogen Storage Materials

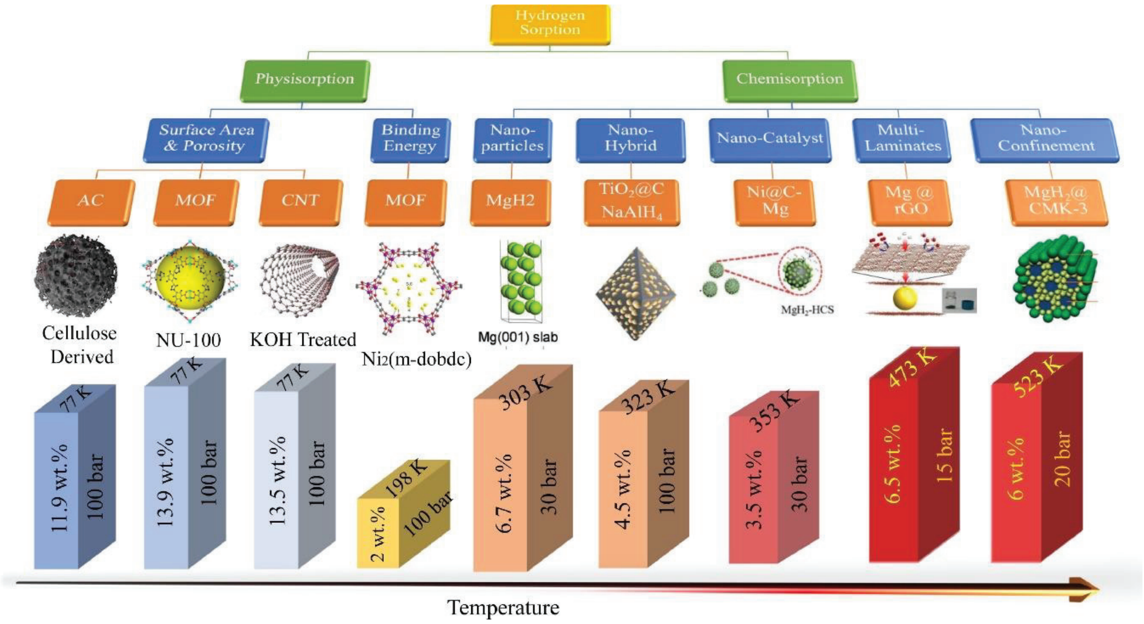

Figure 1.3 A comparison of hydrogen storage capacity of the various materials with increasing temperature. The materials presented above are (i) AC, (ii) MOF, (iii) CNT, (iv) MOF, (v) MgH_2, (vi) TiO_2@C,$NaAlH_4$, (vi) Ni@C-Mg, (vii) Mg@rGO and (viii) MgH_2@CMK-3. [1-26]

1.5.1 Challenges of using Hydrogen as an Energy Carrier

Table 1.2 Hydrogen storage materials and their corresponding challenges are tabulated in the table. [1-15-33]

H_2 storage system	Advantages	Disadvantages	Ongoing efforts
Compressed H_2	Commercially available	Low volumetric capacity High compression energy Heat management during charging required	Develop and design cost-effective vessel/container.
Liquid H_2	Commercially available	H_2 loss Safety issue High liquefaction energy Heat management to reduce boil-off	
Cryo-compressed	High volumetric capacity	High compression/liquefaction energy loss	
Metal hydride	Reversible on-board	Low gravimetric/volumetric capacity Heat management during charging required High operating temperature for H_2 release	Improve kinetics of hydrogen adsorption/desorption along with heat management.
Sorbent and carbon-based materials	Reversible on-board	Low volumetric density Loss of useable H_2	Increase dihydrogen binding energies Optimize material's properties (pore size,

		Low operating temperature for H_2 uptake	pore-volume, surface area, among others).
Chemical hydride	Good volumetric capacity Proper operating temperatures	Thermal management required Off-board regeneration	Develop cost-effective and energy efficient regeneration methods for the spent material.

1.6 Kinetics of Metal Hydrogen-System

The kinetics of hydrogen sorption is defined as the rate of hydrogen absorption and desorption by materials. Like thermodynamics, kinetics is also equally important and decisive for hydrogen storage materials.

The hydrogen desorption reactions in a metal involve several steps as follows:

① Physisorption: molecular hydrogen adsorbed on the solid surface

② Chemisorption: dissociation of molecular hydrogen into atomic hydrogen and it is chemically adsorbed on the solid surface.

③ Migration: penetration of the atomic hydrogen through the surface layer

④ Diffusion: hydrogen atom reached inside bulk either by an interstitial or vacancy mechanism

⑤ Solid solution or hydride formation: finally, new hydride phase formation ensued

where the above order is for the absorption process.

Among all the above-mentioned steps for hydrogen absorption, one of these steps is considered as a rate-determining step. As physisorption of H_2 molecule requires almost no activation energy, hence it is not a rate-determining step. As the concentration of hydrogen molecule impinged on the surface of the metal is directly proportional to applied pressure. All other steps can be rate-determining steps for hydrogen sorption.

The hydrogen desorption follows the same path in a completely reverse direction as shown in figure 1.4.

① Hydride decomposition: started at solid/ hydride surface ($\beta \rightarrow \alpha$)

② Diffusion: hydrogen atoms will be diffused through α-phase

③ Surface penetration: hydrogen atoms move across bulk to an outer surface

④ Recombination: chemisorbed hydrogen will recombine to form molecular hydrogen

⑤ Desorption of gas: physisorbed hydrogen will eliminate from the surface

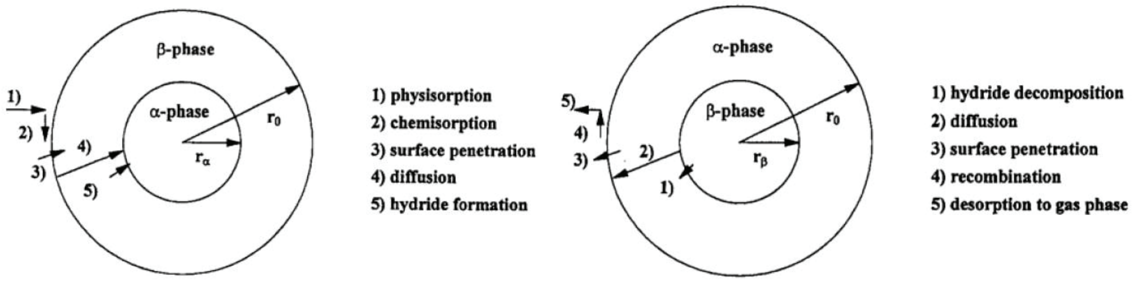

Figure 1.4 Reaction partial steps for the absorption (left) and desorption (right) of hydrogen by a spherical metal/hydride powder particle [1-34]

During the desorption process diffusion coefficient is an important parameter as hydrogen diffuses through the metal/hydride phase. Through the desorption process hydrogen just need to recombine, need to cross a small activation barrier, whereas the absorption process requires dissociation of hydrogen at the metal/hydride surface. As absorption and desorption both occurred through the surface so surface properties of the metal can play an important role to define the kinetics of sorption in the metal hydrogen system. [1-33-37]

The kinetic of hydrogen sorption can be defined as a function of concentration C and temperature T in this way, suppose, kinetics are controlled by only hydride concentration:

$$\theta = \frac{C}{C_0} \tag{3}$$

$$Absorption: \frac{d\theta}{dt} = K_{ab}(T) \cdot (1-\theta), \quad \theta: 0 \rightarrow 1,$$

$$K_{ab}(T) = K_{ab}^{0} \, exp\left(-\frac{E_a^{ab}}{RT}\right), \tag{4}$$

$$Desorption: \frac{d\theta}{dt} = K_{de}(T) \cdot (-\theta), \quad \theta: 0 \leftarrow 1,$$

$$K_{de}(T) = K_{de}^{0} \, exp\left(-\frac{E_a^{de}}{RT}\right), \tag{5}$$

where the parameters of C, C_0, $K_{ab,}^{0}$ $E_{a,}^{ab}$ and $K_{de,}^{0}$ $E_{a,}^{de}$ are the concentration of a reactant at time t, the maximum concentration, the frequency factors, and the activation energies of absorption and desorption processes. The activation energy E_a can be obtained from the slope of ln $K(T)$ versus $1/T$ (Arrhenius plot) by measuring the rate constant $K(T)$ at different temperatures as the following equation:

$$ln\, K(T) = -\frac{E_a}{RT} + ln\, K^0 \tag{6}$$

In real-time practical applications, various types of essential and experimental factors that affect the reaction kinetics of hydrogen-metal systems must be considered. The chemical potential of the surrounding hydrogen gas changed by pressure variation, and the local heat generation caused by the formation of solid solution or hydride changes generally changed the reaction kinetics for hydrogen sorption. The reaction mechanism (order) is one of the most important parameters that need to be considered, to understand the essential kinetic properties of the reaction. Apart from it, various other factors also affect the reaction kinetics like the stabilities of the temperature and pressure in the experimental systems and/or the sample conditions, which are quality, quantity, particle size, porosity, thermal conductivity, and so on. Therefore, the reaction models, experimental as well as instrumental conditions should be considered to discuss the essential kinetic properties of the chemical reactions.

Till now various kind of research and development has been made to enhance the kinetics of hydrogen sorption. In most cases, it either includes nano scaling or the use of catalysts.

Few researchers tried to include alloying as a tool of altering the kinetics, to enhance the hydrogen sorption behavior. However, in our group's opinion alloying mainly affects the thermodynamics of a system, by changing the entire path of hydrogen sorption of a metal/solid-state hydrogen system. The inclusion of alloy generally made the thermodynamic modification, by forming an intermetallic phase in combination with metal/ solid surface which effectively reduced the operating temperature reported by the various researcher. Accordingly, kinetic alteration done by the use of catalysts or nanosizing by reducing the activation barrier reported by various researchers is completely different from thermodynamic alteration. [1-37-42]

The hydrogen sorption kinetics are effectively controlled and enhanced by altering the activation barrier involved with:

① Dissociation of H_2 on the metal surface,

② Diffusion of hydrogen atoms throughout the metal/ solid surface

③ Nucleation (beginning of physical or chemical changes at a discrete point in a system, such as a crystalline formation) of the hydride phase by

The figure shows a sketch of the kinetic barrier for the hydrogen sorption reaction. The energy barrier in a reaction can be estimated using an Arrhenius rate equation as illustrated in the above para.

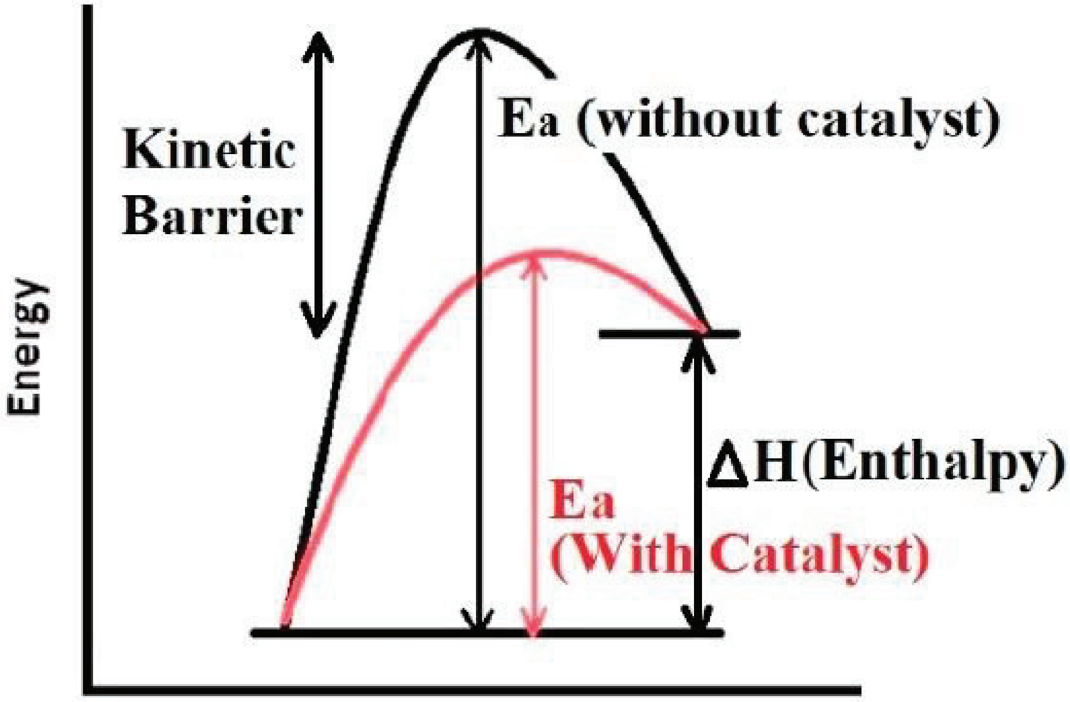

Figure 1.5 Representation of the kinetic barrier of the reaction and lowering the activation energy (Ea) using catalyst [1-71]

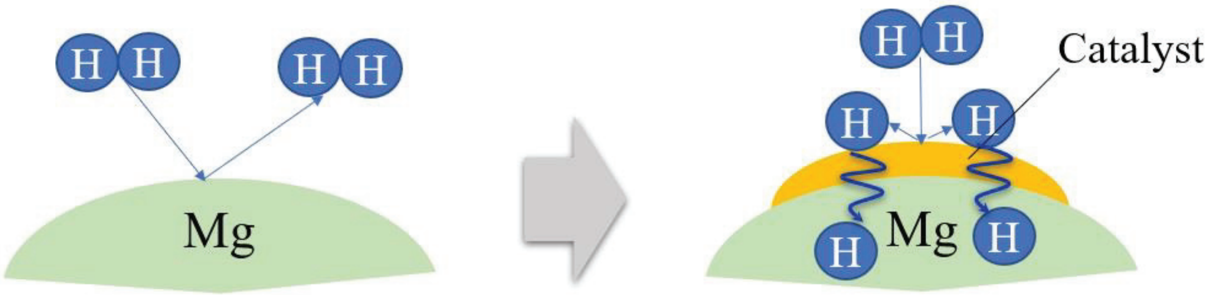

Figure 1.6 Shows the catalysts spread on Mg surface provided the dissociation of the hydrogen molecule

1.6.1 Role of Catalysts

A catalyst is a substance that can be added to a reaction to increasing the reaction rate without getting consumed in the process. Catalysts typically speed up a reaction by reducing the activation energy or changing the reaction mechanism. Catalysts generally speed up a chemical reaction by lowering the amount of energy in any chemical reaction process. In the case of hydrogen storage materials, catalysts provided the interface to reduce the kinetic barrier, to provide faster sorption kinetics.

1.7 Thermodynamics of Metal-Hydrogen System

The thermodynamic destabilization can be achieved by two methods:

① One of which is downsizing the particles; however, it can be achieved only if the size is reduced to several nanometers, which is neither easy to achieve nor to maintain.

② The second approach of introducing an intermediate stage.

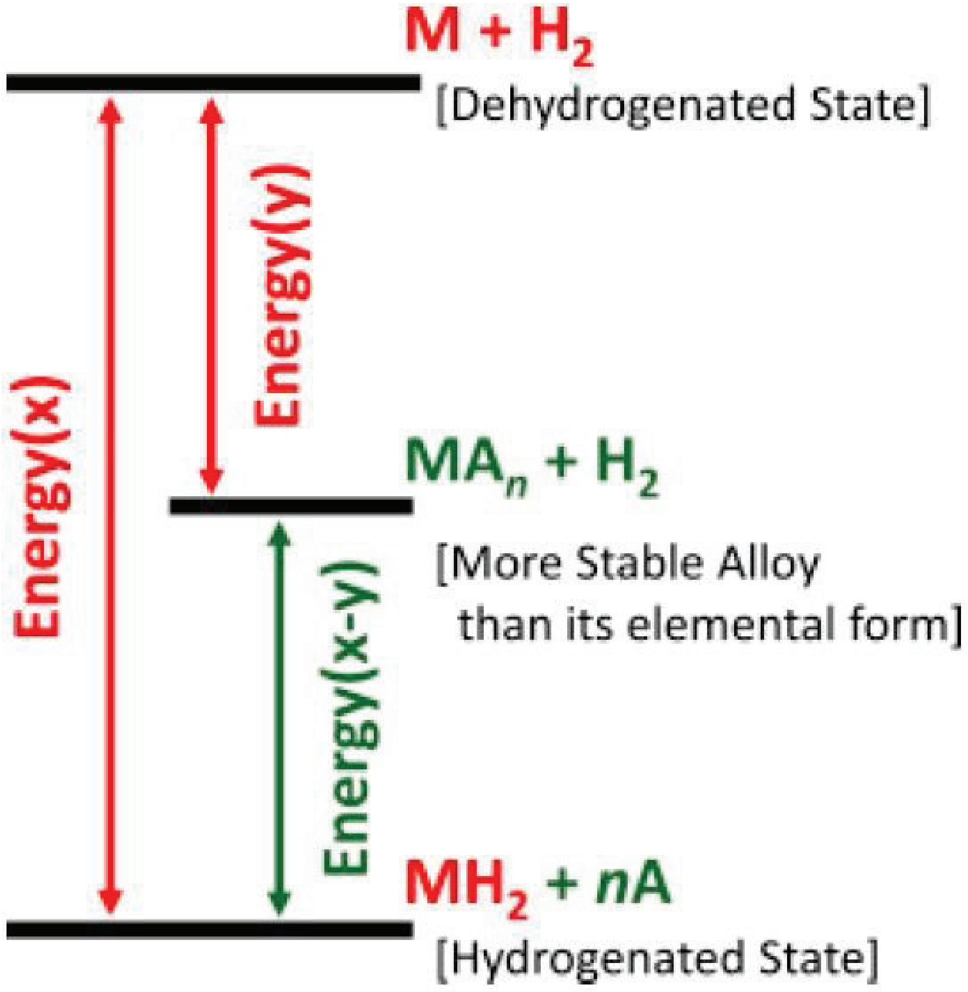

Figure 1.7 Schematic of destabilization process of a hydride MH using third element [1-72].

Thus, nano-scaling/destabilization (thermodynamic modification) using high energy ball milling can accelerate the kinetics through

① Creation of fresh surface for chemisorption,

② Decreased diffusion distance for H atoms,

③ By increasing surface to volume ratio

Thus, nano crystallites provide the sorter diffusion distance for hydrogen sorption and enhance the kinetics. The figure 1.8 combinedly talks about the kinetics as well as thermodynamic alteration, whereas nano-crystallization falls in both kinetic as well as thermodynamic alteration.

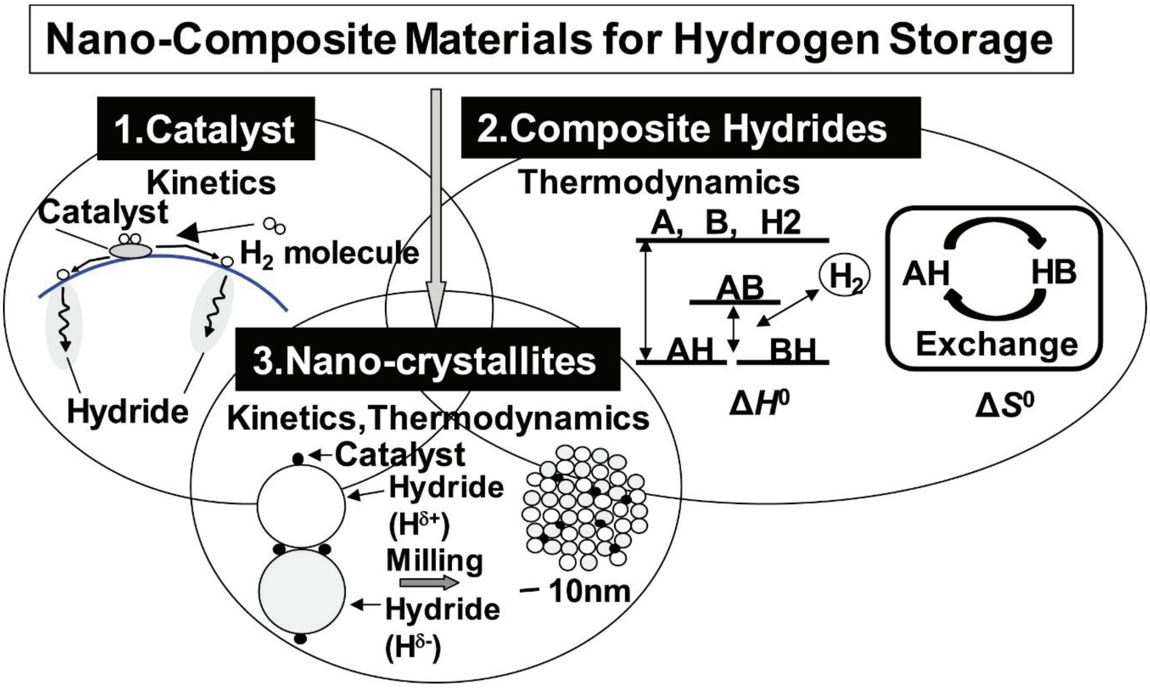

Figure 1.8 Design concept of nano composite materials for hydrogen storage [1-41]

Even though the nano sizing showed outstanding performance, we generally avoid its use for practical applications, especially because:

① to develop such a small nano-sized structure is not easy on commercial/industrial level,

② the cyclability (hydrogenation and dehydrogenation) of these nanostructures is not so good as these agglomerates during the sorption cycles and they lose the benefits of nano-sizing

So, in the modern era, most researchers prefer the use of a catalyst to enhance the hydrogen sorption kinetics.

A catalyst is defined as a material that enhances the sorption rate of a metal/alloy without participating in the chemical reaction and reducing the activation barrier only. [1-36-43]

1.8 Magnesium and Magnesium Hydride

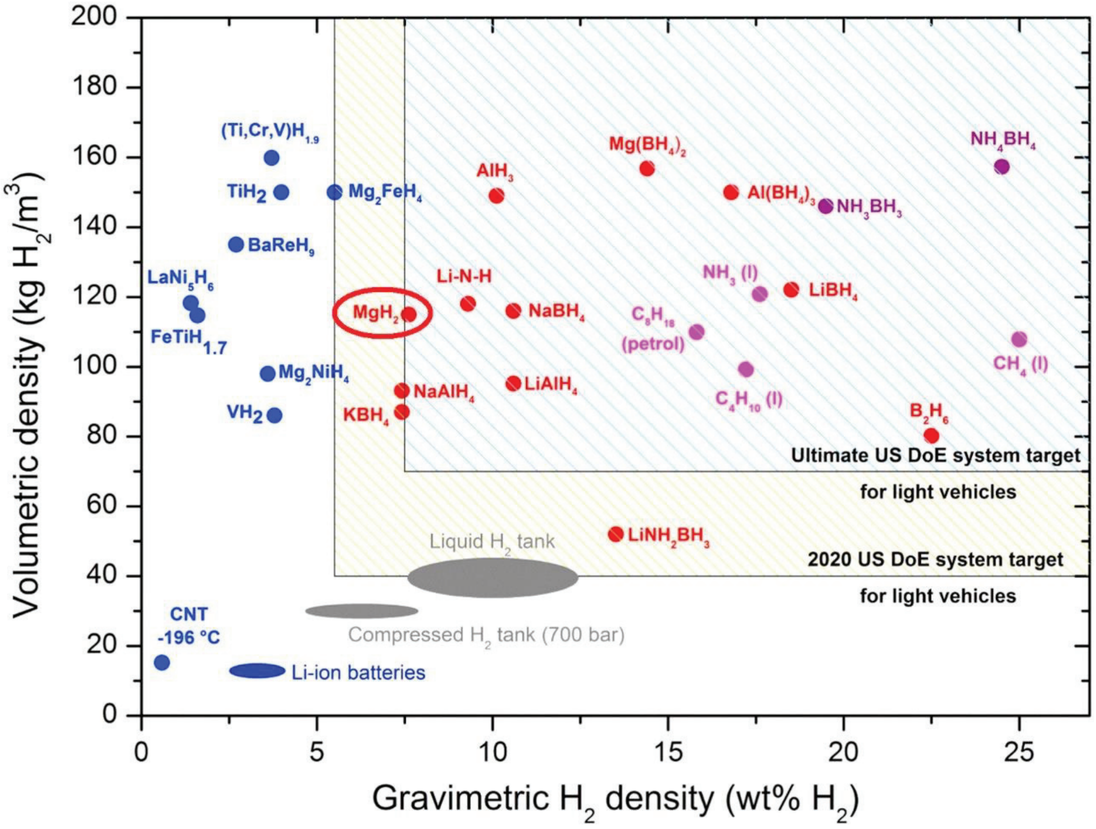

Figure 1.9 Overview of selected materials and their volumetric and gravimetric hydrogen density. The U.S. Department of Energy targets for the hydrogen storage system is also shown for comparison.

The volumetric hydrogen storage density for MgH_2 is 120 kg H_2/m^3 on the other hand gravimetric hydrogen storage density of MgH_2 is 7.6 wt.% as shown in Figure 1.8 reveals the Mg as a potential hydrogen storage materials.

1.8.1 Magnesium as an important Hydrogen Storage Materials

① Its relatively high gravimetric ($\rho_m(\gamma\text{-}MgH_2) = 7.6$ wt.% of H

② Volumetric densities $\rho_V = 0.11$ kg H/dm^3

③ Natural abundance, cost-effective and user safety

④ Volumetric density is about twice that of liquid H_2

⑤ Has highest energy density of (9MJ/kg Mg) of all reversible hydrides applicable for hydrogen storage (reversible in nature)

⑥ MgH_2 differs from other metal hydrides according to the type of M-H bonds, crystal structure, and properties and like ionic hydrides of alkali and alkaline earth metals

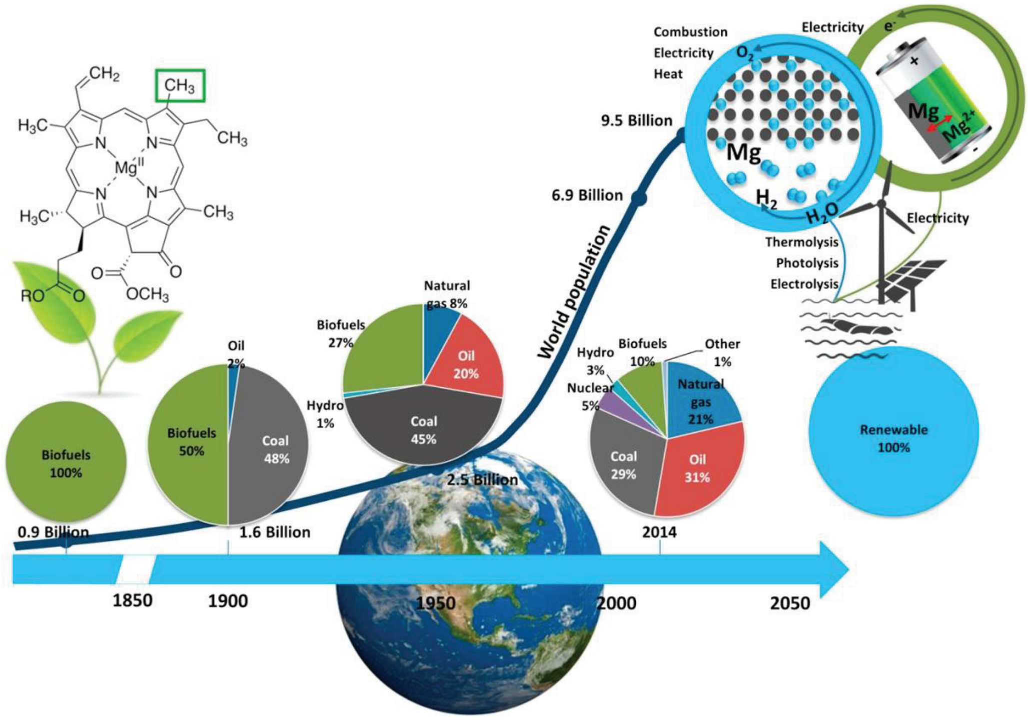

Figure 1.10 Evolution of the world totals primary energy supply and the world population supported by the earth ecosystem. Nature has found ways to effectively utilize Mg to perform vital functions sustaining life, e.g. Mg is at the core of the functions of many cells in the human body and the center of photosynthetic processes sustaining life on earth. Mimicking natural systems by

creating "artificial" energy ecosystems based on abundant resources easily recyclable has the potential to sustain a population of 10 billion. The possibility of developing better batteries based on Mg has been reviewed elsewhere [1-42].

Magnesium hydride (MgH_2) was first synthesized using by pyrolysis method with the help of ethyl magnesium halides in 1912. Later, Wiberg and Bauer synthesized the MgH_2 using the pyrolysis method by di-alkyls of Mg in 1950. Two solvent-based synthesis methods were demonstrated to produce magnesium hydride, the pyrolysis of magnesium dialkylene and hydrogenation of magnesium dialkylene with diborane. During a similar time, the hydrides of beryllium, lithium, and magnesium were prepared using lithium aluminum hydride in ethyl ether or diethyl ether solution, with a yielded purity of about 75 % for magnesium hydride production. Subsequently, synthesis methods involving the thermal decomposition of magnesium diethyl at 200 °C in high vacuum, the hydrogenolysis of Grignard reagents

$$2RMgX + 2H_2 \rightarrow 2RH + MgX_2 + MgH_2 \qquad (7)$$

catalytic magnesium hydrogenation with anthracene in THF via anthracene-magnesium as an intermediate and the reaction of phenyl silane and dibutyl magnesium were employed.

Around 1960, J. J. Reilly, a researcher at the Brookhaven National Laboratory in the United States, discovered a hydrogen storage alloy based on Mg named as Mg_2Ni, with a reversible hydrogen storage capacity of 3.6 wt.%. Of particular interest, solutions to tailor magnesium (Mg) toward practical targets have remained at the center of investigations because hydrides based on Mg have the potential to lead high capacity and low-cost materials for reversibly absorbing hydrogen.

1.8.2 Magnesium Hydride Polymorph and its Phase diagram

Magnesium hydride has various kinds of known polymorphs that are thermodynamically stable at different temperatures and pressures. Bastide et al. experimentally demonstrated these polymorphs and later proposed modeling work. Moser et al. proposed pressure-temperature phase diagrams for magnesium hydride and its isotopic analogs shown in figure 1.11. It is important to understand the stability and changes of MgH_2, especially after ball milling, after dehydrogenation, after re-hydrogenation, and at higher temperature and pressure conditions. Generally, magnesium hydride exists as an α-MgH_2 (with a rutile structure) phase under ambient conditions.

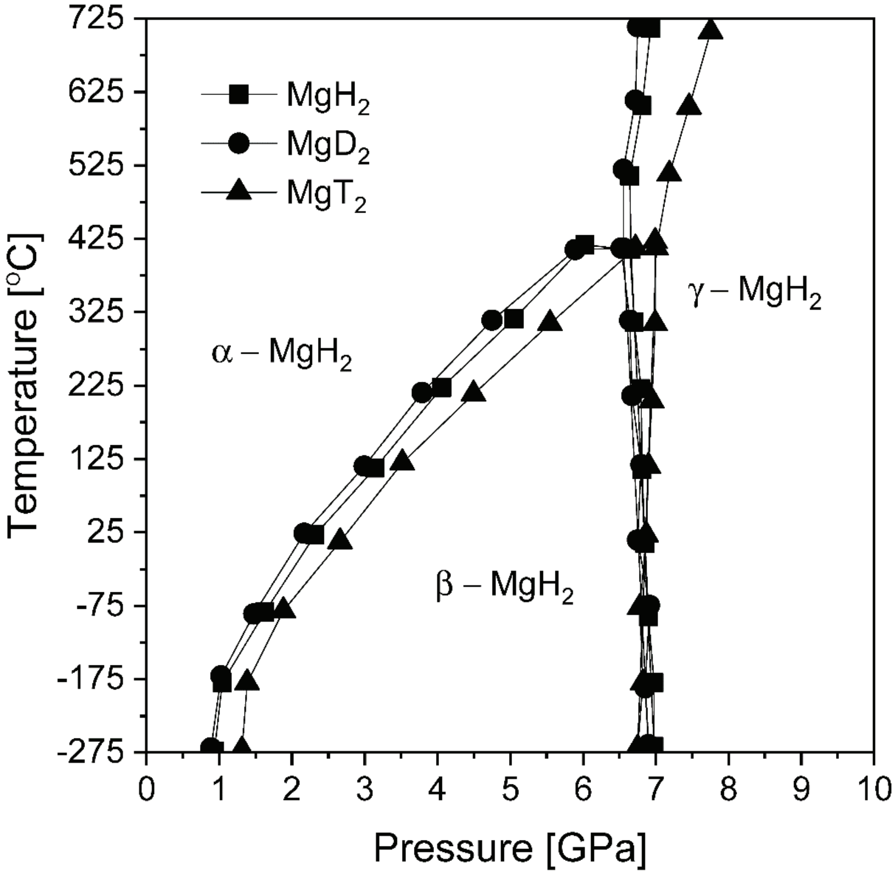

Figure 1.11 Pressure-temperature (P–T) phase diagrams for three studied isotopic analogs of magnesium dihydride: MgH_2, MgD_2, and MgT_2. The graph was prepared based on the reported data [1-44]

A further change in the temperature and pressure leads to a change in the phase transformation. At low temperatures, if you want to transform α-MgH_2 (TiO_2 type structure) to β- and γ-MgH_2 then you need to apply high pressure. The transformation of the β-MgH_2 phase (with a modified CaF_2 structure) is possible only at temperatures below 700 °C. Above that temperature, the direct transformation from α-MgH_2 to γ-MgH_2 (the PbO_2-type structure) with an orthorhombic structure occurs. From a practical point of view, for the research related to hydrogen storage materials, only two polymorphs are important i.e., α-MgH_2 (TiO_2 type structure) and γ-MgH_2 (the PbO_2-type structure). Originally named α-MgH_2 (TiO_2 type structure) nowadays known as the β-MgH_2 phase, in most of the current papers. Fortunately, the γ phase is still pronounced with its original name γ phase. The one polymorph (the TiO_2 structure) β-MgH_2 phase is completely stable under ambient conditions. When the β-MgH_2 phase ball is milled for a longer duration, by the collisions of balls with milled sample and vessel walls, high pressure is generated inside the vessel which caused the phase transformation of β-MgH_2 phase (the TiO_2 structure) to the metastable γ-MgH_2 (the PbO_2-type structure). The γ phase (γ-MgH_2) is a high-pressure polymorphic form of the β-MgH_2 phase.

1.8.3 Thermodynamic of MgH_2

The high thermodynamic stability of MgH_2 is always a serious drawback for it, which up to some extent restricts the practical application of this material.

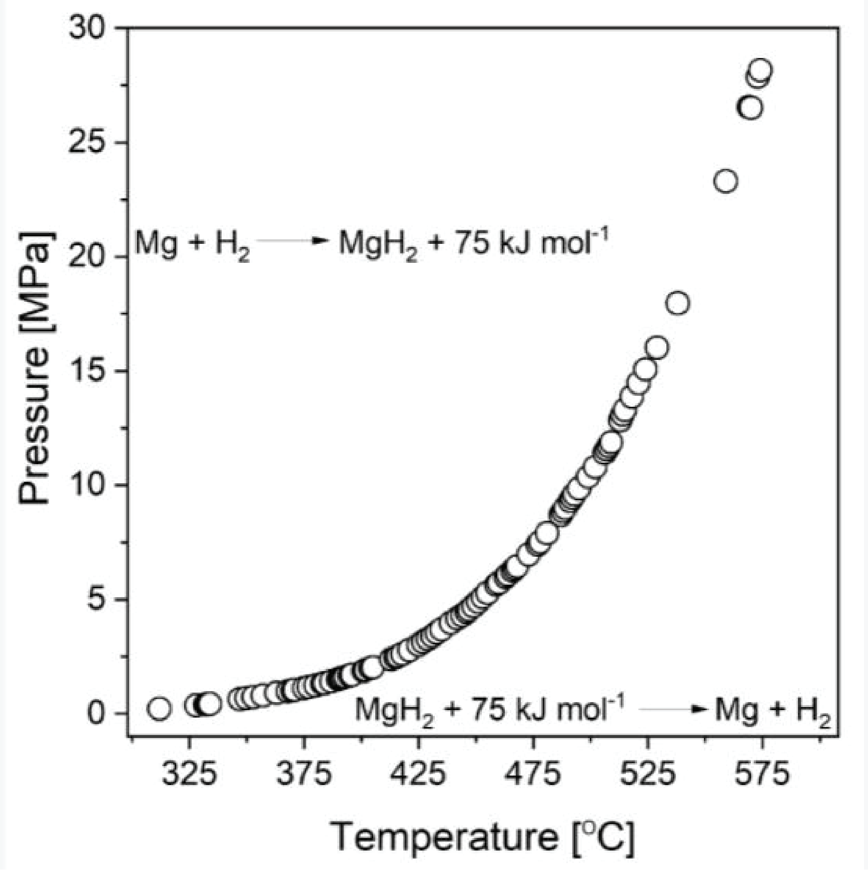

Figure 1.12 Temperature dependence of the MgH_2 dissociation pressure. The graph was prepared based on data from Stampfer et al. [1-49]

Stampfer et al. firstly reported the dissociation enthalpy of MgH_2 based on decomposition pressure measurements between 314 and 576 °C. MgH_2 is considered a highly stable hydride because it holds high enthalpy of formation. The dependence of the decomposition plateau pressure on temperature for magnesium hydride was shown in Figure 1.12, prepared based on data obtained from Stampfer's measurements.

Desorption thermodynamics of Mg:

① Usually, for pristine MgH_2, hydrogen desorption generally starts from 400 °C at 1 bar pressure, which determines that the H value is high for MgH_2.

Absorption thermodynamics of Mg:

① The hydride (hydride phase formation) growth rate of the Mg phase depends on the hydrogen pressure since, as the pressure increases, the thermodynamic driving force for the reaction increases.

A high thermodynamic barrier can be resolved by (a) Nanosizing, (b) Alloying, or by introducing an intermediate stage. [1-33-44]

1.8.4 Kinetic of MgH_2

Various factors hinder the kinetics of a clean MgH_2/ Mg surface:

Desorption kinetics of Mg:

① The velocity of atomic hydrogen at magnesium/ magnesium hydride interface during phase transformation started at solid/ hydride surface ($\beta \rightarrow \alpha$)

② Recombination of atomic hydrogen

Absorption kinetics of Mg shown schematically in figure 1.13:

① It required a very high energy of approximately 110 kJ/mol Mg surface for dissociation of the hydrogen atom.

② Penetration of the atomic hydrogen through the surface layer also needs the energy of approximately 21 kJ/ mol of H_2.

③ The diffusion of dissociated hydrogen atoms within metal hydride is also a difficult process, which needs the energy of approximately 250 kJ/mol of H_2 to form the hydride phase. [1-33-46]

Several research and development are going on to overcome problems associated with sluggish reaction kinetics of MgH_2. Two important approaches were generally made by the researcher to solve the kinetic issues namely: (a) Nanosizing and (b) Use of catalysts.

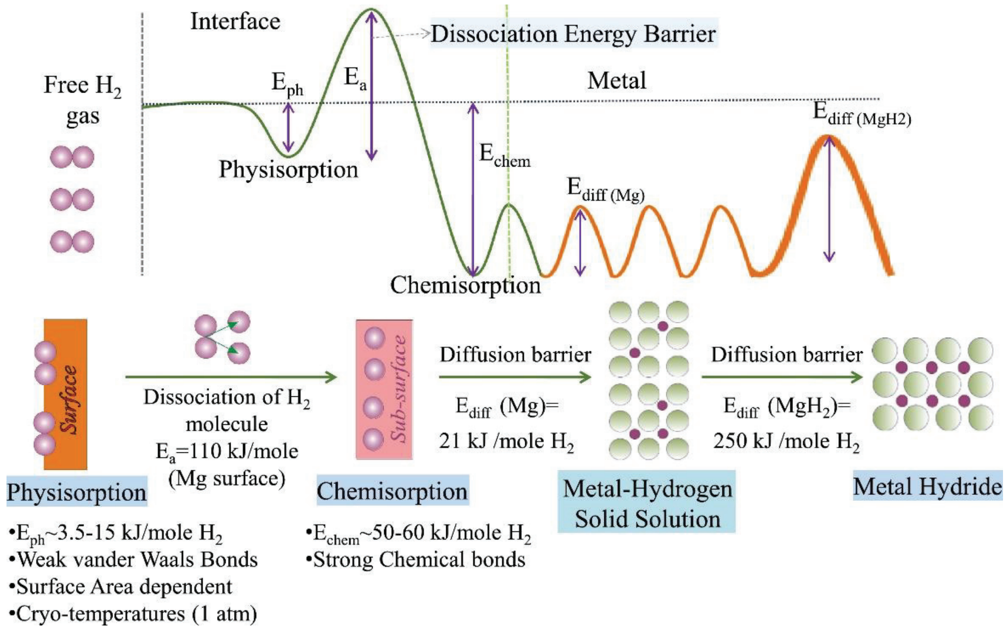

Figure 1.13 Interaction of hydrogen with the material in various steps: (i) Physisorption (ii) Chemisorption (iii) solid solution and (iv) compound formation [1-27, 52]

1.8.5 Other important properties of MgH_2

MgH_2 was firstly synthesized by Wiberg et al. in 1951, even after it is difficult to find commercial magnesium hydride with the highest purity (despite the official specifications given by manufacturers). In the magnesium hydride sample lot, there is always a mixture of magnesium hydride, magnesium metal, and magnesium hydroxide contamination. The magnesium hydroxide Mg $(OH)_2$ is generally present in the form of an amorphous layer on the surface of the particles, while magnesium is present in the core of the particles making it very difficult to observe using X-ray diffraction or some other method. In a few other cases, like in coarser particles (a coarse powder or turnings), it is almost impossible to say about small Mg particle which is inside of coarser particle of MgH_2, on the other hand at the same time after dehydrogenation, hydrogenation of inner Mg is really difficult even at much higher temperature and pressure, due to the formation of a hydride layer on the outside, preventing the reaction from striking hydrogenation throughout the whole volume of the particle, even though the analyzed sample was a commercial product. [1-50-55]

With the help of the above discussion, we reached to following important conclusion for MgH_2:

① An initial problem with magnesium is its strong affinity to oxygen, resulting in a formation of a thin oxide layer on the surface of the Mg particles which limits the hydrogen diffusion. On the other hand, it also causes the formation of MgO during ball milling with oxide yields to decrease in the hydrogen weight loss compared to the theoretical value.

② Similarly, a small presence of water leads to the surface formation of magnesium hydroxide ($Mg(OH)_2$). The presence of magnesium metal and magnesium hydroxide as contamination inside pure MgH_2 determines the hydrogen capacity weight loss, which generally leads to the difference between theoretical capacity and experimental capacity. By using the purity of MgH_2, it was generally calculated by various researchers and theoretically proposed. It is important to note that we can easily observe the presence of hydroxide group either using thermogravimetric analysis (release of -OH groups from hydroxides) or using differential scanning calorimetry curve (heat effect could be seen).

③ It is really difficult to execute hydrogenation of inner Mg (inside the coarser particle of Mg), even at a much higher temperature and pressure, as well as regardless of the initial material either coarser or fine, once the magnesium starts hydride formation, the layer of

MgH_2 impedes the diffusion of hydrogen to the remaining unreacted metal due to the formation of initial hydride layer at the outer surface which restricted the nucleation sites, causes a decrease in the hydrogenation capacity up to some extent.

1.9 Thermodynamic modification of Magnesium-Hydrogen System

As explained before, the stable thermodynamics of MgH_2 is the major drawback. Based on the Van't Hoff equation, we can conclude that changing the enthalpy and entropy of the hydrogenation reaction is an efficient way to decrease the desorption temperature of Mg/MgH_2 systems. Taking into account that changing the entropy has little effect on metal hydrogen systems, decreasing the enthalpy change for the reaction is the basic guideline for decreasing the desorption temperature of Mg/MgH_2 systems. There were many thermodynamic modifications of MgH_2 was achieved by alloying, nanostructuring, metastable phase formation and changing the reaction pathways.

Vajo et. al. reported the desorption enthalpy decreased to 36.4 kJ/mol due to the formation of Mg_2Si, following chemical reactions was proposed. [1-73]

$$MgH_2 + Si \rightarrow Mg_2Si + 2H_2 \tag{8}$$

Walker et al. milled MgH_2 with Ge under an Ar atmosphere. The desorption temperature of MgH_2/Ge dramatically decreased to 130 °C. Unfortunately, the desorption product Mg_2Ge could not absorb hydrogen to form MgH_2 and Ge. [1-74]

$$MgH_2 + Ge \rightarrow Mg_2Ge + 2H_2 \tag{9}$$

Vajo et. al. reported the decrease in desorption enthalpy of MgH_2 by introducing $LiBH_4$. [1-75]

$$MgH_2 + 2LiBH_4 \leftrightarrow 2LiH + MgB_2 + 4H_2 \tag{10}$$

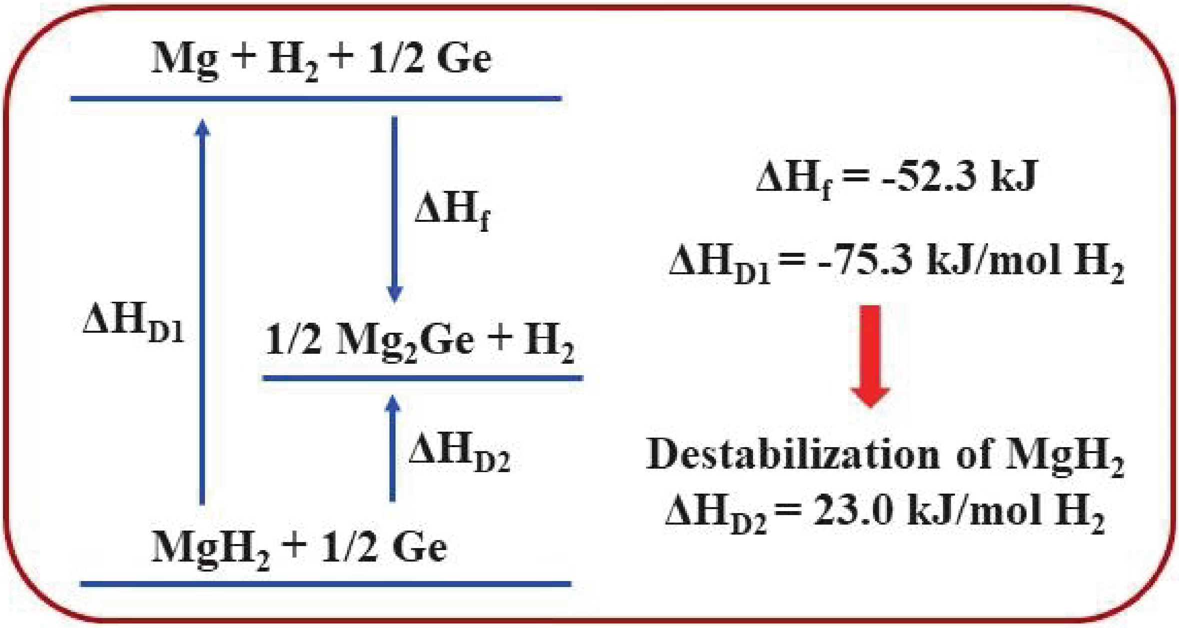

Figure 1.14 Thermodynamic modification of MgH_2 by introducing Ge as an intermediate element

Imamura et. al. reported the decrease in desorption enthalpy by introducing Al as an intermediate element. For the first step (Equation (11), the reaction enthalpy is approximately 62.7 kJ/mol. Although the whole dehydriding reaction enthalpy is 77.7 kJ/mol, which is slightly higher than that of pure MgH_2, the whole reaction entropy increased from 139 to 144 J/(mol·K). Therefore, the desorption temperature of MgH_2-Al would be slightly lower than pure MgH_2. The system can reversibly store 4.4 wt. % H_2. [1-76]

$$2MgH_2 + 3Al \leftrightarrow Mg_2Al_3 + 2H_2 \qquad (11)$$

$$9MgH_2 + 4Mg_2Al_3 \leftrightarrow Mg_{17}Al_{12} + 9H_2 \qquad (12)$$

1.10 Kinetic modification of Magnesium-Hydrogen System using various catalysts

Light s- and p-block elements, such as lithium (Li), sodium (Na), magnesium (Mg), calcium (Ca), and their compounds, are promising candidates for storing massive amounts of hydrogen for stationary and onboard applications. Among all the light element-based materials, magnesium has been researched as a hydrogen storage material in several decades with 7.6 wt.% of hydrogen storage capacity.

As MgH_2 has the highest energy density (9 MJ/kg Mg) of all reversible hydrides applicable for hydrogen storage. The hydrogen absorption and desorption processes of Mg and Mg-based compounds have been studied extensively. Most of these studies on the Mg-MgH_2 system have targeted the issues of stringent hydrogen absorption and desorption kinetics. Remarkable catalytic effects for these phenomena have been found by milling MgH_2 with 3d transition metal elements and oxides. Hanada et al. reported that the composite, MgH_2 with 1 mol% Nb_2O_5 milled for 20 h, was able to absorb 4.5 wt.% of hydrogen after full desorption even at room temperature under a pressure lower than 1.0 MPa within 15 s. The improvement of the desorption properties was caused by the catalytic effect of reduced niobium oxide. It is noteworthy that Kimura et al. reported the hydrogen absorption of MgH_2 with 1 mol% of Nb_2O_5 even at 150°C. In addition to the above-mentioned reports as related works, the catalytic effects of characteristic Ta_2O_5 have also been investigated. Despite this much investigation still, the catalytic mechanism of oxides is not completely understood yet in detail. The difficulty in understanding the detailed catalysis is caused by the difference between the preparation processes of the oxides and their starting states. In addition, ineffective processes, such as extensive milling duration, are sometimes required to obtain highly catalytic active states. Owing to the above-mentioned complicated process, it is difficult to compare the essential catalytic properties of oxides. [1-57-70].

1.10.1 Transition Metal

Of all the groups of elements available in the universe, the transition metals are the most confusing to define because there are different definitions of which elements should be included. According to the IUPAC, a transition metal is any element with a partially filled d electron sub-shell. This describes groups 3 through 12 on the periodic table, although the f-block elements (lanthanides and actinides, below the main body of the periodic table) are also transition metals. The d-block elements are named transition metals, while the lanthanides and actinides are named "inner transition metals”. [1-38]

The elements are called "transition" metals because the English chemist Charles Bury used the term in 1921 to describe the transition series of elements, which referred to the transition from an inner electron layer with a stable group of 8 electrons to one with 18 electrons or the transition from 18 electrons to 32.

Because they possess the properties of metals, the transition elements are also known as transition metals. These elements are very hard, with high melting points and boiling points. Moving from left to right across the periodic table, the five *d* orbitals become more filled. The *d* electrons are loosely bound, which contributes to the high electrical conductivity and malleability of the transition elements. The transition elements have low ionization energies. They exhibit a wide range of oxidation states or positively charged forms. The positive oxidation states allow transition elements to form many different ionic and partially ionic compounds. The formation of complexes causes the *d* orbitals to split into two energy sublevels, which enables many of the complexes to absorb specific frequencies of light. Thus, the complexes form characteristic-colored solutions and compounds. Complexation reactions sometimes enhance the relatively low solubility of some compounds.

There are several properties shared by the transition elements that are not found in other elements, which result from the partially filled d subshell.

1.10.2 The Oxidation States

The oxidation state of any atom is defined as the ability of an atom to oxidize (to lose electrons) or to reduce (to gain electrons) or combined with other elements and forms a chemical compound. It talks about the number of electrons that an atom loses, gains, or appears to use when bonding with another atom in a compound.

It means the valence electrons of the transition elements are in (n-1) d and ns orbitals which have little difference in energies. Both energy levels can be used in bond formation. They show the +2-oxidation state due to the 2 electrons in ns orbitals when the electrons of (n-1) d remain unaffected. The higher oxidation state from +3 to +7 is due to the use of all 4s and 3d electrons in the transition series of elements. To fully understand the phenomena of oxidation states of transition metals, we must understand how the unpaired d-orbital electrons take participation in bonding. There are five orbitals in the d subshell manifold. As the number of unpaired valence electrons increases, the d-orbital increases, the highest oxidation state increases. This is because unpaired valence electrons are unstable and eager to bond with other chemical species. This means that the oxidation states would be the highest in the very middle of the transition metal periods due to the presence of the highest number of unpaired valence electrons. It means the excited state, the (n-1) d electrons become bonding and give the variable states to the atom. Thus, the variable oxidation state is due to the participation of both ns and (n-1) d orbitals in bonding.

Highest oxidation state for a Transition metal = Number of unpaired d-electrons + Two s-orbital electrons

Scandium is one of the two elements in the first transition metal period which has only one oxidation state (zinc is the other, with an oxidation state of +2). All the other elements have at least two different oxidation states. Manganese, which is in the middle of the period, has the highest number of oxidation states, and indeed the highest oxidation state in the whole period since it has five unpaired electrons.

Table 1.3 Variation in oxidation state of 3d series

Elements	Oxidation States
Sc	+2, +3
Ti	+2, +3, +4
V	+2, +3, +4, +5
Cr	+2, +3, +4, +5, +6
Mn	+2, +3, +4, +5, +6, +7
Fe	+2, +3, +4, +5, +6
Co	+2, +3, +4
Ni	+2, +3, +4
Cu	+1, +2
Zn	+2

Table 1.4 Variation in oxidation state of 4d series

Elements	Oxidation States
Y	+3
Zr	+3, +4
Nb	+2, +3, +4, +5
Mo	+2, +3, +4, +5, +6
Tc	+2, +4, +5, +7
Ru	+2, +3, +4, +5, +6, +7, +8
Rh	+2, +3, +4, +6
Pd	+2, +3, +4
Ag	+1, +2, +3
Cd	+2

Table 1.5 Variation in oxidation state of 4d series

Elements	Oxidation States
La	+3
Hf	+3, +4
Ta	+2, +3, +4, +5
W	+2, +3, +4, +5, +6
Re	+1, +2, +4, +5, +7
Os	+2, +3, +4, +6, +8
Ir	+2, +3, +4, +6
Pt	+2, +3, +4, +5, +6
Au	+1, +3
Hg	+1, +2

1.11 References

[1-1] Share of Renewable Energy Power in Japan, 2018 (Preliminary Report)

[1-2] T. Aderinto, H. Li, Review of power performance and efficiency of wave energy converters. Energies, 2019, 12 (22), 4329.

[1-3] Barbier, E., Nature and technology of geothermal energy: A review. Renewable and Sustainable Energy Reviews SU1, 1997, (1-2), 1-69

[1-4] Renewable Energy: Sources and Types, https://www.greenesa.com/public/article/renewable-energy-sources-types

[1-5] Kojima , Y., Chapter 5 Hydrogen Storage materials, in New and future Developments in catalysis. 2013, Elsevier: Amsterdam. P. 99-136.

[1-6] Fukai, Y., ed. The metal hydrogen system. Materials Science, Springer. 14

[1-7] National Institute of Standards and technology, NIST, Hydrogen

[1-8] Züttel A. Hydrogen storage methods. Springer-Verlag (2004); 91,157–172.

[1-9] Züttel A, Remhof A, Borgschulte A F. Hydrogen: the future energy carrier. Phil. Trans. R. Soc. A (2010); 368, 3329–3342.

[1-10] Schlapbach L, Züttel A. Hydrogen-storage materials for mobile applications. Nature (2001); 414,353-358.

[1-11] https://www.japan.go.jp/g20japan/index.html

[1-12] Züttel A. Materials for hydrogen storage. Materials today (2003); 6-9, 24-33.

[1-13] Lototskyy M V, Yartys V A, Pollet B G, Bowman R C. Metal hydride hydrogen compressors: A review. Int. J. Hydrogen Energy (2014); 39, 5818-5851.

[1-14] Kawasaki Hydrogen Road: Paving the way for a hydrogen-based society. http://global.kawasaki.com/en/stories/hydrogen/.

[1-15] Endo, N., Suzuki, S., Goshome, K. & Maeda, T. Operation of a bench-scale TiFe-based alloy tank under mild conditions for low-cost stationary hydrogen storage. *Int. J. Hydrogen Energy* **42**, 5246–5251 (2017).

[1-16] Takeichi, N. *et al.* "Hybrid hydrogen storage vessel", a novel high-pressure hydrogen storage vessel combined with hydrogen storage material. *Int. J. Hydrogen Energy* **28**, 1121–1129 (2003).

[1-17] I.P. Jain, P. Jain and A. Jain: Novel hydrogen storage materials: A review of lightweight complex hydrides; J. Alloy. Compd. 503 (2010) 303-339.

[1-18] Renewable energy: Sources and types, https://www.greenesa.com/public/article/renewable-energy-sources-types

[1-19] L. Schlapbach and A. Züttel: Hydrogen-storage materials for mobile applications; Nature 414 (2001) 353-358.

[1-20] N.K. Zhevago: Other methods for the physical storage of hydrogen, (Compendium of Hydrogen Energy, Elsevier, 2016) pp. 189-218.

[1-21] National Council of Educational Research and Training, https://ncert.nic.in/textbook.php

[1-22] V. Charbonnier, J. Zhang, J. Monnier, L. Goubault, P. Bernard, C. Magén, V. Serin and M. Latroche: Structural and Hydrogen Storage Properties of Y_2Ni_7 Deuterides Studied by Neutron Powder Diffraction. J. Phys. Chem. C 119 (2015) 12218-12225.

[1-23] S. Kumar, A. Jain, T. Ichikawa, Y. Kojima and G.K. Dey: Development of vanadium-based hydrogen storage material: A review Renew. Sustain. Energy Rev. 72 (2017) 791-800.

[1-24] M. Spodaryk, N. Gasilova and A. Züttel: Hydrogen storage and electrochemical properties of $LaNi_{5-x}Cu_x$ hydride-forming alloys; J. Alloy. Compd. 775 (2019) 175-180.

[1-25] U. Eberle, M. Felderhoff, and F. Schüth, Chemical and Physical Solutions for Hydrogen Storage, Angew. Chem. Int. Ed. 2009,48, 6608 – 6630.

[1-26] Gupta, G. V. Baron, P. Perreault, S. Lenaerts, R. Ciocarlan, P. Cool, P.G.M. Mileo, SvenRogge, V. Speybroeck, G. Watson, P. Voort, M. Houlleberghs, E. Breynaert, J. Martens, J.F.M. Denayer,

[1-27] Hydrogen Clathrates: Next Generation Hydrogen Storage Materials, Energy Storage Materials, 41, 2021, 69-107.

[1-28] T.S. Blankenship II, N. Balahmar, R. Mokaya Nat. Commun., 8 (2017), p. 1545

[1-29] Ahmed, S. Seth, J. Purewal, A.G. Wong-Foy, M. Veenstra, A.J. Matzger, D.J. Siegel Nat. Commun., 10 (2019), p. 1568 J. Lyu, V. Kudiiarov, A. Lider, Nanomaterials, 10 (2020)

[1-30] J.D. Tarver, H.Z.H. Jiang, M.T. Kapelewski, K.E. Hurst, P.A. Parilla, A. Ayala, T. Gennet t, S.A. Fitzgerald, C.M. Brown, R. Long Chem. Mater., 30 (2018), pp. 8179-8189

[1-31] X. Zhang, Y. Liu, Z. Ren, X. Zhang, J. Hu, Z. Huang, Y. Lu, M. Gao, H. Pan Energy Environ. Sci., 14 (2021), pp. 2302-2313

[1-32] D. Peng, Z. Ding, Y. Fu, Y. Wang, J. Bi, S. Han, RSC Adv, 8 (2018), 28787-28796

[1-33] E.S. Cho, A.M. Ruminski, S. Aloni, Y. Liu, J. Guo, J.J. Urban, Nat. Commun. (2016), 1-8

[1-34] Y. Jia, C. Sun, L. Cheng, M. Abdul Wahab, J. Cui, J. Zou, M. Zhu, X. Yao, Phys. Chem. Chem. Phys., 15 (2013), 5814-5820

[1-35] Martin, M.; Gommel, C.; Borkhart, C.; Fromm, E. Absorption and desorption kinetics of hydrogen storage alloys, J. Alloy. Compd, 1996, 238, 193–201.

[1-36] H. Wang, H.J. Lin, W.T. Cai, L.Z. Ouyang and M. Zhu: Tuning kinetics and thermodynamics of hydrogen storage in light metal element based systems – A review of recent progress; J. Alloy. Compd. 658 (2016) 280-300.

[1-37] F. Leardini, J.R. Ares, J.F. Fernández, J. Bodega and C. Sánchez: An investigation on the thermodynamics and kinetics of magnesium hydride decomposition based on isotope effects; Int. J. Hydrogen Energy 36 (2011) 8351-8357.

[1-38] A.S. Pedersen, J. Kjøller, B. Larsen and B. Vigeholm: Magnesium for hydrogen storage; Int. J. Hydrogen Energy 8 (1983) 205-211.

[1-39] I.P. Jain, C. Lal and A. Jain: Hydrogen storage in Mg: A most promising material; Int. J. Hydrogen Energy 35 (2010) 5133-5144.

[1-40] V. Be´rube´, G. Radtke, M. Dresselhaus, G. Chen, Size effects on the hydrogen storage properties of nanostructured metal hydrides: A review, INTERNATIONAL JOURNAL OF ENERGY RESEARCH, Int. J. Energy Res. 2007; 31:637–663

[1-41] U. S. Department of Energy: http://www.energy.gov/.

[1-42] Y. Kojima, Hydrogen storage materials for hydrogen and energy carriers, Int. J Hydrogen Energy, 44, 2019, 18179-18192.

[1-43] Key world energy statistics, Int. Energy Agency (2014).

[1-44] Shterenberg, M. Salama, Y. Gofer, E. Levi, D. Aurbach, The challenge of developing rechargeable magnesium batteries, MRS Bull. 39 (2014) 453–460. Figure 1.7

[1-45] Baran, M. Pola´nski, Magnesium-Based Materials for Hydrogen Storage - A Scope Review, Materials 2020, 13, 3993.

[1-46] J. Zhang, S. Yan, H. Qu, Recent progress in magnesium hydride modified through catalysis and nanoconfinement. Int. J. Hydrogen Energy 2018, 43, 1545–1565.

[1-47] J.P. Bastide, B. Bonnetot, J. M. Letoffe, P. Claudy, Polymorphism of Magnesium Hydride under high-pressure. Mater. Res. Bull. 1980, 15, 1215–1224.

[1-48] Colozza AJ. Hydrogen Storage for Aircraft. 2002.

[1-49] Krishna R, Titus E, Salimian M, Okhay O, Rajendran S, Rajkumar A, et al. Hydrogen Storage for Energy Application, 2020.

[1-50] J.F.J. Stampfer, C.E.J. Holley, J.F. Suttle, The magnesium-hydrogen system. J. Am. Chem. Soc. 1960, 82, 3504–3508.

[1-51] Kurtz J, Ainscough C, Simpson L, Caton M. Hydrogen Storage Needs for Early Motive Fuel Cell Markets 2012:85.

[1-52] Chen P, Zhu M. Recent progress in hydrogen storage. Mater Today 2008; 11:36–43.

[1-53] D.P. Broom, Hydrogen Storage Materials, Springer London, London (2011)

[1-54] Andersson J, Grönkvist S. Large-scale storage of hydrogen. Int J Hydrogen Energy 2019; 44:11901–19.

[1-55] Rivard E, Trudeau M, Zaghib K. Hydrogen Storage for Mobility: A Review. Mater 2019;12.

[1-56] F. Leardini, J.R. Ares, J.F. Fernández, J. Bodega and C. Sánchez: Int. J. Hydrogen Energy 36 (2011) 83518357.

[1-57] A.S. Pedersen, J. Kjøller, B. Larsen and B. Vigeholm: Int. J. Hydrogen Energy 8 (1983) 205211.

[1-58] U. S. Department of Energy: http://www.energy.gov/.

[1-59] M. Dornheim, N. Eigen, G. Barkhordarian, T. Klassen and R. Bormann: Adv. Eng. Mater. 8 (2006) 377385.

[1-60] C. Pistidda et al.: J. Power Sources 270 (2014) 554563.

[1-61] J.C. Crivello, B. Dam, R.V. Denys, M. Dornheim, D.M. Grant, J. Huot, T.R. Jensen, P. de Jongh, M. Latroche, C. Milanese, D. Milčius, G.S. Walker, C.J. Webb, C. Zlotea and V.A. Yartys: Appl. Phys., A Mater. Sci. Process. 122 (2016) 97.

[1-62] V.A. Yartys et al.: Int. J. Hydrogen Energy 44 (2019) 78097859.

[1-63] O. Friedrichs, F. Aguey-Zinsou, J.R.A. Fernández, J.C. Sánchez-López,

[1-64] A. Justo, T. Klassen, R. Bormann and A. Fernández: Acta Mater. 54 (2006) 105110.

[1-65] N. Hanada, T. Ichikawa and H. Fujii: J. Alloy. Compd. 404406 (2005) 716719.

[1-66] S. Kumar and G.P. Tiwari: J. Mater. Sci. 52 (2017) 69626968.

[1-67] T. Kimura, H. Miyaoka, T. Ichikawa and Y. Kojima: Int. J. Hydrogen Energy 38 (2013) 1372813733.

[1-68] T. Kimura, H. Miyaoka, N. Hanada and T. Ichikawa: J. Japan Inst. Met. Mater. 79 (2015) 107111.

[1-69] N. Hanada, T. Ichikawa, S. Isobe, T. Nakagawa, K. Tokoyoda, T. Honma, H. Fujii and Y. Kojima: J. Phys. Chem. C 113 (2009) 1345013455.

[1-70] N. Hanada, T. Ichikawa, S. Hino and H. Fujii: J. Alloy. Compd. 420 (2006) 4649.

[1-71] A. Jain, S. Agrawal, T. Ichikawa, Catalysts, 2018, 8, 651.

[1-72] A. Jain, H. Miyaoka, T. Ichikawa, A review. Int. J. Hydrogen Energy 2016, 41, 5969–5978.

[1-73] J. J. Vajo, F. Mertens, C. C. Ahn, R. C. Bowman and B. Fultz, Cheminform, 2004, 35, 13977–13983.

[1-74] G. S. Walker, M. Abbas, D. M. Grant, C. Udeh, Chem. Commun., 2011, 47, 8001–8003.

[1-75] J. Jepsen, C. Milanese, J. Puszkiel, A. Girella, B. Schiavo, G. A. Lozano, G. Capurso, J.M. B. Colbe, A. Marini, S. Kabelac, M. Dornheim, T. Klassen, Energies, 2018, 1-15.

[1-76] H. Imamura, Y. Hashimoto, T. Aoki, T.Ushijima, Y. Sakata, Materials Transc., 2014, 55, (3), 572-576.

2. Purpose of this thesis

In this thesis, I focused mainly on the systematic study on oxide catalysts and thermodynamic modification on MgH_2, as Magnesium has always been the center of extensive investigations for its potential use as a medium for storing hydrogen as a basic technology for next-generation hydrogen transportation and increasing the amount of hydrogen flow because it is an abundant and low-cost metal that can store up to 7.6 mass % of hydrogen. However, the practical use of magnesium as a hydrogen storage material has always been restrained by the poor kinetics and high stability of its hydride ($\Delta H = -74$ kJ.mol^{-1} H_2) when it comes to releasing or absorbing hydrogen. Considering the above-mentioned discussion, we tried to enlighten the following important facts about transition metal oxide catalysts and magnesium hydride.

Catalyst amount and milling time also greatly influenced the catalytic activity of the transition metal oxide. Various studies show that the reduction of oxide to its various lower oxidation states was also responsible for the catalytic mechanism of transition metal oxide. Despite this much of investigations still, the effective factors for catalysis were not completely understood yet in detail. The difficulty in understanding the detailed catalysis is caused by the differences between preparation processes of the oxides and lack of well-fashioned study by considering the uniformity in oxidation state, amount of oxide as a catalyst (in mg), the particle size of starting state, and milling time, etc. Owing to the above-mentioned complicated process, it is difficult to define and compare the essential catalytic properties of oxides.

① The catalytic behavior of **single phase** of TiO_2, ZrO_2, HfO_2, V_2O_5, Nb_2O_5, Ta_2O_5, CrO_3, MoO_3, and WO_3 (Nb_2O_5 and its neighboring oxide) with Mg-MgH_2 system were investigated. Each oxide was taken in its maximum oxidation state followed by a possibility to reduce in a number of lower oxidation states causes catalysis.

② The catalytic tendency among every 9 oxides on Mg-MgH_2 system was discussed from physical and chemical points of view.

③ The thermodynamic routes for all oxides with MgH_2 system were estimated by using the thermodynamic database.

④ Following the catalytic activity of oxides, the effective factors for the catalysis of oxide catalysts were discussed and determined.

In the search of newest and best catalysts various kinds of research and development is going on. In many conditions, not only low catalysis but also extremely high catalysis (in a few conditions) was not suitable for practical application because the former requires excess energy input and later is dangerous due to the high activity. Many times, in research we need middle properties or some suitable properties or some suitable combination of materials as per our need for application purposes. There are various kinds of research and development is going on inserach of new class of catalysts, in connection to that transition metal ternary oxides as a catalysis is a new direction of research, using ternary oxides as a catalyst with single phase. Thus, I tried to find the catalysis by exchanging/replacing the element by combining the catalytic active elements and inactive elements (formation of ternary oxides $A_xB_yO_z$) and vice versa for Mg-H system in connection to above study. The purpose is to find new catalysts along with control or tune catalysis same as the alloy studies for hydrogen storage, as in the case of alloy systems generally, we controlled the properties for our practical necessity by altering the weight % of each element among overall composition. If the exchange of elements of oxide catalysis could be established, we can control the catalysis and design the suitable catalyzed Mg for practical application together with the search for the newest and best catalyst. There are various kinds of combination is possible, in first step we tried to synthesize the transition metal ternary oxide as a catalyst for Mg-H system. In further study, ternary transition metal oxide replaced by various column of periodic table like alkali, alkaline elements, VII column, VIII column IX column and so on to develop a new combination of ternary metal oxides with single phase. This theme would be a novel guideline for academic and practical research in search of newest and best catalysts for hydrogen storage fields.

① Single-phase of transition metal ternary oxides was synthesized by ball milling followed by high-temperature heat treatment and so on.

② The hydrogen desorption and absorption properties of MgH_2 with the ternary oxides were investigated through thermal and structural analyses. The change in catalysis (tuning) of MgH_2 was compared with its oxide.

③ The reduction state and mechanism of ternary oxide were determined that it was reduced in AO_X or BO_Y or $A_XB_YO_Z$.

So far, the oxides are generally prepared by heat treatment at high temperature and dispersed on MgH_2 surface by ball-milling for a long time such as 20 h to form a homogeneous and highly active state. The purpose of this work is to synthesize highly activated Mg by using simpler and easier processes than conventional ones from the practical point of view.

① Nb, Ta, and Nb-Ta gel oxides were synthesized by a simple sol-gel method and dispersed on Mg by ball milling for 10 times shorter milling time than conventional processes. Here, Na and Ta were chosen as representative active and inactive elements as the catalysts for Mg.

② The catalysis for the hydrogen desorption and absorption of MgH_2 was investigated with Nb and Ta gel oxides through thermal and structural analyses. Based on the experimental results, the catalytic properties of Nb and Ta oxides were compared.

The thermodynamic destabilization can be achieved by introducing an intermediate stage by the formation of either intermetallic or solid solution phase which could further reduce the decomposition temperature easily.

① Theoretically, it was expected that thermodynamic modification of MgH_2 can be achieved by introducing CaH_2 in the ratio of 2:1 respectively by the formation of $2MgH_2$-CaH_2 composite. Simultaneous desorption of $2MgH_2$-CaH_2 composite leads to the formation of Mg_2Ca intermetallic or solid solution, further reducing the decomposition temperature compared to individual CaH_2 or MgH_2 was achieved.

3. Experimental Procedures

3.1 Materials

Commercial MgH_2 powder (99.8%, FUJIFILM Wako Pure Chemical Corp.) was used as the starting material. Gel samples as the catalyst were synthesized using the solution gel method. Niobium(V) ethoxide ($Nb(OC_2H_5)_5$) or Tantalum (V) ethoxide ($Ta(OC_2H_5)_5$) was solved in ethanol (C_2H_5OH). Then purified water was added to the solution to form Nb or Ta gel. Finally, the solid product was collected and dried. Six types of Nb_2O_5 and Ta_2O_5 gel oxides were synthesized followed by heat tratement at 500 °C for 3h (for few oxides), namely Nb_2O5 gel, Nb_2O_5 gel heat treated, Ta_2O_5 gel, Ta_2O_5 gel heat treated, Nb_2O_5+Ta_2O_5 gel and Nb_2O_5+Ta_2O_5 gel heat treated respectively. Single-phase of TiO_2, ZrO_2, HfO_2, V_2O_5, Nb_2O_5, Ta_2O_5, CrO_3, MoO_3, WO_3 was also used as a catalyst with MgH_2. In a later work, single phase of transition metal ternary oxides as a catalysts were used as purchased as well as synthesized by ball milling followed by heat treatment of transition metal oxides. CaH_2 was used with MgH_2 to form CaH_2-MgH_2 composite and $ZrCl_4$ was investigated as a catalyst for hydrogen desorption and absorption of the composite.

3.2 Synthesis of Ternary Oxide

The theory originated as, when two different, single phases of transition metal oxide ball milled for a quite long time for around 10h, 12h, 18h or 20h, etc. as per the requirement, oxides completely mixed up with each other. The ball milling should be done in some suitable milling vessel by using quite hard milling balls like ZrO_2. Before milling, the batch size and number of milling balls must be optimized as per the vessel volume. The stoichiometric calculations of each oxide were also calculated as per the batch size (in mg). The inactive Ar atmosphere always is a good choice but as we are mixing oxide so atmospheric air also will not affect the circumstances. The concept behind longer milling is either to find completely disappearance of the initial phase by the formation of

Table 3.1 General information of materials used

S. No.	**Materials**	**Purity (%), state**	**Company**
1.	Magnesium hydride (MgH_2)	99.8%	Fujifilm Wako pure chemical corp.
2.	Niobium(V) ethoxide ($Nb(OC_2H_5)_5$)	-	Fujifilm Wako pure chemical corp.
3.	Tantalum (V) ethoxide ($Ta(OC_2H_5)_5$)	-	Hokko Chemical Industry Co. Ltd.
4.	Ethanol (C_2H_5OH)	99.5%	Nacalai Tesque
5.	Acetone (CH_3CoCH_3)	99.5%	Nacalai Tesque
6.	Hexane ($CH_3(CH_2)_4CH_3$)	97%	Nacalai Tesque
7.	Calcium hydride (CaH_2)	99.9%	Sigma Aldrich
8.	Zirconium(IV) chloride $ZrCl4$	99.9%	Sigma Aldrich
9.	Titanium(IV) oxide (TiO_2) Anatase type	-	-
10.	Zirconium(IV) oxide (ZrO_2)	-	Sigma Aldrich
11.	Hafnium(IV) oxide (HfO_2)	98%	Sigma Aldrich
12.	Vanadium(V) oxide (V_2O_5)	99.6%	Sigma Aldrich
13.	Niobium(V) oxide (Nb_2O_5)	-	-
14.	Tantalum(V) oxide (Ta_2O_5)	99.9%	Sigma Aldrich
15.	Chromium(VI) oxide (CrO_3)	99.9%	Sigma Aldrich
16.	Molybdenum(VI) MoO_3	99.5%	Sigma Aldrich
17.	Tungsten(VI) oxideWO_3	-	Sigma Aldrich
18.	$TaVO_5$ (ternary oxide) (Self-prepared using V_2O_5 and Ta_2O_5)	-	Using ball milling followed by heat treatment in atmospheric air
19.	Nb_9VO_{25} (ternary oxide) (Self-prepared using V_2O_5 and Nb_2O_5)	-	Using ball milling followed by heat treatment in atmospheric air
20.	$Nb_{(0.6)}Cr_{(0.4)}O_2$ (ternary oxide) (Self-prepared using Nb_2O_5 and CrO_3)	-	Using ball milling followed by heat treatment in atmospheric air

new phase or formation of the amorphous phase, both situations support the synthesis of ternary oxide.

The ball-milled sample should be collected in Alumina or some suitable crucible to do high-temperature heat treatment. The high-temperature heat treatment around 1000 °C or more for 10h or 12h as per need will give you ternary oxide. The new single-phase must always be different from the initial phase of both the oxide. In some cases, you again need to hand mill the heat-treated sample using mortar and pestle and again heat treatment will give you ternary oxide.

3.3 Mechanical Ball Milling Method

Ball-milling is a technique for mixing and pulverization of samples by adding physical energy to the sample. It is commonly used for the synthesis of different kinds of alloys, synthesis of composite, for nano sizing of particles, dispersion of catalyst, the inclusion of defects inside the particle, and so on. In this thesis work, planetary ball-milling (PM) apparatus (Fritsch P7) was used for mixing MgH_2 with different kinds of oxides and $ZrCl_4$ as a catalyst. In the case of PM method, the vessel and the disk are rotated simultaneously as shown in figure 3.1. Therefore, centrifugal force is applied to the sample and balls. The Chromium steel ball-milling vessels (inner volume 30 cm^3) were used for sample preparation during ball milling. A quick connector (Swagelok) was attached with a Chromium (Cr) steel vessel either to fill hydrogen or to remove Ar gas from the vessel chamber. This vessel was sealed by O-ring (Viton®, fluorine rubber) to prevent the inner chamber from atmospheric air. In this thesis basically, various types of samples prepared, we can categorize into four parts, explained further.

(a) Ball milling of MgH_2 with 9 types of single-phase transition metal oxides i.e., TiO_2, ZrO_2, HfO_2, V_2O_5, Nb_2O_5, Ta_2O_5, CrO_3, MoO_3, WO_3 respectively. All the samples were prepared with 2 atoms per mole of transition metal on Mg surface in the molar ratio of 2:99. For 300 mg of samples, 20 stainless steel balls were used of 7 mm diameter. All these samples were prepared in 1MPa of hydrogen atmosphere to suppress the hydrogen desorption of MgH_2 into Mg during the ball milling process. The rotational speed was 370 rpm for 2h milling followed by 1h milling 30 min pause time. All the preparation and collection of samples before and after the ball milling were taken inside the glove box filled with highly purified Ar gas.

(b) (i) Two different transition metal oxides were taken, and the ball milled for a long time until the appearance of both the single-phase was completely disappeared from the mixed sample followed by the formation of a new phase with it. The milling time was 10 h, 12 h, 12 h for a combination of (Nb_2O_5 and V_2O_5), (Ta_2O_5 and V_2O_5), and (Nb_2O_5 and CrO_3), respectively. The sample was ball milled in a Cr steel pot (30 cm^3) containing 20 pieces of ZrO_2 balls with diameters of 8 mm. Ball milling was performed in a completely Ar atmosphere at 370 rpm. The sample was ball milled with a pattern of 1 h milling followed by a half-hour pause time to avoid the overheating inside vessel. All samples were collected in an Al_2O_3 crucible to perform the heat treatment. The heat treatment was done for milled samples inside a muffle furnace in atmospheric air at 1000 °C for 16h, 12h, 12h respectively, and successful synthesis of Nb_9VO_{25}, $TaVO_5$, $Nb_{0.6}Cr_{0.4}O_2$ ternary oxide was achieved.

(ii) The MgH_2 powder was milled with 2 atoms per mole of transition metal on Mg surface in the molar ratio of 2:99 i.e., MgH_2 with $TaVO_5$, Nb_9VO_{25}, and $Nb_{0.6}Cr_{0.4}O_2$ respectively. Other all milling conditions were the same as explained above in (a).

(c) The MgH_2 powder was milled with 1 mol% of each synthesized oxide i.e., Nb_2O_5 gel, Nb_2O_5 gel heat treated (HT), Ta_2O_5 gel, Ta_2O_5 gel HT, Nb_2O_5 +Ta_2O_5 gel, and Nb_2O_5 +Ta_2O_5 gel HT, respectively. Oxide-doped MgH_2 samples were prepared using 300 mg of as-received MgH_2 with 1 mol% of oxide in every batch. The sample was ball milled in a Cr steel pot (30 cm^3) containing 20 pieces of steel balls with diameters of 7 mm. Ball milling was performed for 2 h in a 1 MPa hydrogen atmosphere at 370 rpm. To avoid temperature increase in the vessel, the ball-milling was stopped for 30 min after every 1 h milling. All the MgH_2 sample synthesis processes were performed in a glove box filled with highly purified Ar to avoid oxidation.

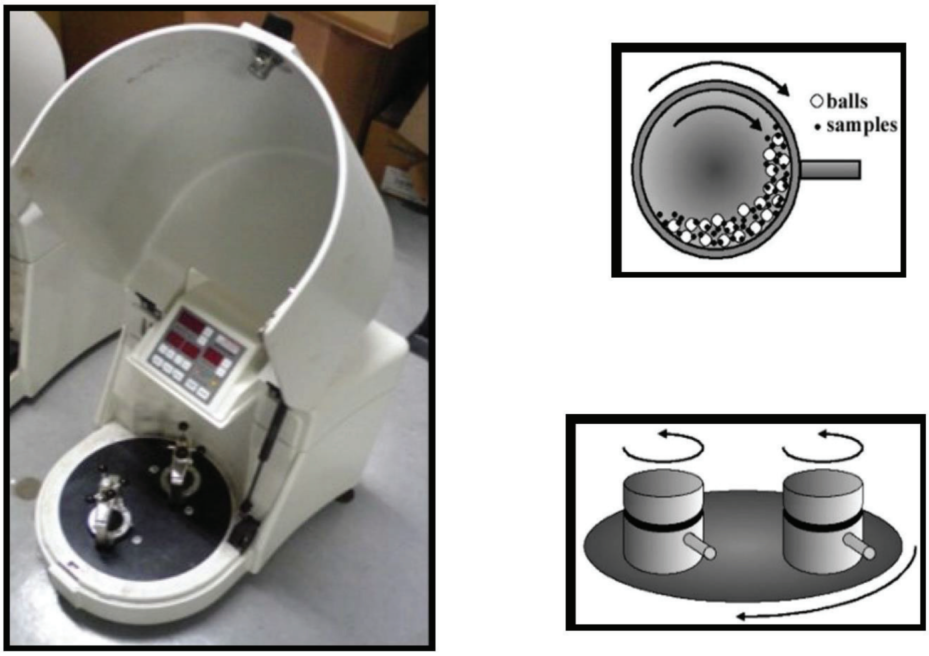

Figure 3.1 Planetary ball mill setup.

(d) MgH_2 and CaH_2 powders were balls milled with and without $ZrCl_4$ as a catalyst. Uncatalyzed MgH_2-CaH_2 composite was prepared by using 1 g of as received MgH_2 and CaH_2 in the ratio of 2:1 respectively. The catalyzed $2MgH_2$-CaH_2-$ZrCl_4$ composite (c-$2MgH_2$-CaH_2) was prepared in the same way by using 1 g of as-received $2MgH_2$-CaH_2-$ZrCl_4$ by adding 5 mass % $ZrCl_4$. The sample was ball milled in a hardened stainless-steel pot containing 20 pieces of hardened stainless-steel balls with a diameter of 7 mm. The ball milling was performed under 1MP hydrogen pressure at a milling frequency of 400 rpm. The sample was ball milled for 2h with 1h milling followed by a half an hour pause time pattern.

3.4 Scanning Electron Microscope (SEM)

Principle

Scanning electron microscope (SEM) works on the principle of spread on kinetic energy for signal production on the contact electron. In a Scanning electron microscope, high energy of electron beam is bombarded onto the specimen surface to get a surface image. Due to the bombardment of electrons on the surface of the sample, both photons, as well as an electron, are produced from the surface layer. In SEM technology, the electrons are collected, and then the high resolution of the picture can be attained. A scanning electron microscope can produce a picture from 20x to 100000x theoretically calculated. The key feature of a scanning electron microscope is the 3D appearance of its pictures due to its high depth of field. Depth of field or focus is described as a kind of position of the object in which the sharpness of the image does not change. In the case of scanning electron microscope depth of focus is proportional to magnification. The supreme resolution of scanning electron microscope is 5-8nm which depends on the electron wavelength which in turn depends on the applied voltage. When there is a comparatively high-energy electron beam striking a sample, the electrons are scattered by atoms of the sample, as displayed in figure 3.2. Electron scattering results in a change of direction of travel of electrons under the specimen surface. Electron trajectories during scattering in a sample are schematically displayed in figure 3.3, the relations between electrons and sampling atoms occur within a definite volume under the sample surface.

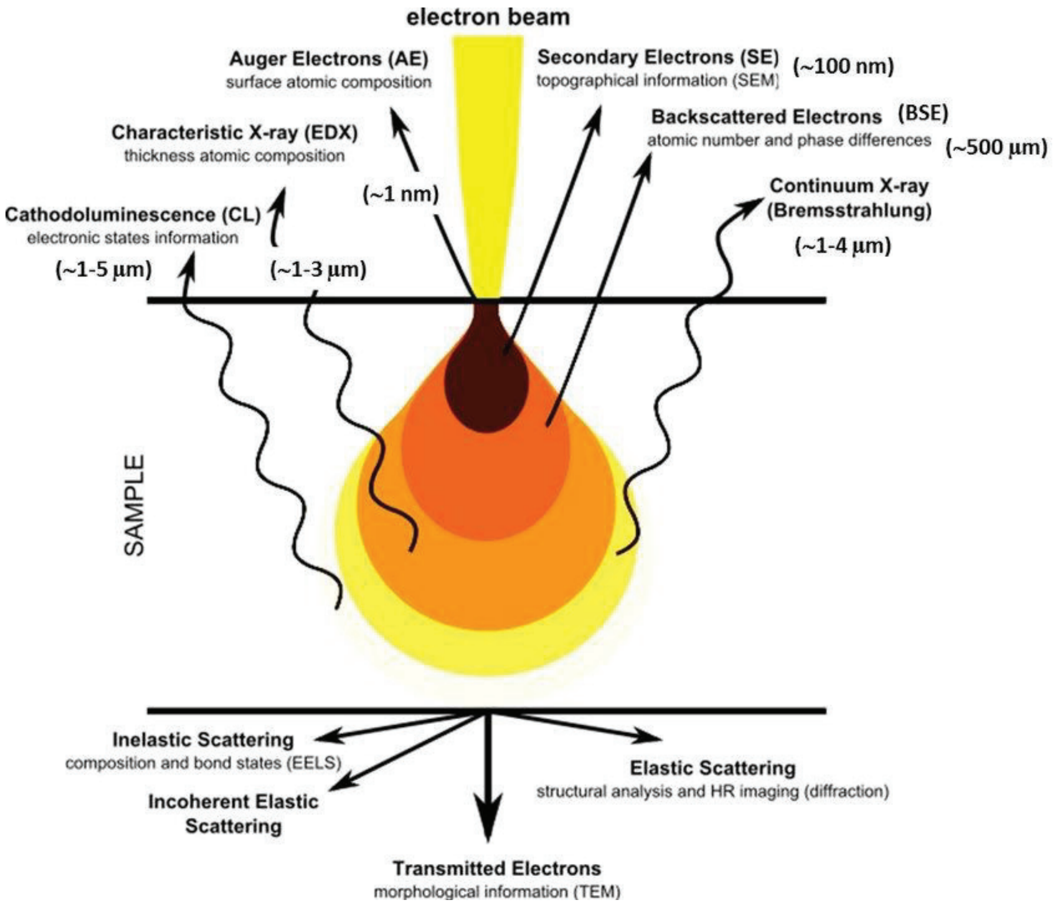

Figure 3.2 Interaction Zone of Electron beam

Figure 3.2 Displays the zone of interaction where electrons scatter under the surface of the sample. The zone is typically defined as peer-shaped, and its size increases with the energy of incident electrons. But, as displayed in figure 3.2, many types of electrons like augur electrons (AEs), secondary electrons (SEs), backscattered electrons (BSEs), characteristic X-ray (EDX), continuum X-ray, and cathodoluminescence (CL), escape from different locations in the sample. SEs and BSEs both created by scattering are identified as signal sources for forming SEM images. Secondary electrons (SEs) are produced by the inelastic collision between the incident electron and loosely bonded outer electron on the surface. It is a kind of low-energy electron from 10-50eV. Using SE topographic facts is achieved as they are observed close to the surface. In the process of emission, number of secondary electrons produced are greater than the number of incoming electrons onto the specimen surface. A small amount of incident electron is by the electromagnetic field of the core and assuming that the scattering angle is more prominent than 180°, the electron escape from the surface known as backscattered electrons (BSE). It produces because of the elastic scattering of bonded electrons and incident electrons on a superficial level. It is a kind of high-energy electron that movements in a straight line. Less topographic information is gotten utilizing BSE.

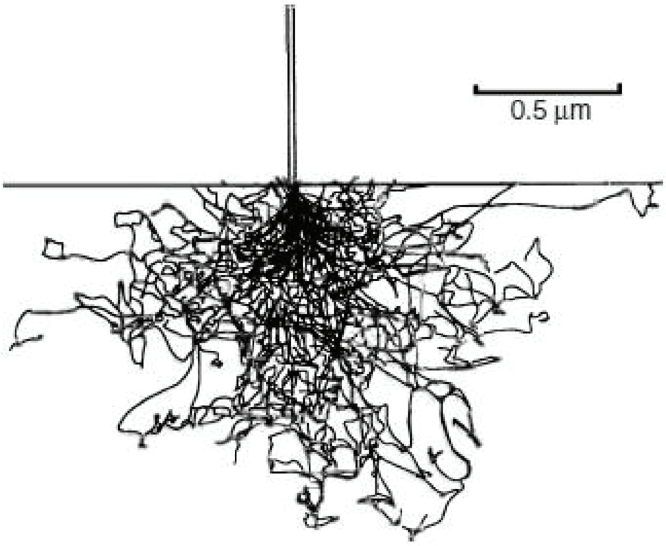

Figure 3.3 Monte Carlo electron trajectory simulation of an electron beam interaction with iron *E*o = 20 keV. (Reproduced with kind permission of Springer Science and Business Media from, 1992, Springer Science.)

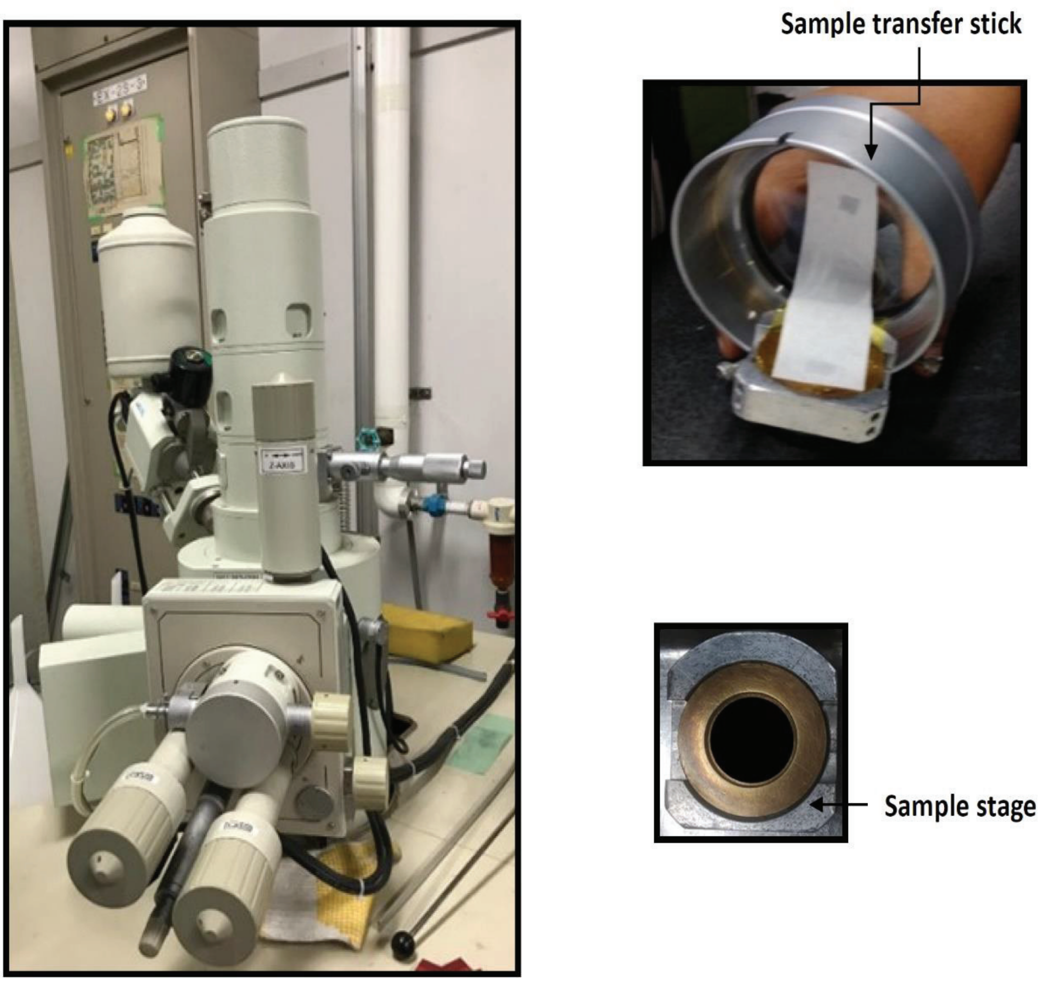

Figure 3.4 Images of the SEM instrument JEOL JSM 6380 (left); other two images belongs to the transfer stick and sample stage

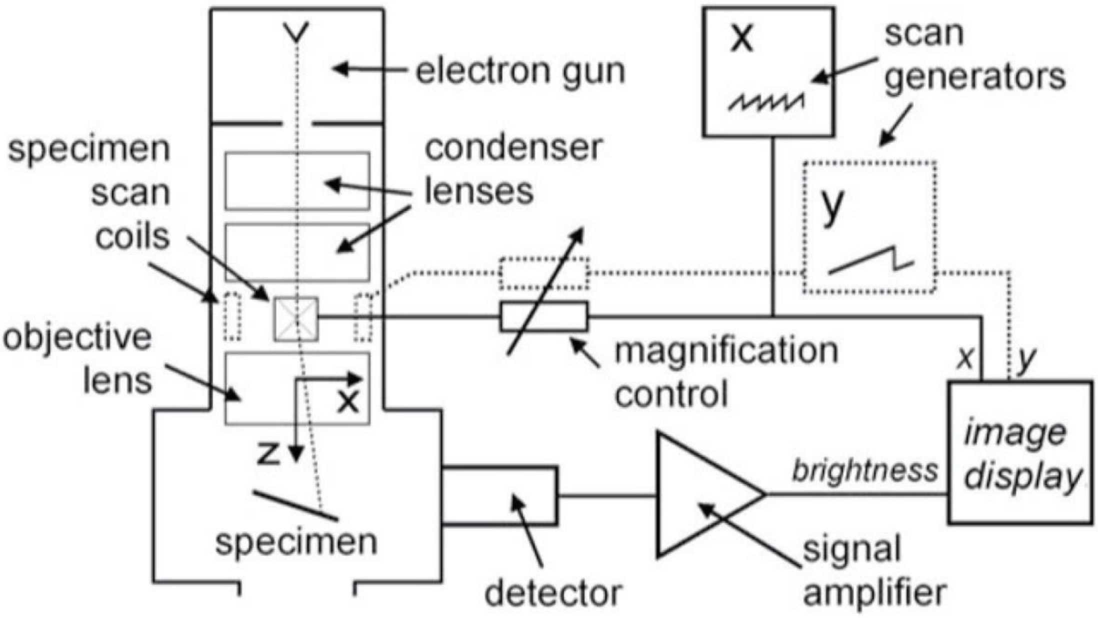

Figure 3.5 Schematic diagram of a scanning electron microscope.

Charge up in an undesirable effect in SEM where the negative charge of the incident electron beam accumulates on the surface of a non-conductive specimen. The charge is caused due to following reasons, when the total number of electrons emitted from a sample, the sum of backscattered electrons, secondary electrons, and absorbed electrons, is less than the incident electrons cause charge up in the SEM. Further, the potential on the specimen surface becomes negative and causes various distortions in secondary electron imaging.

On the other hand, as in the case of nonconductive samples the negative charge electron accumulated on the sample surface, there is a gap between the sample surface and carbon tape causes charge up in the SEM. In general carbon tape is used to provide conductivity between the sample-to-sample stage to minimize the charge-up effect.

3.5 Energy Dispersive Spectroscopy (EDS)

X-ray spectroscopy is a method of utilizing characteristic X-rays to recognize chemical elements; it is to be recognized from X-ray diffraction for crystal structure analysis. X-ray spectroscopy decides the presence and quantities of chemical elements by detecting characteristic X-rays that are produced from particles irradiated by a high-energy beam. From the characteristic X-rays radiated from test samples, chemical elements can be recognized either from the X-ray wavelenth, as in X-ray wavelength dispersive spectroscopy (WDS), or from the X-ray energy, as in X-ray energy dispersive spectroscopy (EDS). The most commonly used spectrometers for X-ray spectroscopy incorporate X-ray fluorescence (XRF) spectrometers and microanalyzers in electron microscopes (EMs). A microanalyzer is an EDS kind of X-ray spectrometer that is generally found in filtering/scanning or transmission electron microscopes (TEM). The EDS microanalyzer in EM usage a primary electron beam to excite the production of characteristic X-rays from the sample. Since the electron beam readily focused on a microscopic area on a sample, the EDS microanalyzer can observe chemical compositions in a microscopic area, while the XRF spectrometer is generally used to examine overall chemical compositions in a sample.

EDS turned into a business item in the mid-1970s and quickly overwhelmed WDS in prevalence. An EDS instrument is simple since it doesn't have moving parts like the rotation detector in case of WDS. EDS instrument are comparatively quicker because the detector collects the signals of characteristics X-ray energies from an entire range of elements in a sample simultaneously instead gathering signals from X-ray wavelength individually. For EDS, the normal resolution of energy dispersion is around 150–200 eV, worse than the equivalent resolution of WDS, and the lightest element that can be detected is Oxygene (Z =8), not Carbon (Z =6). But these drawbacks are not as main as the benefits of an EDS system, which are low cost and fast analysis.

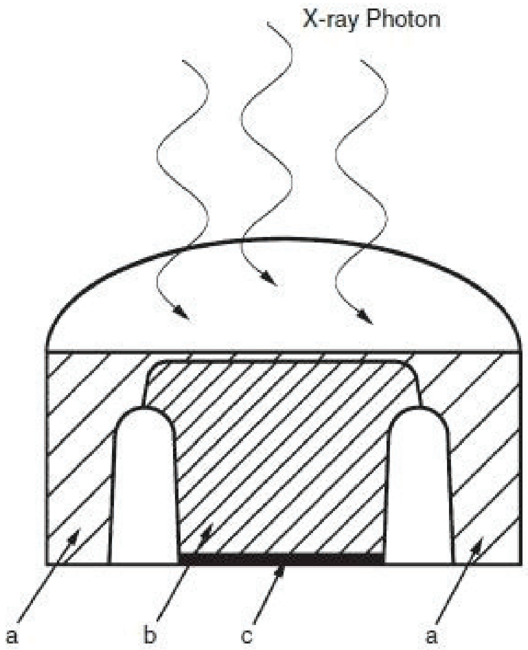

Figure 3.6 A Si(Li) cylinder with annular groove construction: (a) p-type silicon; (b) lithium compensated region; and (c) n-type silicon.

The Si (Li) is the most frequently used detector in an EDS analysis instrument. The Si (Li) detector consists of a small cylinder of p-type silicon and lithium in the form of a Si(Li) diode, as shown in figure 3.6. X-ray photons collected by the detector produce a specific number of electrons–hole pairs. The average energy of photons needed to produce an electron-hole pair (e_i) is about 3.8 eV in the Si (Li) diode. The higher the photon energy, the more pairs are produced. Characteristic X-ray photons can be detached by their energy levels according to the numbers of electron-hole pairs they produce.

The electron-hole pairs, as the electric charge, are carried from the detector diode. A preamplifier gathers the charge to produce an output of an electrical pulse whose voltage amplitude is proportional to the X-ray photon energy. The energy resolution of the detector (R) in eV can be estimated by

$$\mathrm{R} = \sqrt{\sigma_{noise}^2 + [2.35(e_i F E)]^2}, \qquad (1)$$

where, E is the energy of the characteristic X-ray line and F is a constant called the Fano factor, which has a value of 0.12 for Si (Li). σ_{noise}, the electronic noise factor, plays an important role in the resolution. A decrease in the electronic noise will increase the resolution of the EDS detector. Accordingly, the Si(Li) diode and the preamplifier are straddling in a cylindrical column (the cryostat) so that they can operate at the temperature of liquid nitrogen (−196 °C) to decrease the electrical noise and rise the signal-to-noise ratio.

X-ray photons should go through a window to arrive at the Si(Li) diode. This window is regularly made of a light component, beryllium. Beryllium, like any material, will ingest X-ray photons, even though its absorption is weak. Subsequently, the sensitivity of the detector will be impacted by the beryllium window. To reduce the photon absorption, the beryllium has to be as thin as possible, particularly for distinguishing light components of which the characteristic energies are on the order for 100 eV. The common thickness of the beryllium window is around 10 μm. EDS spectra are like WDS spectra, but identification of individual elements from EDS spectra is more straightforward than from WDS spectra because each characteristic line is produced by a specific element exhibits unique X-ray energy. But the signal-to-noise ratio is lesser than that of WDS, and the resolution, in terms of energy, is about 10 times lower than that of WDS. Even so, EDS is an attractive technique for qualitative analysis of elements.

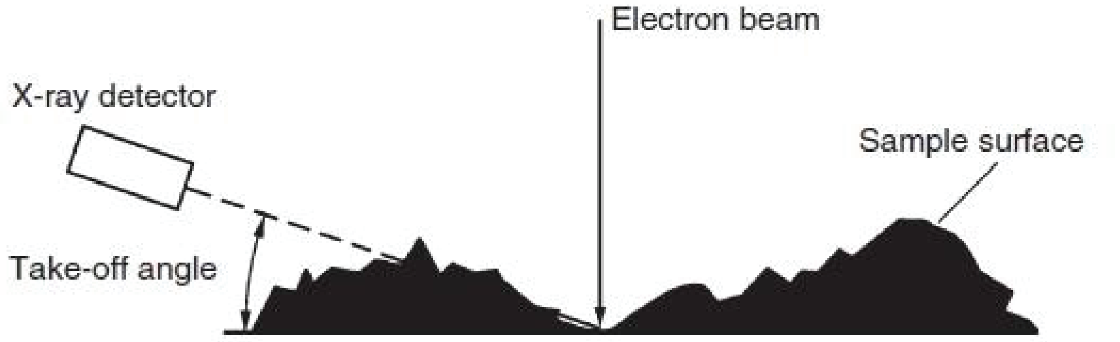

Figure 3.7 Potential interference of X-ray detection due to low take-off angle in the SEM

The EDS type of X-ray spectrometer is usually included as a part of scanning electron microscopes (SEMs). The reason for using EDS rather than WDS is its simplicity and compactness. With EDS in an EM, we can find elemental analysis while observing the microstructure of materials. The main difference between EDS in an EM and a standalone XRF is the source to excite characteristic X-rays from a specimen. Although an X-ray beam is used for the excitation in the XRF, a high-energy electron beam (the same beam for image formation) is used by the X-ray spectrometer in the microscopes. EDS in an EM is appropriate for analyzing the chemical elements in microscopic volume in the specimen since the electron probe can be focused on a very small area. Thus, the technique is often referred to as *microanalysis*. In the SEM, the electron beam aligns with the vertical axis of the microscope so that the Si(Li) detector has to be placed at a certain angle from the vertical. The angle between the surface plane of the specimen and detector is called the *take-*

off angle and is often suggested as the *angular position of the detector*. The take-off angle can be changed by rotating the specimen surface relating to the detector. For a low take-off angle, a rough surface may affect with the collection of X-ray photons emitted from a valley area, as illustrated in figure 3.7. Such problems do not occur if the specimen has a microscopically flat surface.

Procedure

In this work, synthesized oxides of Nb_2O_5 gel, Nb_2O_5 gel heat treated (HT), Ta_2O_5 gel, Ta_2O_5 gel HT, Nb_2O_5 +Ta_2O_5 gel, and Nb_2O_5 +Ta_2O_5 gel HT were characterized using EDS (EX-2300, JEOL) equipped with SEM (6380A, JEOL). Another sample was $2MgH_2$-CaH_2-$ZrCl_4$ composite also characterized using the same EDS equipped with SEM. All the sample preparation took place inside a highly purified Ar gas atmosphere inside glove box. The sample was prepared on the sample stage. We generally used carbon tape in first step on the sample stage and later we spread the sample onto carbon tape homogeneously. Carbon tape also helped in providing the conductivity to the sample to prevent the charge up phenomenon during SEM and EDS measurement. The sample was transferred from the glove to the main chamber of SEM using sample transfer stick as shown in figure 3.4. To protect the sample from air we covered the sample stage using polyimide sheed with the help of grease all around it on the outer border of sample stage. At the final stage of transfer inside SEM chamber, we removed the polyimide sheet to make the direct interaction electron with sample.

3.6 X-Ray diffraction (XRD)

X-ray diffraction is a non-destructive technique in nature. X-ray diffraction by crystals was discovered in 1912, and since then it has been the most significantly studied and used technique for materials characterization. The atomic planes of a crystal cause an incident beam of X-rays to interfere with one another as they leave the crystal, this phenomenon is called X-ray diffraction.

As the wavelength of X-rays is close to interatomic spacing i.e., 0.2-0.3 nm, we use the X-ray to study the crystal structure. X-rays are short-wavelength and high-energy beams of electromagnetic radiation. X-ray energy is distinguished either by wavelength or photon energy. Production of X-rays took place by acceleration of high-speed electrons by a high-voltage field colliding with a metal target. The rapid deceleration of electrons on the target enables the kinetic energy of electrons to be converted to the energy of X-ray radiation. The wavelength of X-ray radiation (λ) is related to the acceleration voltage of electrons (V) as shown in the following equation:

$$\lambda = \frac{1{\cdot}2398\times10^3}{V}(nm) \qquad (2)$$

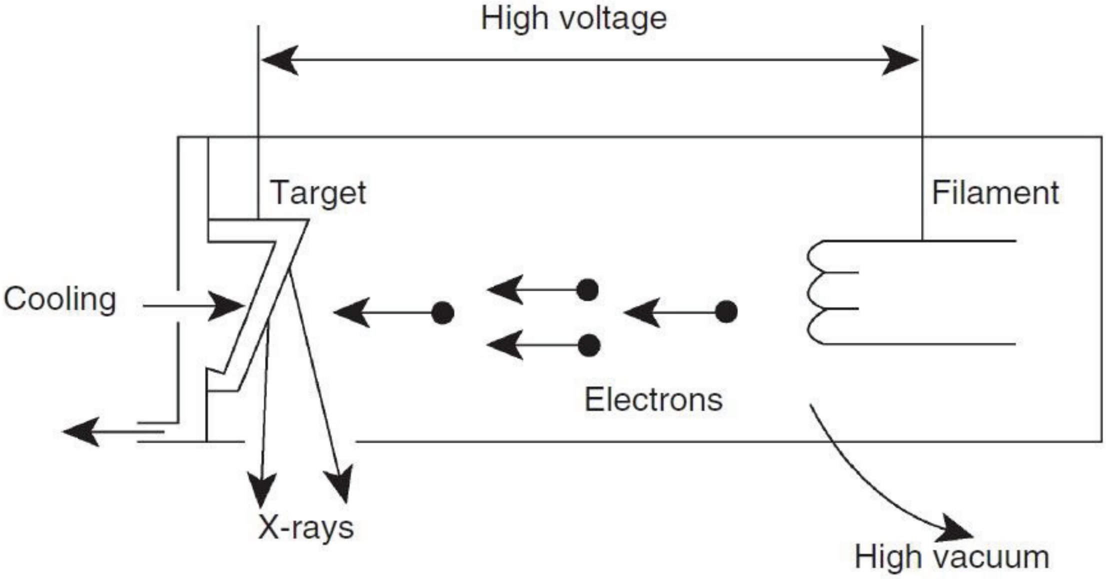

Figure 3.8 X-ray tube structure. X-ray radiation from the anode is guided by the windows of the tube to produce an X-ray beam for diffraction.

To generate X-rays, we need a device called an *X-ray tube*. Figure 3.8 illustrates the structure of an X-ray tube having a source of electrons and two metal electrodes in a vacuum tube. The high voltage kept across these electrodes rapidly attracts the electrons to the anode (target). X-rays are generated at the point of impact on the target surface and radiate in all directions. There are windows to drive X-rays out of the tube. A proper cooling system is required for the X-ray tube because most of the kinetic energy of electrons is converted into heat; less than 1% is transformed into X-rays. So to make it cool and operating we need a cooling system.

The X-ray tube produces the X-ray radiation with a range of wavelengths starting from a minimum λ, called *continuous X-rays* or *white X-rays*, as shown in Figure 3.9. The minimum λ (with the maximum radiation energy) of continuous X-rays is described by the maximum acceleration voltage of electrons in the X-ray tube according to Eq. (2). For example, the minimum λ is 0.062nm at an acceleration voltage of 20 kV. Figure 3.10 shows that there are sharp intensity maxima at particular wavelengths superimposed on a continuous X-ray spectrum. These intensity maxima are the *characteristic X-rays*. In other definition, we can say that X-ray of different wavelength or energy is known as continuous X-ray where as X-ray of particular wavelength or energy is known as characteristic X-rays.

Table 3.2 Characteristic X-rays of anode materials

Target Materials	λ of K_α radiations (Å)	
Mo	0.71	
Cu	1.54	Commonly Used
Co	1.79	
Fe	1.94	
Cr	2.29	

X-ray diffraction techniques generally need a source with single-wavelength (monochromatic) X-ray radiation. The monochromatic radiation required to be come from the characteristic X-rays that are produced by filtering out other radiations from the spectrum. The physical principles of characteristic X-ray generation are shown in Figure 3.10. When an incident electron possesses sufficient energy to excite an electron in the inner shell of an atom to a higher-energy state, the vacancy left in the inner shell will be filled by an electron in an outer shell. As the electron falls from the outer shell to fill the vacancy, created by electron at the inner shell, energy will be released in the form of X-ray with a specific wavelength or photons with a specific energy.

For example, if a *K*-shell vacancy will be filled by an electron either from the *L* shell or *M* shell, which results in radiating the characteristic K_α or K_β X-rays, respectively as shown in Figure 3.10. In the same way, when a vacancy in the *L* shell is filled by an electron of the *M* shell, then L_α X-rays will be emitted. Correspondingly, the probability of an *L* shell electron filling the *K* shell vacancy is much higher than that of an *M* shell electron. Thus, the intensity of K_α X-rays is higher than that of K_β X-rays. If you will talk in a more accurate manner, *Kα* contains two characteristic lines: $K_{\alpha 1}$ and $K_{\alpha 2}$, with the latter wavelength being slightly longer than the former. This phenomenon results from the subshell structure of the *L* shell as indicated by L_1 and L_2 and L_3 respectively. $K_{\alpha 1}$ is the radiation when electrons fall down from the L_3 to *K* shell; $K_{\alpha 2}$ is generated when electrons fall down from the L_2 to *K* shell as shown in Figure 3.10. $K_{\alpha 1}$, $K_{\alpha 2}$, and K_β are the three strongest characteristic X-rays that are used for diffraction radiation in X-ray diffraction method.

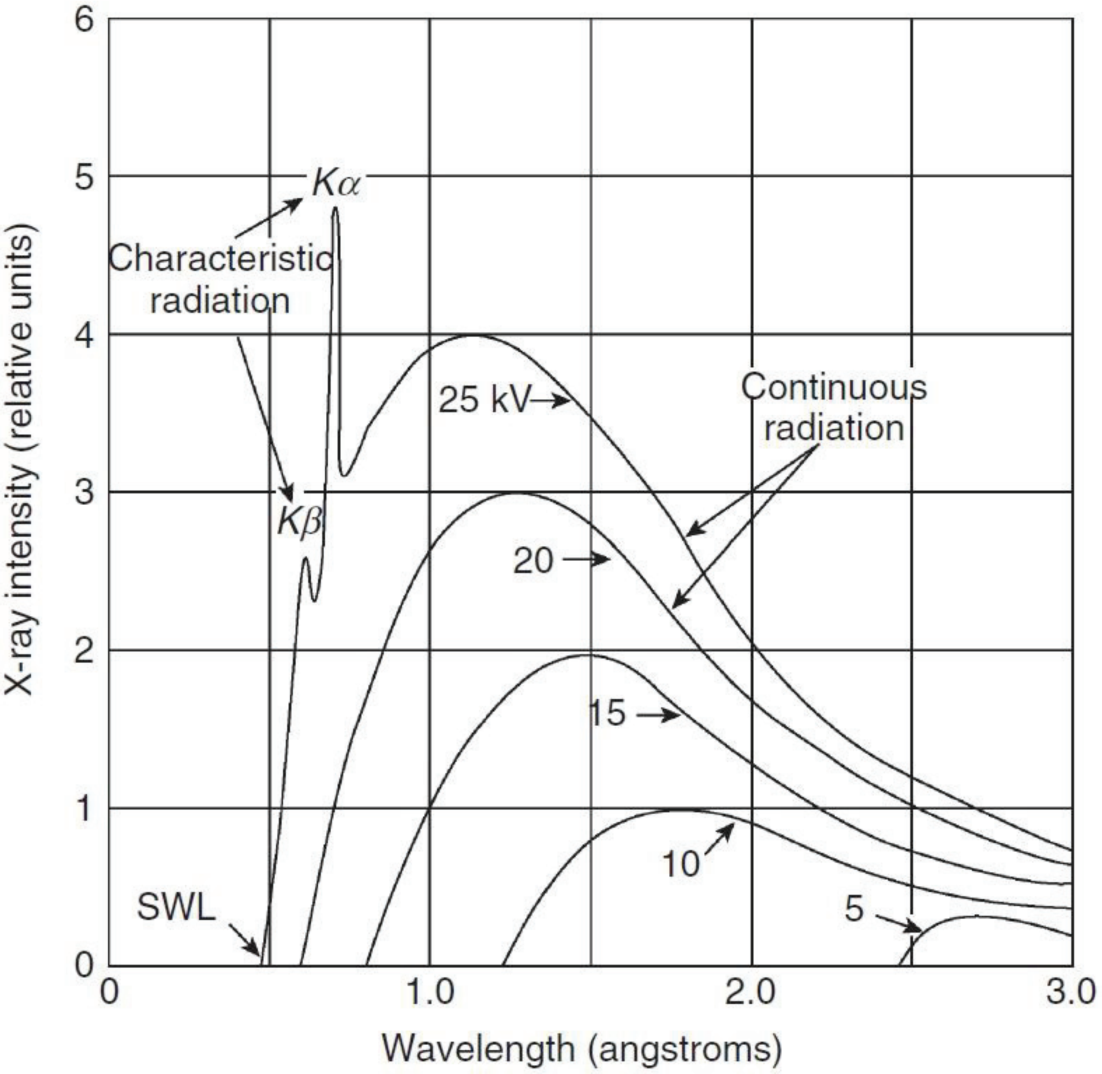

Figure 3.9 X-ray spectra generated with a molybdenum target at various acceleration voltages. Continuous X-rays have a short wavelength limit (SWL). Characteristic radiations exhibit single wavelengths of high intensity superimposed on the continuous radiation background.

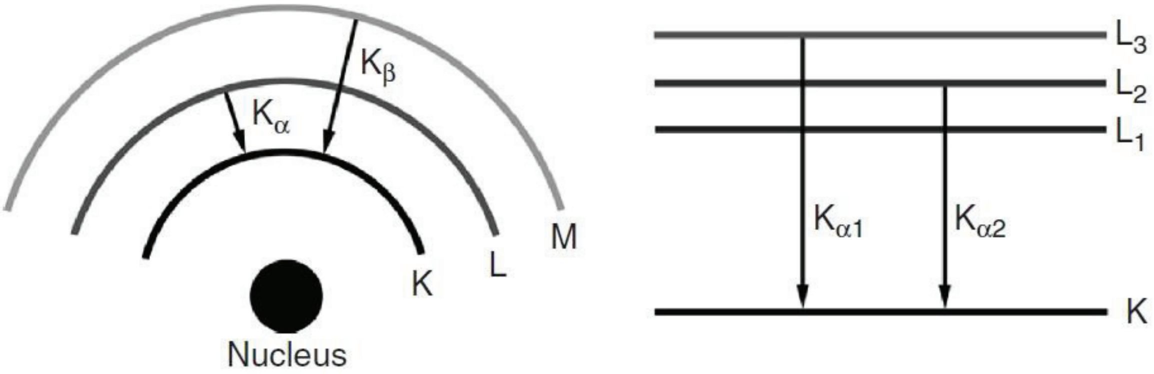

Figure 3.10 Schematic illustration of characteristic X-ray radiation.

The wavelength differences between $K_{\alpha1}$ and $K_{\alpha2}$ are very small that they are not always resolved as distinct radiation. For example, wavelengths produced by a copper target are approximately listed following.

$$\lambda_{K\alpha1} = 0.15406 \text{ nm}$$

$$\lambda_{K\alpha2} = 0.15444 \text{ nm}$$

$$\lambda_{K\beta} = 0.13922 \text{ nm}$$

We frequently call $K_{\alpha1}$ and $K_{\alpha2}$ radiations as K_α *doublet*. The K_α doublet is the most commonly used monochromatic X-ray source for diffraction analysis.

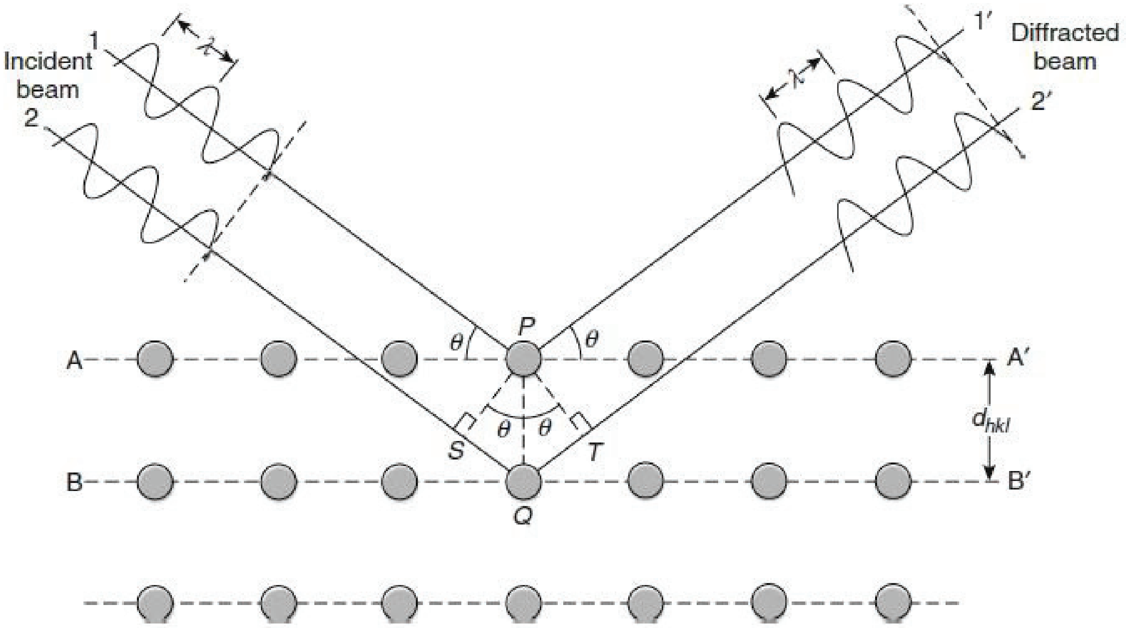

Figure 3.11 Bragg diffraction by crystal planes. The path difference between beams 1 and 2 is SQ+QT=2PQ sin θ.

Bragg's Law

X-rays are categorized as electromagnetic waves and the wavelength of X-ray is much shorter than visible light, of the order of 0.1 nm. X-ray diffraction techniques are based on the phenomenon of wave interferences. When two X-rays of the same wavelength and traveling in the same direction can either reinforce or cancel each other, depending on their phase difference. When they have a phase difference of $n\lambda$ (n is an integer), called ''*in phase*,'' constructive interference occurs and will stisfy the equation (3) called Bragg's law as shown in Figure 3.11. However, when they have a phase difference of $n\lambda/2$, called ''completely out of phase,'' completely destructive interference occurs, causes no diffraction peak formation. When two-inphase X-rays, beam 1 and beam 2, incident on two crystal planes A and B respectively, and deflected by same two crystal planes (A and B) will be in phase when it will satisfy the following relationship.

$$n\lambda = 2d \sin \theta \qquad (3)$$

Equ. (3) is the basic law of diffraction called *Bragg's Law*. In other word when two X-rays reflected by successive planes will be inphase if the extra distance travelled by the second ray is an integral multiple of wavelength.

Bragg's Law can be obtained by determining the path differences between the two beams as shown in Figure 3.11. The path difference depends on the incident angle (θ) and the spacing between the parallel crystal planes (d) or atomic layers. To get a diffraction peak, these beams should be in phase, their path difference (SQ+QT=$2d \sin \theta$) must equal one or integral multiple X-ray wavelengths ($n\lambda$). The information about the spacing between two atomic planes of a crystal can be determined when constructive interference is observed at a given incident angle and a wavelength of the incident beam, based on Bragg's Law. To determine the d spacings of crystallographic planes by diffraction techniques, initially we have to determine the crystal structure of materials. For example, the plane spacing of a cubic crystal relates to the lattice parameter (a) cab be determined by the following equation.

$$d_{hkl} = \frac{a}{\sqrt{h^2+k^2+l^2}} \qquad (4)$$

The Miller indices (hkl) represent a series of parallel planes in a crystal with the spacing of d_{hkl} respectively. With the help of Eq. (3) and (4), we can establish the following relationship between diffraction data and crystal parameters for a cubic crystal system.

$$\sin^2\theta = \frac{\lambda^2}{4a^2}(h^2 + k^2 + l^2) \qquad (5)$$

Using Eq. (5) we cann't directly determine the Miller indices of crystallographic planes. The parameter ($h^2 + k^2 + l^2$) need to be convert to (hkl) or {hkl}. This is not a difficult calculation for low-index planes of cubic crystal structure. For example, when ($h^2 + k^2 + l^2$) is equivalent to 1, the plane index should be {001}; and when it is equivalent to 2 then plane index should be {110}.

Unfortunately such kind of calculations is not necessary because the relationship between deflection angle and Miller indices for most of the crystalline materials, for a given λ, has been determined and published by the International Center for Diffraction Data (ICDD).

Figure 3.12. Picture of Rigaku RINT 2500 XRD equipment

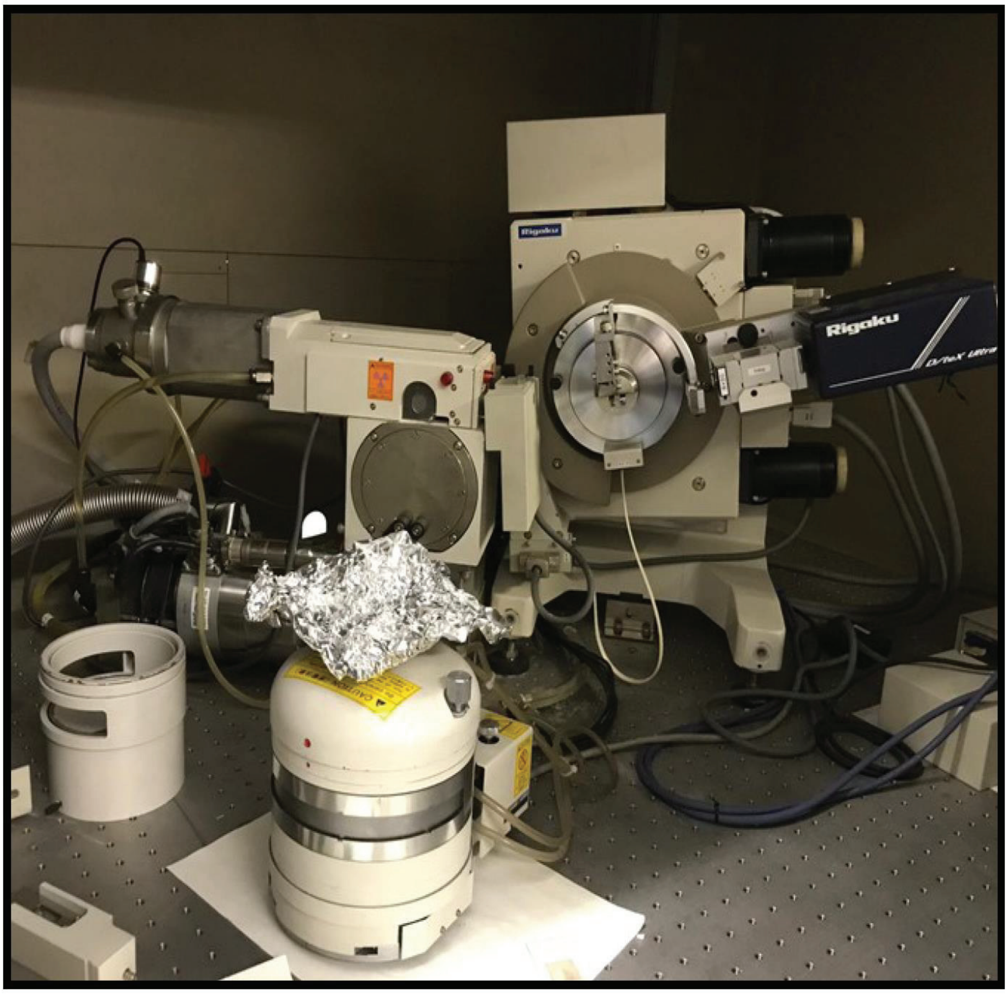

Figure 3.13 Plate preparation using grease and polyamide sheet for XRD measurement

Procedure

In this work, X-ray characterization was done on the XRD instrument (Rigaku RINT 2500V) for phase identification. The target element Cu was used as an X-ray source (Cu-Kα: λ= 1.54 Å). The current load of filament and accelerating voltage of thermal electrons were 200 mA and 40 kV, respectively to keep the energy output 8kW throughout the sample measurement. Silicon semiconductor (Rigaku D/teX Ultra) was used as a detector. For XRD measurement, a glass plate marked with a circular cavity was carefully cleaned using ethanol and acetone to remove the atmospheric and previously used sample contamination from its surface before usage. The grease (Apiezon® H grease, Leef Energy Co. Ltd.) was carefully spread homogeneously in a good fashion onto the glass plate so that the sample and polyimide sheet can be fixed properly to avoid the effect of air and moisture. The thickness of the polyimide sheet (Kapton®, Du Pont-Toray Co. Ltd.) was 8μm. The transfer of XRD glass plate was carefully carried out from the glove box to XRD instrument using a cuboidal box. The XRD sample plate marked with the circular cavity is shown in the Figure 3.13. The XRD patterns were analyzed by comparing to database [ICDD, JICST, COD2019] using the PDXL software.

3.7 Thermal Analysis Technique

The thermal analysis technique is a group of analytical techniques that measures properties or property changes of materials as a function of temperature. Changes in materials properties with respect to temperature are considered as thermal events. The properties that can change include dimension, mass, phase, and mechanical behavior. Thermal Analysis techniques are comparatively simple because changing the temperature of a sample is less challenging than probing a sample using high-energy X-ray, electron, or ion beams in techniques of spectroscopy.

3.7.1 Enthalpy Change

The thermodynamic parameter enthalpy is used to describe the thermal events of a material at a constant pressure, such as 1 atm. With the help of the first law of thermodynamics, we can understand the meaning of enthalpy and entropy change.

$$\Delta U = Q - W \tag{6}$$

The change in internal energy ΔU of a system is a sum of the heat flowing into it (Q) and the work done by the system ($-W$). Heat is defined as the energy transfer between the system and its surroundings due to its temperature difference. Apart from heat, work includes all types of energy transfer. If the work is mechanical work involving a volume change in a system under constant pressure, the first law should be written as follows

$$\Delta U = Q_P - P\Delta V \tag{7}$$

Q_P represents the heat required for internal energy change under constant pressure.

Enthalpy is defined as H.

$$H \equiv U + PV \tag{8}$$

Thus, under constant pressure, the enthalpy change will be written

$$\Delta H = \Delta U + P\Delta V$$

or

$$\Delta U = \Delta H - P\Delta V \tag{9}$$

Comparing Eqs. (7) and (9), we can conclude the following.

$$\Delta H \equiv Q_P \tag{10}$$

As a result, the enthalpy change ΔH of a system under constatnt pressure is equal to the heat flow in or out of it. The heat flow at constant pressure will be measured as the enthalpy change, ΔH. Quite often we simply refer to ΔH as ‘‘enthalpy,’’ not ‘‘enthalpy change,’’ although the latter is technically correct.

3.7.2 Thermogravimetry (TG)

TG is primarily used to investigate the decomposition of materials by monitoring mass change as a function of temperature. Oxidation study can also be carried out and the kinetics of oxidation, reduction studies can be studied using TG. The main application of TG is to analyze material decomposition and thermal stability through mass change. A sample to be measured is placed in a furnace and its mass change is monitored by a thermobalance or microbalance. A typical microbalance can measure ±1 gm mass change. The primarly use of TG is to examine material decomposition and thermal stability by measuring mass change as a function of temperature in scanning mode or time in isothermal mode. TG curves is a representation of mass change expressed in percent on y-axis versus temperature or time on x-axis. A sample and reference are symmetrically placed in a furnace. The reference should be manufactured from a material that meets the following criteria: it does not undergo thermal events throughout the operational temperature range, it does not react with any instrument component, and it has similar thermal conductivity and heat capacity to the sample being examined. Sample mass and sample form (solid or powder) are the most important parameter for TG analysis. Thermal analysis can be run in either a reactive or nonreactive atmosphere. Reactive atmospheres include corrosive, oxidizing, and reducing gases. Nonreactive atmospheres should be inert gas with little water vapor. Dry Ar and N_2 are commonly used for nonreactive atmospheres. Gas flows through the furnace tube around the sample and carries volatile products out. For a sample mass of 2-10 mg, a flow rate of 15–25 ml min^{-1} is suggested. However, gas flow generates issues about possible thermal shielding and/or buoyancy effects. We can use all types of heating in TG like linear heating, stepwise heating, and dynamic heating as per our experimental need/requirement.

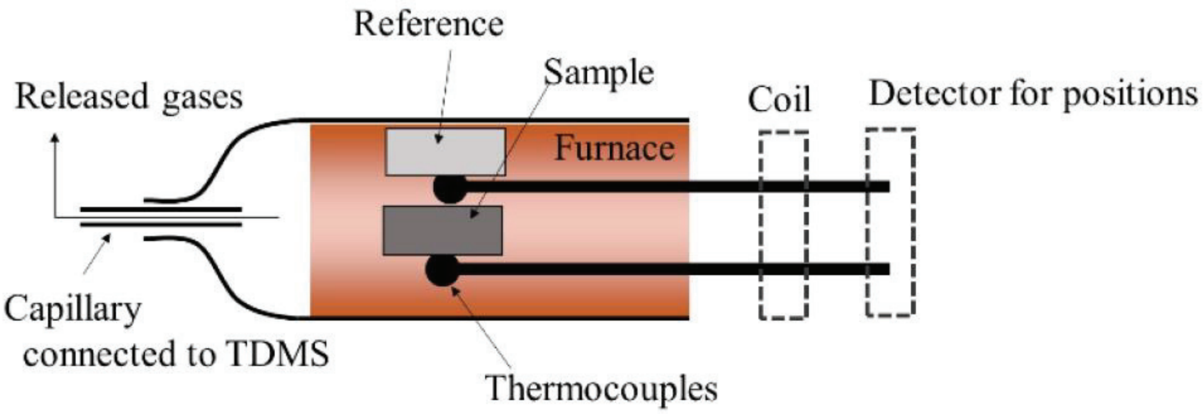

Figure 3.14. Reactor of TG – DTA apparatus

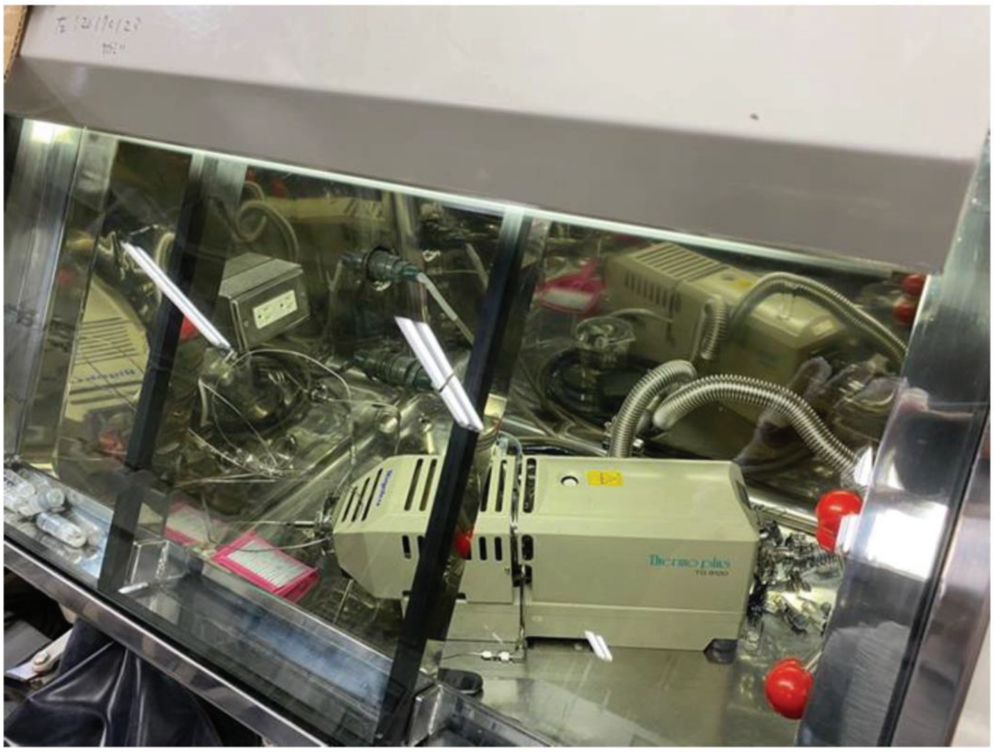

Figure 3.15 Picture of TG-DTA apparatus located in the glove box.

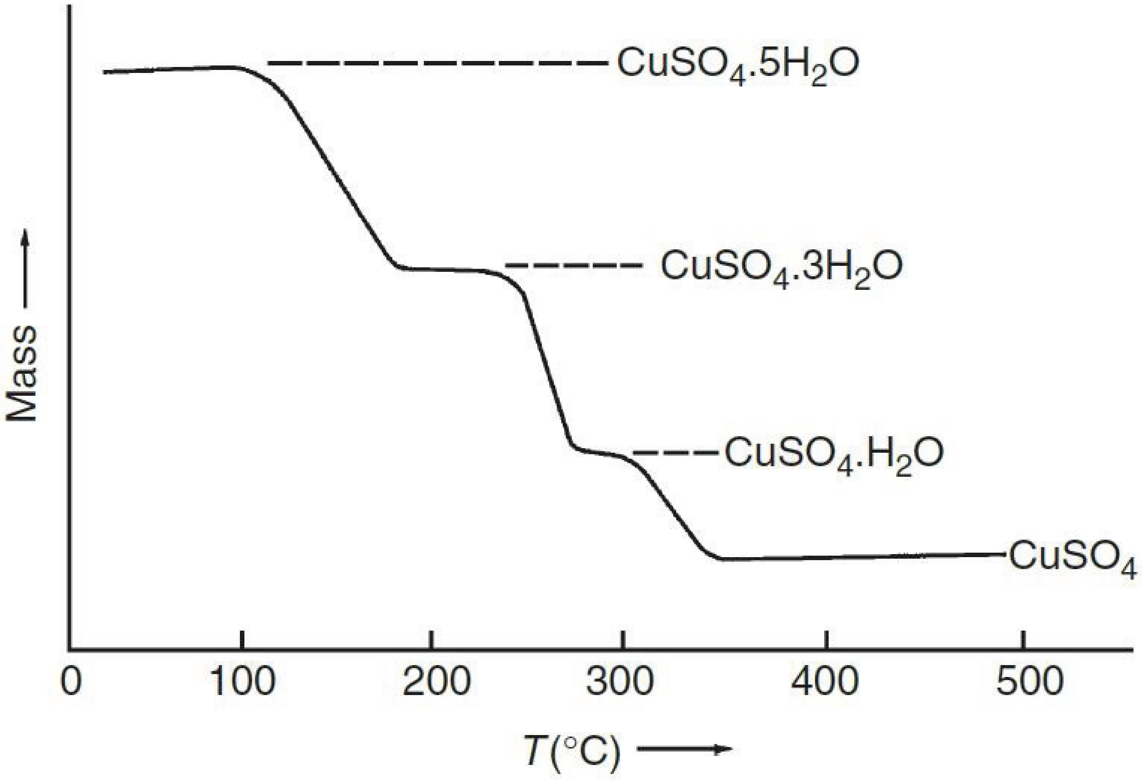
CuSO4.5H2O
CuSO4.3H2O
CuSO4.H2O
CuSO4
Mass
0
100
200
300
400
500
T(°C)

Figure. 3.16 TG curves of $CuSO_4.5H_2O$ in a range of ambient temperature to 500 °C. (Reproduced with kind permission of Springer Science and Business Media from 2001 Springer Science.)

Figure 3.16 shows the TG analysis of the thermal stability of $CuSO_4.5H_2O$. A slope change of a TG curve is the main feature used to analyze a sample. When the slope change is unclear, a derivative thermogravimetry (DTG) curve can be employed. A plot of dm/dT vs temperature is the DTG curve.

3.7.3 Differential Thermal Analysis (DTA)

The most widely used thermal analysis approach is differential thermal analysis (DTA). This technique also has the same purpose like TG : to examine thermal events in a sample by heating or cooling without mass exchange with its surroundings. The thermal events like solid-phase transformation, glass transition, crystallization, and melting are investigated by differential thermal analysis. The term ‘‘Differential’’ signifies that analysis is based on differences between the sample material and reference material in which the examined thermal events being investigated do not occur. Two thermocouples monitor the temperature differential between the sample and the reference: one is in contact with the sample holder (also known as the crucible), and the other is in contact with the reference holder.

Since the sample and reference have comparable thermal conductivity and heat capacity, the temperature difference between them (ΔT) should be zero when no thermal event happens in the sample. When a thermal event happens in the sample, nonzero ΔT will be generated. If the thermal event is endothermic (absorbing heat), ΔT will be negative; if the thermal event is exothermic, (releasing heat) ΔT will be positive. When an endothermic event occurs, the sample temperature falls below the reference temperature, which closely follows the heating program.

On the other hand, an exothermic event makes the sample temperature higher than the reference temperature. A DTA curve will shows thermal events over a certain temperature range, as shown in Figure 3.17. When the heating rate is constant, the DTA curve is a plot of ΔT versus reference temperature or heating time.

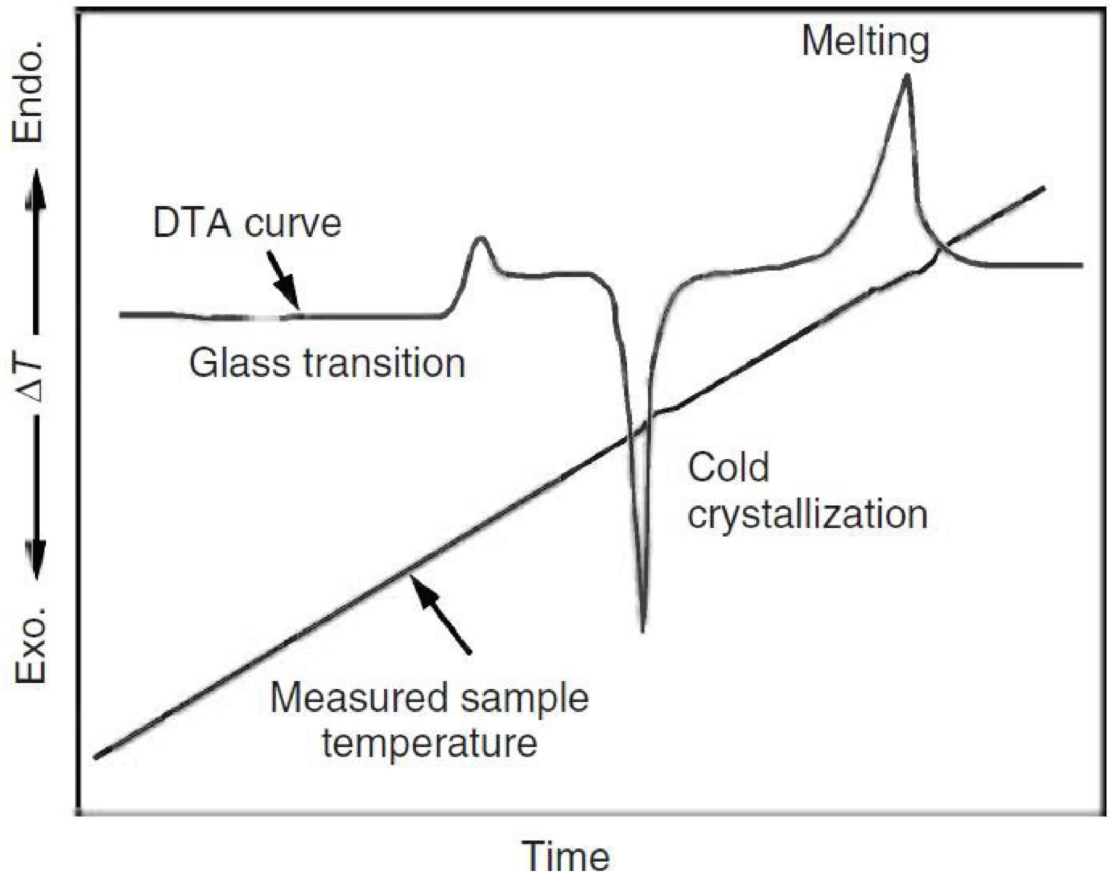

Figure 3.17 DTA curve for a polymer sample under a constant heating rate. Reproduced with permission from, 1999 John Wiley & Sons Ltd.

Procedure

In this study, TG-DTA apparatus (Rigaku, TG8120) was used to investigate the hydrogenation and dehydrogenation temperature of the Mg samples. The TG-DTA apparatus was located in the glove box (Miwa MFG, MDB-2BL, $H_2O < 0.2$ppm) as shown in Figure 3.15. When Mg absorbs hydrogen, the weight of the sample increases. Therefore, the hydrogenation temperature can be measured by using TG-DTA apparatus under H_2 flow. Hydrogen absorption measurement was carried out by following processes. The Mg sample was heated from room temperature to 40 °C under Ar flow, then the carrier gas was switched from Ar to H_2 at 40 °C. After switching the carrier gas, the temperature was kept for 30 min to investigate the hydrogen absorption at around room temperature. After keeping the temperature for 30 min, the sample was heated up to 250 °C @ 5 °C /min. In this work, the reactivity of each sample with H_2 was evaluated by comparing the onset temperatures of weight gain. Here, isotherm measurement is required for quantitative analysis of hydrogen absorption kinetics. However, the temperature immediately increases when Mg absorbs hydrogen. For the analysis of the hydrogen desorption properties of the catalyzed MgH_2 samples, the sample was heated up to 400 °C under Ar flow. Desorbed gas during heating was analyzed by thermal desorption mass spectroscopy connected with TG-DTA apparatus.

3.8 X-Ray Photoelectron Spectroscopy (XPS)

X-ray photoelectron spectroscopy (or XPS) is also known as electron spectroscopy for chemical analysis (ESCA). It is one of the surface analysis methods and is widely used to investigate the chemical composition of surfaces.

XPS technique first discovered by Heinrich in 1887 based on photoelectric effect. X-ray Photoelectron Spectroscopy (XPS) is based on the photo electric effect, and it was developed in the mid-1960 by Dr. Kai Siegbahn and his research team at the University of Uppsala, Sweden. In 1981, Dr. Siegbahn received a Nobel Prize for his work on high resolution electron spectroscopy, which was initially referred to as electron spectroscopy for chemical analysis (ESCA).

X-ray photoelectron spectroscopy is a surface sensitive analytical technique, in which x-rays of particular energy or wavelength bombard on the surface of a material and the kinetic energy of the emitted electrons is measured using hemispherical energy analyzer. The chemical composition and physical properties of a solid's surface differ from those of the solid's core/interior. Analyzing surface sensitivity and chemical state information from the elements in the sample are two important findings makes this technique as a important analytical tool in the field of Science. It can detect all elements except hydrogen and helium. XPS has been used to study the surface of almost every material from plastics to textiles to soil to semiconductors. As every materials have surfaces, these surfaces interact with other materials. Factors such as surface wettability, adhesion, corrosion, charge transfer, and catalysis are all determined by surfaces and surface contamination, and, therefore, studying and understanding surfaces is important aspect in research and development.

Basic Principle of X-ray spectroscopy

When an X-ray will incident onto the sample the X-ray energy will be absorbed by the sample and eject the photoelectron from the surface of the sample. The interacted energy of X-ray (hν) should always be greater than the binding energy of electron and kinetic energy of ejected electron otherwise photo electron ejection is not possible from the surface of the sample.

In other words when a X-ray of suitable energy interacted with an atom, an electron is emitted. Therefore emitted electron is called as photoelectron. The word 'photo' is related to 'light' and therefore this effect is known as photoelectric effect. Many pioneers including Plank, Einstein and Robert Millikan contributed to describing this process. Unlike the photon, the photoelectron have the mass and charge.

In XPS, the sample is irradiated with soft X-rays and the kinetic energy of the ejected photoelectron was measured. The emission of the photoelectron is the result of complete transfer of X-ray energy to the core level of electron and expressed mathematically by equation (11).

$$E_{(h\nu)} = E_b + E_k + (\phi_{spec}) \qquad (11)$$

It simply states that the x-ray energy $(h\nu)$ is equal to the electron's binding energy (E_b) (how firmly it is bonded to the atom/orbital to which it is associated), plus the kinetic energy (E_K) of the ejected electron, plus the spectrometer work function (ϕ_{spec}), which is a constant number.

Because energy of an X-ray with particular wavelength is known (for example Al K_α X-rays, $E_{photons} = 1486.7\ eV$) and as the kinetic energy of the emitted photoelectron will be measured, then binding energy of each photoelectron can be measured by rearranging the equation (11).

$$E_b = E_{(hv)} - (E_k + (\phi_{spec})) \qquad (12)$$

This concept is also demonstrated graphically in Fig. 3.18. Where, E_k is kinetic energy evaluated by equipment. ϕ_{spec} depends on each piece of equipment, which is decided by measuring a standard sample such as Ag film.

Note that the photoelectron binding energy is measured with respect to the sample Fermi level (not the vacuum level) which is the reason that ϕ_{spec} is included. The binding energy is defined as the energy transferred from each orbital's electron level to the Fermi level. The work function is defined as the energy difference between Fermi level and vacuum level, and it depends on various factors such as element, the shape of the surface, lattice plane. However, for determining the binding energy, it is not necessary to calculate the sample's work function. When the sample is electrically connected to the spectrometer, it is reasonable to assume that their Fermi levels become identical as shown in Figure 3.18. As a result, if the spectrometer's work function (ϕ_{spec}) is known, the binding energy can be determined using the equation (12).

By the element and orbital from which photoelectron were ejected, peaks were noted. Any electron released from the material with a binding energy less than the x-ray source energy should be noticed using the XPS method. An electron's binding energy is a material property and is independent of the x-ray source used to eject it. The binding energy of photoelectrons does not change when tests are carried out with different x-ray sources; however, the kinetic energy of the photoelectrons emitted will vary as described by equation (12).

In XPS charge up effect occurred due to mainly following reasons, the ejected photoelectron create the positive charge around the nucleus and surface. On the other hand the given energy of X-ray (hν) is always greater than the work function and binding energy of photo electron.

The ejection of photoelectrons in the core-levels and valence band are responsible for the XPS peak. In quantum mechanics, the nomenclature for a core level is nlj. The nlj is defined as; n: principal quantum number, l: orbital angular momentum quantum number, s: spin angular momentum quantum number, and j =|l ± s|: total angular momentum quantum number. Figure 3.19 Shows the spin-orbit splitting and degeneracy corresponding to s, p, d, and f orbital respectively. In XPS, orbit split into two peaks due to l and s coupling and degeneracy. If l=0, single XPS peak, if l > 0, a doublet peak spin orbit (l-s) coupling. For l = 0, s levels are singlets, no splitting however for l > 0, p, d, f levels give rise to doublets, because the unpaired electron left in an orbital can have its spin and orbital angular momentum either parallel or anti-parallel. The degeneracy, 2j+1, determines how many possibilities exist for parallel or anti-parallel pairing and thus the relative peak ratio of the two doublet components. Binding Energy (BE) of lower j value in doublet is higher (BE 2p1/2 > BE 2p3/2). The magnitude of spin-orbit splitting increases with an increase in atomic number value (Z). The magnitude of spin-orbit splitting decreases with distance from the nucleus (increased nuclear shielding).

XPS Instrumentation

a. Ultra High Vacuum System

The ultra high vacuum system provides longer photoelectron path length, it also helps in keeping clean surface and preventing the contaminations to produce X-ray signal. A ultra

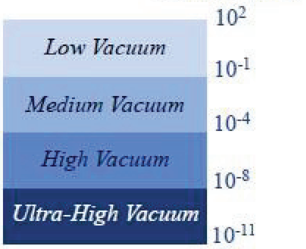

high vacuum is required < 10^{-8} Torr. Various kinds of vacuum pump will be used like Roughing pump, turbo pump, and ion pump to maintain the vacuum.

b. X-ray source

The mechanism of the X ray generation for the X ray source is the same as that of the XRD equipment, although the energy range of X ray is different for both techniques. In case of XRD generally Cu K_α (1.54 Å) used as incident X-ray source, the energy of X-ray is 8.05 keV. However, in case of XPS, (Al K_α) 1.49 keV or (Mg K_α) 1.25 keV are used as a X-ray energy source for XPS measurement. The other different X-ray source is mentioned in Table 3.3. Generally, the natural width of X-ray should be 0.8~0.6 eV, monochromator is frequently used to minimize the width of an X-ray.

Table 3.3 Different types of X-ray source

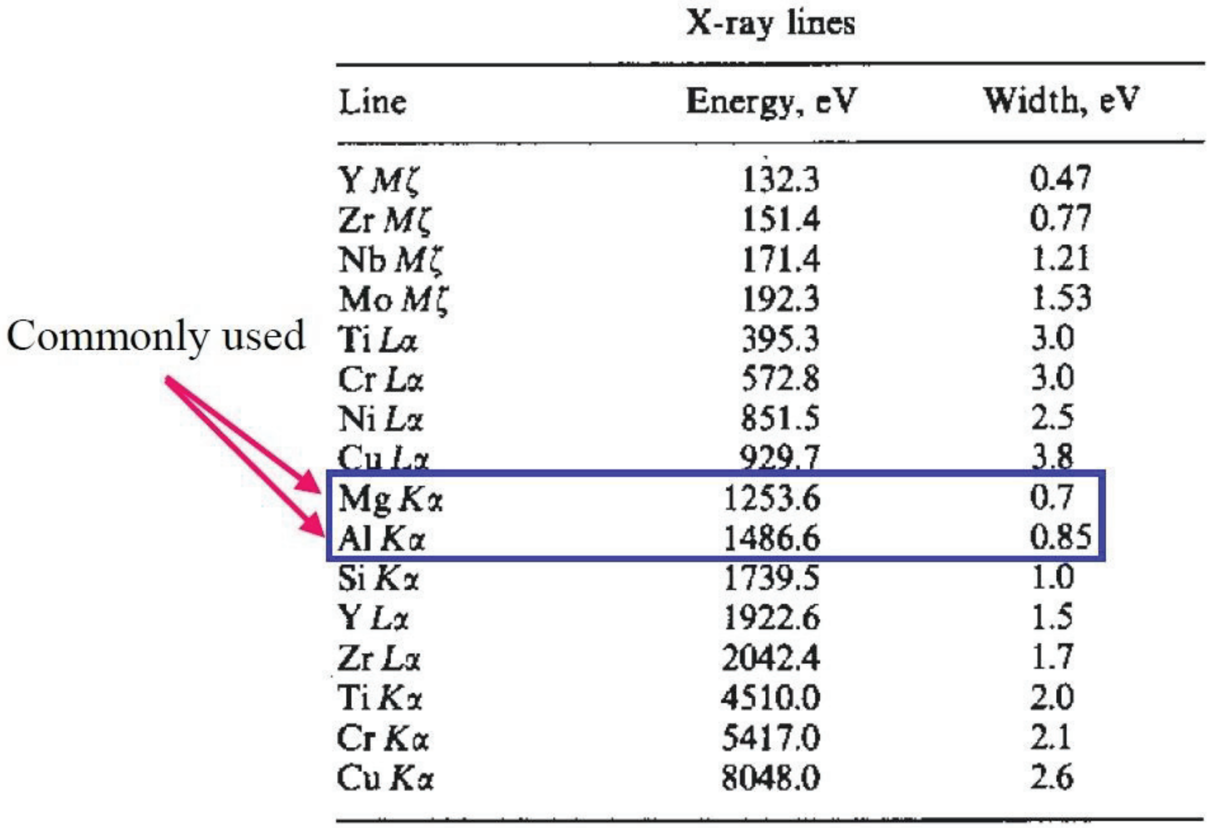

X-ray lines

Line	Energy, eV	Width, eV
Y $M\zeta$	132.3	0.47
Zr $M\zeta$	151.4	0.77
Nb $M\zeta$	171.4	1.21
Mo $M\zeta$	192.3	1.53
Ti $L\alpha$	395.3	3.0
Cr $L\alpha$	572.8	3.0
Ni $L\alpha$	851.5	2.5
Cu $L\alpha$	929.7	3.8
Mg $K\alpha$	1253.6	0.7
Al $K\alpha$	1486.6	0.85
Si $K\alpha$	1739.5	1.0
Y $L\alpha$	1922.6	1.5
Zr $L\alpha$	2042.4	1.7
Ti $K\alpha$	4510.0	2.0
Cr $K\alpha$	5417.0	2.1
Cu $K\alpha$	8048.0	2.6

c. Electron Analyzer

   Electrons of different energies are identified by applying electrostatic and magnetic fields. Hemispheric Energy analyzers are used.

d. Detector and signal processor

Applications

a. Elemental composition of the surface (top 0 –10 nm usually)

b. Surface composition of catalyst

c. Empirical formula of pure materials

d. Elements that contaminate a surface

e. Chemical or electronic state of each element in the surface

f. Uniformity of elemental composition across the top surface (or line profiling or mapping)

g. Uniformity of elemental composition as a function of ion beam etching (or depth profiling)

Procedure

In this thesis, XPS measurements were conducted using two apparatuses of ESCA lab 250Xi (Thermo Fisher), and JPS-9200 (Japan Electro-Optical Laboratory Co. Ltd.) with Al-Kα(1486.6 eV) to analyze chemical states of surface for each sample. The samples were fixed with the help of carbon tape, on the sample holder. To avoid the charge-up effect, a flood gun was used during the XPS measurements to obtain an accurate result. The spectra were calibrated with the C1s (285.0 eV) of each sample. The samples were transferred with the help of a closed setup to transfer the samples from the glove box to the XPS instrument.

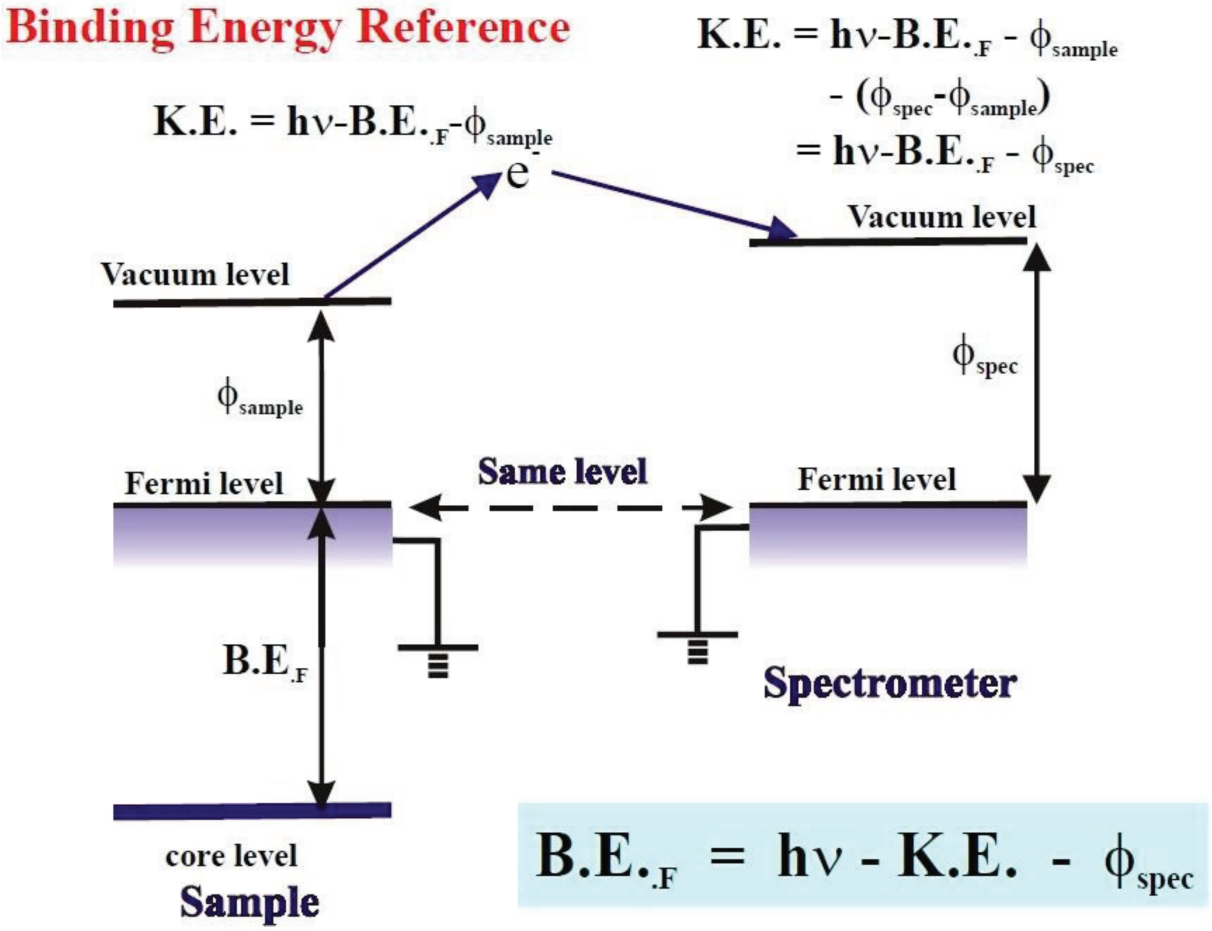

Figure 3.18 Model of energy level when analyzer and sample are electrically connected.

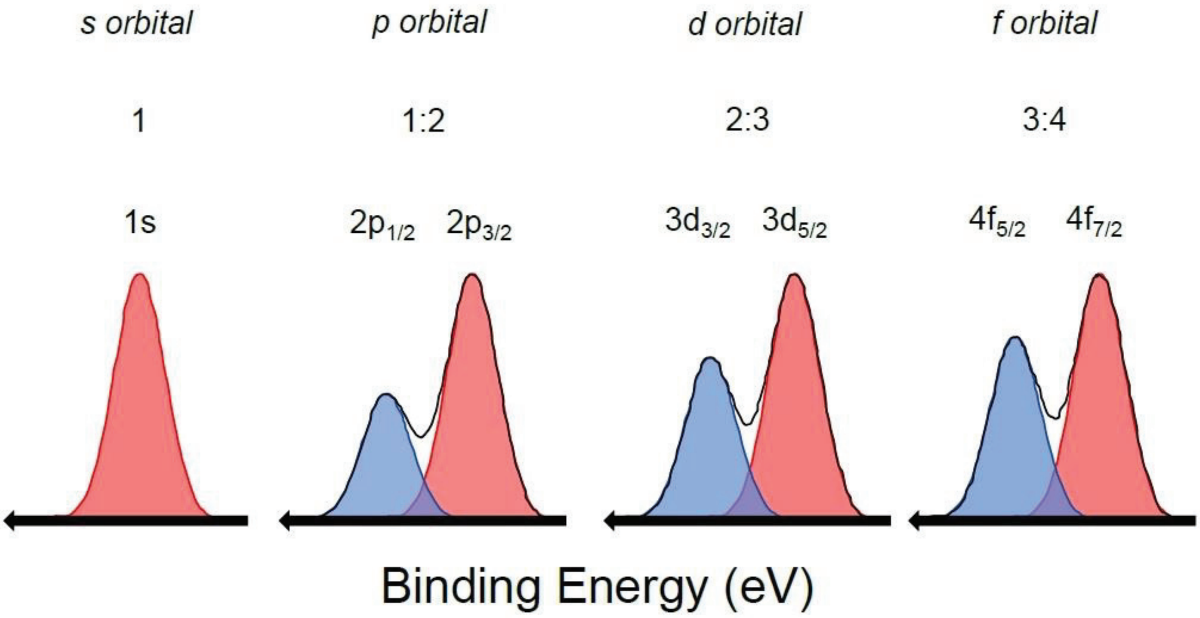

Figure 3.19 Shows the spin orbit splitting corresponding to s, p, d and f orbital

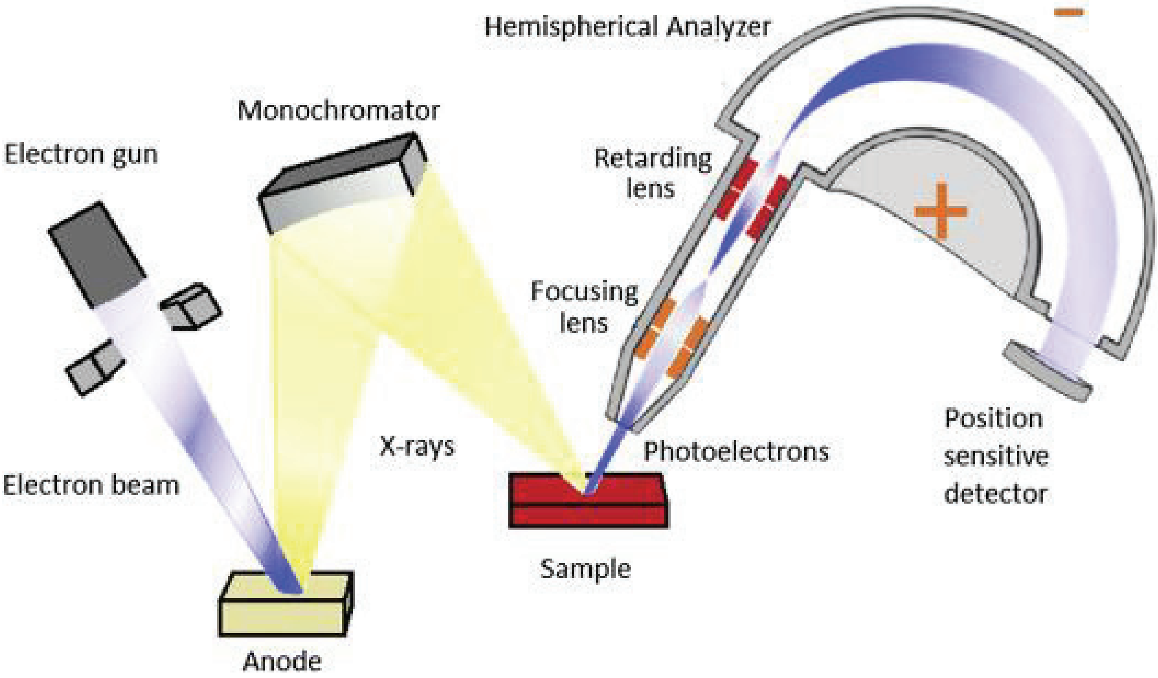

Figure 3.20 Scamatic diagram of photoelectron spectroscopy (XPS) instrument

3.9 References

[3-1] Yang L., Material Characterization Technique, WILEY-VCH, Verlag GmbH & Co. KGaA.

[3-2] Barkhordarian, G., Klassen, T. & Bormann, R. Fast hydrogen sorption kinetics of nanocrystalline Mg using Nb_2O_5 as catalyst. Scr. Mater. 49, 213–217 (2003).

[3-3] Denis, A., Sellier, E., Aymonier, C. & Bobet, J. L. Hydrogen sorption properties of magnesium particles decorated with metallic nanoparticles as catalyst. J. Alloys Compd. 476, 152–159 (2009).

[3-4] Imamura, H., Tabata, S., Shigetomi, N., Takesue, Y. & Sakata, Y. Composites for hydrogen storage by mechanical grinding of graphite carbon and magnesium. J. Alloys Compd. 330–332, 579–583 (2002).

[3-5] Emami, H., Edalati, K., Matsuda, J., Akiba, E. & Horita, Z. Hydrogen storage performance of TiFe after processing by ball milling. Acta Mater. 88, 190–195 (2015).

[3-6] Wang, C. et al. XPS study of the deoxidization behavior of hydrogen in TiH_2 powders. Powder Technol. 302, 423–425 (2016).

[3-7] Wang, C., Pan, L., Zhang, Y., Xiao, S. & Chen, Y. Deoxidization mechanism of hydrogen in TiH_2 dehydrogenation process. Int. J. Hydrogen Energy 41, 14836–14841 (2016).

[3-8] Koch, C. C., Cavin, O. B., McKamey, C. G. & Scarbrough, J. O. Preparation of 'amorphous' $Ni_{60}Nb_{40}$ by mechanical alloying. Appl. Phys. Lett. 43, 1017–1019 (1983).

[3-9] Hanada, N., Ichikawa, T. & Fujii, H. Catalytic effect of Ni nano-particle and Nb oxide on H-desorption properties in MgH_2 prepared by ball milling. J. Alloys Compd. 404–406, 716–719 (2005).

[3-10] Toshiyuki, S. & Hisanobu, W. Introduction of equipment for analytical chemistry. *SANKYO SHUPPAN CO., Ltd.* (1998).

[3-11] Toshiaki, O., Shigeo, H., Yuichi, I. & Kiichi, H. Transmission Electron Microscope. *Maruz. Co., Ltd.* (2002).

[3-12] Web page. https://photographylife.com/what-is-spherical-aberration.

[3-13] Akiba, E. *et al.* Practice of Powder X-ray analysis-Rietveld Refinement-. *Asakura Publ. Co., Ltd.*

[3-14] Shimazu, M. & Nakazawa, H. Semiconductor Detector and Its Applications to the X-ray Diffraction Method. *J. Mineral. Soc. Japan* **11**, 411–431 (1974).

[3-15] Sawada, T. *et al.* X-ray photoelectron spectroscopy. *Maruz. Co., Ltd.*

[3-16] Surfaces & Interfaces Section, National Physical Lab, www.npl.co.uk/npl/cmmt/sis

[3-17] Quases-IMFP-TPP2M QUASES-Tougaard Inc.:www.quases.com

[3-18] ASTM International: www.astm.org

[3-19] NIST X-ray Photoelectron Spectroscopy Database: www.srdata.nist.gov/sps/

[3-20] AVS Science & Technology Society: www.avs.org

[3-21] AVS Surface Science Spectra: www.avs.org/literature.sss.aspx

[3-22] ASTM International: www.astm.org

[3-23] XPS MutiQuant www.chemres.hu./aki/XMQpapes/XMQhome.htm

[3-24] Evans Analytical Group: www.cea.com

[3-25] PNNL EMSL: www.emsl.gov

4. Result and Discussion

4.1. Study on effective factors of oxide catalysts for the Mg-H system

As described in the purpose of this thesis, the effective factors to form the highly catalytic active state of oxides for the Mg-H system are not completely understood yet in details. The difficulty in understanding the detailed catalysis is caused by the difference in preparation processes of the samples performed by different research groups. Owing to the above-mentioned complicated process, it is difficult to define and compare the essential catalytic properties of oxides for the Mg-H system. [4-1-15]. Therefore, we have undertaken a systematic study to investigate the catalytic behavior of transition-metal oxides and discuss important factors for producing the catalytic active state. To perform this study, we took Nb as a standard element because it was reported that Nb oxide shows excellent catalysis for the Mg-H system, and its nearby neighboring element oxides (Nb_2O_5 and its neighboring element oxides TiO_2, ZrO_2, HfO_2 V_2O_5, Ta_2O_5, CrO_3, MoO_3, and WO_3) shown in Table 4.1. The initial state of all the oxides were taken in its maximum oxidation state. TiO_2, ZrO_2, HfO_2 present in its +4 oxidation state, V_2O_5, Nb_2O_5, Ta_2O_5 present in its +5 oxidation state, and CrO_3, MoO_3, and WO_3 present in its +6 oxidation state, respectively. It is interesting to know that all the periodic table transition metal oxide shows a wide range of oxidation states or positively charged forms, because of partially filled d and s orbitals.

In this work, the oxides are dispersed on the Mg surface by the same conditions, and the hydrogen desorption and absorption properties are investigated systematically and compared to discuss the critical factors to form catalytic active states.

4.1.1 Structural properties of MgH_2 with oxides

Table 4.1 Nb and its neighboring oxide with its maximum oxidation state

All oxide in its maximum oxidation state		
+4	+5	+6
TiO_2	V_2O_5	CrO_3
ZrO_2	Nb_2O_5	MoO_3
HfO_2	Ta_2O_5	WO_3

The XRD profile of each oxide are shown in Figure 4.1 (a), (b), (c), (d), (e), (f), (g), (h) and (i). Each XRD profile matched with its available database provided the single-phase configuration with the presence of main peaks. From the XRD profiles, it was confirmed that oxides samples were crystalline and single-phase for TiO_2, ZrO_2, HfO_2, V_2O_5, Nb_2O_5, Ta_2O_5, CrO_3, MoO_3, and WO_3, respectively. Here, among all the above-mentioned oxides, a few of them had coarser particle sizes and a few of them have smaller particle sizes. Each oxide was crushed by using agate mortar to form fine powders and make homogeneous throughout the oxide samples as pre-treatment before dispersing on the MgH_2 surface.

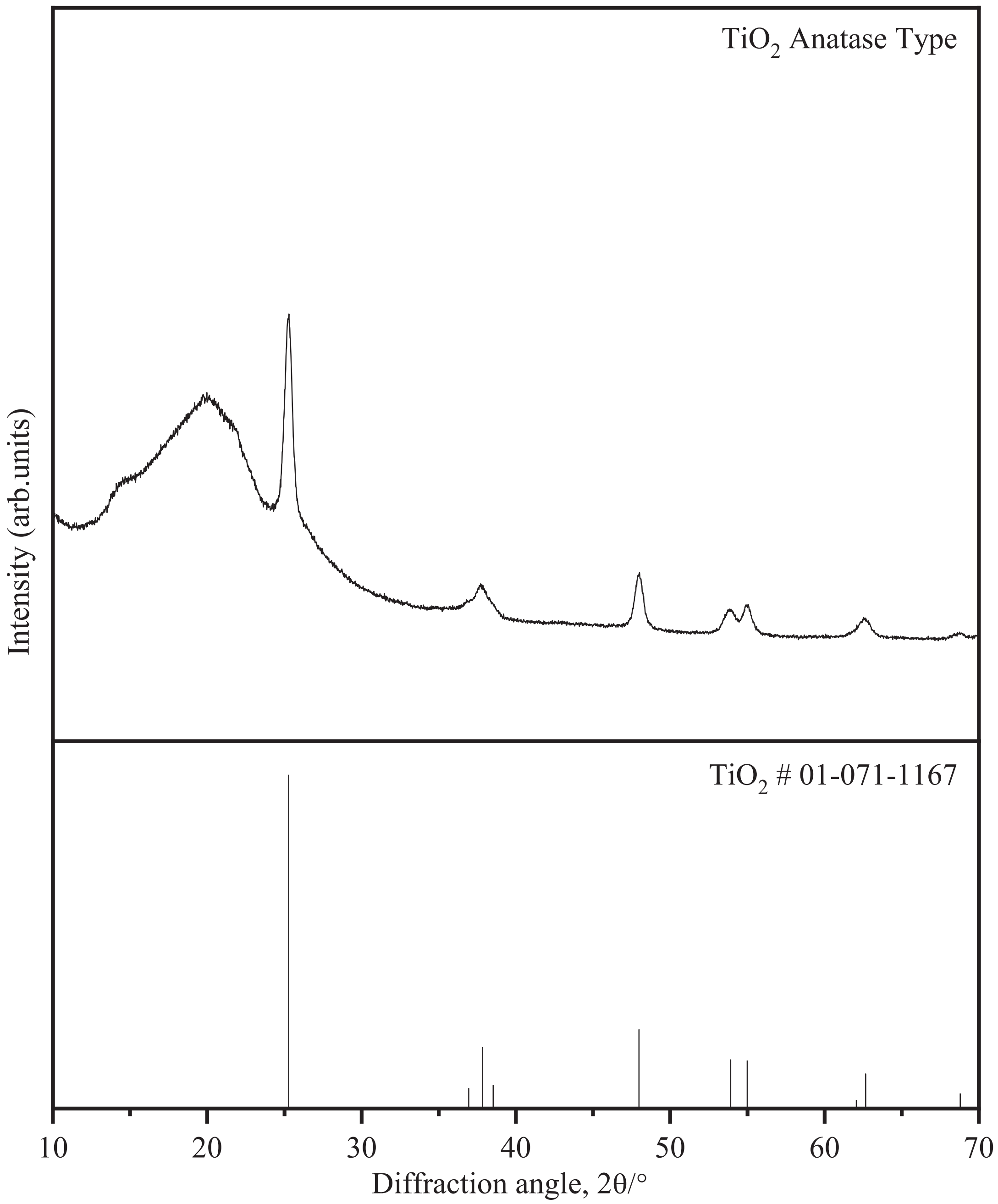

Figure 4.1 (a) XRD confirmed single phase of TiO_2 oxide

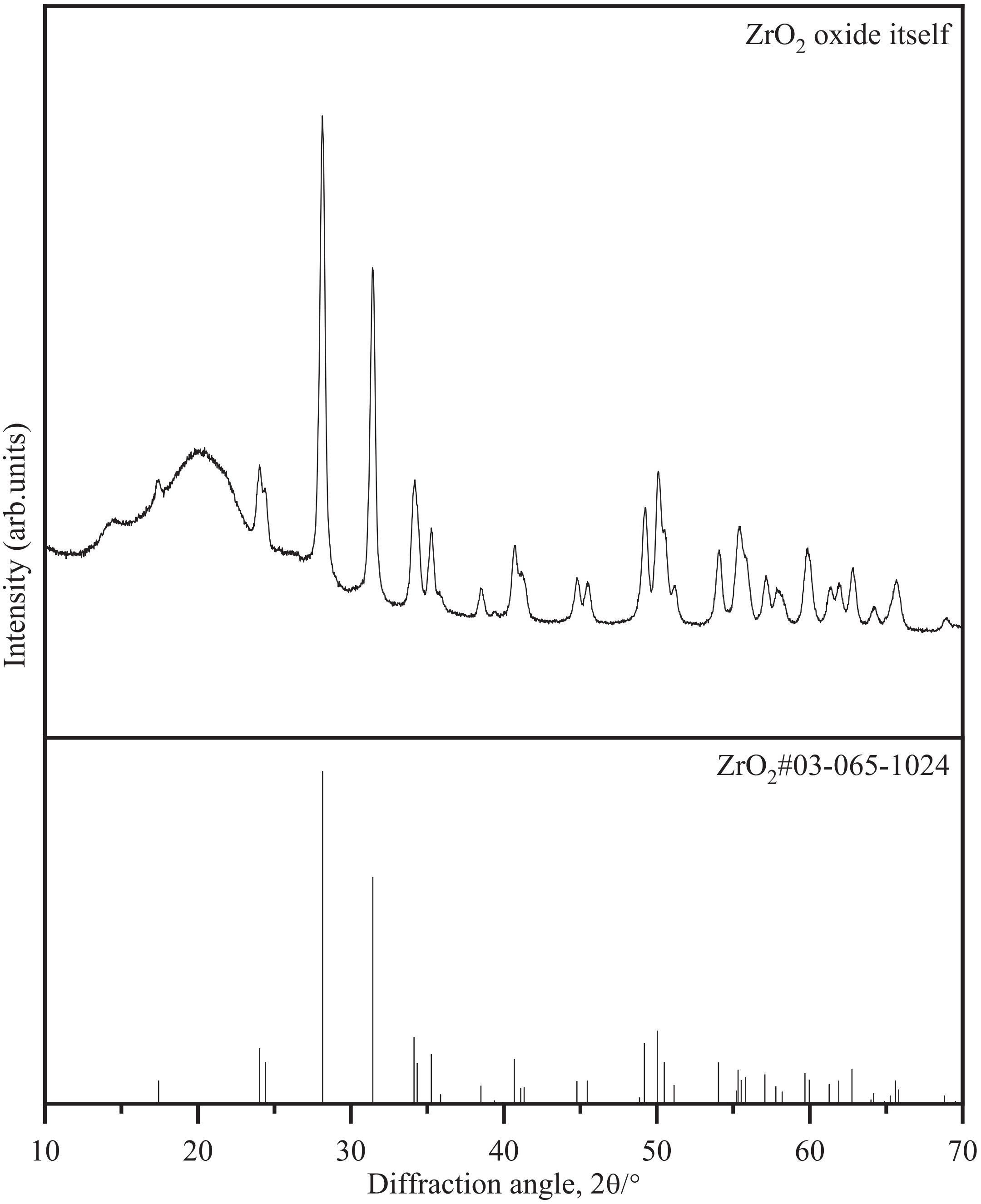

Figure 4.1 (b) XRD confirmed single phase of ZrO$_2$ oxide

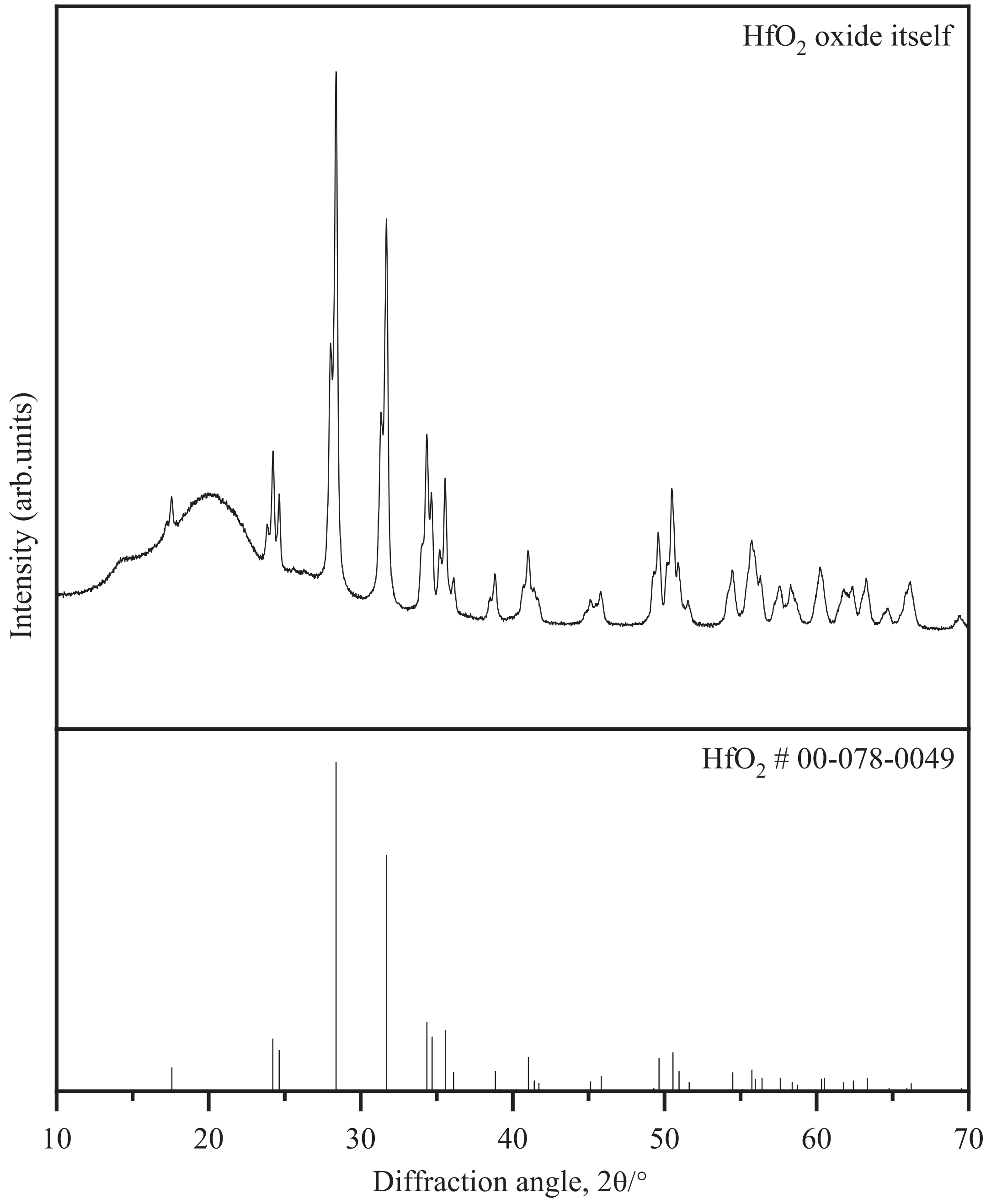

Figure 4.1 (c) XRD confirmed single phase of HfO$_2$ oxide

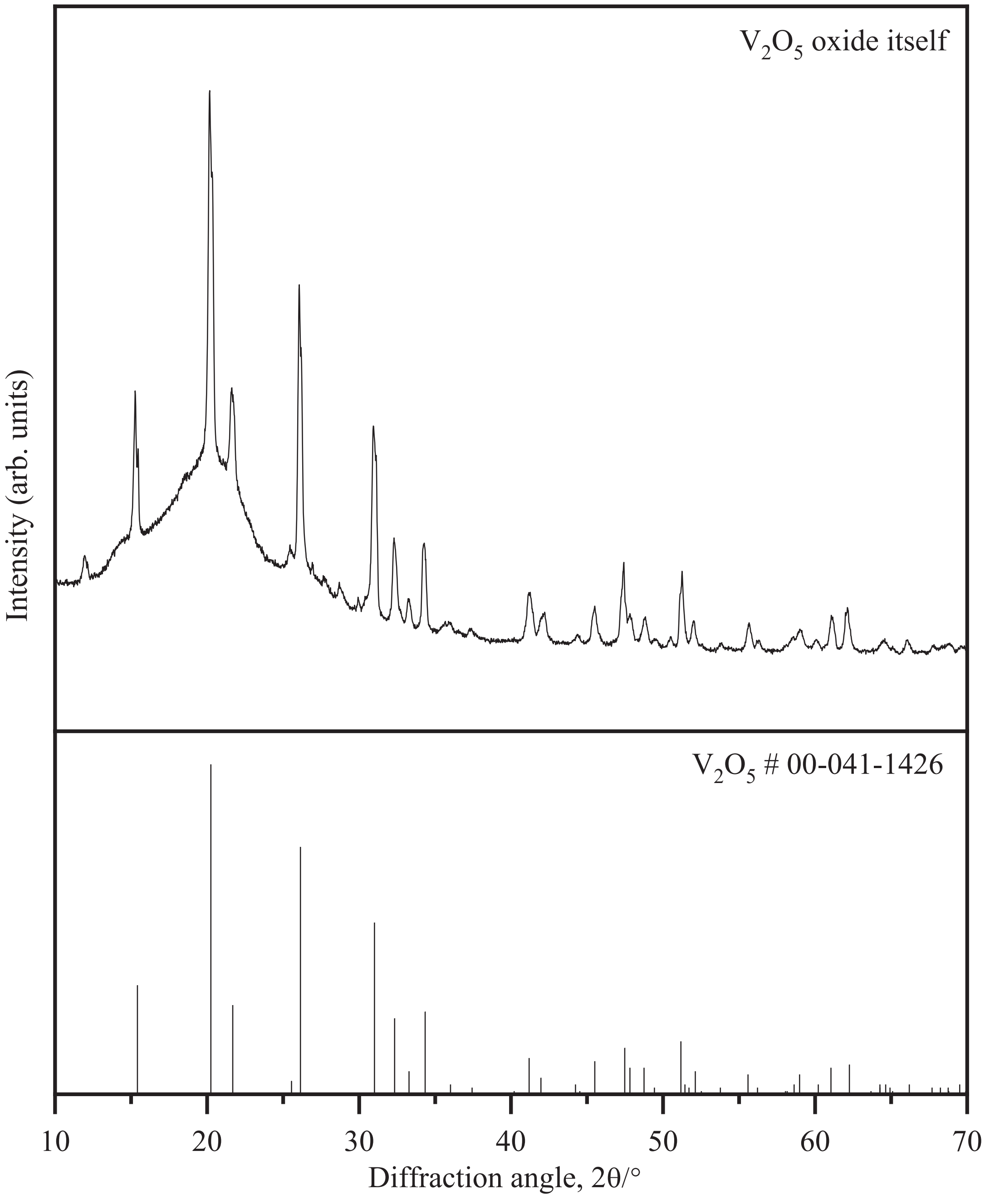

Figure 4.1 (d) XRD confirmed single phase of V_2O_5 oxide

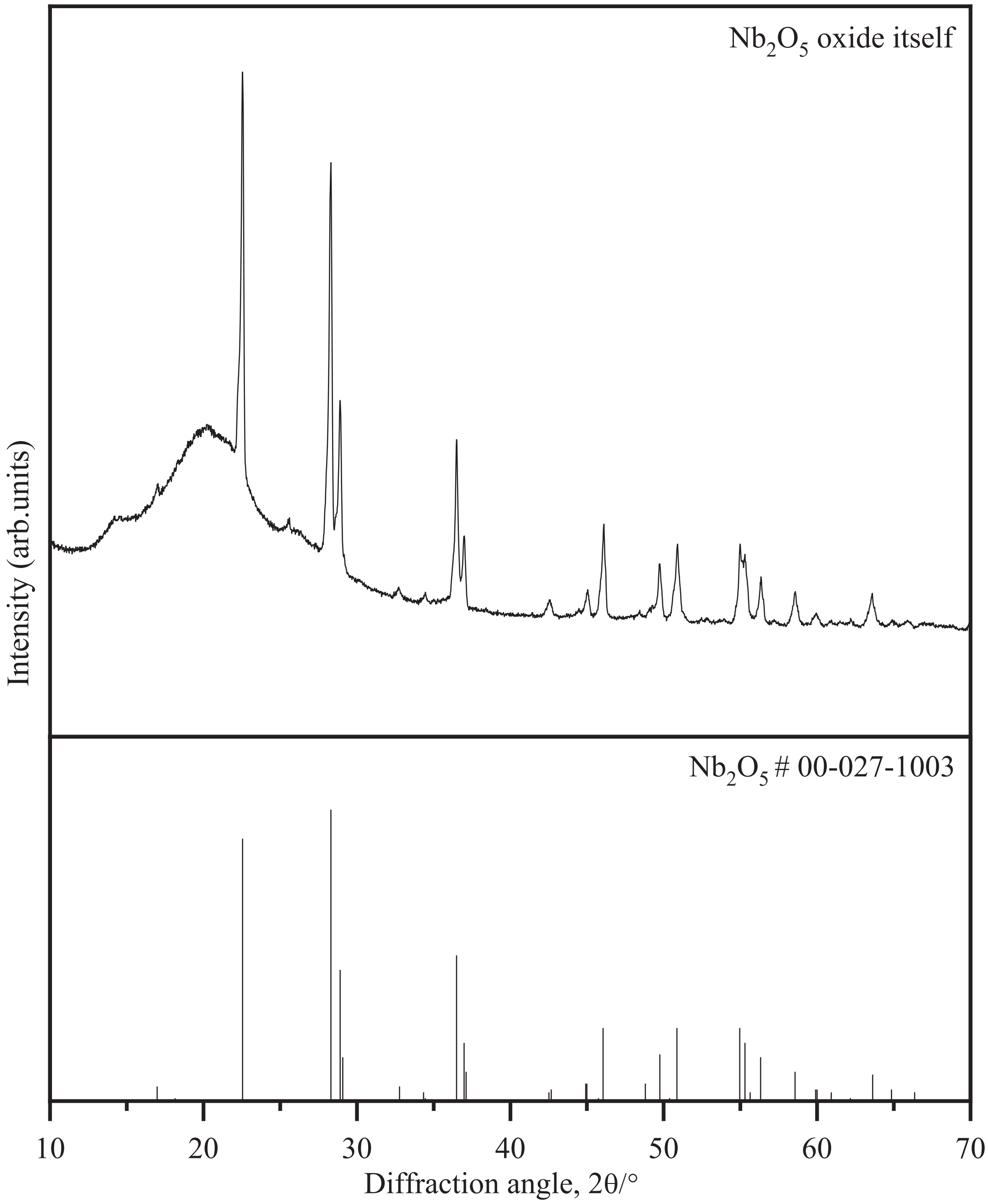

Figure 4.1 (e) XRD confirmed single phase of Nb_2O_5 oxide

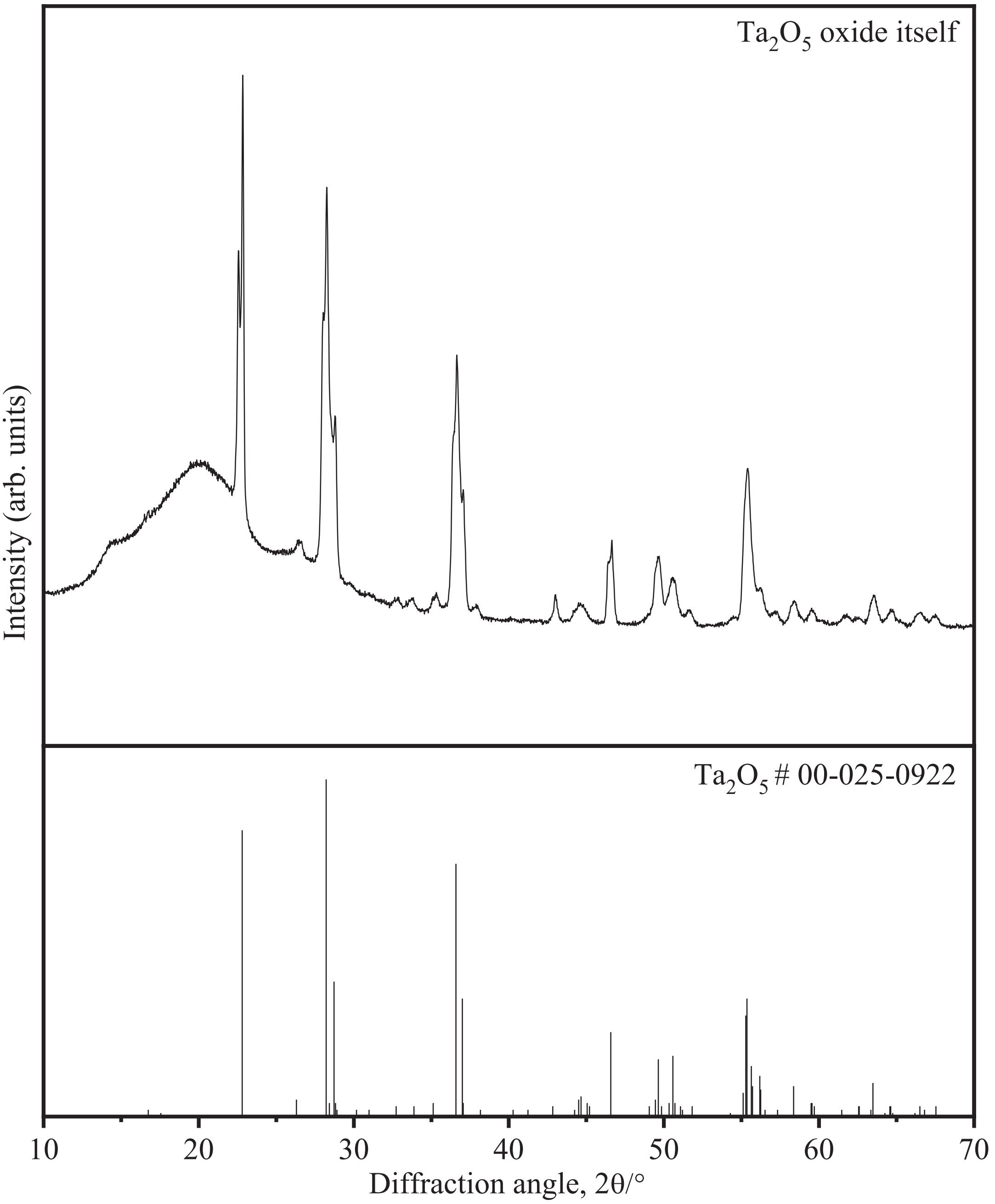

Figure 4.1 (f) XRD confirmed single phase of Ta_2O_5 oxide

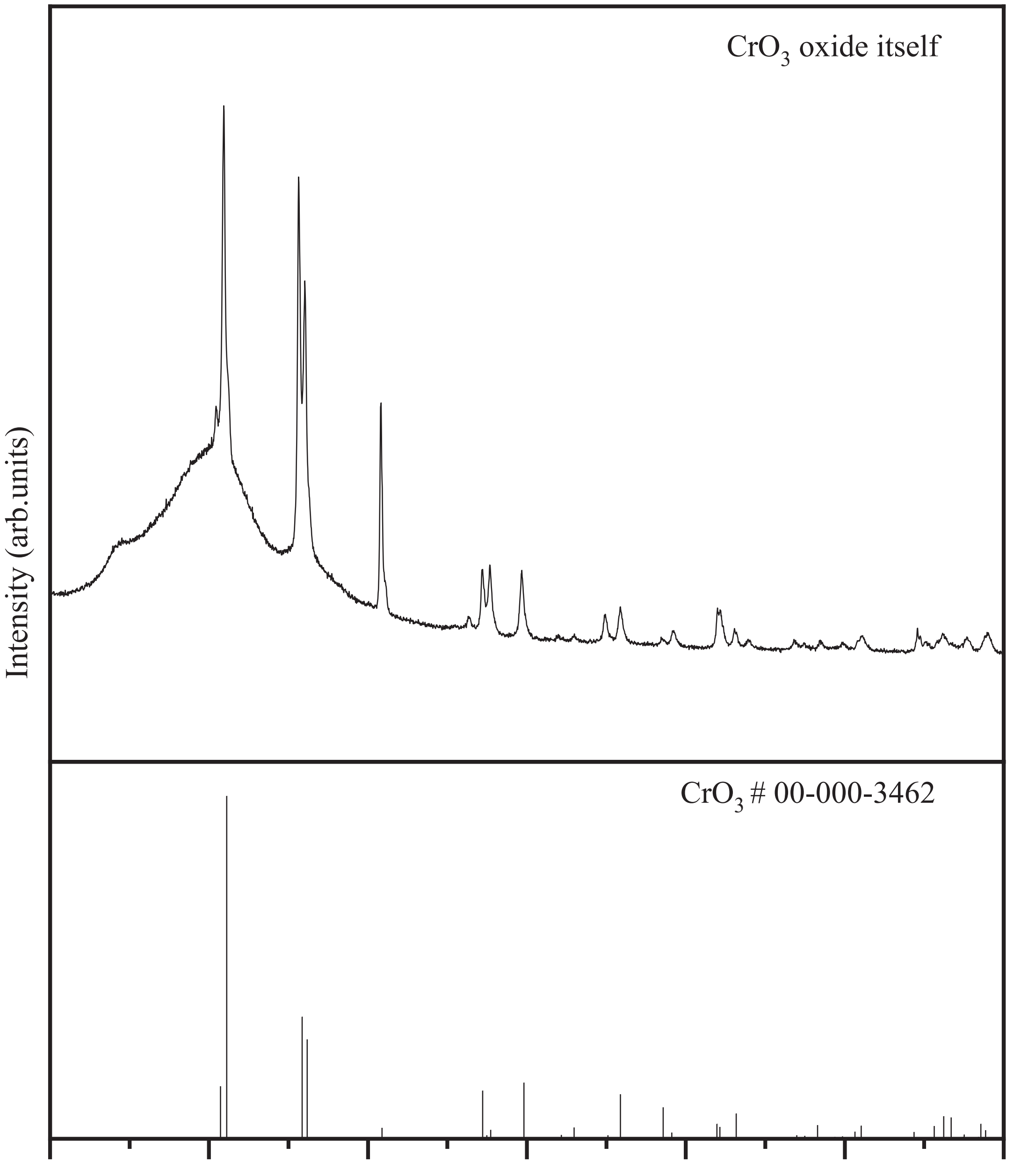

Figure 4.1 (g) XRD confirmed single phase of CrO_3 oxide

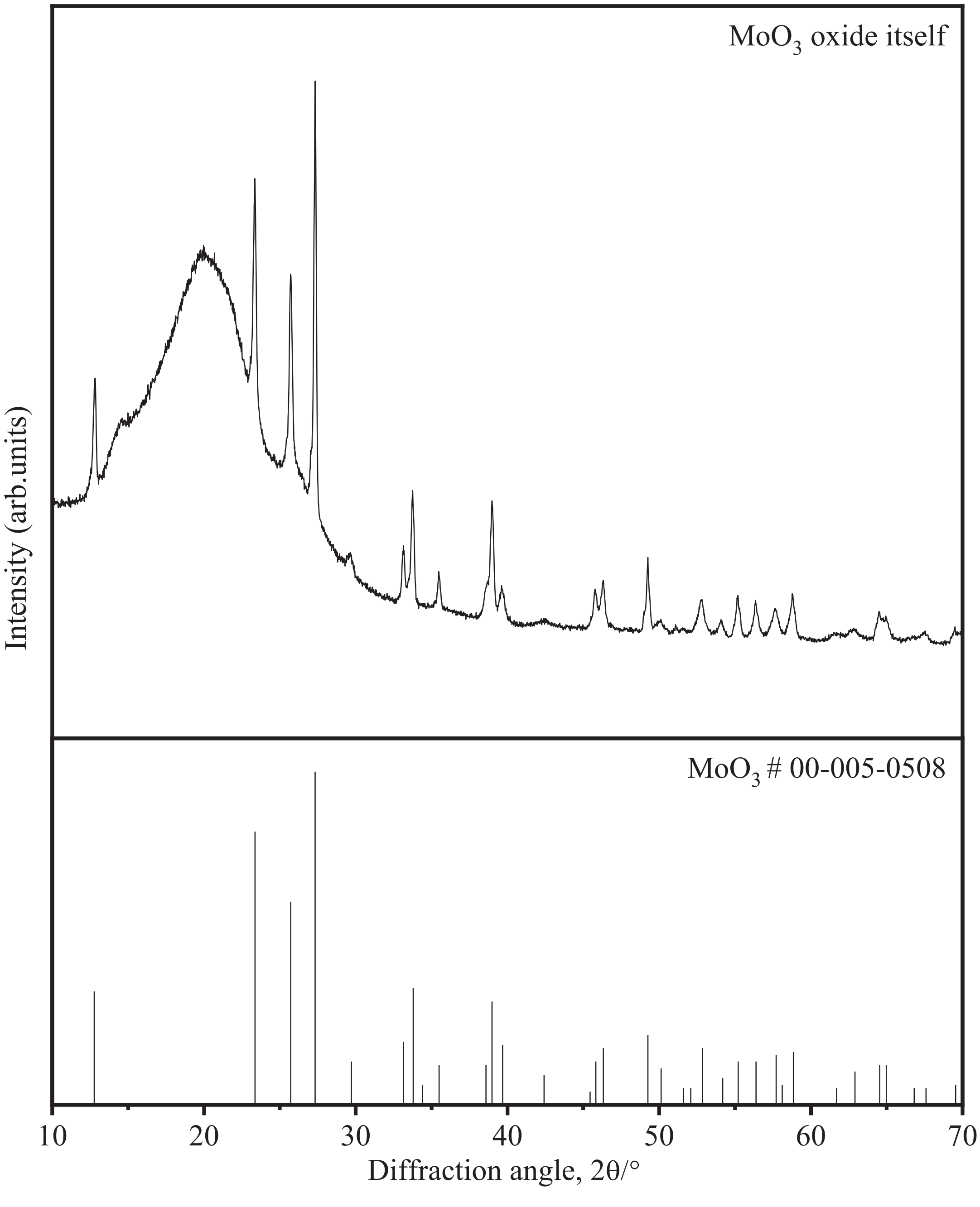

Figure 4.1 (h) XRD confirmed single phase of MoO$_3$ oxide

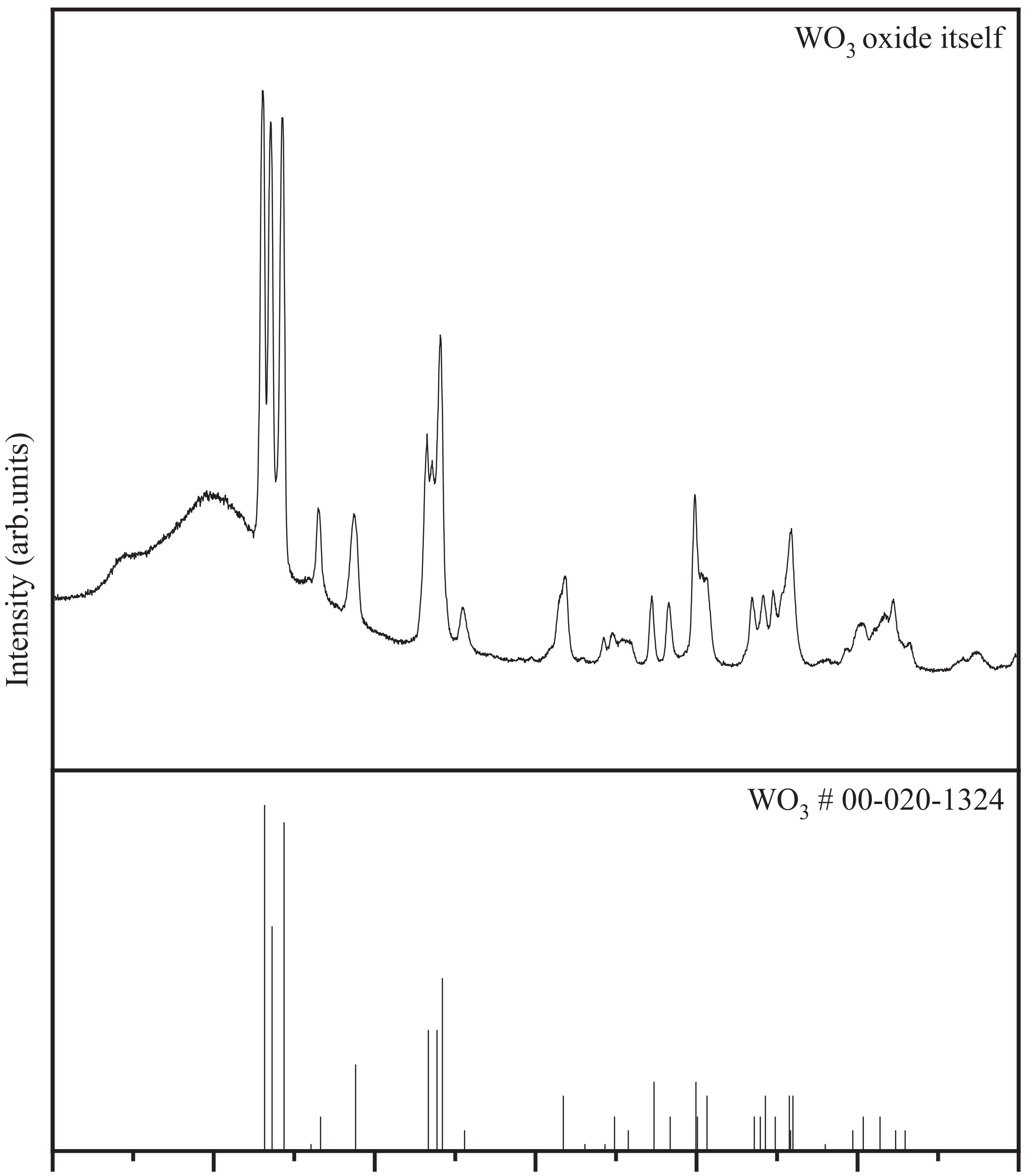

Figure XRD 4.1 (i) confirmed single phase of WO$_3$ oxide

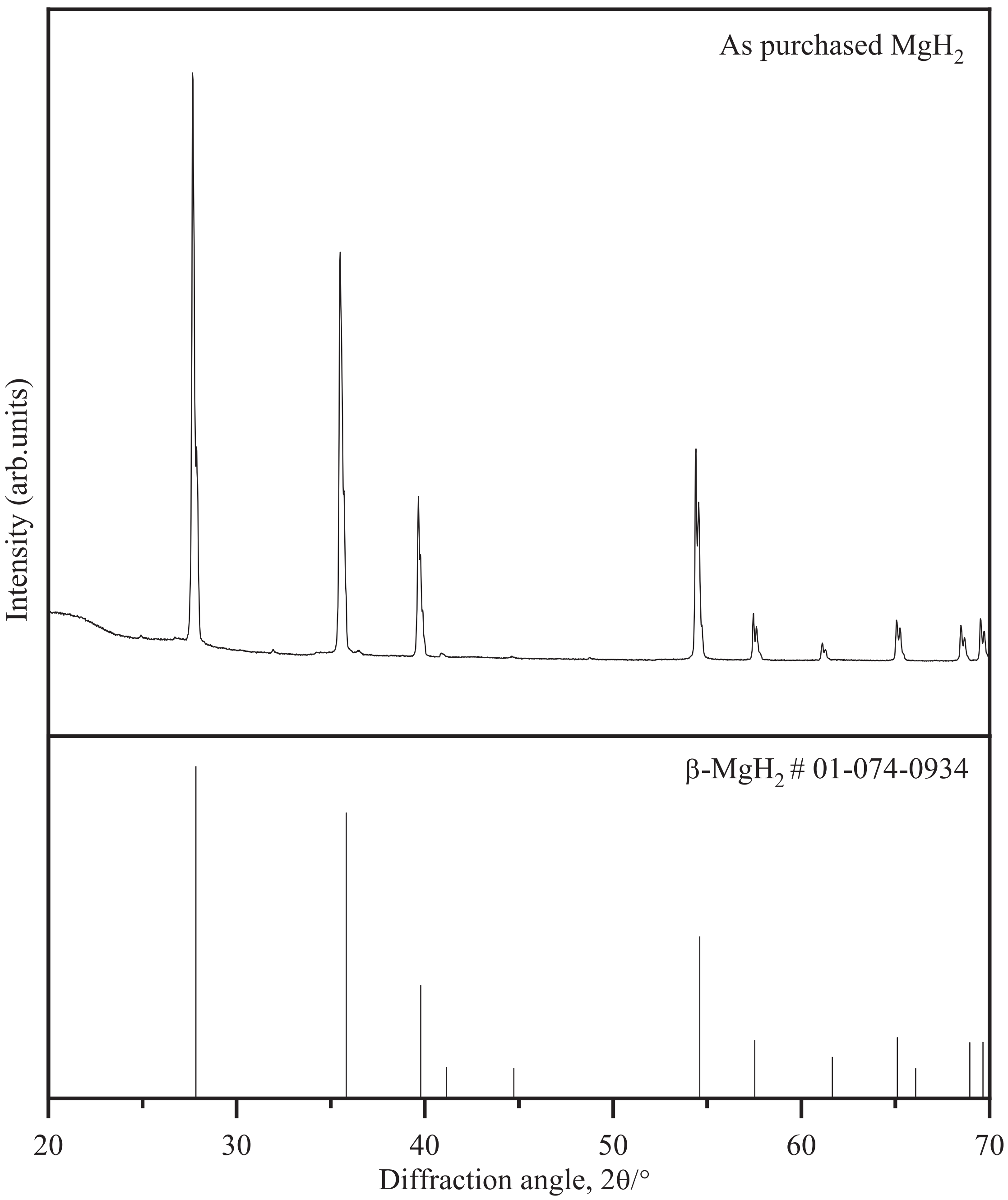

Figure 4.2 XRD confirmed the single phase of the pristine β-MgH_2 phase

To analyze the catalytic behavior, nine types of samples were synthesized by the ball-milling method, and these were denoted as MgH_2 + TiO_2, MgH_2 + ZrO_2, MgH_2 + HfO_2, MgH_2 + V_2O_5, MgH_2 + Nb_2O_5, MgH_2 + Ta_2O_5, MgH_2 + CrO_3, MgH_2 + MoO_3, and MgH_2 + WO_3 respectively. All the preparation process is explained in the experimental section. Figure 4.3 shows the XRD profile for the as-milled samples. Each XRD profile shows the formation of metastable γ-MgH_2 phase with β-MgH_2 phase. The as purchased MgH_2 used for each sample preparation was completely β-MgH_2 phase (single-phase), in its crystalline form as shown in Figure 4.2. When the β-MgH_2 phase is ball milled for a longer duration, high-pressure stress generated by the collisions of balls with the samples and vessel wall causes the phase transformation of the β-MgH_2 phase to the metastable γ-MgH_2. The XRD profiles reveals that the peak intensity of MgH_2 decreases compared to that of the pristine one. The peak intensity decreased because of crystallinity change caused by high energy ball milling leads to amorphization of the sample which further triggers complete loss of long-range crystalline structure. On careful observation, we found that there was peak broadening intended for each peak with all XRD profiles. The peak broadening was caused by the formation of the finite size of crystals as d spacing was disturbed during nanosizing which further causes disordered structure, as the ball milling was a high energy milling process. For the XRD profile of MgH_2 + TiO_2 as shown in figure 4.3, initial oxide TiO_2 peaks were not observed. Several possibilities lead to the undetectable TiO_2 peaks, as oxide possesses brittle nature therefore high energy ball milling causes nanosizing and amorphization, alternatively less sample amount can also be a reason. Hanada et. al. reported MgH_2 catalyzed with 1 mol% of Nb_2O_5, V_2O_5, and TiO_2. The XRD profiles with the absence of initial oxide peaks after ball milling are originated in a highly dispersed state of oxides on the Mg surface. The probability of highest dispersion of TiO_2 oxide on the Mg surface might be a cause for untraceable TiO_2 peak consistent with previous works. [4-23] The same phenomenon was also observed for MgH_2 + V_2O_5, MgH_2 + Nb_2O_5, and MgH_2 + CrO_3,

MgH_2 + ZrO_2, and MgH_2 + MoO_3 samples respectively. For MgH_2 + ZrO_2, ZrO_2 main peak overlapping was observed with MgH_2 in conjunction with quite low-angle small peaks. While for MgH_2 + MoO_3, two peaks of MoO_3 almost overlapped with MgH_2 at diffraction angles 27.29° and 35.48° respectively. However, since other clear peaks assigned to oxides were not observed, both ZrO_2 and MoO_3 were also changed to be almost nano-size particles. In other words, the high dispersion state of ZrO_2 and MoO_3 would happen on the Mg surface. Although in the case of MgH_2 + HfO_2, we assign several broad peaks of HfO_2 oxide at different diffraction angles including the overlapping of HfO_2 peak with MgH_2 around 28.41°, 31.68°, and 35.61°, suggesting that the oxidation state of HfO_2 is not changed. Namely, HfO_2 would not be highly dispersed on the Mg surface compared with the above oxides. On the other hand, peak lowering and broadening indicate the milling effects are applied. A similar phenomenon was also found for MgH_2 + Ta_2O_5 and MgH_2 + WO_3. Finally, the samples are categorized into two group; group A: MgH_2 + TiO_2, MgH_2 + V_2O_5, MgH_2 + Nb_2O_5, MgH_2 + CrO_3, MgH_2 + ZrO_2, MgH_2 + MoO_3 (without initial oxide peaks called highly dispersed state) and group B: MgH_2 + HfO_2, MgH_2 + Ta_2O_5 and MgH_2 + WO_3 (with initial oxide peaks called low dispersed state).

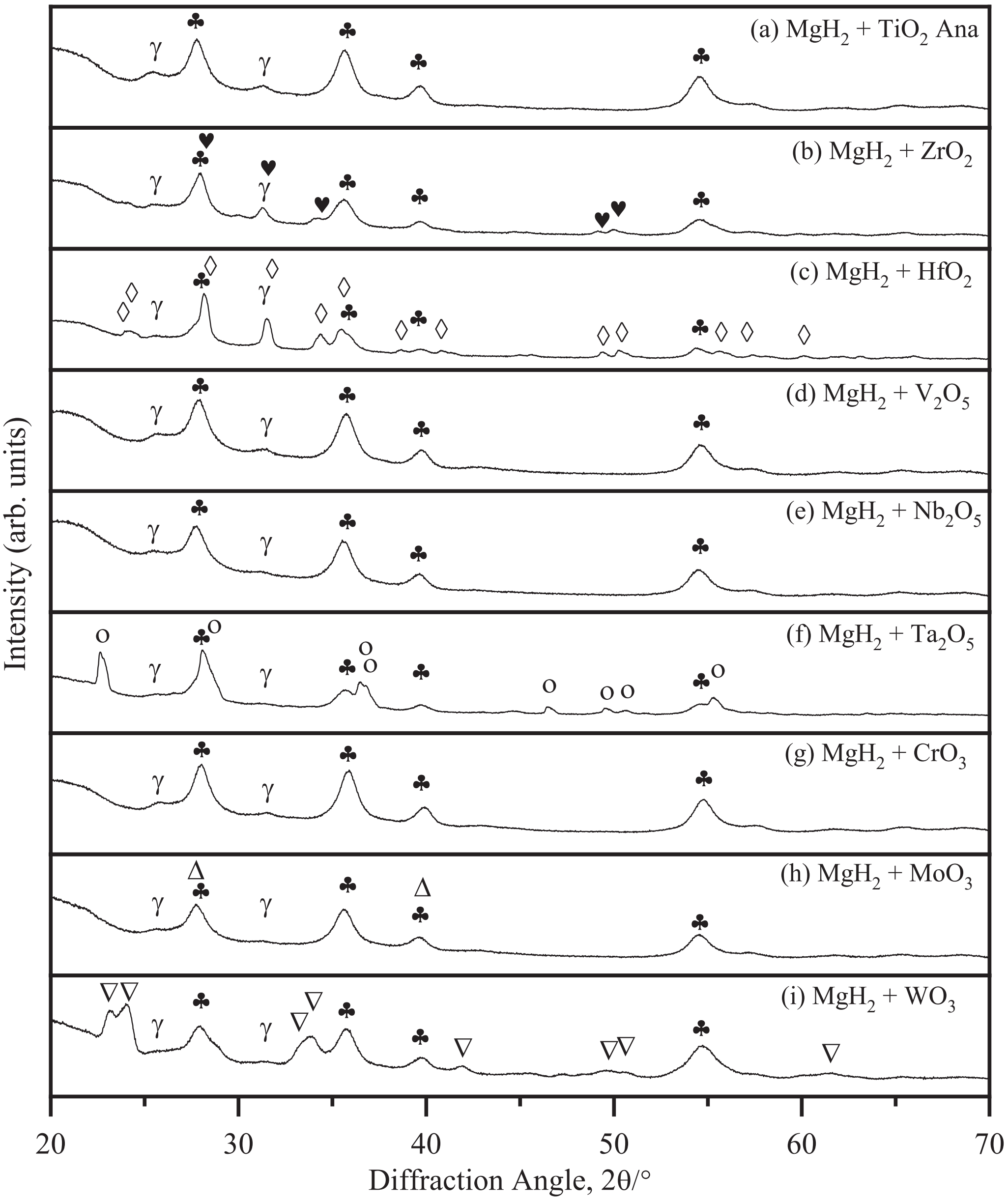

Fig. 4.3 XRD confirmed the ball milling of single phase of (a) $MgH_2 + TiO_2$ Ana; (b) $MgH_2 + ZrO_2$; (c) $MgH_2 + HfO_2$; (d) $MgH_2 + V_2O_5$; (e) $MgH_2 + Nb_2O_5$; (f) $MgH_2 + Ta_2O_5$; (g) $MgH_2 + CrO_3$; (h) $MgH_2 + MoO_3$; (i) $MgH_2 + WO_3$ with presence of β-MgH_2 and γ-MgH_2

PDF card No. β-MgH_2 ♣ #01-074-0934; γ-MgH_2 γ #01-089-7886; ZrO_2 ♥ #03-065-1024; HfO_2 ◊ #01-078-0049; Ta_2O_5 ○ #00-025-0922; MoO_3 Δ #00-005-0508; WO_3 ∇ #00-020-1324

4.1.2 Hydrogen desorption properties of MgH_2 with oxides

The hydrogen desorption kinetics of the catalyzed MgH_2 have been studied using the TG-DTA-MS measurements at a constant heating rate of 5 °C/min in Ar atmosphere, and the results are presented in Figure 4.4. Here, it was confirmed by the XRD measurements for the samples after the TG-DTA-MS experiments shown in Figure 4.5 that MgH_2 was fully decomposed to the Mg phase. The hydrogen desorption peak temperature for pristine MgH_2 as purchased was found around 420 °C. The hydrogen desorption peak temperature for $MgH_2 + CrO_3$, $MgH_2 + TiO_2$, $MgH_2 + V_2O_5$, and $MgH_2 + Nb_2O_5$ was observed between 206 °C to 222 °C. Among all these catalyzed samples, $MgH_2 + CrO_3$ shows the lowest peak temperature 206 °C among 9 samples. Here, although the hydrogen desorption temperature of $MgH_2 + TiO_2$, $MgH_2 + V_2O_5$, $MgH_2 + Nb_2O_5$, $MgH_2 + ZrO_2$ is slightly higher than that of the MgH_2+CrO_3, the difference between peak temperature lies within 16 °C. It will be difficult to discuss the small difference for the ball-milled samples under thermally activated conditions. Kinetics for hydrogen desorption is affected by catalysts and heat. The heating is an easy way to activate the reaction in general. Specifically, in the hydrogen desorption process, every time both effects are included and cannot be distinguished. Conversely, $MgH_2 + Ta_2O_5$, $MgH_2 + HfO_2$, $MgH_2 + WO_3$, and $MgH_2 + MoO_3$ shows the peak temperature about 285, 303, 310, and 324°C, respectively. On comparing the peak temperature with pristine MgH_2, it was clarified that all the oxides showed catalysis for the hydrogen desorption of MgH_2. Concerning the catalysis, the samples are classified into two groups. The addition of TiO_2, ZrO_2, V_2O_5, Nb_2O_5, and CrO_3 decreases the hydrogen desorption temperature (around 200 °C), suggesting that the catalytic activity of these oxides is high. Another group consists of MoO_3, HfO_2, Ta_2O_5, and WO_3. Careful observation of DTA curve parallel to MS yield's $MgH_2 + TiO_2$, $MgH_2 + V_2O_5$, $MgH_2 + Nb_2O_5$, MgH_2+CrO_3, MgH_2+MoO_3, shows single endothermic peak for hydrogen desorption, although

MgH_2 + ZrO_2, MgH_2 + Ta_2O_5, MgH_2 + HfO_2, MgH_2 + WO_3, shows two endothermic peak for hydrogen desorption. It can be discussed based on homogeneity of catalytic active states, which are simply well- and poor-catalyzed sites generated during the milling. Namely, the homogeneous well-catalyzed MgH_2 shows the one peak hydrogen desorption, whereas well-catalyzed with remaining poor-catalyzed portion show two peak hydrogen desorption. Such two peak hydrogen desorption profiles were reported for MgH_2 with different active sites by Hanada et. al. In addition, the different catalyzed states were also found when the repeatability was examined in this work as shown in Figure 4.6 (a), (b), (c), (d), and (e). Although the temperature region of hydrogen desorption was almost the same, the peak shape in MS spectra was slightly changed. This is one of the difficulties for sample synthesis by the ball-milling method. The TG curves show the hydrogen desorption starting point and end point on the x-axis whereas experimental hydrogen capacity is on the y-axis. For MgH_2+CrO_3, the hydrogen desorption started at 170 °C and consequently increases for MgH_2 + V_2O_5 at 177 °C, MgH_2 + TiO_2 at 178 °C, MgH_2 + ZrO_2 at 188 °C, MgH_2 + Nb_2O_5 at 189 °C approximately whereas at a much higher temperature for other samples. The theoretical hydrogen capacity for pristine MgH_2 was 7.6 weight % of hydrogen. On the other hand, the theoretical hydrogen storage capacity for catalyzed MgH_2 with TiO_2, ZrO_2, HfO_2, V_2O_5, Nb_2O_5, Ta_2O_5, CrO_3, MoO_3, and WO_3 was calculated as 7.16, 6.94, 6.54, 7.10, 6.99, 6.49, 7.05, 6.84 and 6.45 respectively. The TG results reveal that experimental hydrogen capacity was lower than the theoretical one. All the samples shows a loss of hydrogen capacity due to the addition of oxides. In addition, the hydrogen capacity is further decreased with the reduction of oxide by reaction with MgH_2 to form MgO during the ball-milling, where the reduction of oxides is reported before and discussed later.

From the above results, the relationship between the catalysis characterized by the TG-DTA-MS experiments and the dispersion state expected from the XRD results is discussed. As described above, when there are no peaks corresponding to initial oxides in the XRD profile after the ball milling, the high dispersion state of oxides can be expected. Thus, the high catalysis of TiO_2, V_2O_5, CrO_3, ZrO_2, and Nb_2O_5 would be explained by the high dispersion state. [4-23] Conversely, HfO_2, Ta_2O_5, and WO_3 with low catalytic activity show clear diffraction peaks corresponding to initial oxide phases. On the other hand, the MgH_2 + MoO_3 showed the highest hydrogen desorption peak temperature approximately around 324 °C even though no clear peaks were observed in the XRD measurements. Therefore, in addition to the dispersion state, different factors should be considered to explain the catalysis.

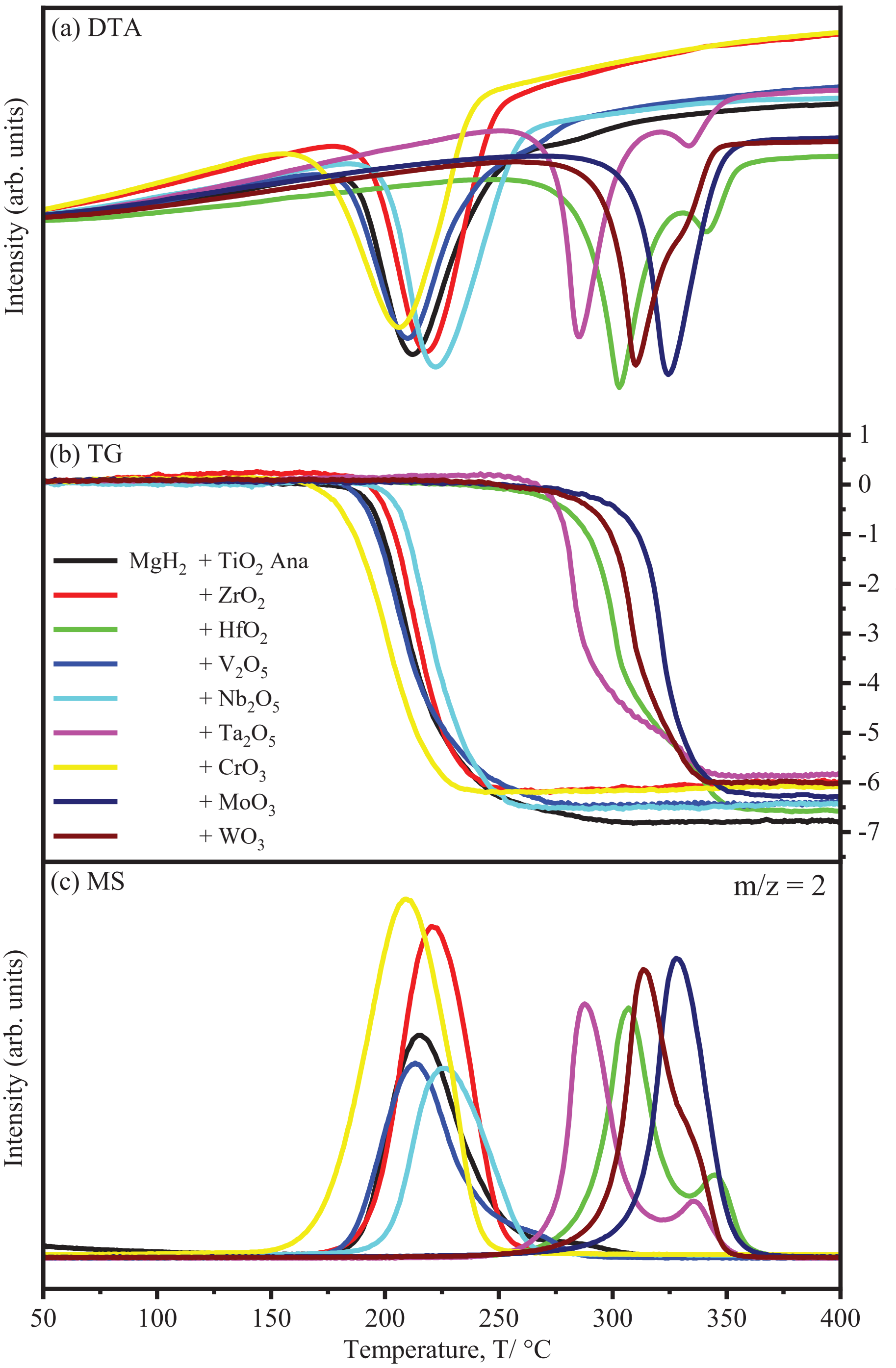

Figure 4.4 TG-DTA-MS analysis for hydrogen desorption of catalyzed (a) MgH_2 + TiO_2 Ana; (b) MgH_2 + ZrO_2; (c) MgH_2 + HfO_2; (d) MgH_2 + V_2O_5; (e) MgH_2 + Nb_2O_5; (f) MgH_2 + Ta_2O_5; (g) MgH_2 + CrO_3; (h) MgH_2 + MoO_3; (i) MgH_2 + WO_3 at the heating rate of 5 °C/min

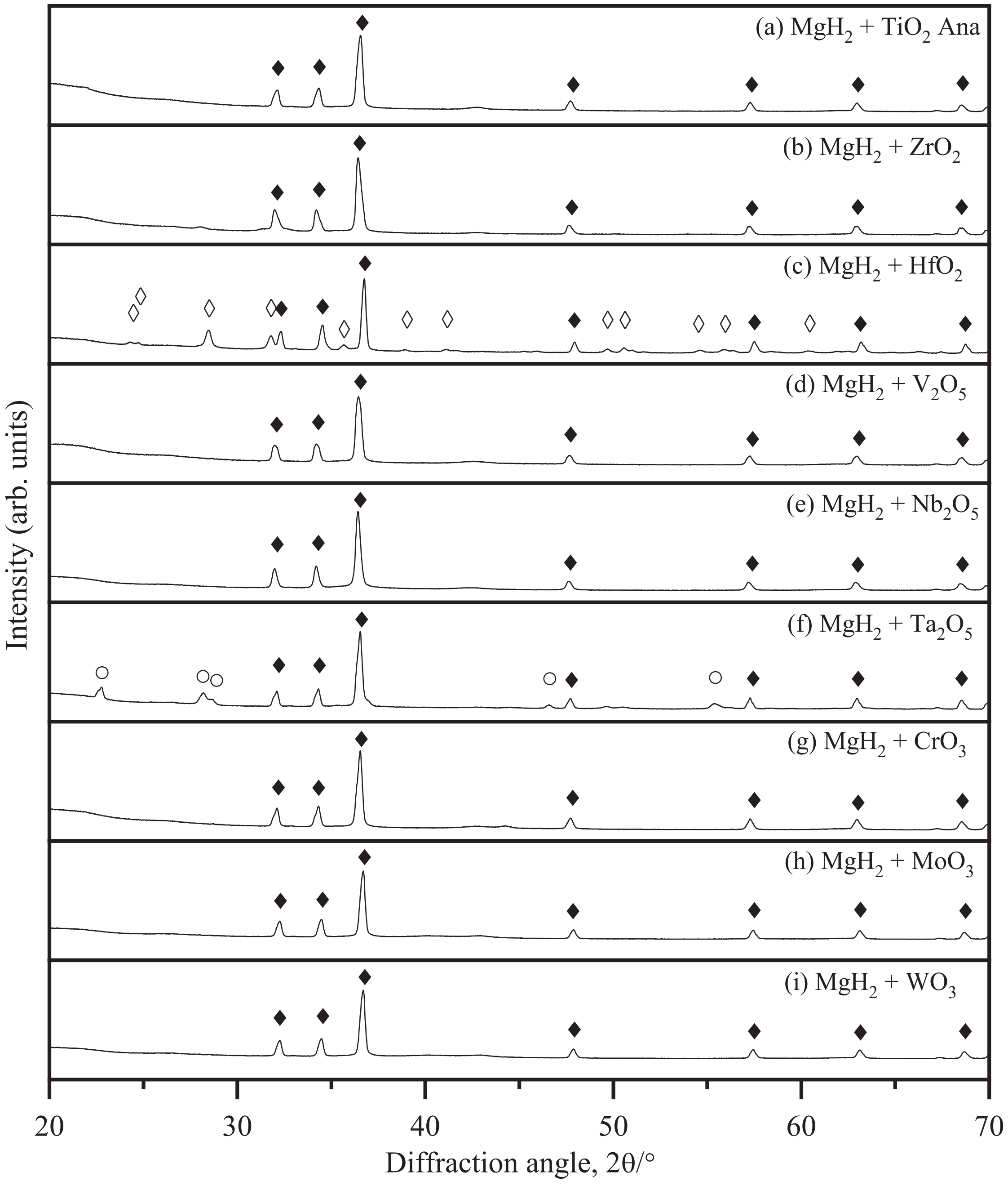

Figure 4.5 XRD patterns of the MgH$_2$ samples with oxide additives after the dehydrogenation.

4.1.3 Instability for catalytic activity of the various catalyzed samples

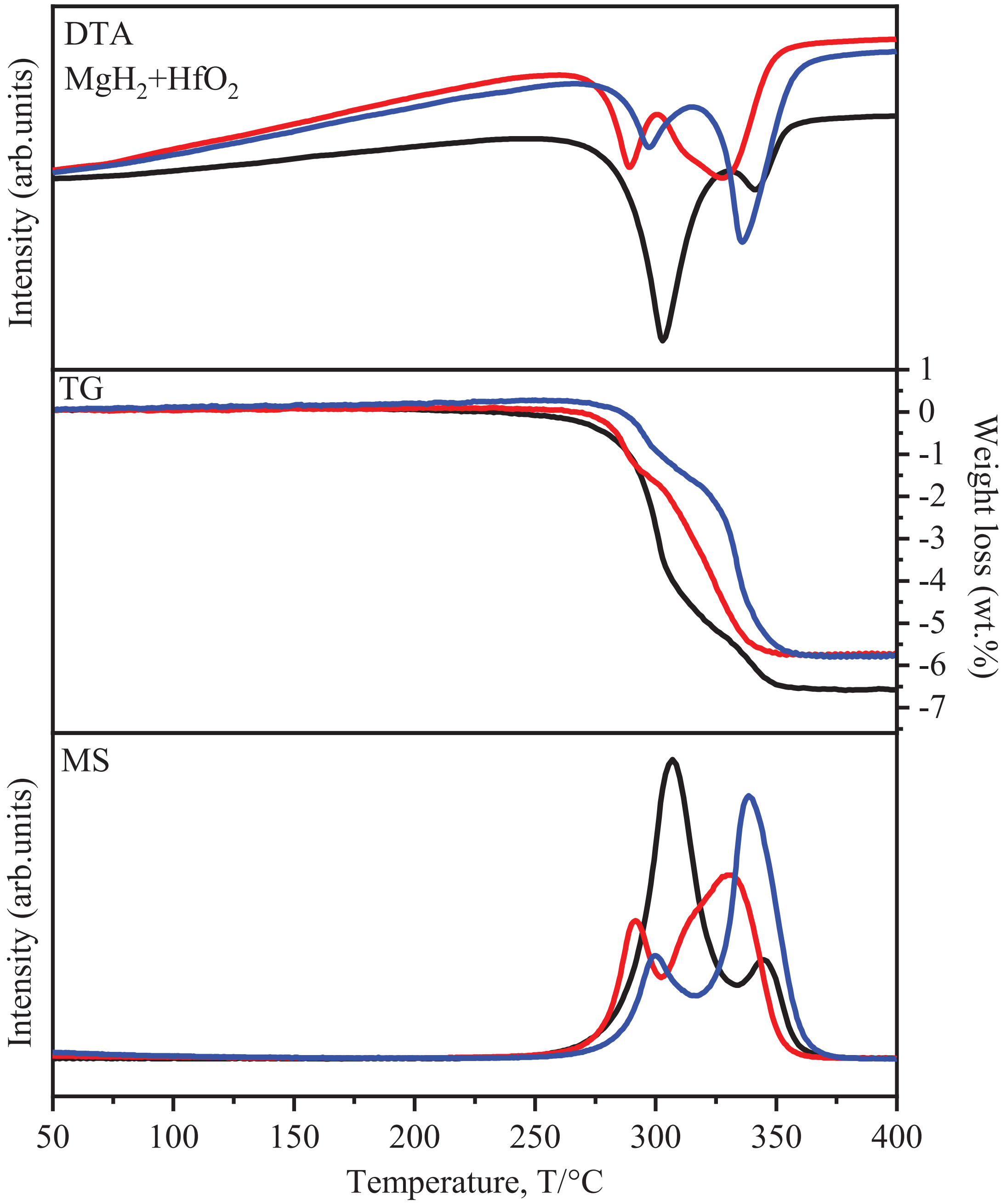

Figure 4.6 (a) Unstable catalytic behavior of MgH_2+HfO_2 sample for each synthesis

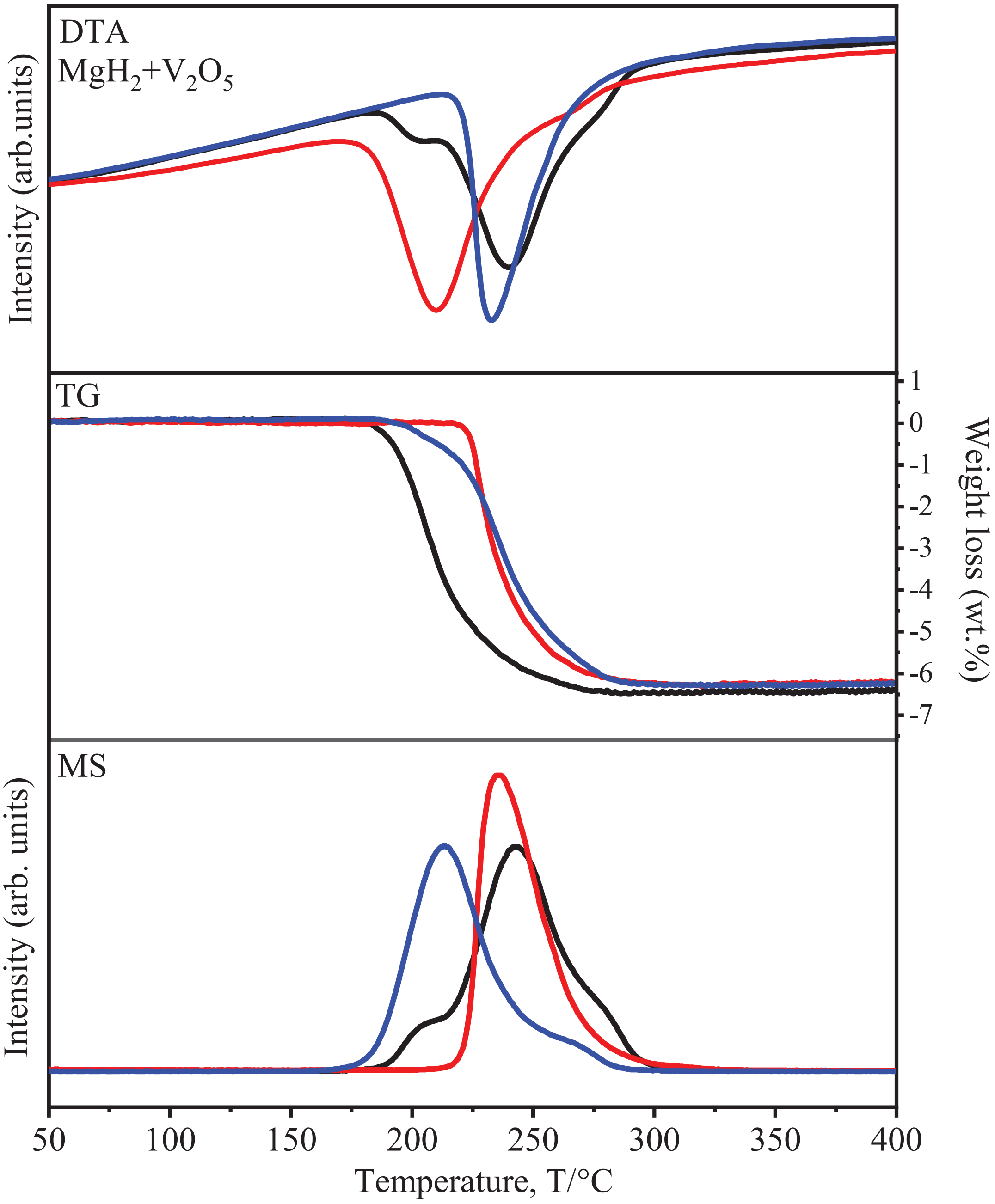

Figure 4.6 (b) Unstable catalytic behavior of MgH_2+V_2O_5 sample for each synthesis

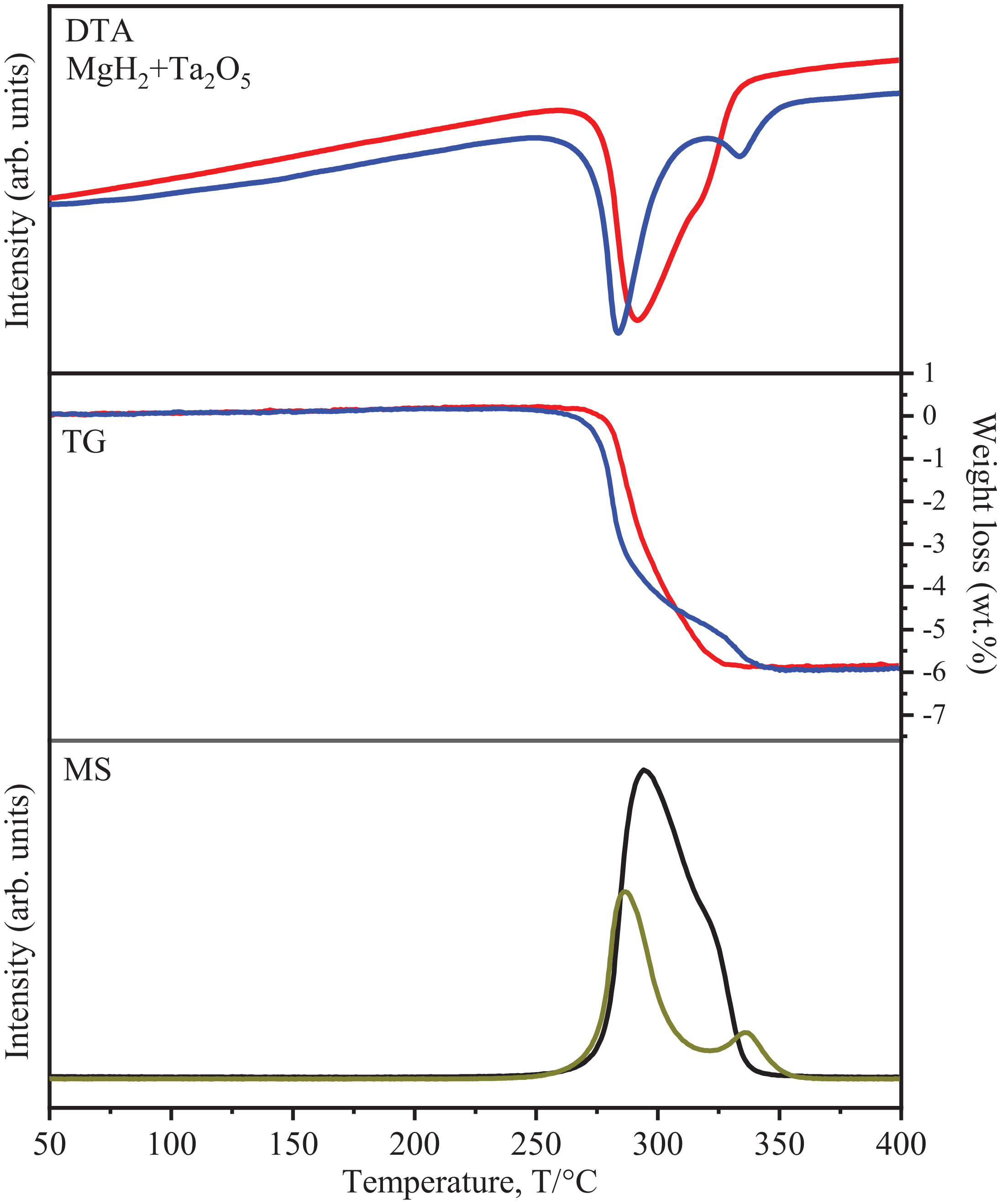

Figure 4.6 (c) Unstable catalytic behavior of MgH_2+Ta_2O_5 sample for each synthesis

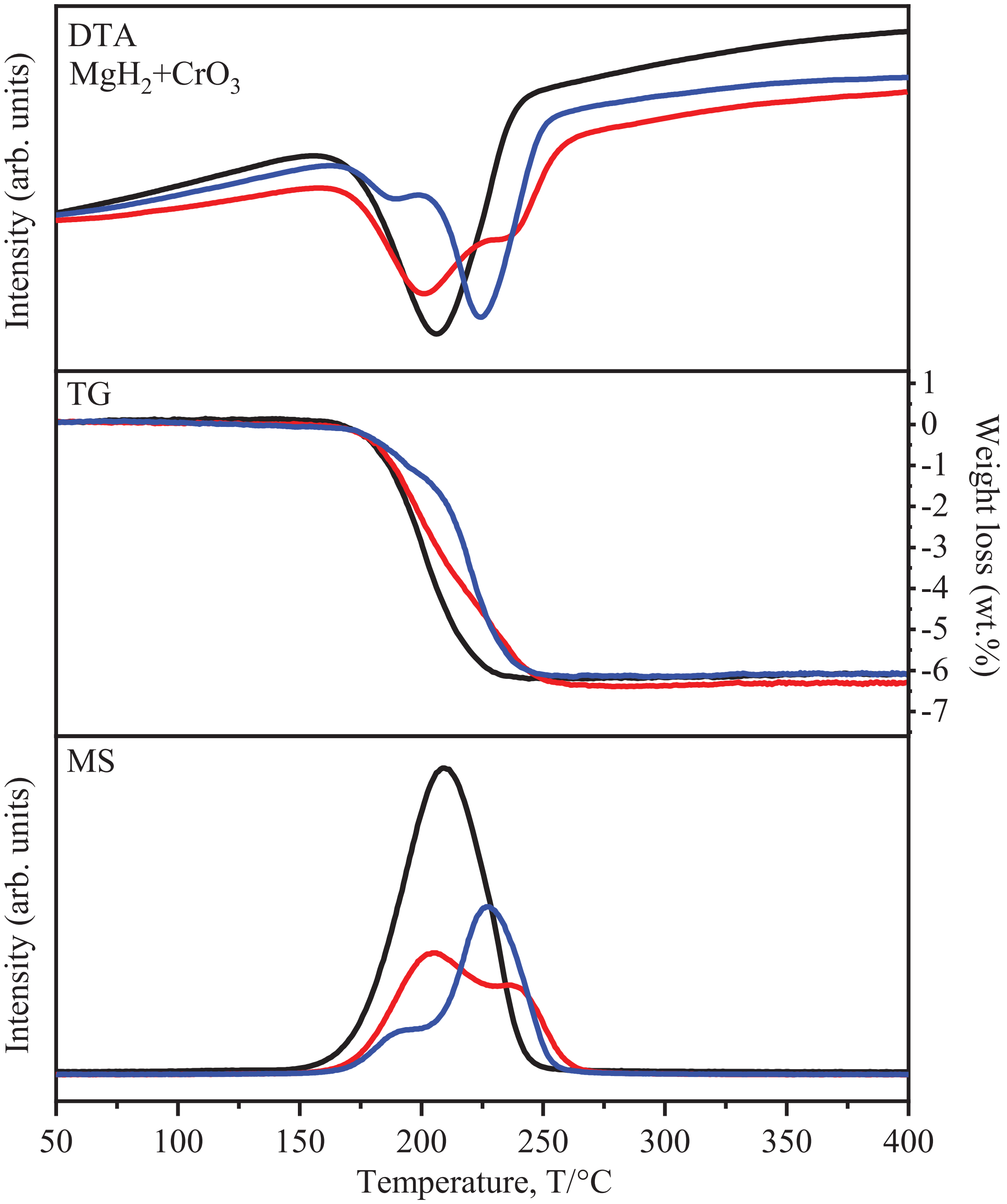

Figure 4.6 (d) Unstable catalytic behavior of MgH_2+CrO_3 sample for each synthesis

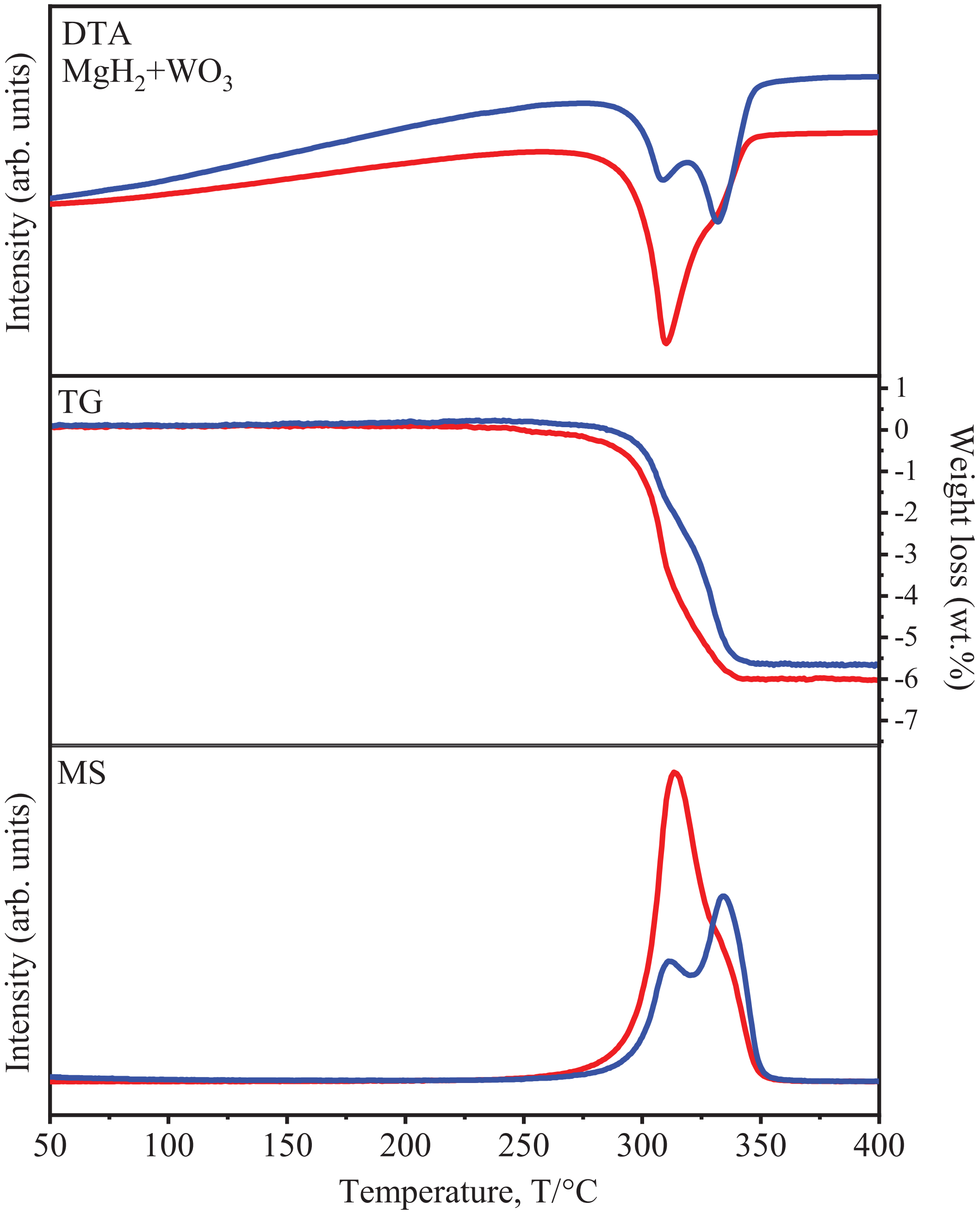

Figure 4.6 (e) Unstable catalytic behavior of MgH_2+WO_3 sample for each synthesis

Figure 4.7 (a) shows the isothermal hydrogen absorption curve of MgH_2 performed at 40 °C under 0.1 MPa hydrogen (H_2) pressure after the hydrogen desorption measurement. The starting point of the experimental data was determined as the switching time of the carrier gas from Ar to H_2. Gi et. al. reported that pristine Mg without catalyst did not absorb hydrogen at 40 °C at 0.1 MPa of H_2. As Kimura et. al. explained that hydrogen dissociation on Mg surface below room temperature is the rate-determining step, this is a reasonable result reported by our group. Among all the samples, the MgH_2 with Nb_2O_5 showed the highest hydrogen absorption rate, and the catalysis of other oxides was better in the order of $ZrO_2 > TiO_2 > V_2O_5 > MoO_3 > CrO_3 > WO_3 > HfO_2 > Ta_2O_5$ for isothermal hydrogen absorption. Some oxides showed a significant catalytic effect by decreasing the activation energy of the surface reaction for the hydrogen absorption of Mg compared to pristine Mg. [4-17] The formation of the MgH_2 phase from Mg and the remaining Mg phase with a reasonable amount was confirmed using XRD measurement as shown in Figure 4.8. On the other hand, the hydrogen absorption was completely changed at higher temperatures due to the change in hydrogenation reaction as the heating rate was continuously increasing with 5 °C/min till 250 °C. Among all the samples, the MgH_2 with Nb_2O_5 and MoO_3 (almost the same 6.5 wt.% of H_2) showed the highest hydrogen absorption rate, and the catalysis was better in the order of $V_2O_5 > WO_3 > CrO_3 > TiO_2 > ZrO_2 > Ta_2O_5 > HfO_2$ for 5 °C/min heating rate till 250 °C. Exceptionally MgH_2 with MoO_3 and WO_3 showed opposite behaviour for hydrogen absorption compared to hydrogen desorption for the same sample, however, this behaviour of MgH_2 with MoO_3 and WO_3 is consistent with its XRD profile shown in Figure 4.8 indicates, almost disappearance of the Mg phase provided by the formation of the MgH_2 phase. As explained in the introduction part, Mg surface needs around 21 kJ/mol of activation energy for penetration of hydrogen for metal hydrogen solid solution, on the other hand it needs a large amount of activation energy around 250 kJ/mol for metal hydride formation. Inconsistent with this explanation as we performed the hydrogenation with a 5 °C/min heating rate till 250 °C, causing thermal activation of Mg surface yields superior hydrogen absorption compared to isothermal hydrogen absorption. From the above experimental results, it is clarified that the effective factors of catalysis for the hydrogen absorption are different from those of the hydrogen desorption processes although the activity of some oxides can be explained by the same factors as those of hydrogen desorption. Further characterization of oxides in the dehydrogenated states is required.

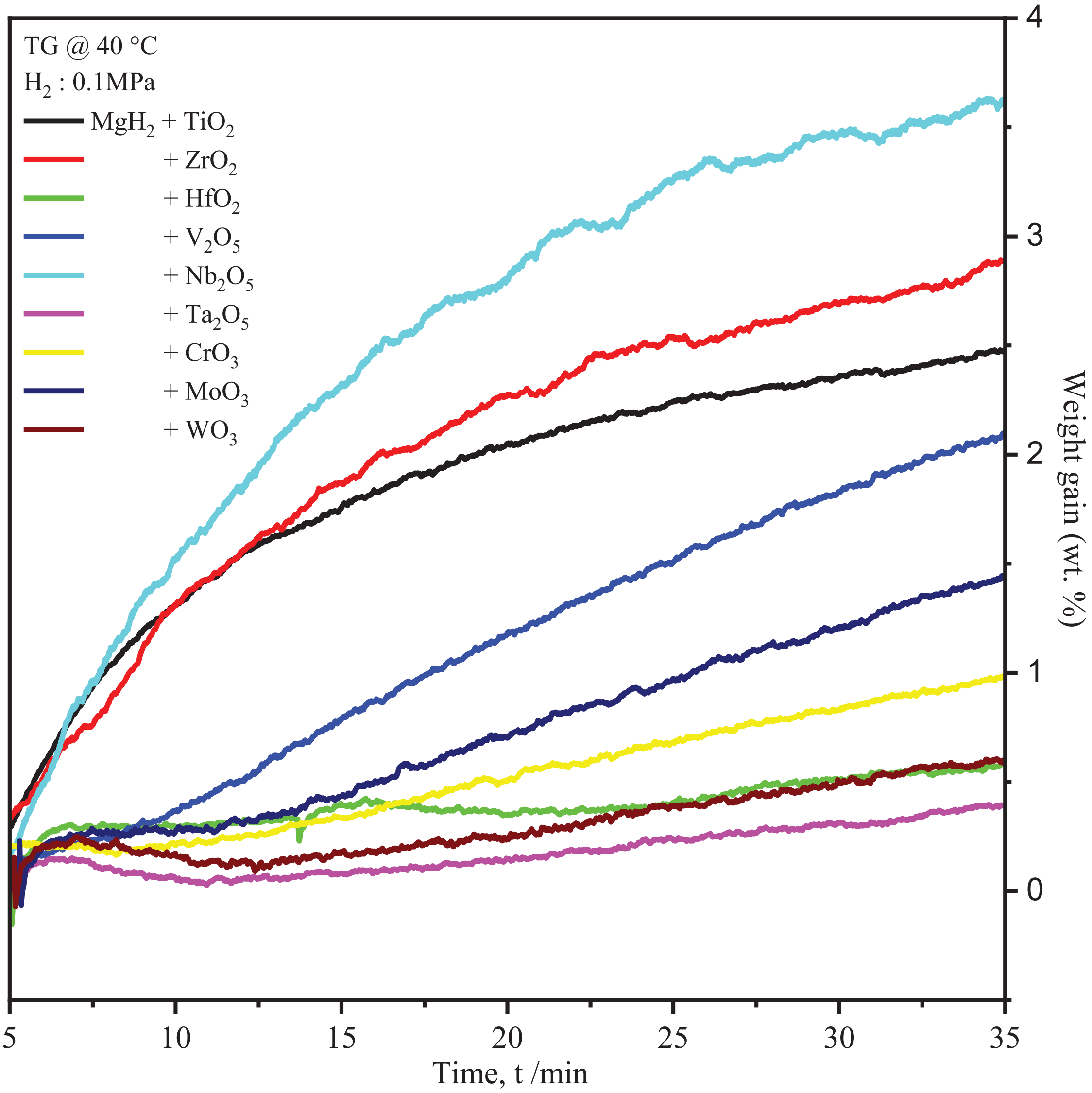

Figure 4.7 (a) TG results for the hydrogen absorption of Mg with the prepared oxides

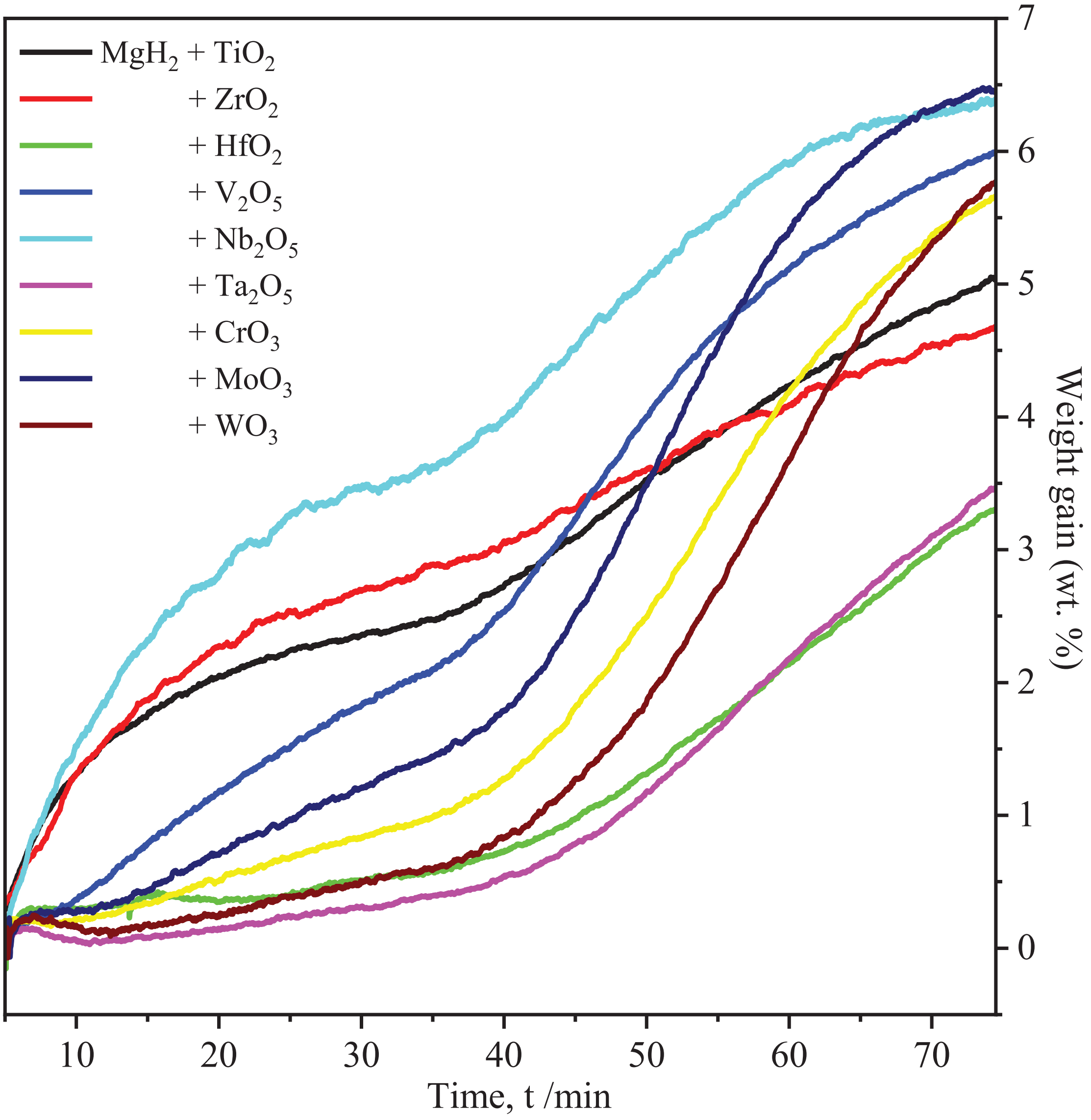

Figure 4.7 (b) TG results for the hydrogen absorption of Mg with the prepared oxides Randomly

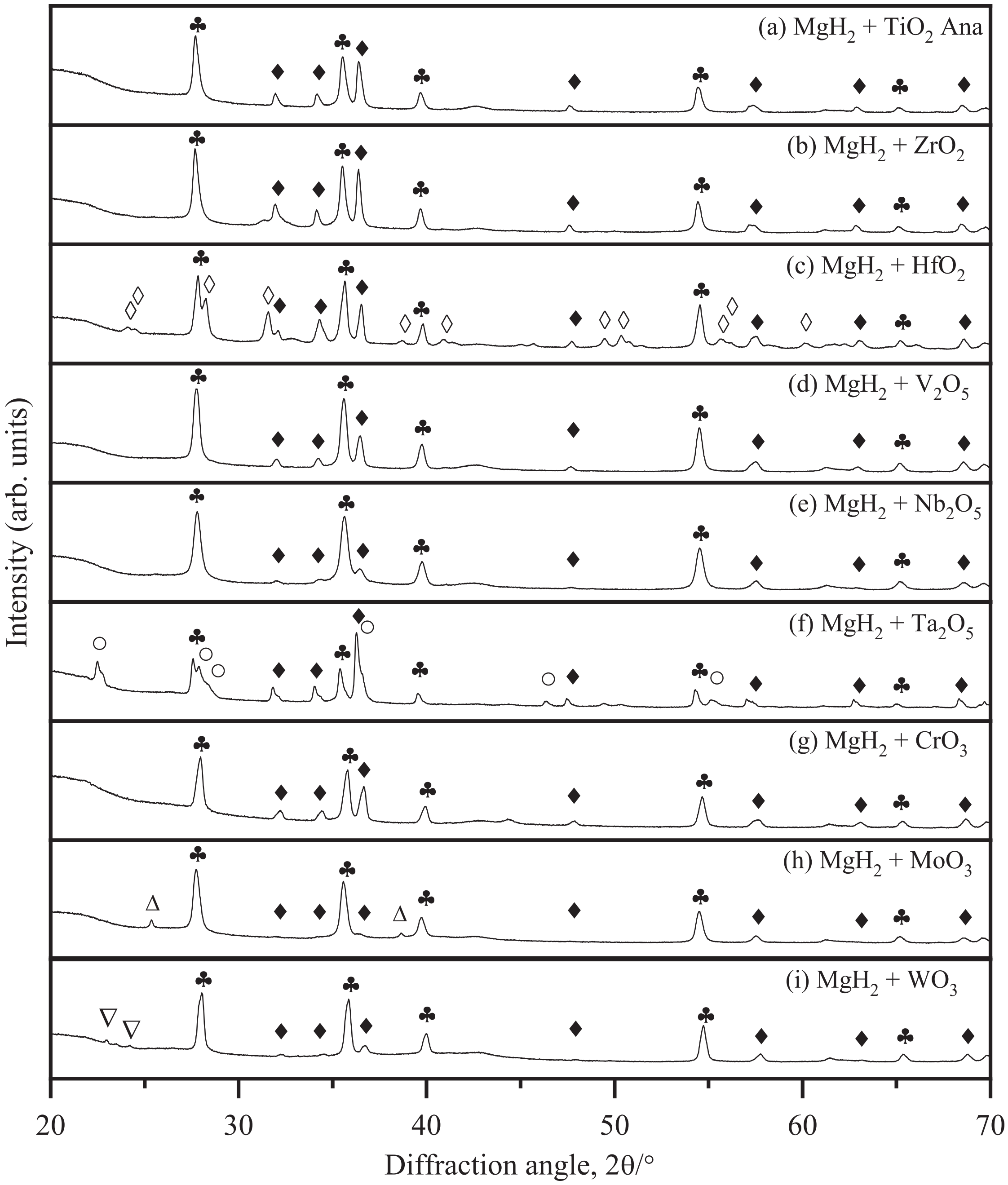

Figure 4.8 XRD patterns of the MgH_2 samples with oxide additives after the dehydrogenation.

4.1.4 Thermodynamic estimation on reduction routes of oxides

For oxide catalysts, it has been reported that a lower oxidation state is formed as the catalytic active state during the ball-milling oxides with MgH_2. [4-10,17] Some other researchers also reported the reduction in an oxidation state of different oxides with MgH_2. [4-4,10,17,19] As per our aim, there is a chance to reduce into several oxidation states which leads to the information about possible intermediate.

The change in enthalpy for reactant vs product, and on behalf of thermodynamics proposed that exothermic reaction will always be feasible for chemical equations. By assuming the feasible intermediates generated by the reaction with MgH_2 to form stable MgO, the probable reduction routes for each oxide were expected. All the possible chemical equations are listed in Table 4.2. Enthalpy and entropy values were taken from the National Bureau of Standard (NBS) tables of chemical thermodynamic properties reported in Journal of Physical and Chemical reference data by Wagman, Evans, Parker, Halow, Bailey, Churney, and Nuttall et. al. [4-13] The entropy and enthalpy values were taken for condensed phase at 298.15K. Direct calculations have been made to determine the change in enthalpy value using standard enthalpy of formation for elements or compounds. The change in Gibbs free energy value was also calculated using the same procedure as that of enthalpy. For proceeding with a reaction, ΔH or ΔG value should be negative from the thermodynamic point of view. Table 4.2 shows the substance formula for possible intermediate concerning each oxide were listed in the column. As we know, the ΔH or ΔG values should be negative to proceed with a chemical equation listed in further next columns. If ΔH will be negative, then the reaction will be exothermic else it will be endothermic, listed in further next column. For each chemical equation, the oxidation state of each possible intermediate was listed further in the next column. From Table 4.2, the following were the important outcomes concerning each oxide.

① Following the thermodynamic estimation of TiO_2 there were four reduction routes possible with Ti, TiO, TiH_2, and Ti_2O_3 as an intermediate with chemical equations 1, 2, 3, and 4. All the reactions for the reduction of TiO_2 were exothermic. The TiO_2 was reduced in various intermediate like Ti, TiO, TiH_2, and Ti_2O_3 followed by 0, +2, +2 and +3 oxidation states respectively as shown in Table 4.2.

② For ZrO_2 there was three reduction route was proposed with Zr, ZrH_2, and ZrO as intermediates with chemical equation 5, 6, and 7. Among which Zr and ZrO as intermediates have got an endothermic reaction with ΔH value 47.76 kJ/mol and 637.16 kJ/mol for chemical equations 5 and 7 respectively, whereas ZrH_2 as an intermediate have got the exothermic reaction for chemical equation 6. As ΔH= 47.76 kJ/mol for chemical equation 5 was a small positive value so further we calculated the change in Gibbs free energy and found ΔG = -24.27 kJ/mol indicates that reduction of ZrO_2 has to be possible with Zr as the intermediate. So, we concluded that reduction of ZrO_2 was possible with Zr and ZrH_2 with 0 and +2 oxidation states respectively.

③ The reduction of HfO_2 was proposed with Hf and HfO as an intermediate followed by the chemical equations 8 and 9 respectively. When we calculated the ΔH value for chemical reactions 8 and 9 found that ΔH value 91.9 kJ/mol and 668.3 kJ/mol respectively. As ΔH value was found to be positive, so reactions were endothermic which reveals reactions were not feasible as per thermodynamic point of view. As a result, we concluded that reduction of HfO_2 was not possible either using any reduction route.

④ The reduction of V_2O_5 was also proposed with V, VO, V_2O_3, V_3O_5, and V_4O_7 as intermediate compounds resulting from chemical equations 10, 11, 12, 13, and 14 respectively. On calculating the change in enthalpy value for reactant vs product, we found negative value that reveals all chemical reactions are exothermic and feasible from the thermodynamic point of view. The possible reduction routes of V_2O_5 were tabulated in table 4.2 with V, VO, V_2O_3, V_3O_5, and V_4O_7 as an intermediate compound followed by 0, +2, +3, (+3,+4) and (+3,+4) oxidation state for chemical equation 10, 11, 12, 13, and 14 respectively.

⑤ The theoretical estimation and reduction of Nb_2O_5 were also proposed with Nb, NbO, and NbO_2 as an intermediates compound subsequently with chemical equations 15, 16, and 17 respectively. The ΔH was obtained and found to be exothermically discussed about the feasibility of each chemical equation for the reduction of Nb_2O_5. As a result, we concluded that reduction of Nb_2O_5 was feasible with intermediate Nb, NbO, and NbO_2 followed by 0, +2, and +4 oxidation states respectively.

⑥ For Ta_2O_5 there were three reduction routes were proposed with Ta, TaO, and TaO_2 as intermediates with chemical equations 18, 19, and 20 respectively. The change in enthalpy was found to be negative reveals exothermic. On the other hand, TaO and TaO_2 as an intermediate have got an endothermic reaction with positive ΔH value for chemical equations 19 and 20 respectively. Therefore, we concluded that reduction of Ta_2O_5 was possible with Ta with oxidation state 0 whereas for TaO and TaO_2 was not possible.

⑦ The reduction of CrO_3 was suggested with Cr, CrO_2, Cr_2O_3, and Cr_3O_4 as an intermediate followed by chemical equations 21, 22, 23, and 24, respectively. The ΔH values for all reactions were found to be exothermic and feasible as per the thermodynamic point of view. As a result, we concluded that reduction of CrO_3 was possible with an intermediate Cr, CrO_2, Cr_2O_3, and Cr_3O_4 followed by 0, +4, +3, and (+2, +3) oxidation state, respectively.

⑧ For MoO_3, three reduction routes are possible with Mo, MoO, and MoO_2 as intermediates with chemical equations 25, 26, and 27, respectively. The change in enthalpy was found to be negative reveals exothermic for Mo and MoO_2 with chemical equations 25 and 27, respectively. On the other hand, MoO as the intermediate has got an endothermic reaction with a positive ΔH value reveals reaction was not possible for chemical equation 26 respectively. In conclusion, the reduction of MoO_3 was feasible with Mo and MoO_2 as an intermediate with 0 and +4 oxidation states, respectively.

⑨ In the case of WO_3, three reduction routes were proposed with W, WO, and WO_2 as intermediates with chemical equations 28, 29, and 30, respectively. The change in enthalpy was found to be negative reveals exothermic for W and WO_2 with chemical equations 28 and 30, respectively. On the other hand, WO as an intermediate has got an endothermic reaction with positive ΔH value reveals reaction was not possible for chemical equation 29 respectively. In conclusion, the reduction of WO_3 was feasible with W and WO_2 as the intermediates with 0 and +4 oxidation states, respectively.

Table 4.2 Thermodynamic reduction route of MgH_2 catalyzed with 9 oxides

	Substance Formula	Possible reactions	ΔH for rxn.	ΔG	Rxn. Types	Oxidation State
A	**TiO_2 Ana**					
1	Ti	$TiO_2 + 2MgH_2 \leftrightarrow Ti+2MgO+2H_2$	-ve		Exo.	**0**
2	TiO	$TiO_2 + MgH_2 \leftrightarrow TiO+MgO+H_2$	-ve		Exo.	**2+**
3	TiH_2	$TiO_2 + 2MgH_2 \leftrightarrow TiH_2+2MgO+H_2$	-ve		Exo.	**2+**
4	Ti_2O_3	$2TiO_2 + MgH_2 \leftrightarrow Ti_2O_3+MgO+H_2$	-ve		Exo.	**3+**
B	**ZrO_2**					
5	Zr	$ZrO_2 +2MgH_2 \leftrightarrow Zr+2MgO+2H_2$	+ve	-ve	Endo.	**0**
6	ZrH_2	$ZrO_2 +2MgH_2 \leftrightarrow ZrH_2+2MgO+H_2$	-ve		Exo.	**2+**
7	ZrO	$ZrO_2 +MgH_2 \leftrightarrow ZrO+MgO+H_2$	+ve		Endo.	
C	**HfO_2**					
8	Hf	$HfO_2+2MgH_2 \leftrightarrow Hf+2MgO+2H_2$	+ve		Endo.	
9	HfO	$HfO_2+MgH_2 \leftrightarrow HfO+MgO+H_2$	+ve		Endo.	
D	**V_2O_5**					
10	V	$V_2O_5 +5MgH_2 \leftrightarrow 2V+5MgO+5H_2$	-ve		Exo.	**0**
11	VO	$V_2O_5 +3MgH_2 \leftrightarrow 2VO+3MgO+3H_2$	-ve		Exo.	**2+**
12	V_2O_3	$V_2O_5 +2MgH_2 \leftrightarrow V_2O_3+2MgO+2H_2$	-ve		Exo.	**3+**
13	V_3O_5	$3V_2O_5 +5MgH_2 \leftrightarrow 2V_3O_5+5MgO+5H_2$	-ve		Exo.	**3+,4+**
14	V_4O_7	$2V_2O_5 +3MgH_2 \leftrightarrow V_4O_7+3MgO+3H_2$	-ve		Exo.	**3+,4+**
E	**Nb_2O_5**					
15	Nb	$Nb_2O_5 +5MgH_2 \leftrightarrow 2Nb+5MgO+5H_2$	-ve		Exo.	**0**
16	NbO	$Nb_2O_5 +3MgH_2 \leftrightarrow 2NbO+3MgO+3H_2$	-ve		Exo.	**2+**
17	NbO_2	$Nb_2O_5 +MgH_2 \leftrightarrow 2NbO_2+MgO+H_2$	-ve		Exo.	**4+**
F	**Ta_2O_5**					
18	Ta	$Ta_2O_5 + 5MgH_2 \leftrightarrow 2Ta+5MgO+5H_2$	-ve		Exo.	**0**
19	TaO	$Ta_2O_5 + 3MgH_2 \leftrightarrow 2TaO+3MgO+3H_2$	+ve		Endo.	
20	TaO_2	$Ta_2O_5 + MgH_2 \leftrightarrow 2TaO_2+MgO+H_2$	+ve		Endo.	
G	**CrO_3**					
21	Cr	$CrO_3 +3MgH_2 \leftrightarrow Cr+3MgO+3H_2$	-ve		Exo.	**0**
22	CrO_2	$CrO_3 +MgH_2 \leftrightarrow CrO_2+MgO+H_2$	-ve		Exo.	**4+**
23	Cr_2O_3	$2CrO_3 +3MgH_2 \leftrightarrow Cr_2O_3+3MgO+H_2$	-ve		Exo.	**3+**
24	Cr_3O_4	$3CrO_3 +5MgH_2 \leftrightarrow Cr_3O_4+5MgO+5H_2$	-ve		Exo.	**2+,3+**
H	**MoO_3**					
25	Mo	$MoO_3 +3MgH_2 \leftrightarrow Mo+3MgO+3H_2$	-ve		Exo.	**0**
26	MoO	$MoO_3 +2MgH_2 \leftrightarrow MoO+2MgO+2H_2$	+ve		Endo.	
27	MoO_2	$MoO_3 +MgH_2 \leftrightarrow MoO_2+MgO+H_2$	-ve		Exo.	**4+**
I	**WO_3**					
28	W	$WO_3 +3MgH_2 \leftrightarrow W+3MgO+3H_2$	-ve		Exo.	**0**
29	WO	$WO_3 +2MgH_2 \leftrightarrow WO+2MgO+2H_2$	+ve		Endo.	
30	WO_2	$WO_3 +MgH_2 \leftrightarrow WO_2+MgO+H_2$	-ve		Exo.	**4+**

ΔH stands for change in enthalpy value for reactant verses product and (+, -) ve stands for positive or negative value

4.1.5 The Chemical States of oxides

In continuation with the theoretical estimation for thermodynamic reduction of each oxide, we performed the X-ray photoelectron spectroscopy (XPS) for each sample to demonstrate the experimental reduction of each oxide with MgH_2. To understand the catalytic active states, XPS analysis was carried out on the oxide series itself as well as oxide with MgH_2 as a representative system. Following were the important outcomes for XPS analysis with each oxide's probable chemical state.

① The TiO_2 oxide itself shows peaks of spectral line 2p1/2 and 2p3/2 with binding energy 463.44 eV and 457.67 eV with TiO_2 formula, which is practically equal to its existing NIST database value 464.19 and 458.00 eV, respectively. [4-21] These would be assigned to +4 oxidation state for TiO_2 anatase type. However, the analysis of MgH_2+TiO_2 is difficult due to the low-intensity spectrum, as shown in Figure 4.9 (a). The no peak observation of Ti might be explained as follows. If enough amount of Ti does not exist on the MgH_2 surface, the intensity should be lowered. Moreover, if the small amount of oxide (only 2 mol%) forms multi phases Ti, TiO, TiH_2, and Ti_2O_3 expected above, the peak intensity should be low as well.

② Figure 4.9 (b) shows the surface analysis of ZrO_2 oxide itself was performed for 3d orbital and the presence of spectral lines 3d3/2 and 3d5/2 was found at binding energy 183.63 eV and 181.31 eV respectively, the surface of ZrO_2 is not +4 possibly, it is around +2. However, the XRD of ZrO_2 is +4 oxidation state; the reason behind this is XPS is a surface analysis only up to 10nm (several nanometers), whereas XRD is bulk analysis. On the other hand, for MgH_2+ZrO_2, the peaks were slightly shifted to the lower energy side, and it is around less than +2. Subsequently, for formula ZrH_2, the spectral line 3d5/2 was available with

NIST database value for binding energy 178.80 eV. [4-21] So, as per the above discussion, we concluded a slight reduction of ZrO_2 less than +2 oxidation state with ZrH_2 as an intermediate, also supported by references.

③ The HfO_2 oxide itself and with MgH_2 were evaluated for surface analysis to determine its chemical state can be seen in figure 4.9 (c). Study of 4f orbital reveals spectral line 4f5/2 and 4f7/2 was found at 17.50eV and 15.90eV, respectively, which should be assigned to HfO_2 considering the XRD result. However, on analyzing MgH_2+HfO_2, we found almost the same peak position and shape consistent with pristine HfO_2. There was no peak shift; namely, reduction of HfO_2 does not occur on the Mg surface. This result is well consistent with the above thermodynamic estimation, which shows no possible reduction routes by exothermic reactions. The presence of a high-intensity peak for catalyzed sample also calls for the uncatalyzed sample.

④ The surface analysis of V_2O_5 oxide itself reveals the presence of spectral lines 2p (1/2) and 2p (3/2) for 2p orbital at binding energy 523.91 eV and 516.51 eV, respectively confirmed the +5 oxidation state of V_2O_5 oxide shown in figure 4.9 (d). However, after dispersing on the MgH_2 surface, no peaks were observed in the XPS spectrum; the same reasons of TiO_2 would cause this result. Furthermore, the five kinds of oxidation states (V, VO, V_2O_3, V_3O_5, and V_4O_7) can be formed from the above thermodynamic estimation, suggesting that detecting peaks might be difficult when multi oxidation states are formed. There is another model, as during ball milling, first oxide will be break and then it will be get reduced on Mg surface one by one. So if there is a one-stage reduction, we found a clear peak, but multi-state so difficult to see a peak.

⑤ As there was various research published by our group on Nb_2O_5 and MgH_2+Nb_2O_5, specifically by P.K. Singh et al. and Gi. et al. [4-17-18] We reported the availability of Nb_2O_5 oxide itself in its +5 oxidation state with the presence of 3d (3/2) and 3d (5/2) spectral lines almost comparable with the NIST database. [4-21] In addition, Gi. et al. reported the reduction of Nb_2O_5 on Mg surface in 4+, 2+, and 0 oxidation states. [4-17-18]

⑥ The surface analysis of Ta_2O_5 oxide was performed with and without MgH_2, using XPS for Ta4f. Figure 4.9 (e) showed the peak position for Ta_2O_5 oxide, found at 26.99 eV and 25.20 eV corresponding to 4f (5/2) and 4f (7/2), respectively. However, the spectrum of MgH_2+Ta_2O_5 was almost the same as pristine MgH_2 in valence state, even though we can't deny the reduction of Ta_2O_5 on the Mg surface. If the Ta_2O_5 phase remains, the pristine Ta_2O_5 peaks are possibly observed for MgH_2+Ta_2O_5 same as the MgH_2+HfO_2 case. There might be a peak at 23.70 eV and 21.90 eV [4-21] in the XPS spectrum, suggesting that Ta_2O_5 might be reduced to Ta (0), which is only one possible route expected from the thermodynamic estimation.

⑦ The analysis of CrO_3 oxide was performed using XPS for Cr2p orbital and found two spectral lines 2p (1/2) and 2p (3/2), corresponding to 587.65eV and 578.42eV, respectively. Both peak positions for CrO_3 for spectral line 2p (1/2) and (3/2) confirmed the +6 oxidation state. However, for MgH_2+CrO_3, there is a possibility to reduce in 0, +2, and +3 oxidation states. The difference between spectral lines 2p (1/2) and 2p (3/2) was calculated around 9.23eV. The corresponding +3, +2 and 0 oxidation state was labeled and can be seen in Figure 4.9 (f). Probably the Cr is available with the existence of spectral lines 2p (1/2) and 2p (3/2) with binding energy 583.50 eV and 574.20 eV corresponding to the Cr formula, which is practically equal with its existing NIST database value. [4-21] Similarly, Cr is available with the presence of spectral lines 2p (1/2) and 2p (3/2) with binding energy 586.30 eV and 576.10 eV analogous to Cr_2O_3 formula, which is practically equal with its existing NIST database value. In our analysis CrO_3 (+6) oxidation state was reduced to +2 and 0 state with a small amount of +3 oxidation state.

⑧ Figure 4.9 (g) shows the chemical state of MoO_3 oxide with and without MgH_2. The Mo 3d orbital with spectral lines 3d (3/2) and 3d (5/2) found at binding energy 235.14 and 232.00 eV, respectively, confirmed the +6 oxidation state of MoO_3. The obtained result for formula MoO_3 is almost equal to its available NIST database value 235.60 eV and 232.10 eV for Mo 3d (3/2) and 3d (5/2) spectral line, respectively. [4-21] However, for MgH_2+MoO_3 available with the existence of spectral line 3d (3/2) and 3d (5/2) with binding energy 231.00 eV and 227.40 eV corresponding to Mo formula, which is practically equal with its existing NIST database value. [4-21] The analysis of catalyzed sample reveals that the MoO_3 oxide reduced to 0 oxidation state, as shown in Figure 4.8 (g). Thus, from above, we concluded that MoO_3 (+6 oxidation state) reduced on Mg surface in 0 oxidation state respectively. The XPS results are well consistent with one of the thermodynamic estimations.

⑨ Inconsistent with the above, Figure 4.9 (h) shows the chemical state of WO_3 oxide with and without MgH_2. Corresponding to WO_3, the W 4f orbital with spectral line 4f (5/2) and 4f (7/2) was found at binding energy 36.94 eV and 34.80 eV, respectively confirming the +6 oxidation state. The obtained experimental value is almost equal and comparable to the NIST database value 37.40 eV and 34.90 eV for W 4f, respectively. [4-21] The MgH_2+WO_3 sample yields oxide reduction in +4 and 0 oxidation states consistent with those of thermodynamic estimation. However, for MgH_2+WO_3 available with the existence of spectral line 4f (5/2) and 4f (7/2) with binding energy 33.40 eV and 31.00 eV corresponding to W formula, which is practically equal with its existing NIST database value. Correspondingly, MgH_2+WO_3 is available with spectral line 4f (7/2) with binding energy 32.90 eV analogous to WO_2 formula, which is practically equal with its existing NIST database value. Thus, we concluded that WO_3 (+6 oxidation state) reduced on Mg surface with +4 and 0 oxidation state respectively. However, a small amount of +6 oxidation state remains as it is; WO_3 oxide exists in the sample. XRD profile of ball-milled MgH_2 + WO_3 also suggested the existence of WO_3.

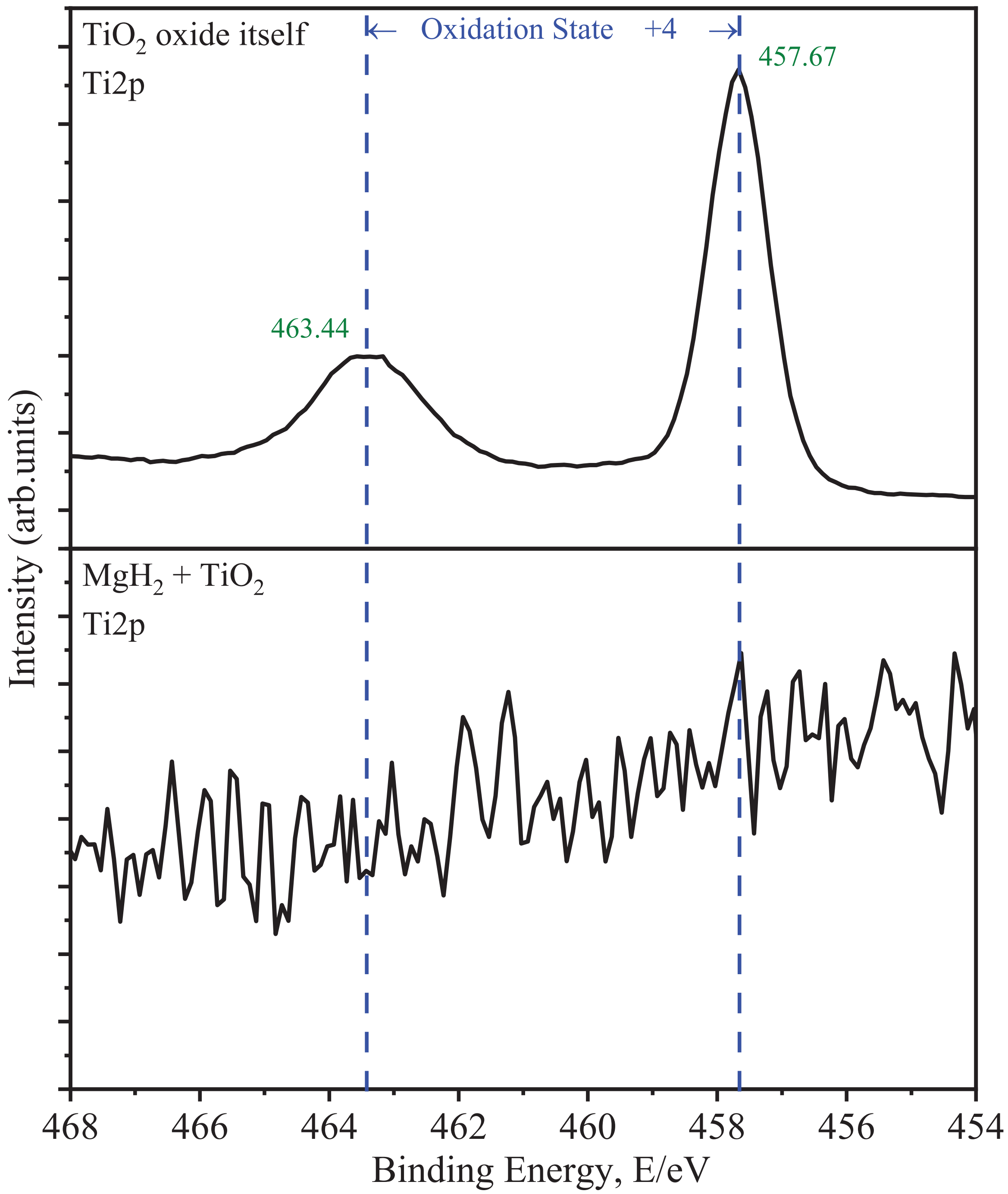

Figure 4.9 (a) XPS spectra of Ti 2p for TiO_2 anatase type and MgH_2+TiO_2 anatase type

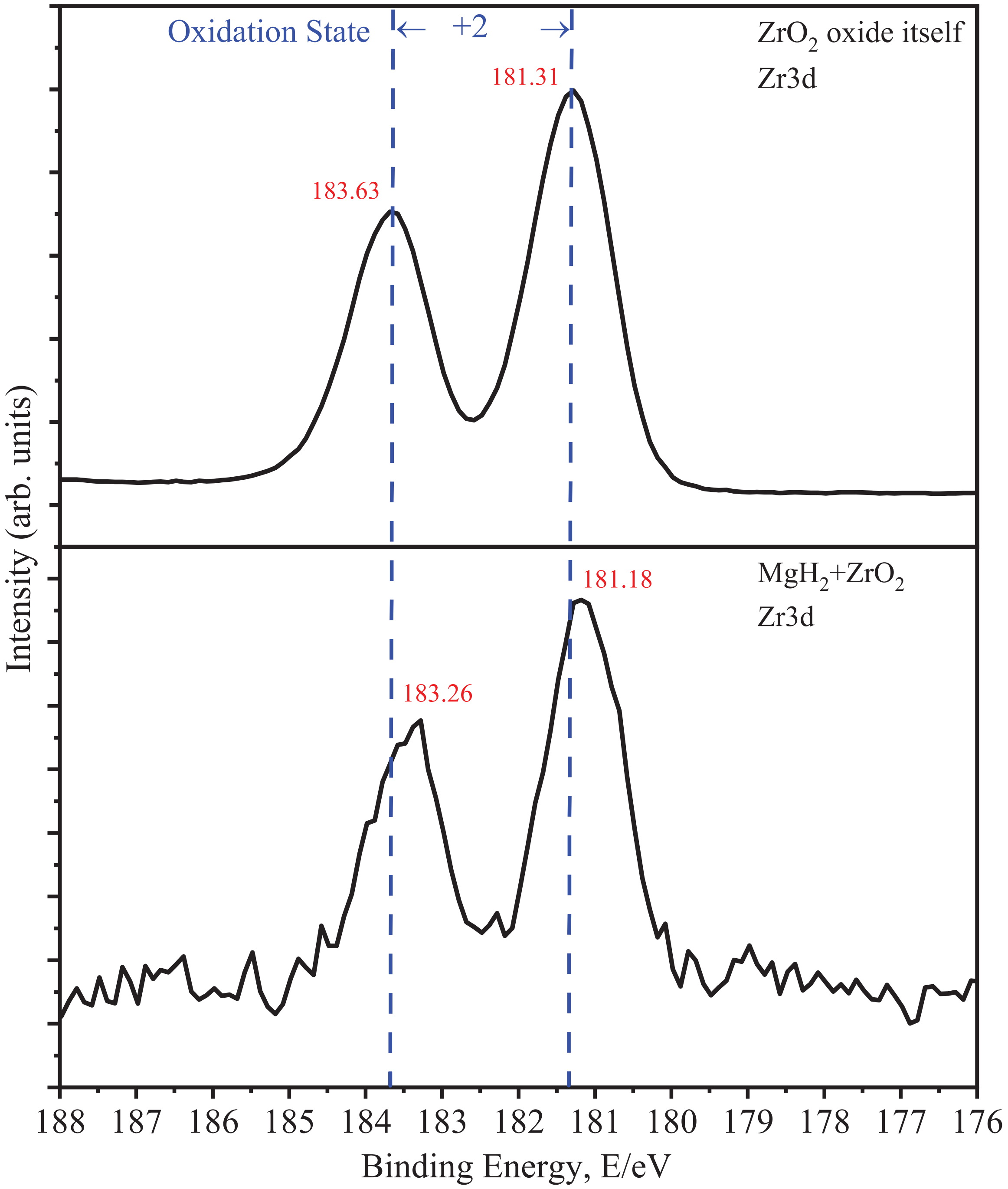

Figure 4.9 (b) XPS spectra of Zr 3d for ZrO_2 and MgH_2+ZrO_2

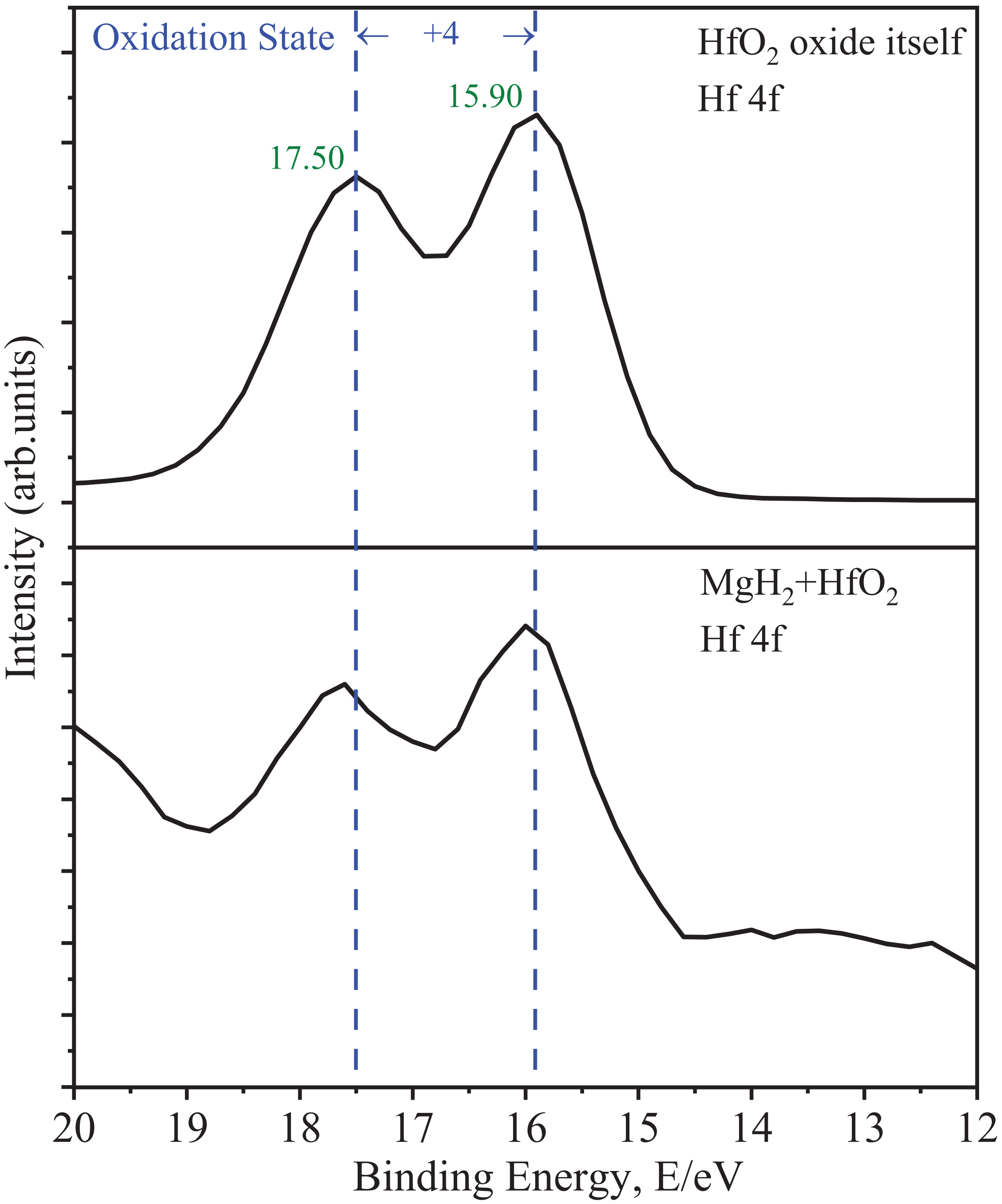

Figure 4.9 (c) XPS spectra of Hf 4f for HfO_2 and MgH_2+HfO_2

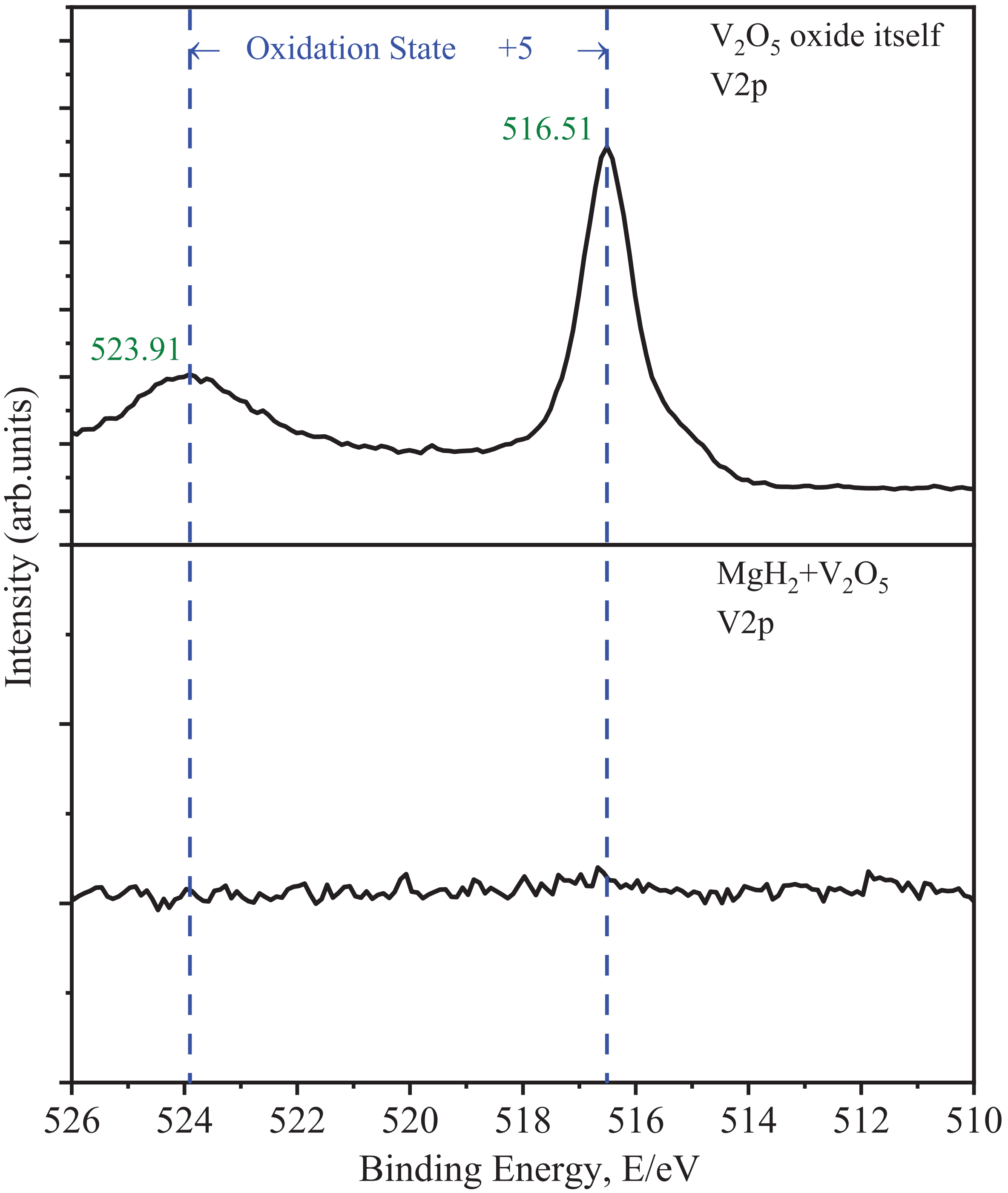

Figure 4.9 (d) XPS spectra of V 2p for V_2O_5 and $MgH_2 + V_2O_5$

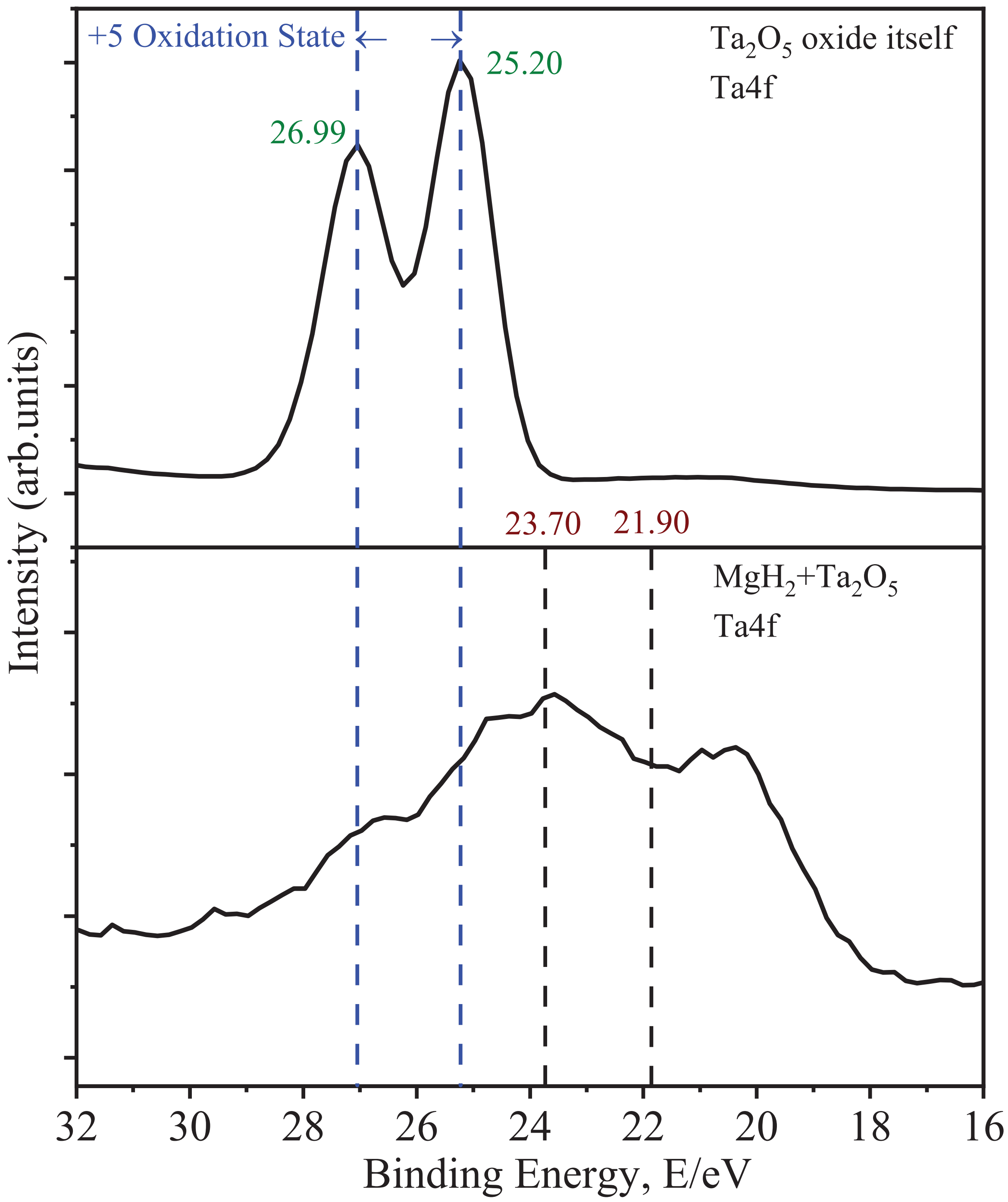

Figure 4.9 (e) XPS spectra of Ta 4f for Ta_2O_5 and MgH_2 +Ta_2O_5

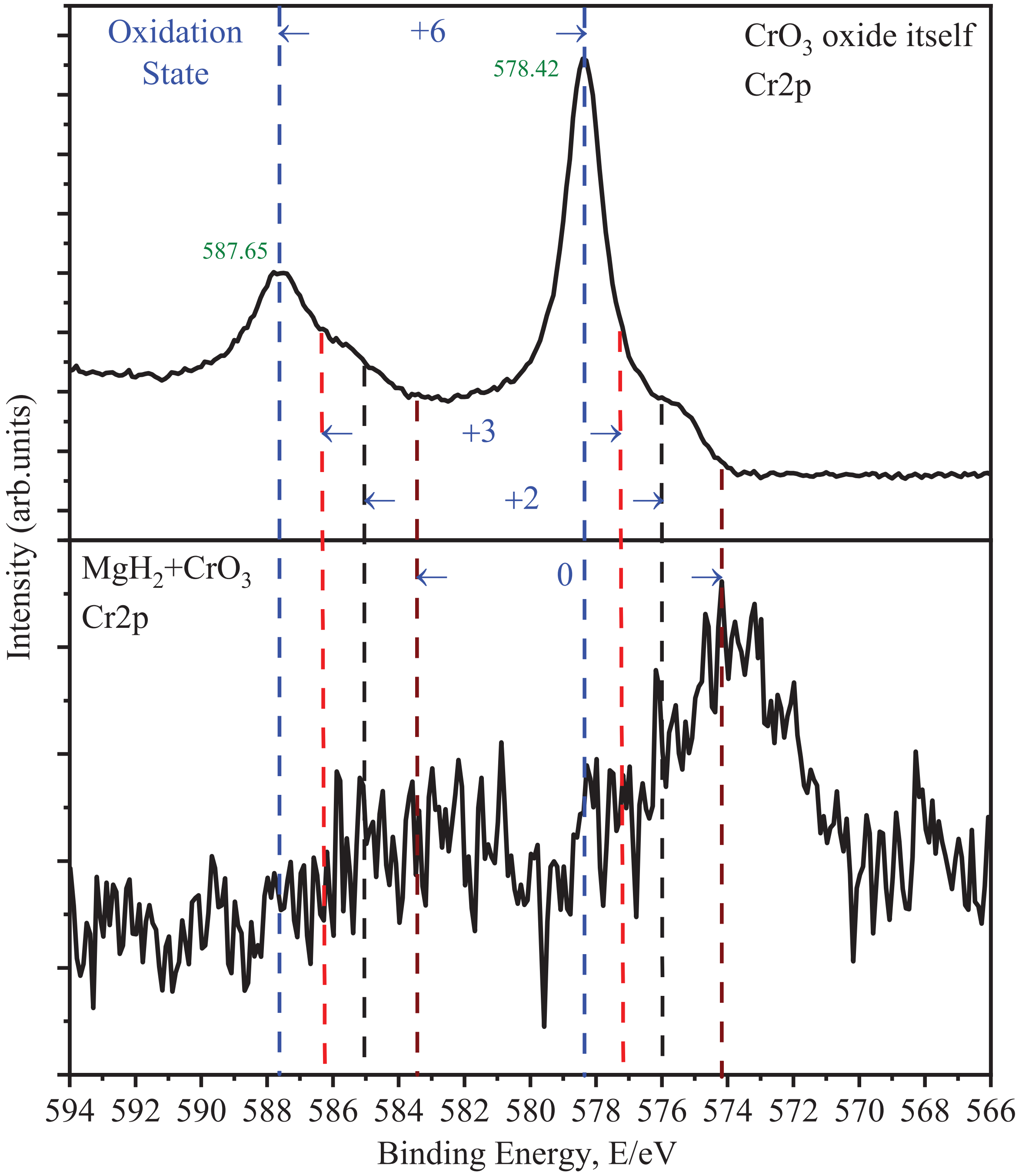

Figure 4.9 (f) XPS spectra of Cr 2p for CrO_3 and MgH_2 +CrO_3

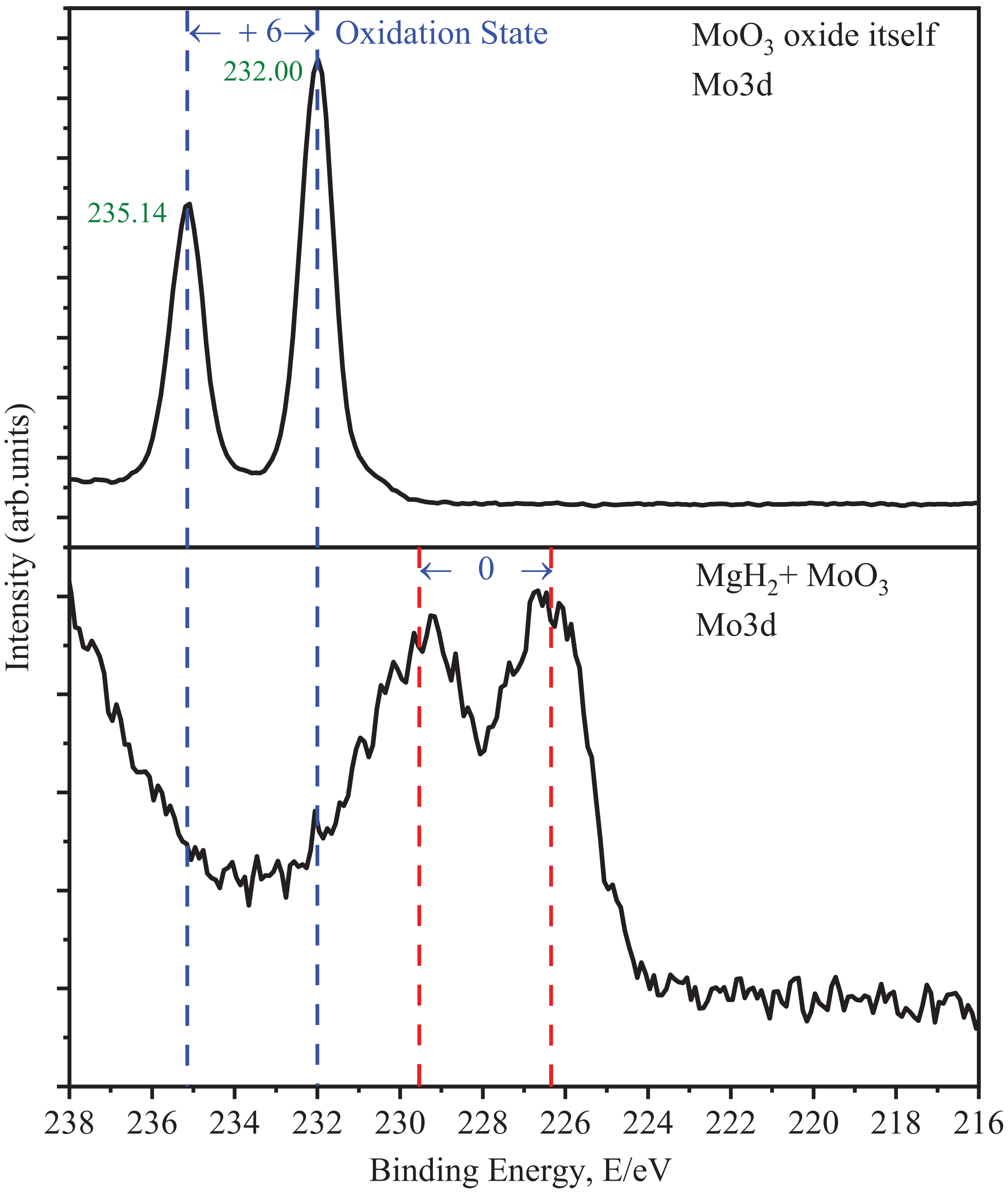

Figure 4.9 (g) XPS spectra of Mo 3d for MoO_3 and MgH_2 +MoO_3

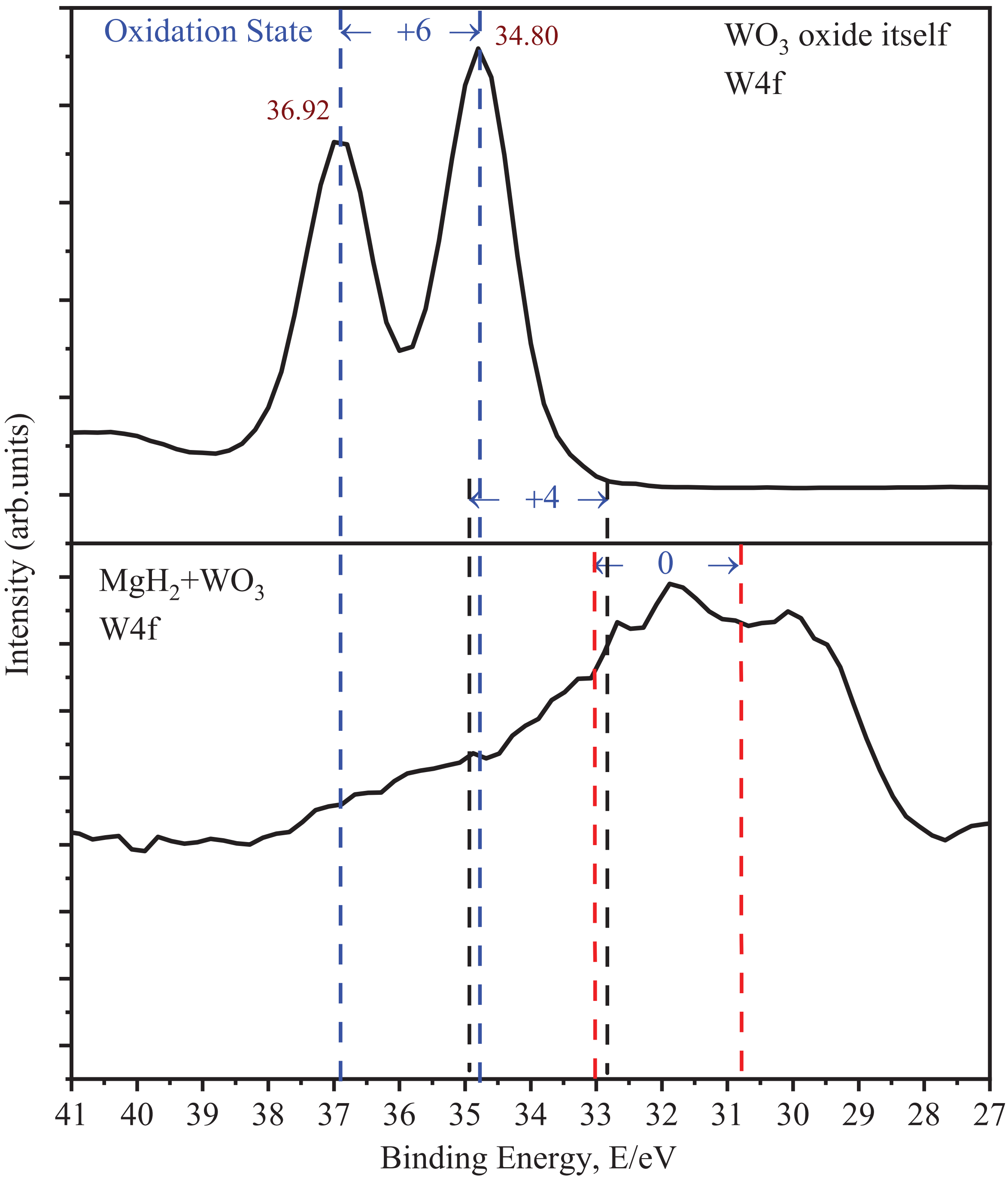

Figure 4.9 (h) XPS spectra of Mo 3d for MoO_3 and MgH_2 +MoO_3

4.1.6 Estimation of effective factors on oxide catalysts

The effective factor for catalysis is discussed below from all the experimental results.

① As expected, in the case of MgH_2+TiO_2, TiO_2 peaks have vanished after ball milling yields for high dispersion of oxide catalysts on the Mg surface. Hanada et al. reported MgH_2 catalyzed with 1 mol% of Nb_2O_5, V_2O_5, and TiO_2, ball-milled XRD profiles with an absence of individual oxide peak after ball milling yields a highly dispersed Mg surface. The high dispersion state of the milled sample offers a high catalytic active surface for hydrogen desorption, and absorption causes overall kinetic enhancement for the system. The hydrogen desorption peak temperature decreased around 212 °C, much lower than pristine MgH_2. However, after the hydrogen desorption measurement, it absorbed 2.4 wt.% of hydrogen at 40 °C at 0.1 MPa H2 pressure. As per the proposed thermodynamic reduction route of TiO_2, three reduction states (0, +2, +3) were generally responsible for Mg's catalytic activity. Hanada et al. reported the reduction of TiO_2 in Ti_2O_3 (+3 oxidation state) responsible for catalytic activity.

② The MgH_2+ZrO_2 sample is categorized as a well-catalyzed sample even though quite low angle peak was observed in the XRD profile. The high dispersion state of catalyzed sample decreased the dehydrogenation peak temperature to around 217 °C. The thermodynamic reduction route reveals the reduction of ZrO_2 with Mg is possible in 0 and +2 states. However, XPS analysis confirmed the presence of ZrO_2 +2 oxidation state, and it slightly reduced on Mg surface in less than +2 oxidation state depending upon the electronic environment of hydrogen. However, XRD confirmed the +4 oxidation state of ZrO_2 as it is bulk analysis.

③ In the case of MgH_2+HfO_2, there was the presence of HfO_2 oxide main peaks after ball milling yields for low/no dispersion of oxide catalysts on the Mg surface. The hydrogen desorption peak temperature was found to be around 303 °C, much higher than MgH_2+Nb_2O_5. The reduction of HfO_2 is not possible with Mg as reactions are endothermic. The XPS spectrum is almost the same for both pristine HfO_2 and MgH_2 with HfO_2. The XPS, XRD, and thermodynamic estimation are consistent; reduction of HfO_2 is not possible on the Mg surface.

④ The XRD peak pattern of MgH_2+V_2O_5 was found consistent with MgH_2+Nb_2O_5, confirming the high dispersion state of Mg as Nb_2O_5. The dehydrogenation peak temperature was found at 209 °C. The thermodynamic estimation reveals the reduction of V_2O_5 is possible in 0, +2, +3, (+3, +4) and (+3, +4) states. However, we cannot discuss the XPS result of the MgH_2+V_2O_5 spectrum due to low intensity. On the other hand, the multi-state reduction of V_2O_5 is also possible like TiO_2, so unable to get a clear peak like other cases. Hanada et al. reported that the XAS analysis revealed VO, +2 state after ball milled MgH_2 samples, which caused the decrease in hydrogen desorption temperature.

⑤ Various research published from our group reported the vanishing of Nb_2O_5 oxide peak after ball milling with MgH_2; almost all results revealed a highly dispersed state. [4-17-18] Although all published results from our group support the thermodynamic reduction of Nb_2O_5 with Mg in 0, +2, and +4 states. [4-17-18] Interestingly, it was reported that Nb^{+2} and Nb^{0} was highly active state compared with Nb^{+4}, concluded that the intermediate stage was highly responsible for catalysis.

⑥ The Ta_2O_5 oxide peaks were detected in the XRD profile of MgH_2+Ta_2O_5 sample yields for low dispersion of oxide catalysts on the Mg surface. The hydrogen desorption peak temperature was found at 285 °C. As discussed above, the thermodynamic estimation reveals that only 0 reduction state is possible for Ta_2O_5 in supporting XPS.

⑦ The MgH_2+CO_3 XRD profile was found consistent with MgH_2+Nb_2O_5, confirming the high dispersion state of Mg like the Nb_2O_5 case. The dehydrogenation peak temperature was found at 206 °C, the lowest among all catalyzed samples. The XPS analysis confirmed the reduction of CrO_3 on Mg surface in +2 and 0 states, with small amount of +3 state consistent with its thermodynamic estimation.

⑧ In the case of MgH_2+MoO_3, the diffraction peaks assigned to MoO_3 were not found after the ball milling, indicating the high dispersion state on the Mg surface would be formed. However, MoO_3 showed low catalytic effects for catalyzed MgH_2 sample, the dehydrogenation peak temperature was found around 324 °C. Both XPS and its one thermodynamic reduction route confirmed the reduction of MoO_3 on Mg surface possible in 0 states.

⑨ For WO_3, oxide peaks were detected in the XRD profile of MgH_2+WO_3 yields for lower dispersion on the Mg surface. As the dispersion state is not good, the dehydrogenation peak temperature was found around 310 °C. The thermodynamic estimation reported two reduction states of WO_3 on Mg surface in +4 and 0 states. The XPS analysis confirmed the thermodynamic estimation, the reduction of WO_3 happened in +4 and 0 reduction states with a small amount of +6 oxidation state.

Therefore, the knowledge in this work is summarized as follows. The dispersion state expected from the XRD patterns is an important factor because almost the samples with no diffraction peaks of oxides showed high catalysis. On the other hand, the catalysis of MoO_3 cannot be explained by the dispersion state. The thermodynamic estimation and XPS analyses clarified that the high catalytic activity was obtained when the intermediate oxidation states such as +2 and +3 will be formed.

4.2 Study on the catalytic tuning of Mg-H system using ternary oxide

4.2.1 Synthesis of $TaVO_5$

$$Ta_2O_5 + V_2O_5 \longrightarrow 2TaVO_5 \qquad (31)$$

Based on the hypothesis behind ternary oxide, we started synthesizing the ternary oxide using a single phase of Ta_2O_5 and V_2O_5 followed by the above equation. Single-phase of Ta_2O_5 and V_2O_5 oxide were ball milled in an argon atmosphere in the stoichiometric ratio of 1:1 as per the chemical equation. In our case, 20 ZrO_2 balls were used of 8mm diameter for 300 mg of batch size followed by 370 rpm. The sample was ball milled for 12h with a pattern of 1 h milling followed by a half an hour pause time to avoid overheating inside the vessel. All samples were carefully collected in an Al_2O_3 crucible to perform the heat treatment. XRD was performed to confirm the changes that emerged after milling shown in Figure 4.10. A longer time milling yields the amorphization of the sample even though with oxide samples as ball milling is high energy milling process. The heat treatment was done for milled samples inside a muffle furnace in atmospheric air at 1000 °C for 12h. Again, XRD was performed to confirm the changes that emerged after heat treatment. The XRD patterns were analyzed by comparing to databases [ICDD, JICST, COD2019] using the PDXL software, we found the successful synthesis of $TaVO_5$ ternary oxide achieved, shown in Figure 4.10.

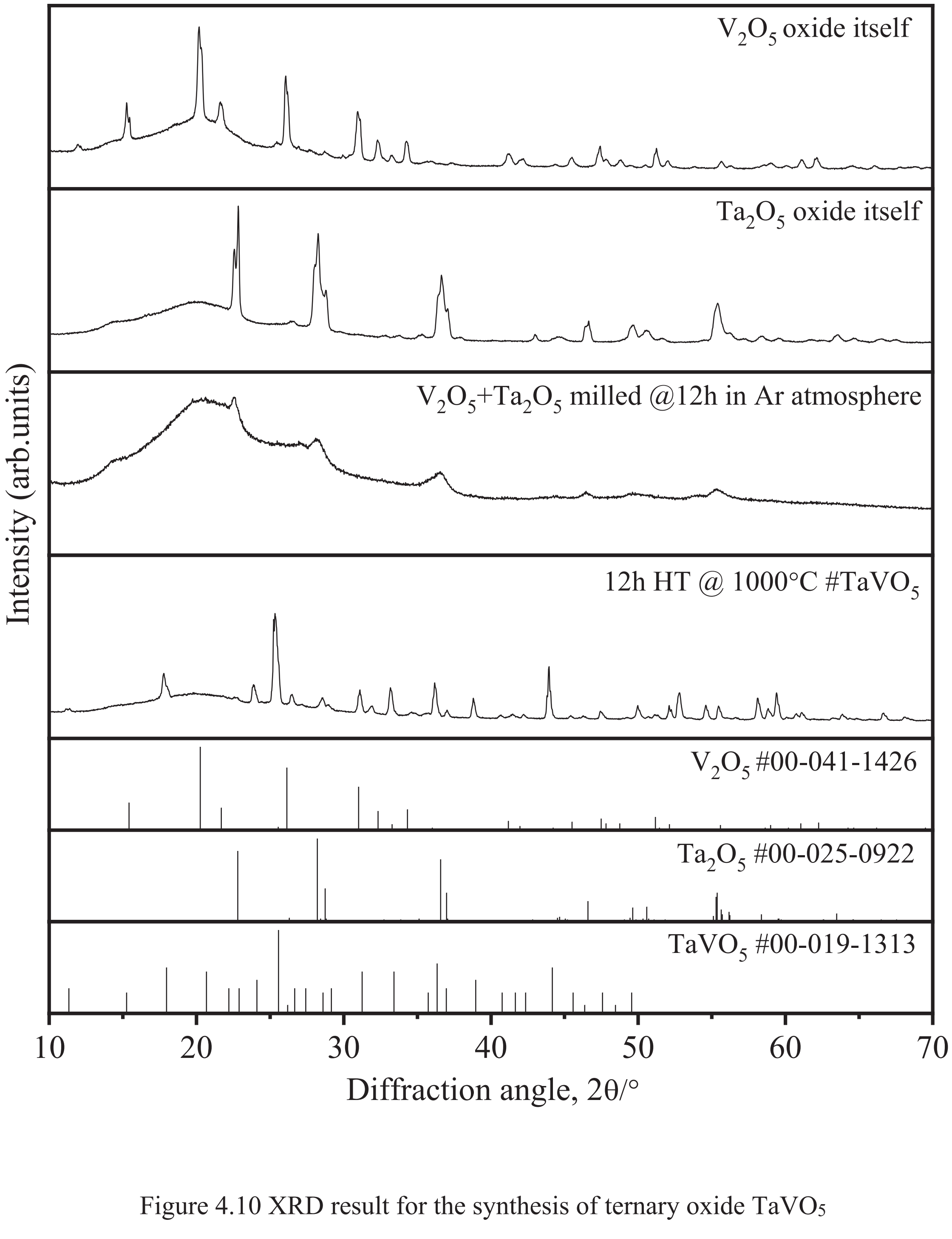

Figure 4.10 XRD result for the synthesis of ternary oxide $TaVO_5$

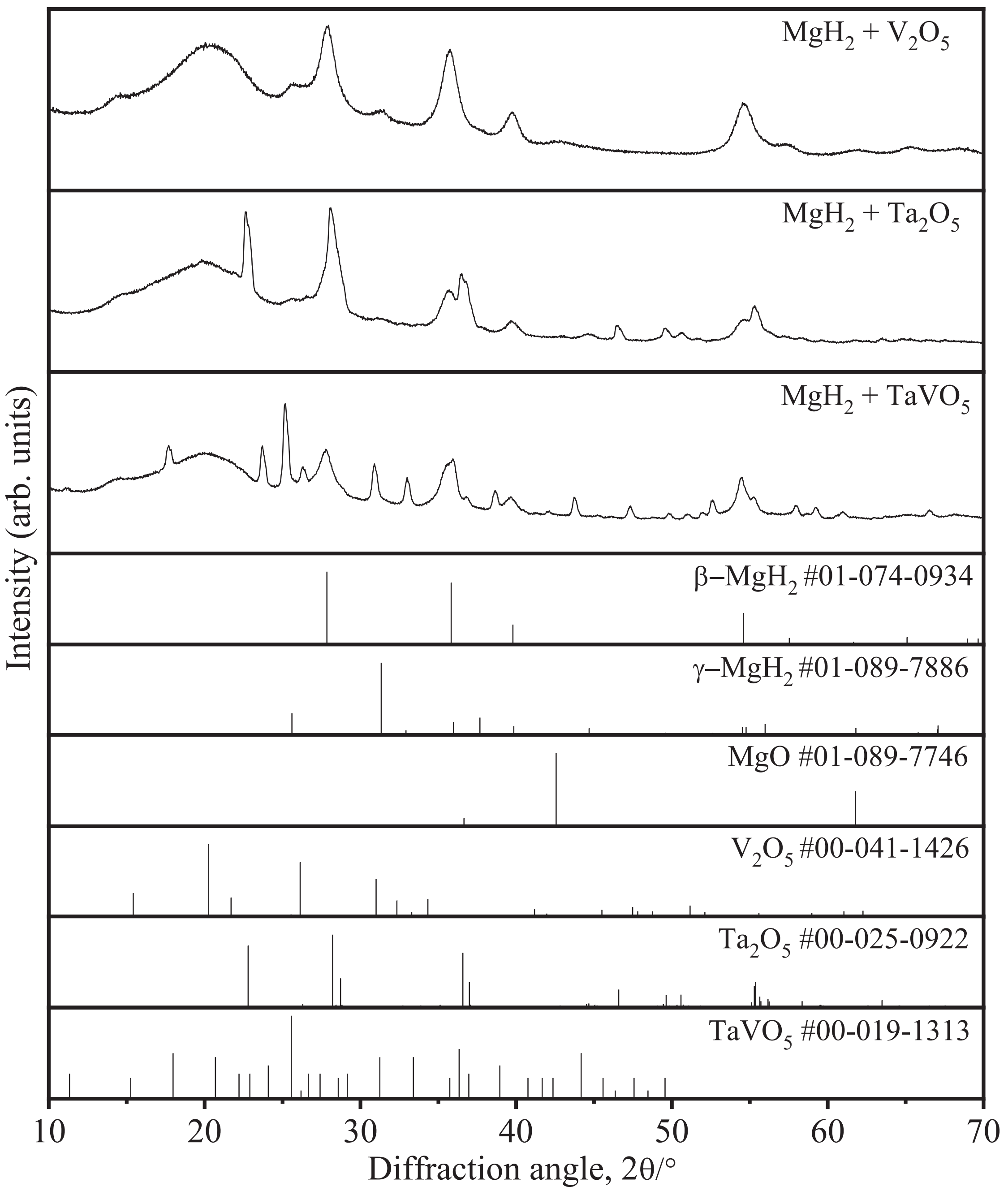

Figure 4.11 XRD pattern of MgH_2 samples with V_2O_5, Ta_2O_5 oxide, and $TaVO_5$ ternary oxide additives

4.2.2 Structural and hydrogen sorption properties of MgH_2 with $TaVO_5$

To analyze the catalytic behavior of synthesized ternary oxide $TaVO_5$, it was ball milled with MgH_2, as Mg is a potential material for hydrogen storage. All the sample preparation processes are explained in the experimental section. All structural analysis of MgH_2+$TaVO_5$ was measured and compared with its fundamental oxide Ta_2O_5 and V_2O_5. The XRD profiles corresponding to each product were labeled in Figure 4.11. The XRD profile of MgH_2+$TaVO_5$ shows the formation of metastable γ-MgH_2 phase with β-MgH_2 phase reveals the consistency with ball-milled MgH_2+V_2O_5 and MgH_2+Ta_2O_5 respectively. In comparison with as purchased pristine MgH_2 (β-phase), ball milling effect dominates causes formation of γ-MgH_2 phase. The XRD profile of MgH_2+$TaVO_5$ reveals a decrease in the peak intensity much lower than pristine MgH_2. But we can’t deny the presence of a small sum of MgO inside MgH_2+Ta_2O_5, even though undetectable using XRD. The formation of MgO was a common phenomenon during ball milling due to the reduction of oxide; alternatively, strong oxygen affinity towards Mg also assists it. On the other hand, individual oxide $TaVO_5$ peak for MgH_2+$TaVO_5$ was consistent with MgH_2+Ta_2O_5, whereas inconsistent with MgH_2+V_2O_5. It will be pretty interesting to know the stability and reduction behavior of $TaVO_5$.

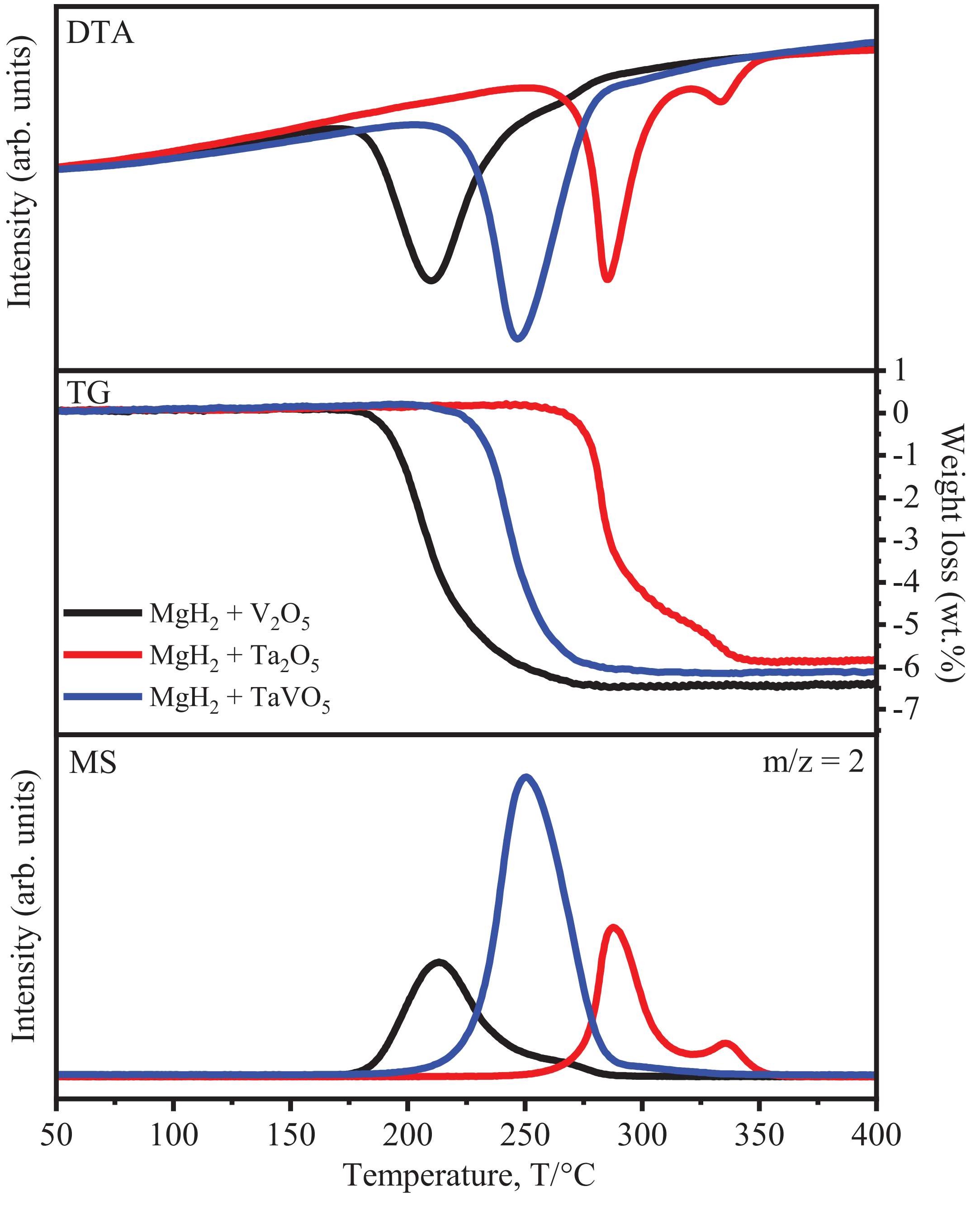

Figure 4.12 TG-DTA-MS results for hydrogen desorption of MgH_2 with V_2O_5, Ta_2O_5 oxide, and $TaVO_5$ ternary oxide additives respectively

The hydrogen desorption measurement of the catalyzed MgH_2 has been investigated using the TG-DTA-MS measurements at a constant heating rate of 5 °C/min in the Ar atmosphere. The results are presented in Figure 4.12. The hydrogen desorption peak temperature for MgH_2 with synthesized $TaVO_5$ oxide was evaluated and found to be 250 °C which is in the middle of MgH_2+V_2O_5 peak temperature 213 °C and Ta_2O_5 peak temperature 288 °C, respectively. This result yields our purpose, and we found the middle properties called tuning of samples. The XRD confirmed the formation of the Mg phase by releasing the hydrogen, as shown in Figure 4.13.

Figure 4.14 shows the isothermal hydrogen absorption curve of Mg performed at 40 °C under a pressure of 0.1 MPa hydrogen (H_2) pressure after the hydrogen desorption measurement. The hydrogen absorption for the catalyzed sample was found in decreasing order of $V_2O_5 > Ta_2O_5 > TaVO_5$ oxide, respectively, least for the ternary oxide (around catalyzed Ta_2O_5). The hydrogen absorption tendency for ternary oxide is entirely different from hydrogen desorption. The above experimental results clarify that the effective factors of catalysis for hydrogen absorption are different from those of the hydrogen desorption processes. However, the same factors can explain the activity of some oxides as those of hydrogen desorption. The formation of the MgH_2 phase from Mg and the remaining Mg phase with a reasonable amount was confirmed using XRD measurement as shown in Figure 4.15.

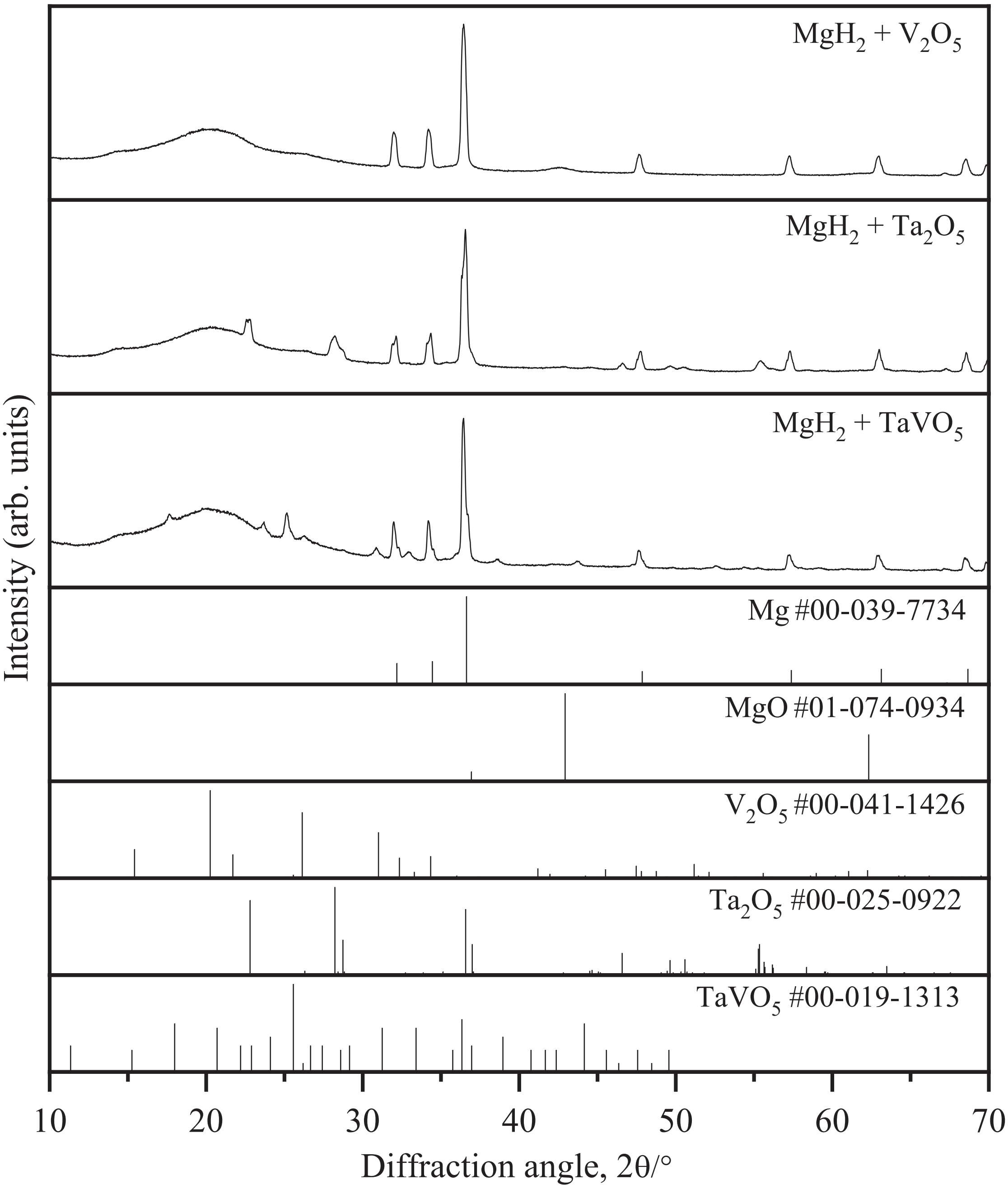

Figure 4.13 XRD pattern of MgH_2 with V_2O_5, Ta_2O_5 oxide, and $TaVO_5$ ternary oxide additives after the dehydrogenation

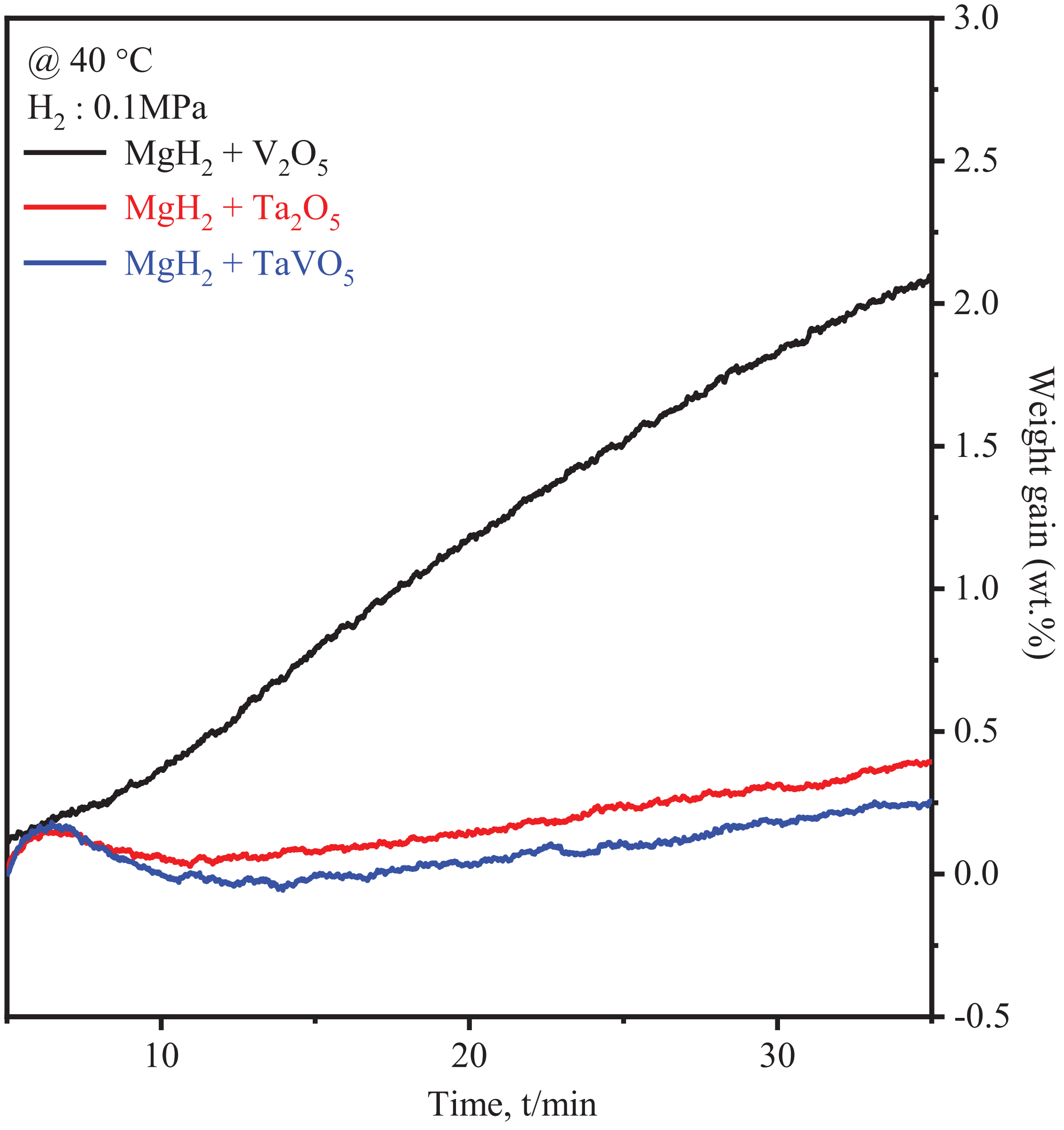

Figure 4.14 TG results for hydrogen absorption of Mg with V_2O_5, Ta_2O_5 oxide and $TaVO_5$ ternary oxide additives after the dehydrogenation

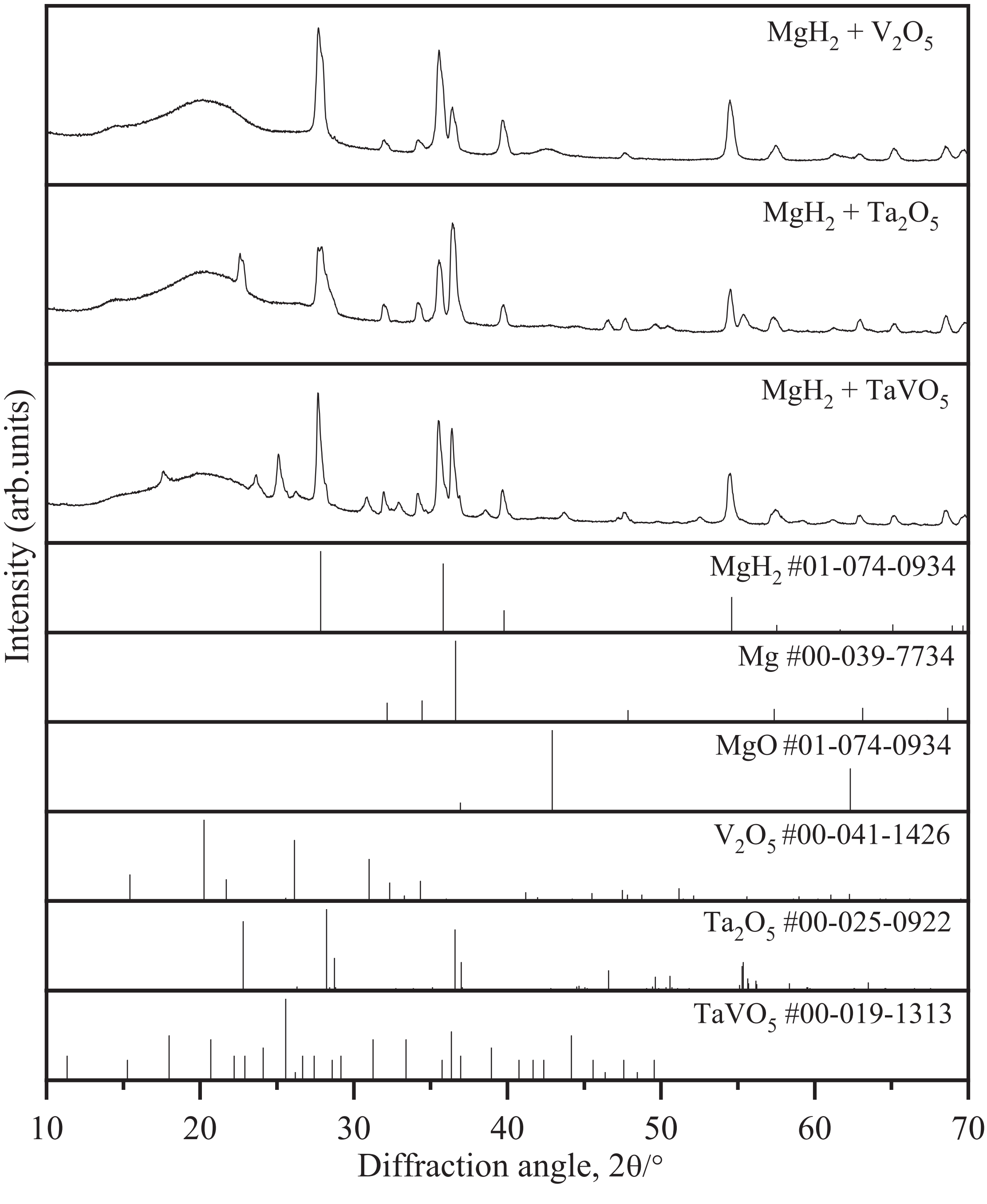

Figure 4.15 XRD pattern of MgH_2 samples with V_2O_5, Ta_2O_5 oxide, and $TaVO_5$ ternary oxide additives after hydrogenation

4.2.3 Synthesis of Nb_9VO_{25}

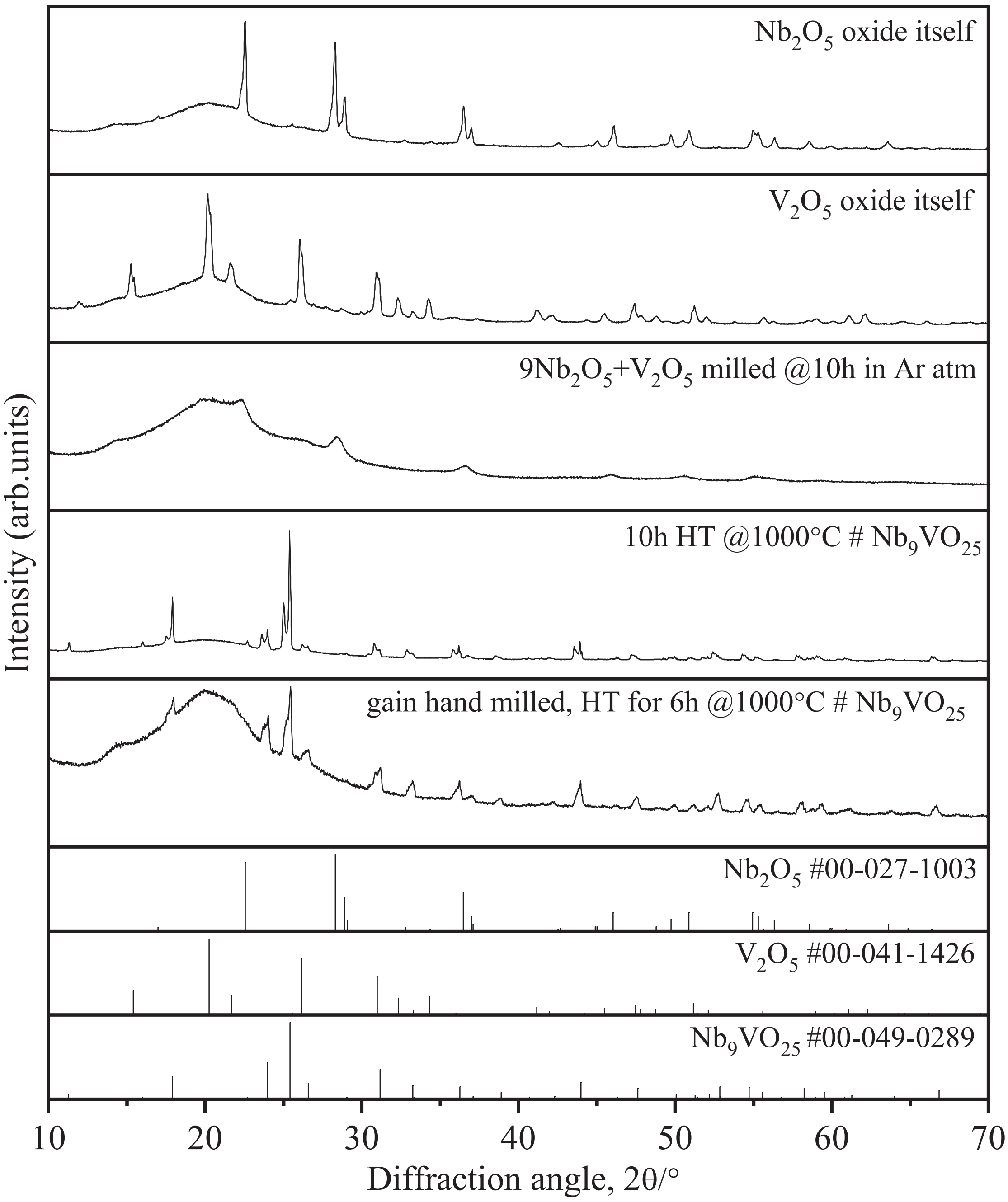

Figure 4.16 XRD confirmation of synthesis of Nb_9VO_{25} ternary oxide

$$9Nb_2O_5 + V_2O_5 \longrightarrow Nb_9VO_{25} \qquad (32)$$

Based on the hypothesis behind ternary oxide we started synthesizing the ternary oxide using a single phase of Nb_2O_5 and V_2O_5 followed by the above equation. Both, single phases of Nb_2O_5 and V_2O_5 oxide were ball milled in an argon atmosphere in the stoichiometric ratio of 9:1 as per the chemical equation (32). In our case, 20 ZrO_2 balls were used of 8mm diameter for 300 mg of batch size followed by 370 rpm. The sample was ball milled for 10h with a pattern of 1 h milling followed by a half an hour pause time to avoid overheating inside the vessel. All samples were carefully collected in an Al_2O_3 crucible to perform the heat treatment. XRD was performed to confirm the changes that emerged after milling shown in figure 4.16. The heat treatment was done for milled samples inside a muffle furnace in atmospheric air at 1000 °C for 10h. Again, XRD was performed to confirm the changes that emerged after heat treatment but after peak analysis found that the sample was not crystalline as much as necessary as shown in figure 4.16. The sample was again milled into a fine powder using a mortar pestle and heat treatment was done at 1000 °C for 6h. After heat treatment XRD was analyzed, perfect crystalline Nb_9VO_{25} phase was confirmed as shown in figure 4.16.

4.2.4 Structural and hydrogen sorption properties of MgH_2 with Nb_9VO_{25}

To analyze the catalytic behavior of synthesized ternary oxide Nb_9VO_{25}, it was ball milled with MgH_2, as Mg is a potential material for hydrogen storage. All the sample preparation processes are explained in the experimental chapter. All structural analysis of MgH_2+ Nb_9VO_{25} was measured and compared with its fundamental oxide Nb_2O_5 and V_2O_5. The XRD profiles corresponding to each product were labeled in figure 4.17. The XRD profile of MgH_2+ Nb_9VO_{25} shows the formation of metastable γ-MgH_2 phase with β-MgH_2 phase reveals the inconsistent with ball-milled MgH_2+Nb_2O_5 and MgH_2+V_2O_5 respectively. XRD profile of MgH_2+ Nb_9VO_{25} reveals a decrease in the peak intensity much lower than pristine MgH_2. On the other hand, the presence of individual oxide Nb_9VO_{25} peak for MgH_2+ Nb_9VO_{25} shows less dispersion of oxide on the Mg surface. As per a previous study, the presence of individual oxide peaks causes low dispersion, yields low catalysis. It will be quite interesting to know the stability and reduction behavior of Nb_9VO_{25}.

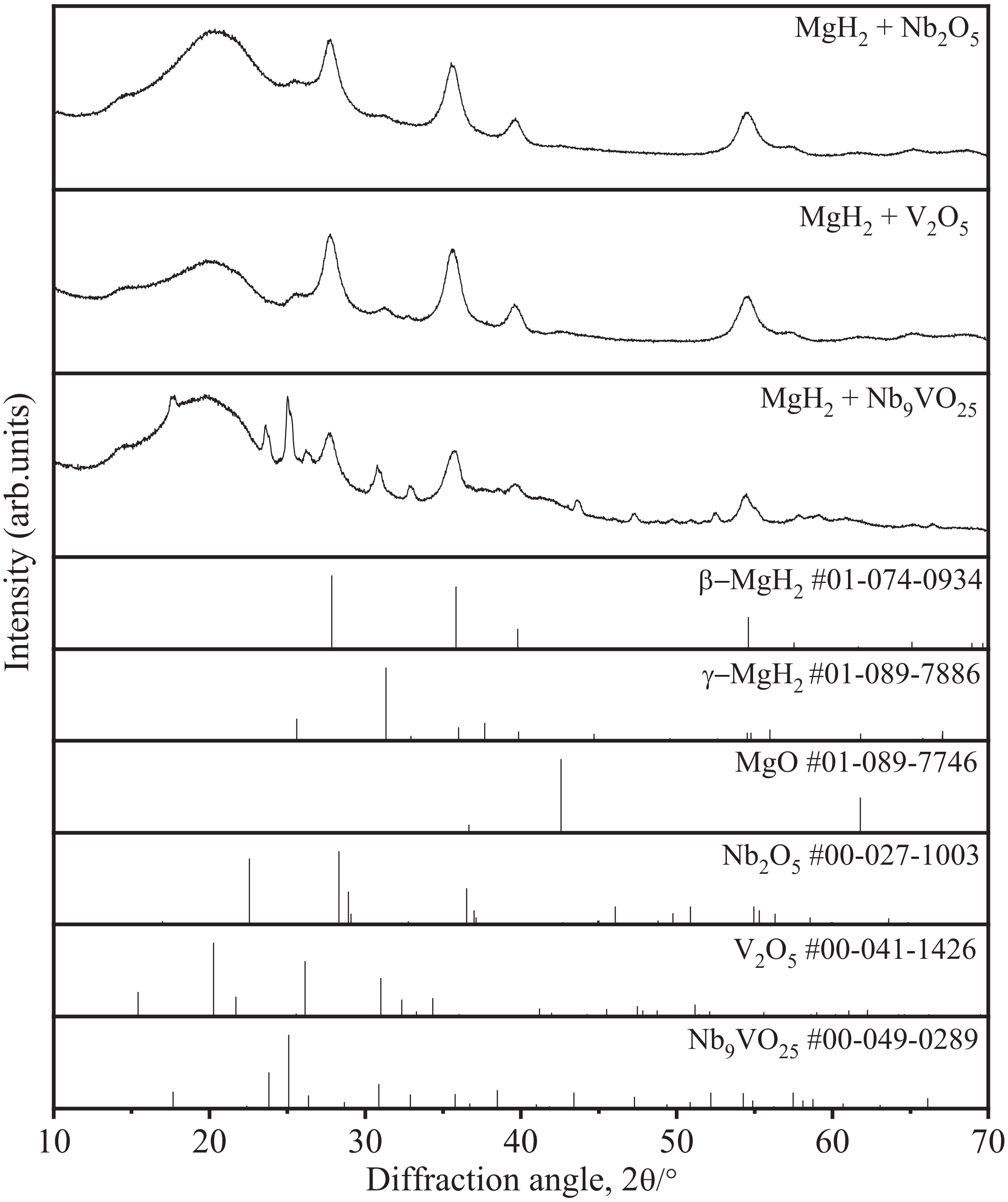

Figure 4.17 XRD pattern of MgH_2 samples with Nb_2O_5, V_2O_5 oxide, and Nb_9VO_{25} ternary oxide additives

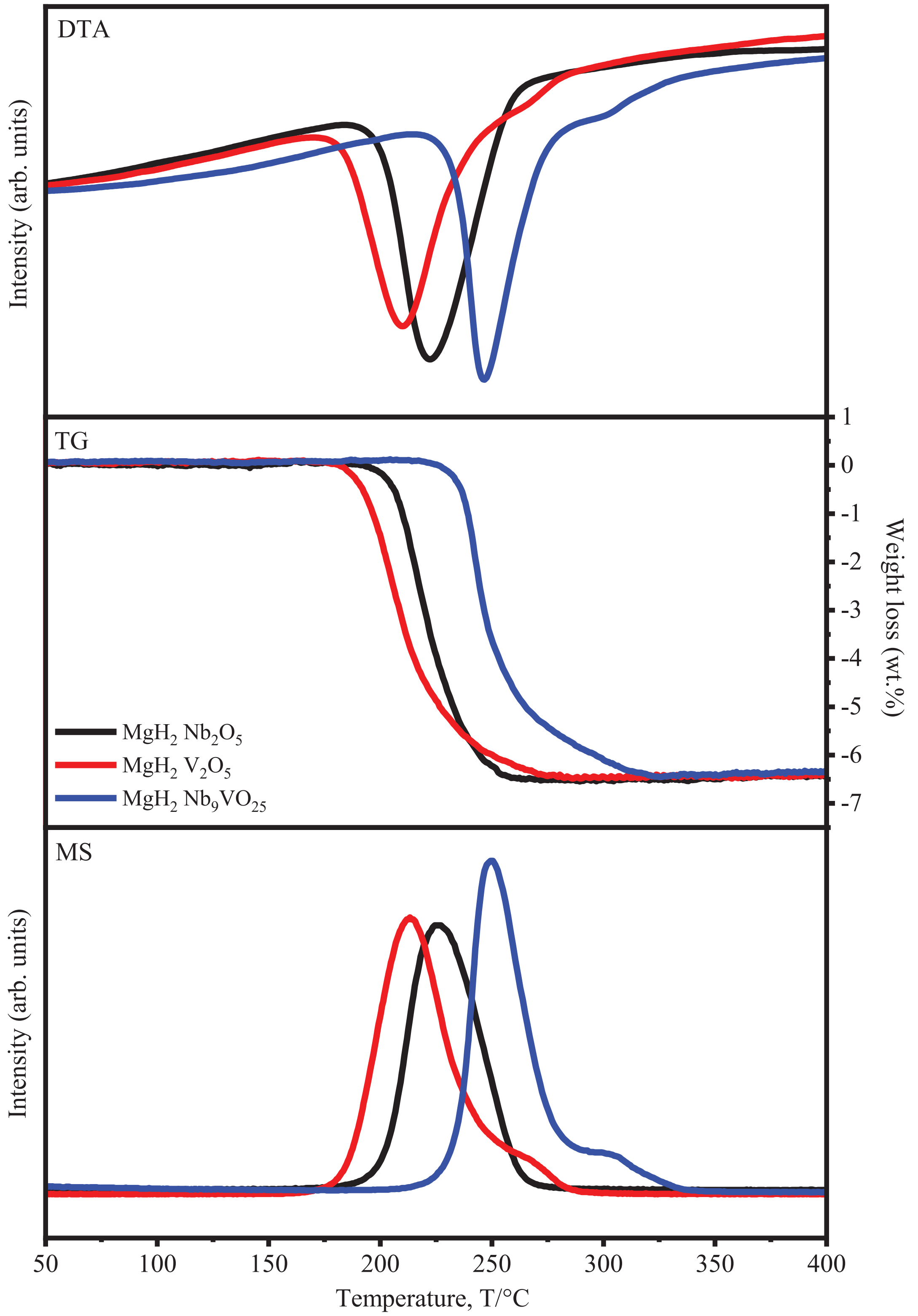

Figure 4.18 TG-DTA-MS results for hydrogen desorption of MgH_2 with Nb_2O_5, V_2O_5 oxide and Nb_9VO_{25} ternary oxide additives respectively

The hydrogen desorption measurement of catalyzed MgH_2 investigated using the TG-DTA-MS measurements at a constant heating rate of 5 °C/min in Ar atmosphere, and the results are presented in Figure 4.18. The hydrogen desorption peak temperature for MgH_2 with synthesized Nb_9VO_{25} oxide was evaluated and found to be 250 °C which is comparatively higher than MgH_2+V_2O_5 peak temperature 220 °C and MgH_2+Nb_2O_5 peak temperature 225 °C, respectively. This result is yielding our purpose, and we found the different hydrogen desorption peak temperatures called tuning of catalysis. The Nb-V-O phase is chemically much more stable than its single oxide. So, the reduction of oxides during ball-milling with MgH_2 will be suppressed; during ball milling, dispersion is difficult due to stable bonding, expecting that the catalytic activity of the ternary oxide will be low than that of single oxide. The XRD confirmed the formation of the Mg phase by releasing the hydrogen, as shown in Figure 4.19.

Figure 4.20 shows the isothermal hydrogen absorption curve of Mg performed at 40 °C under a 0.1 MPa hydrogen (H_2) pressure after the hydrogen desorption measurement. The hydrogen absorption for the catalyzed sample was found in decreasing order of $Nb_2O_5 > V_2O_5 > Nb_9VO_{25}$ oxide, respectively, different from hydrogen desorption. Inconsistent with the previous result explained for hydrogen absorption at room temperature, it is clarified that the effective factors of catalysis for the hydrogen absorption are different from those of the hydrogen desorption processes, although the activity of some oxides can be explained same factors as those of hydrogen desorption. The formation of the MgH_2 phase from Mg and the remaining Mg phase with a reasonable amount was confirmed using XRD measurement, as shown in Figure 4.21.

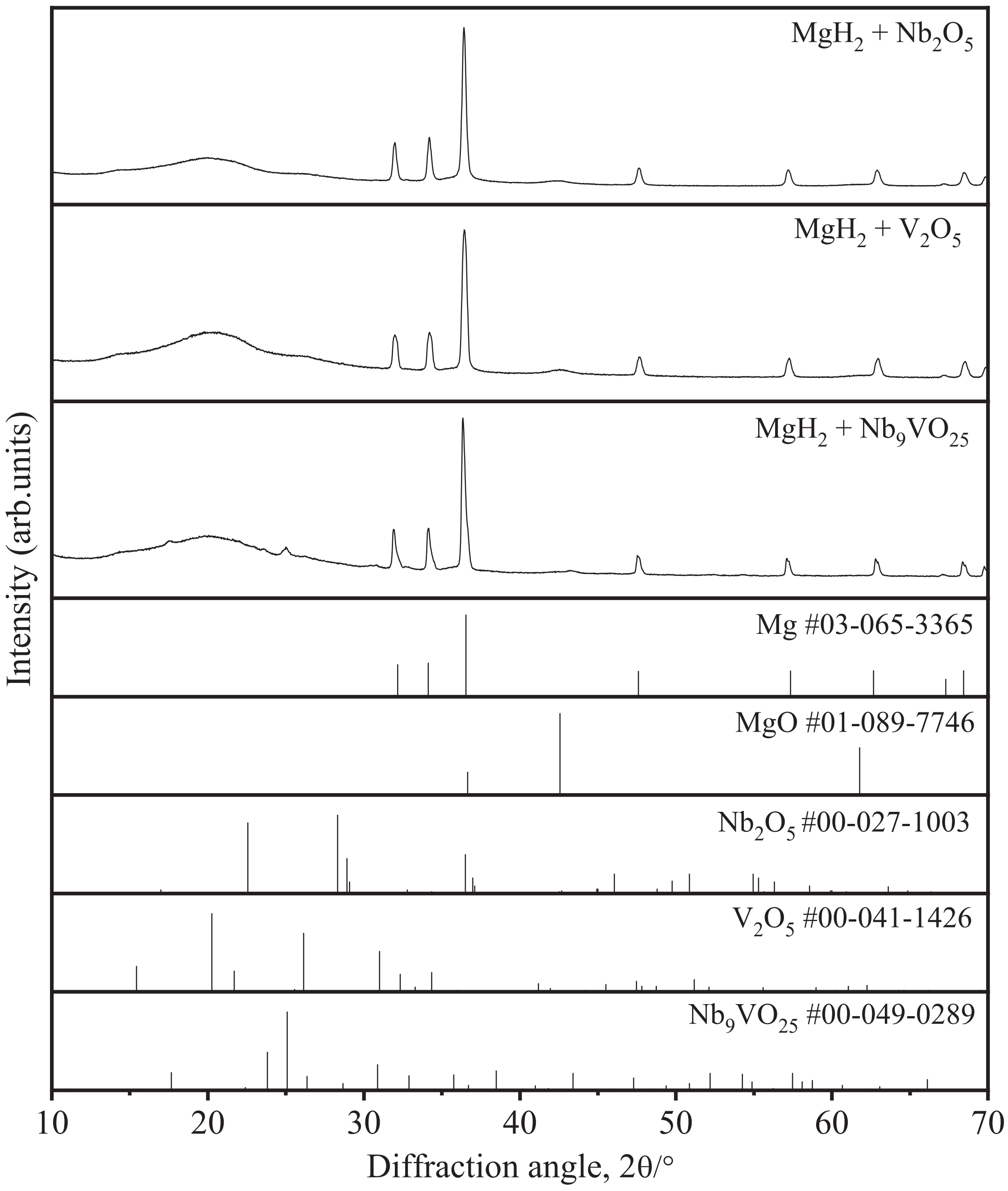

Figure 4.19 XRD pattern of MgH_2 samples with Nb_2O_5, V_2O_5 oxide and Nb_9VO_{25} ternary oxide additives dehydrogenation

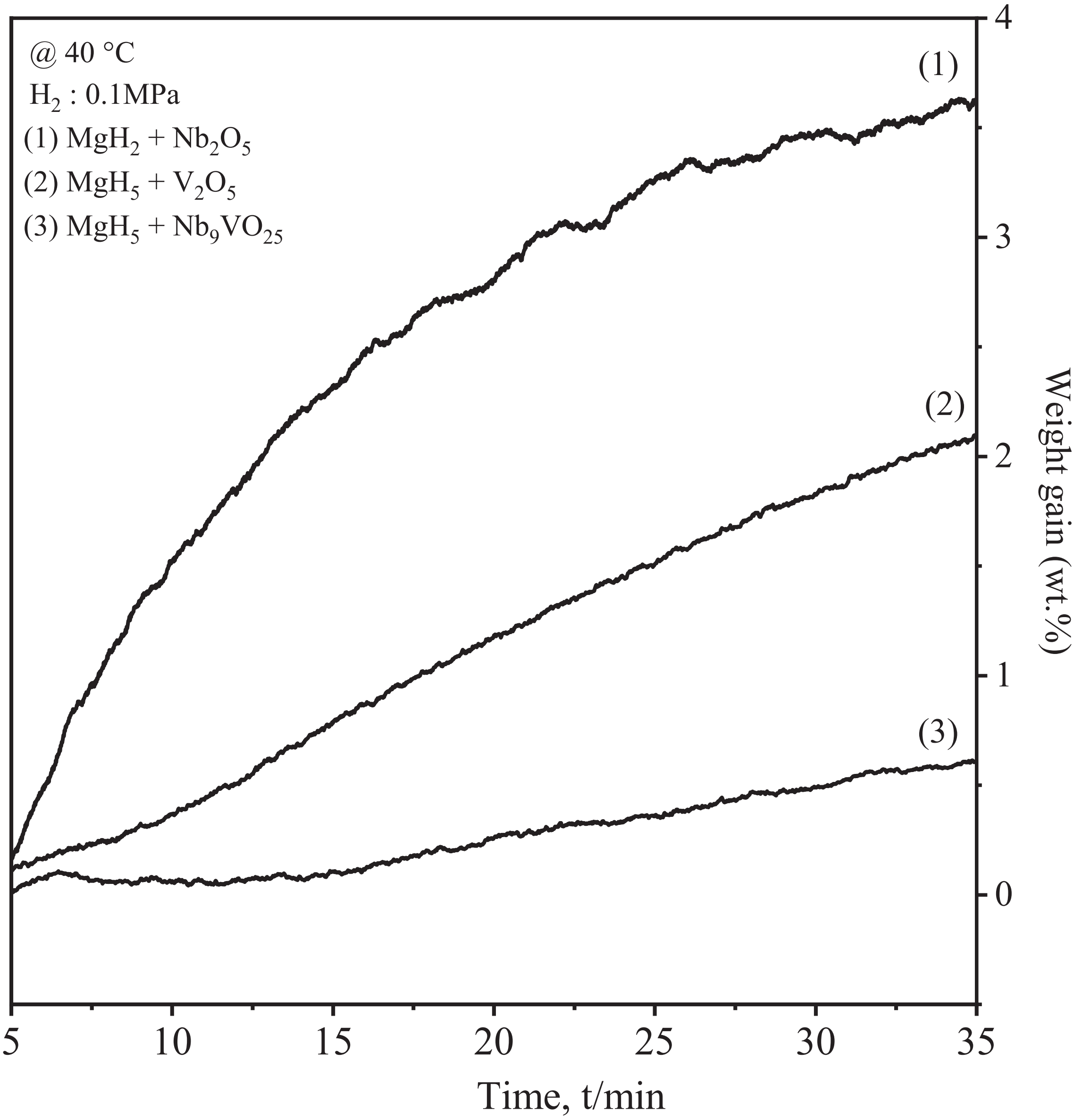

Figure 4.20 TG results for hydrogen absorption of Mg with Nb_2O_5, V_2O_5 oxide and Nb_9VO_{25} ternary oxide additives after the dehydrogenation

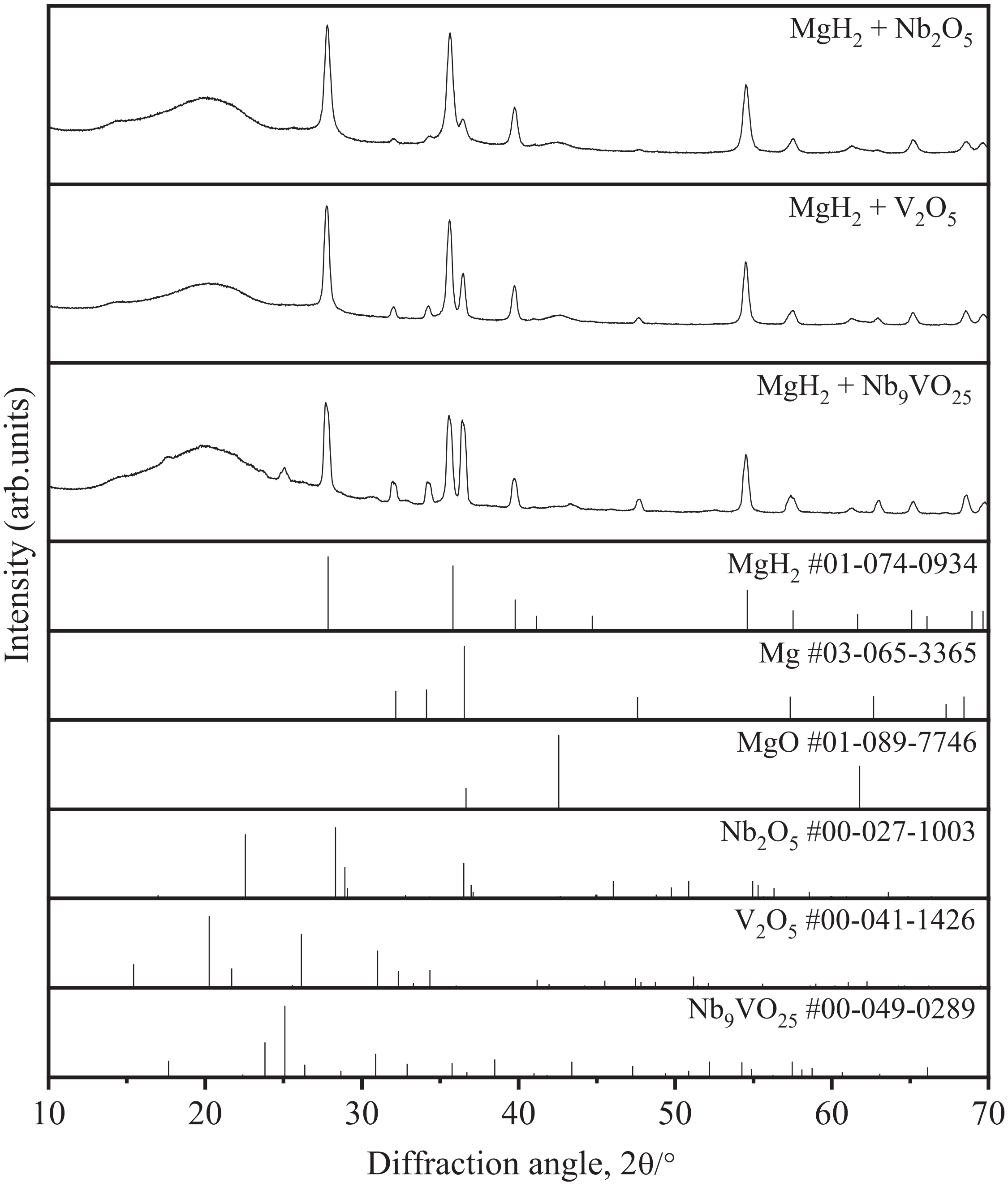

Figure 4.21 XRD pattern of MgH_2 samples with Nb_2O_5, V_2O_5 oxide and Nb_9VO_{25} ternary oxide additives after hydrogenation

4.2.5 Synthesis of $Nb_{0.6}Cr_{0.4}O_2$

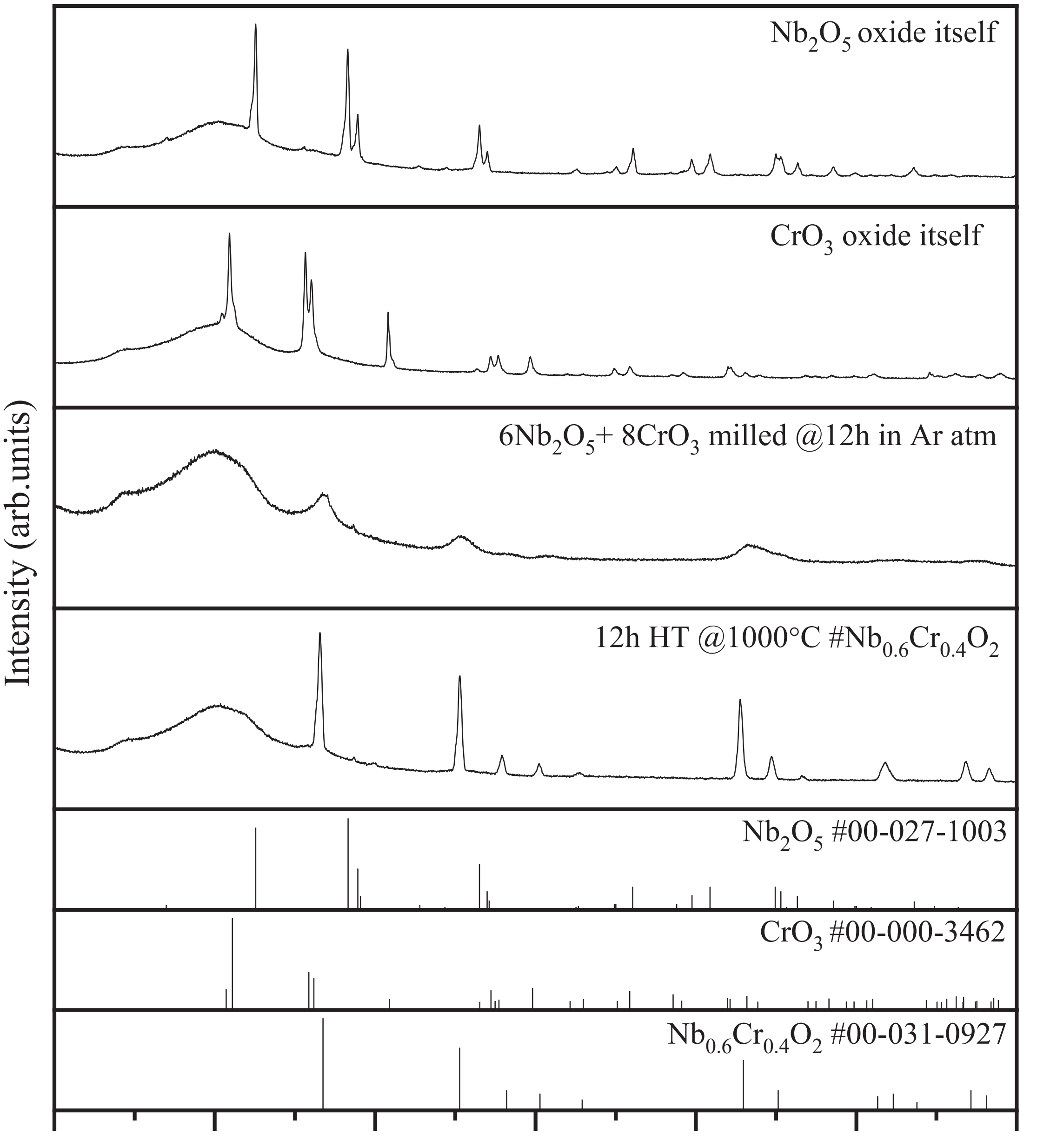

Figure 4.22 XRD confirmed the perfect synthesis of $Nb_{0.6}Cr_{0.4}O_2$ ternary oxide

$$6Nb_2O_5 + 8CrO_3 \longrightarrow 20Nb_{0.6}Cr_{0.4}O_2 + 7O_2 \qquad (33)$$

Based on the hypothesis behind ternary oxide we started synthesizing the ternary oxide using a single phase of Nb_2O_5 and CrO_3 followed by the above equation. Both, single phases of Nb_2O_5 and CrO_3 oxide were ball milled in the stoichiometric ratio of 6:8 respectively as per the chemical equation (33). Ball milling was done for 300 mg of batch size using 20 ZrO_2 balls, followed by 370 rpm in Ar atmosphere. The sample was ball milled for 12h with a pattern of 1 h milling followed by half an hour pause time to avoid the overheating inside vessel. All samples were carefully collected in an Al_2O_3 crucible to perform the heat treatment. XRD was performed to confirm the changes that emerged after milling, which we can see from figure 4.22. that there was the origination of new phase occurred, crystalline nature completely changed towards amorphous. The heat treatment was done for milled samples inside a muffle furnace in atmospheric air at 1000 °C for 12h. XRD was performed to confirm the changes that emerged after heat treatment and found that perfect crystalline $Nb_{0.6}Cr_{0.4}O_2$ ternary oxide phase confirmed as shown in figure 4.22.

To analyze the catalytic behavior of synthesized ternary oxide $Nb_{0.6}Cr_{0.4}O_2$, it was ball milled with MgH_2, as Mg is a potential material for hydrogen storage. All the sample preparation processes are explained in the experimental section. All structural analysis of MgH_2+ $Nb_{0.6}Cr_{0.4}O_2$ was measured and compared with its fundamental oxide Nb_2O_5 and CrO_3. The XRD profiles corresponding to each product were labeled in figure 4.23. The presence of ternary oxide $Nb_{0.6}Cr_{0.4}O_2$, peak in XRD profile itself an indication of low catalytic activity of the sample, on the other hand, Nb_2O_5 and CrO_3 completely dispersed onto the Mg surface.

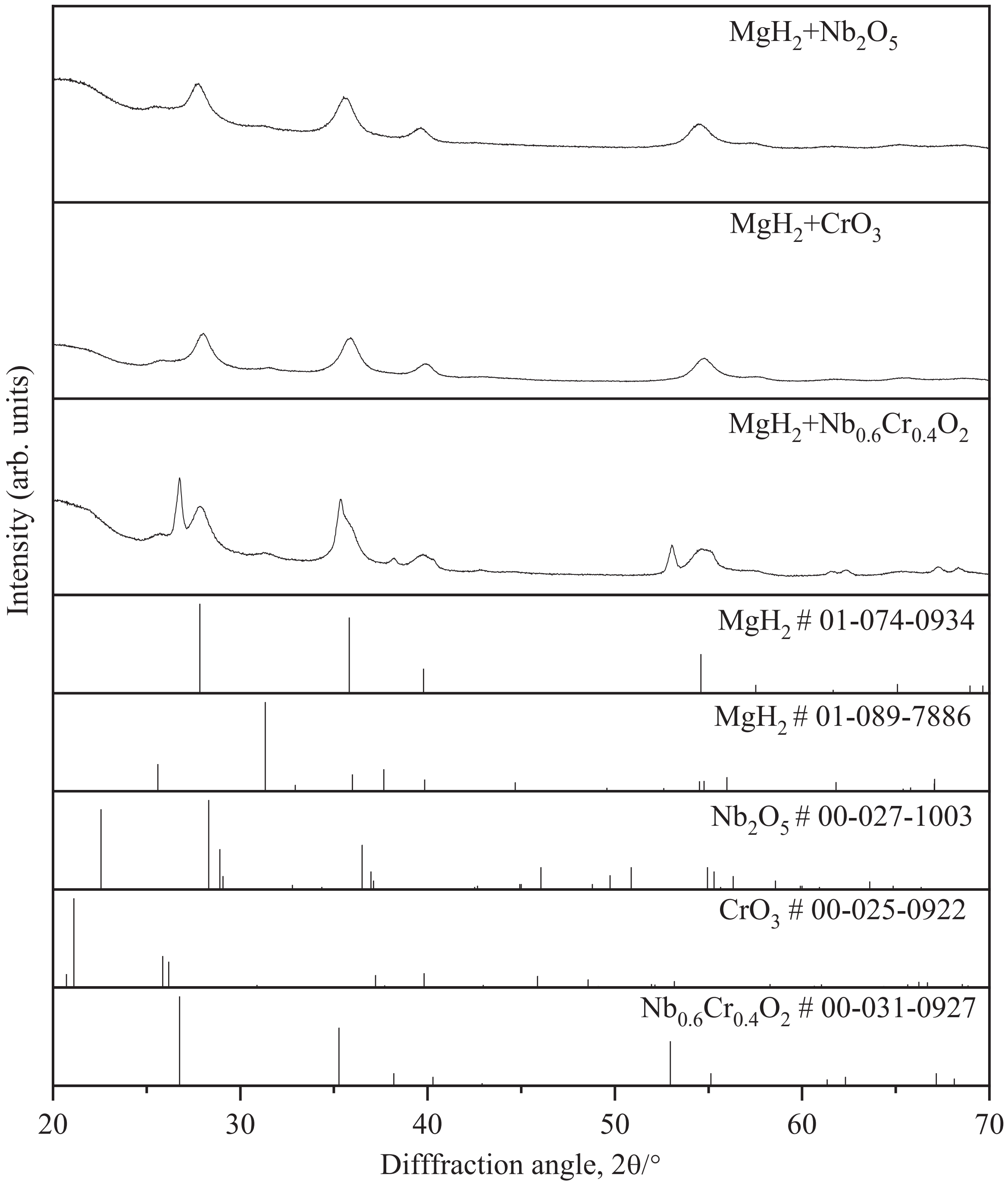

Figure 4.23 XRD pattern of MgH_2 samples with Nb_2O_5, CrO_3 oxide, and $Nb_{0.6}Cr_{0.4}O_2$ ternary oxide additives

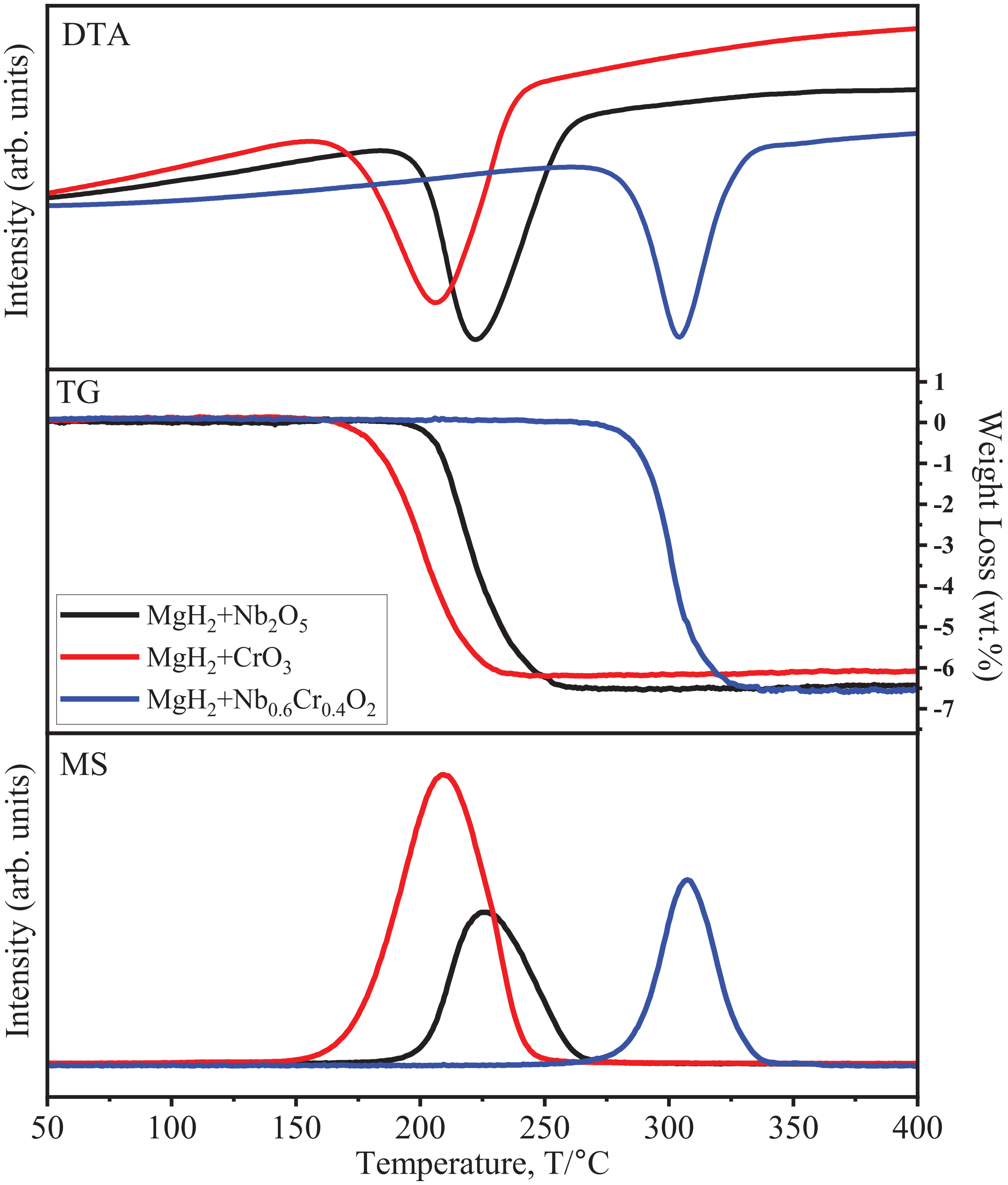

Figure 4.24 TG-DTA-MS results for hydrogen desorption of MgH_2 with Nb_2O_5, CrO_3 oxide, and $Nb_{0.6}Cr_{0.4}O_2$ ternary oxide additives respectively

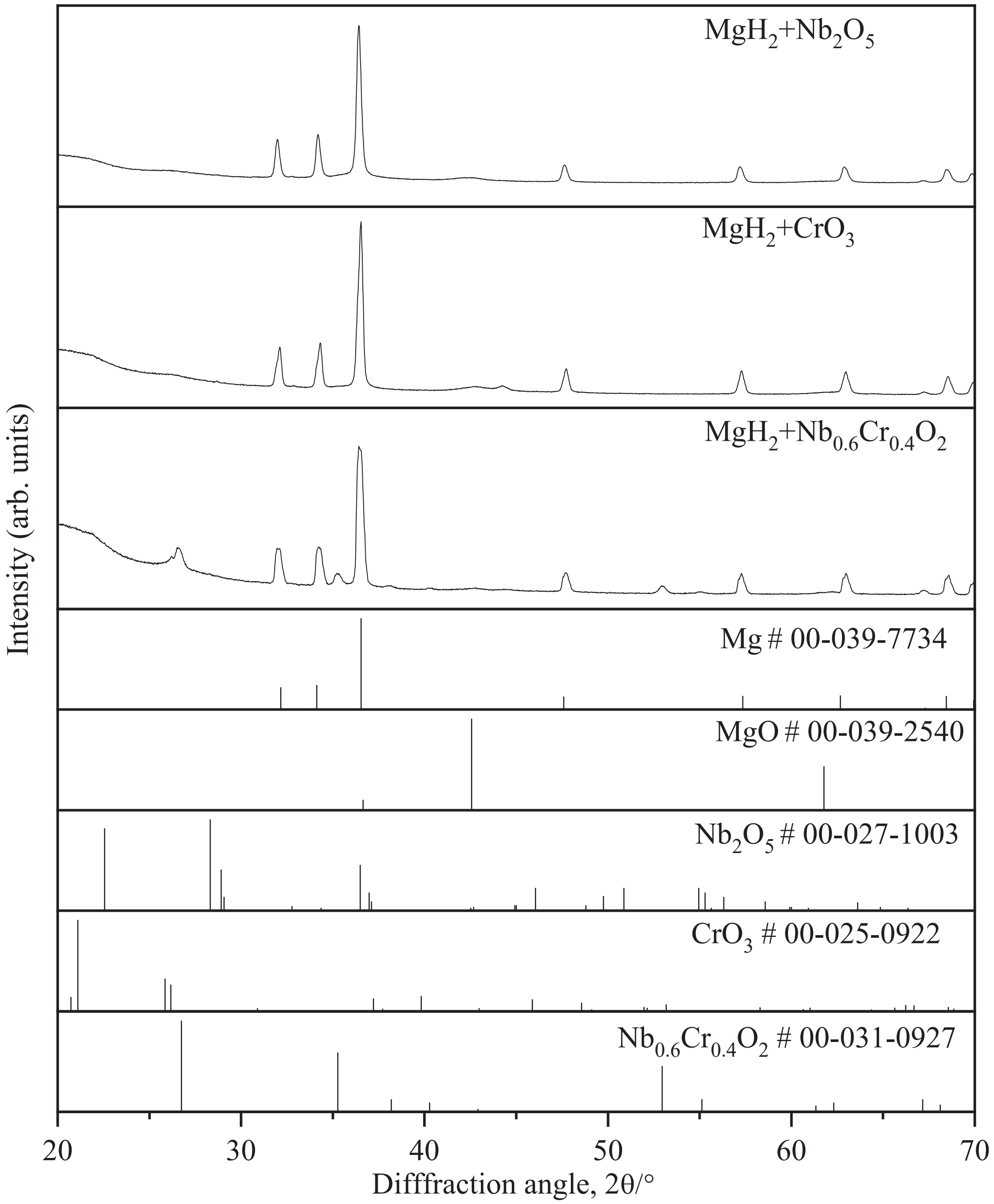

Figure 4.25 XRD pattern of MgH_2 samples with Nb_2O_5, CrO_3 oxide, and $Nb_{0.6}Cr_{0.4}O_2$ ternary oxide additives dehydrogenation

4.2.6 Structural and hydrogen sorption properties of MgH_2 with $Nb_{0.6}Cr_{0.4}O_2$

The hydrogen desorption measurement of the catalyzed MgH_2 have been investigated using the TG-DTA-MS measurements at a constant heating rate of 5 °C/min in Ar atmosphere, and the results are presented in Figure 4.24. The hydrogen desorption peak temperature for MgH_2 with synthesized $Nb_{0.6}Cr_{0.4}O_2$ ternary oxide was evaluated and found to be 303 °C which is comparatively much higher compared to MgH_2+Nb_2O_5 peak temperature 222 °C and MgH_2+CrO_3 peak temperature 206 °C respectively. This result is yielding our purpose and we found the different hydrogen desorption peak temperatures called tuning of catalysis. The Nb-Cr-O phase is chemically much more stable than its single oxide. So, the reduction of oxides during ball-milling with MgH_2 will be suppressed, expecting that the catalytic activity of the ternary oxide will be low than that of single oxide.

The XRD confirmed the formation of the Mg phase by releasing the hydrogen as shown in figure 4.25.

Figure 4.26 shows the isothermal hydrogen absorption curve of Mg performed at 40 °C under a pressure of 0.1 MPa hydrogen (H_2) pressure after the hydrogen desorption measurement. The hydrogen absorption for the catalyzed sample was found in decreasing order of $Nb_2O_5 > CrO_3 > Nb_{0.6}Cr_{0.4}O_2$ oxide respectively, different from hydrogen desorption. Inconsistent with the previous result explained for hydrogen absorption at room temperature, it is clarified that the effective factors of catalysis for the hydrogen absorption are different from those of the hydrogen desorption processes although the activity of some oxides can be explained same factors as those of hydrogen desorption. The formation of the MgH_2 phase from Mg and the remaining Mg phase with a reasonable amount was confirmed using XRD measurement as shown in Figure 4.27.

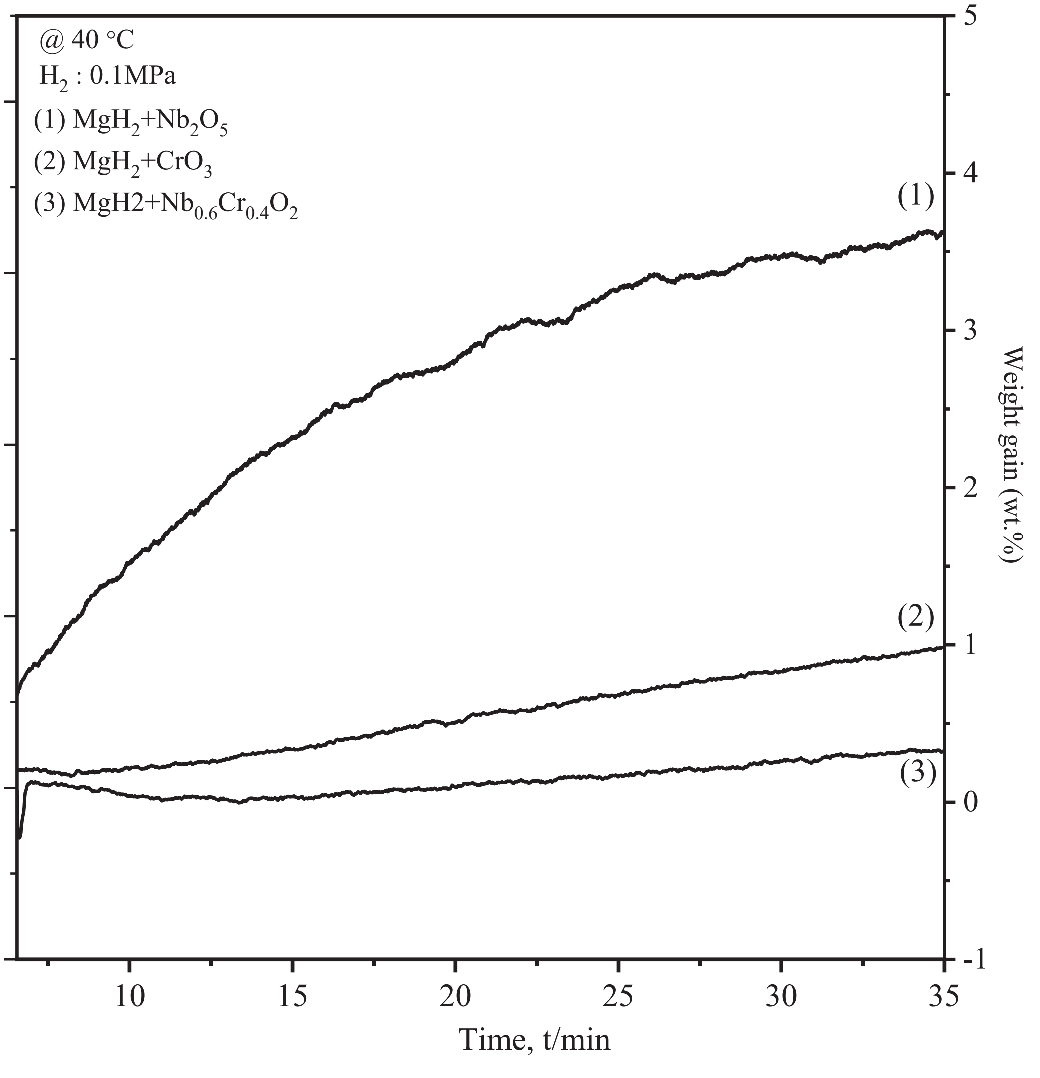

Figure 4.26 TG results for hydrogen absorption of Mg with Nb_2O_5, CrO_3 oxide and $Nb_{0.6}Cr_{0.4}O_2$ ternary oxide additives after the dehydrogenation

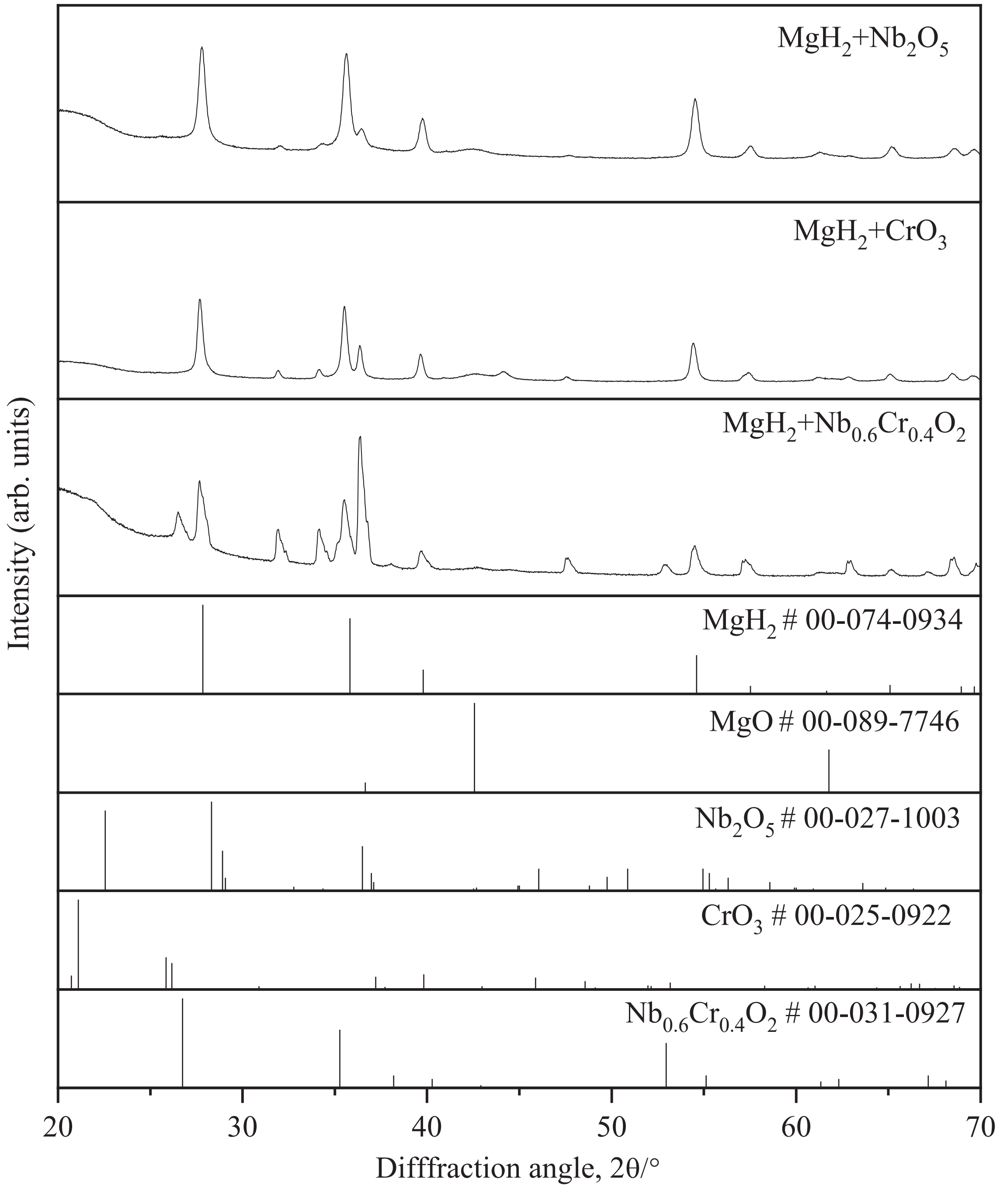

Figure 4.27 XRD pattern of MgH_2 samples with Nb_2O_5, CrO_3 oxide and $Nb_{0.6}Cr_{0.4}O_2$ ternary oxide additives after hydrogenation

4.3 Study on synthesis technique of highly activated Mg

4.3.1 Structural properties of gel oxides with MgH_2

As shown in Figure 4.28, no diffraction peaks were observed in the XRD measurements of all the oxides, suggesting that the catalysts are amorphous. Here, the broad kinks observed around 20-40 and 40-60 ° are background originated in the grease and polyimide sheets.

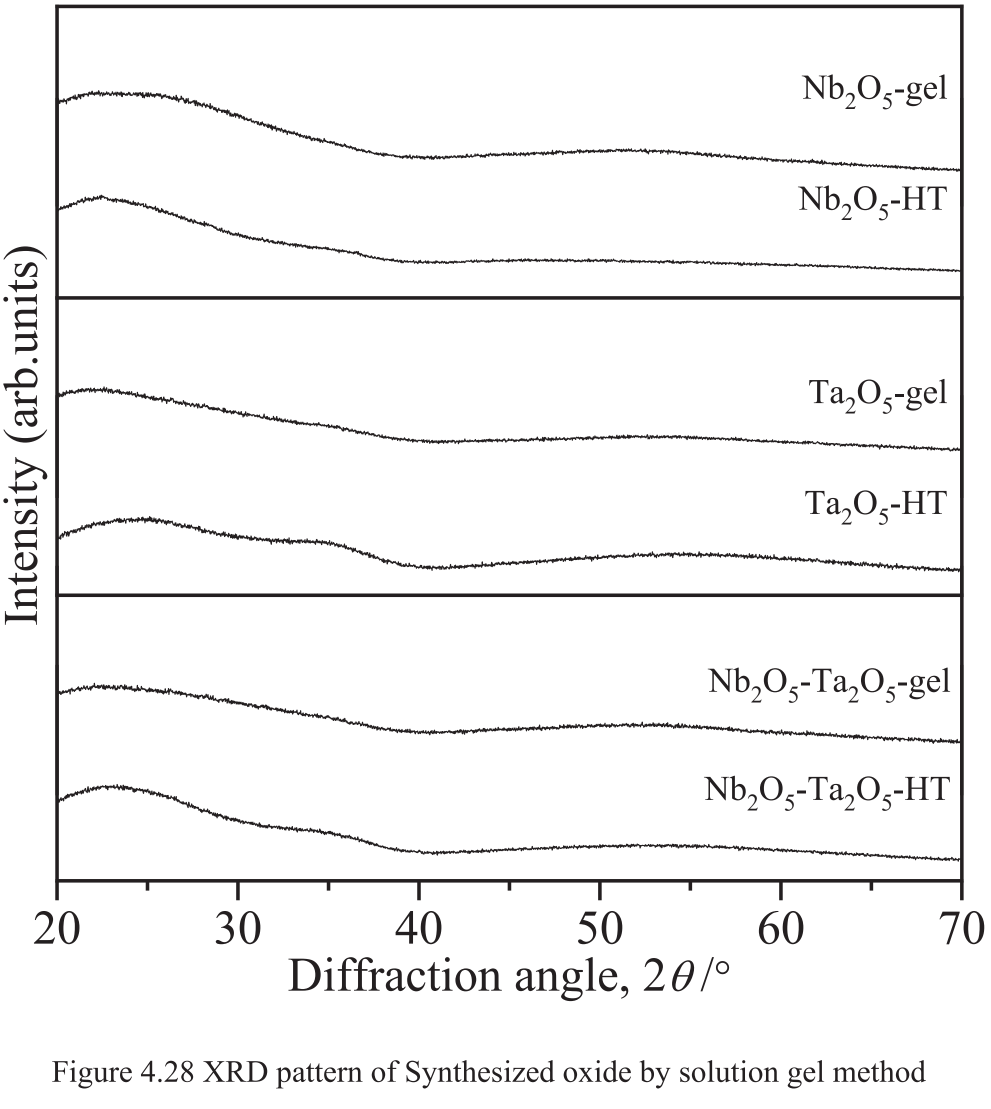

Figure 4.28 XRD pattern of Synthesized oxide by solution gel method

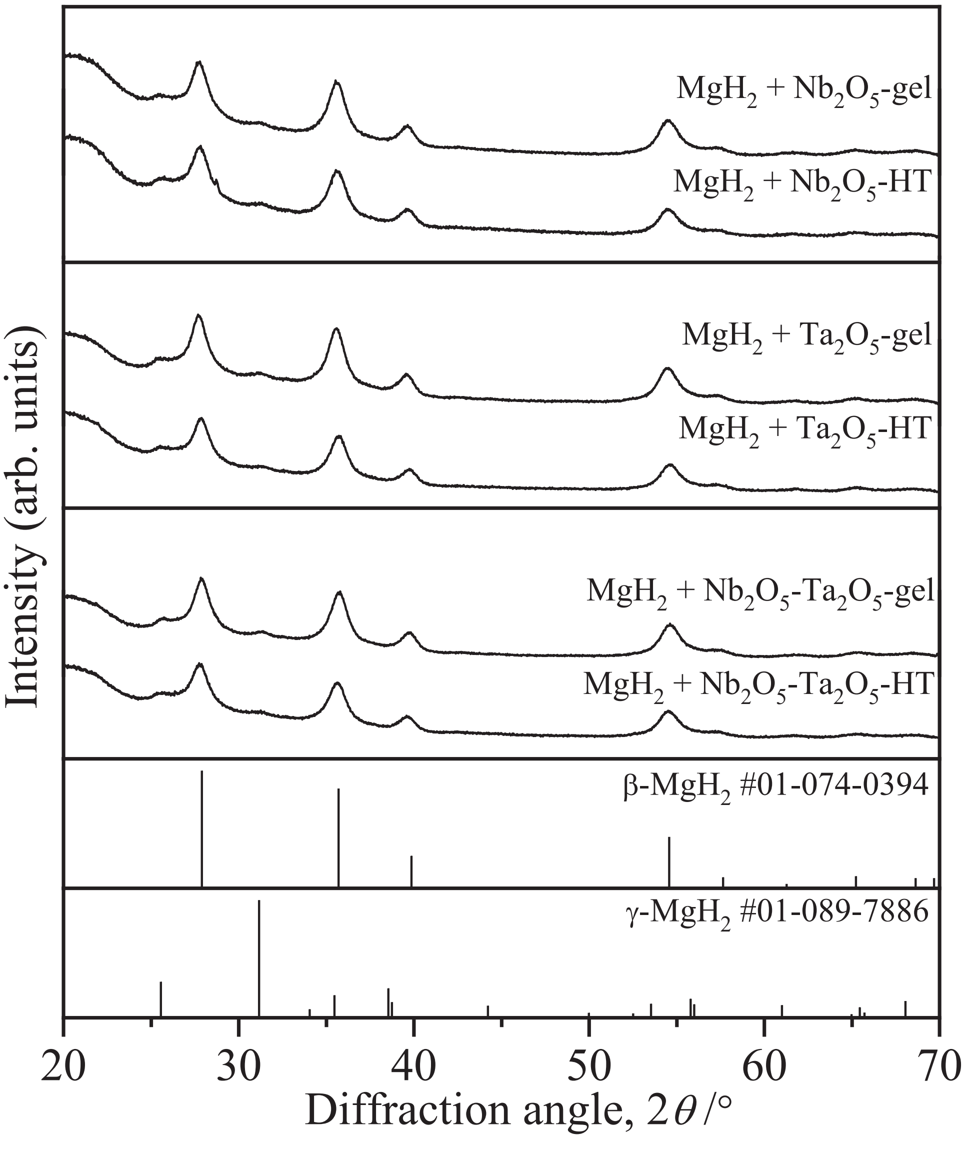

Figure 4.29 XRD patterns of the MgH$_2$ samples with oxide additives.

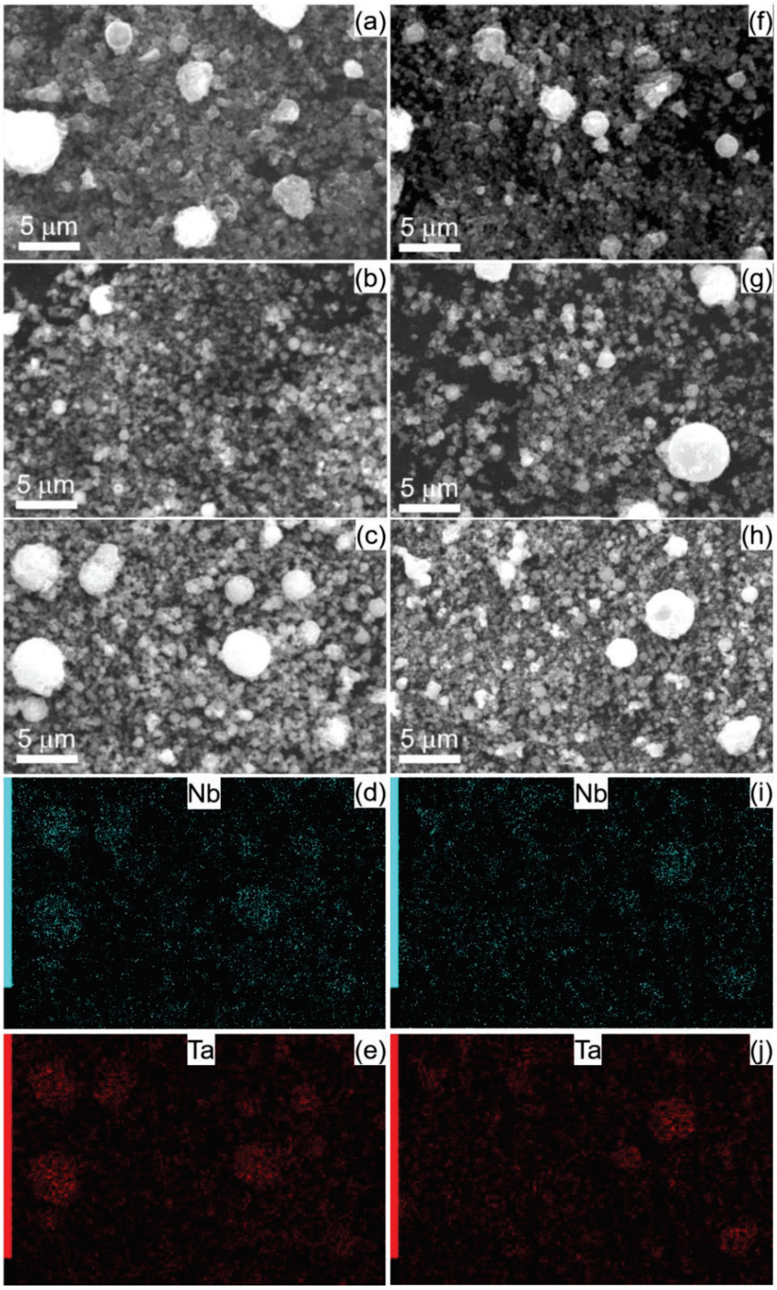

Figure 4.30 SEM images of (a) Nb_2O_5-gel, (b) Ta_2O_5-gel, (c) Nb_2O_5-Ta_2O_5-gel, EDS mapping of (d) Nb and (e) Ta for Nb_2O_5-Ta_2O_5-gel, SEM images of (f) Nb_2O_5-HT, (g) Ta_2O_5-HT, (h) Nb_2O_5-Ta_2O_5-HT, EDS mapping of (i) Nb and (j) Ta for Nb_2O_5-Ta_2O_5-HT

Figure 4.30 (a-c) and (f-h) show the SEM image of all the oxide samples. The mixed states of small and agglomerated particles are observed in all the oxide samples. All the particles are approximately spherical, and there was a random particle size distribution. The gel samples and heat-treated samples have approximately the same kind of images by particle size, agglomeration, and distribution; there was no such big difference among all the oxides. Figure 4.30 (d, e) and (i, j) show the SEM-EDS images of Nb_2O_5-Ta_2O_5-gel and Nb_2O_5-Ta_2O_5-HT. The molar ratio obtained by estimation using the EDS results was approximately 1: 1, consistent with the initial stoichiometric ratio of Nb_2O_5 and Ta_2O_5 (1: 1). It was clarified that Nb and Ta atoms were homogeneously distributed without particle dependence, suggesting that both fine and agglomerated particles are composed of Nb and Ta mixture. The above structural properties show that the prepared oxides possess a similar structure and morphology.

4.3.2 Hydrogen desorption properties of MgH_2 with gel oxides

The kinetics of hydrogen desorption of catalyzed MgH_2 have been studied in the TG-DTA measurements at the constant heating rate of 5 °C/min, and the result is presented in Figure 4.31. Here, XRD patterns of all the samples after the ball-milling shows no diffraction peaks corresponding to by-products except for MgH_2, as shown in Figure 4.29. The hydrogen desorption took place by the following reaction,

$$MgH_2 \leftrightarrow Mg+H_2 \qquad (34)$$

Here, it was confirmed by XRD measurements that the MgH_2 phases were changed entirely to Mg after the TG measurements, as shown in Figure 4.32. The hydrogen desorption peak temperatures for MgH_2+Nb_2O_5-gel and -HT were least and about 225 °C, on the other hand, those for MgH_2+Ta_2O_5-gel and -HT were the highest and about 255 °C. For the hydrogen desorption reaction, the catalytic effects of the gel and heat-treated oxides are almost the same.

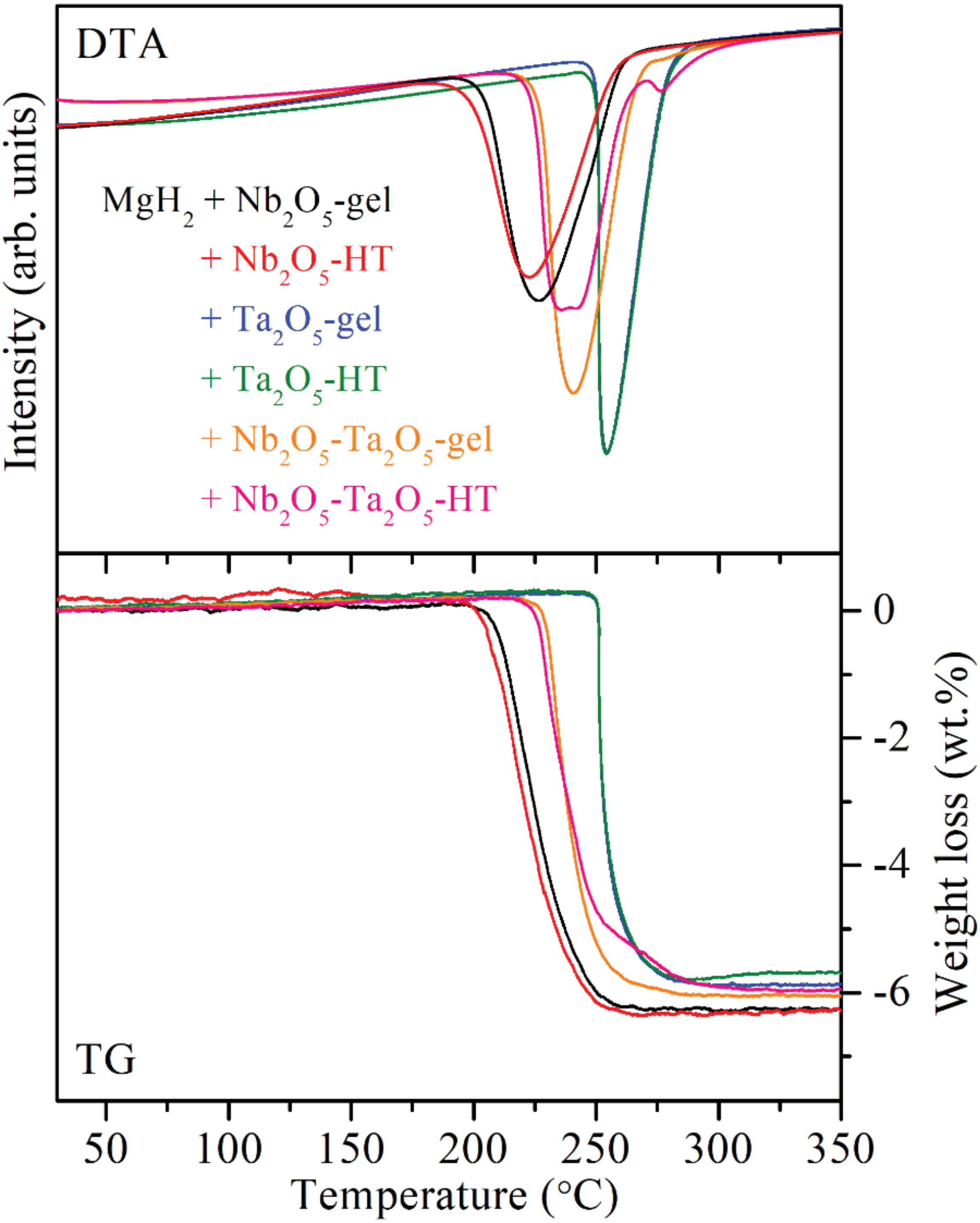

Figure 4.31 TG-DTA results for hydrogen desorption of MgH_2 with the prepared oxides

Here, although the hydrogen desorption temperature of MgH_2+Nb_2O_5-HT is slightly lower than that of MgH_2+Nb_2O_5-gel, the difference between peak temperatures is within 5 °C. It is essentially difficult to discuss the tiny difference for the ball-milled samples in thermally activated conditions. The hydrogen desorption profiles of MgH_2+Nb_2O_5 are broader than those of Ta oxides, suggesting that the ball-milling conditions are not optimized to obtain the best catalysis [4-8]. In the case of mixtures, the catalytic effects are almost middle between those of Nb and Ta oxide themselves. As described in the experimental part, the molar amount of Nb_2O_5 in MgH_2+Nb_2O_5-Ta_2O_5 is the half value of MgH_2+Nb_2O_5 because the total amount is fixed to be 1 mol% for MgH_2. Thus, the catalytic effects of the mixture might be explained by the Nb amount in the samples. As another possibility, it is considered that both oxides interact with each other and form a different catalytic state. Suppose each oxide in the mixture independently produces the catalytic active sites. In that case, the DTA profile is expected to show two hydrogen desorption peaks, which are observed around 220 and 250 °C due to the Nb and Ta oxide effects, respectively. Two peak hydrogen desorption profiles were reported for the MgH_2 with different active sites [4-8]. However, this work observed the single hydrogen desorption peak for the MgH_2 with Nb_2O_5-Ta_2O_5 samples. Thus, although the highly synergetic effects to enhance the catalysis of these oxides were not found. Unfortunately, it is possible that an interaction between Nb and Ta exists and slightly improves the catalytic effects of Ta_2O_5. Among those oxides, Nb2O5-Ta2O5-HT showed the multi-peaks profile, indicating that the catalytic states were not homogeneous. The difference of weight loss observed in the TG results for Nb_2O_5, Ta_2O_5, and Nb_2O_5-Ta_2O_5 would be explained by the weight difference between Nb and Ta. Interestingly, the catalytic effects of Nb_2O_5 gel with and without the heat treatment are comparable to those of previously reported MgH_2 with excellent performance prepared by the ball-milling for 20 h [4-8-9,11]. Thus, the Nb_2O_5 synthesized in this work can be converted to the highly active states even by the ball-milling for only 2 h.

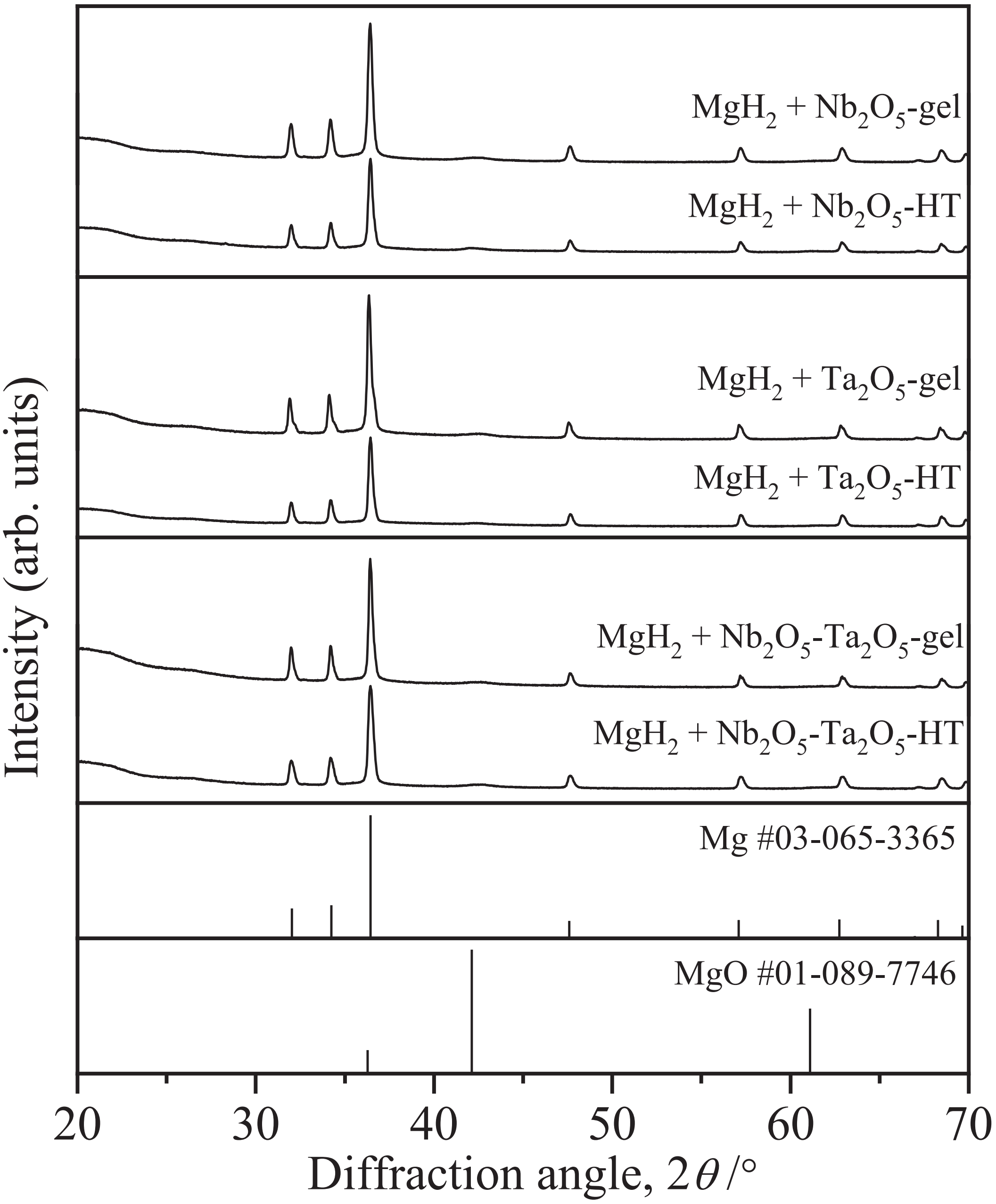

Figure 4.32 XRD patterns of the MgH$_2$ samples with oxide additives after the dehydrogenation.

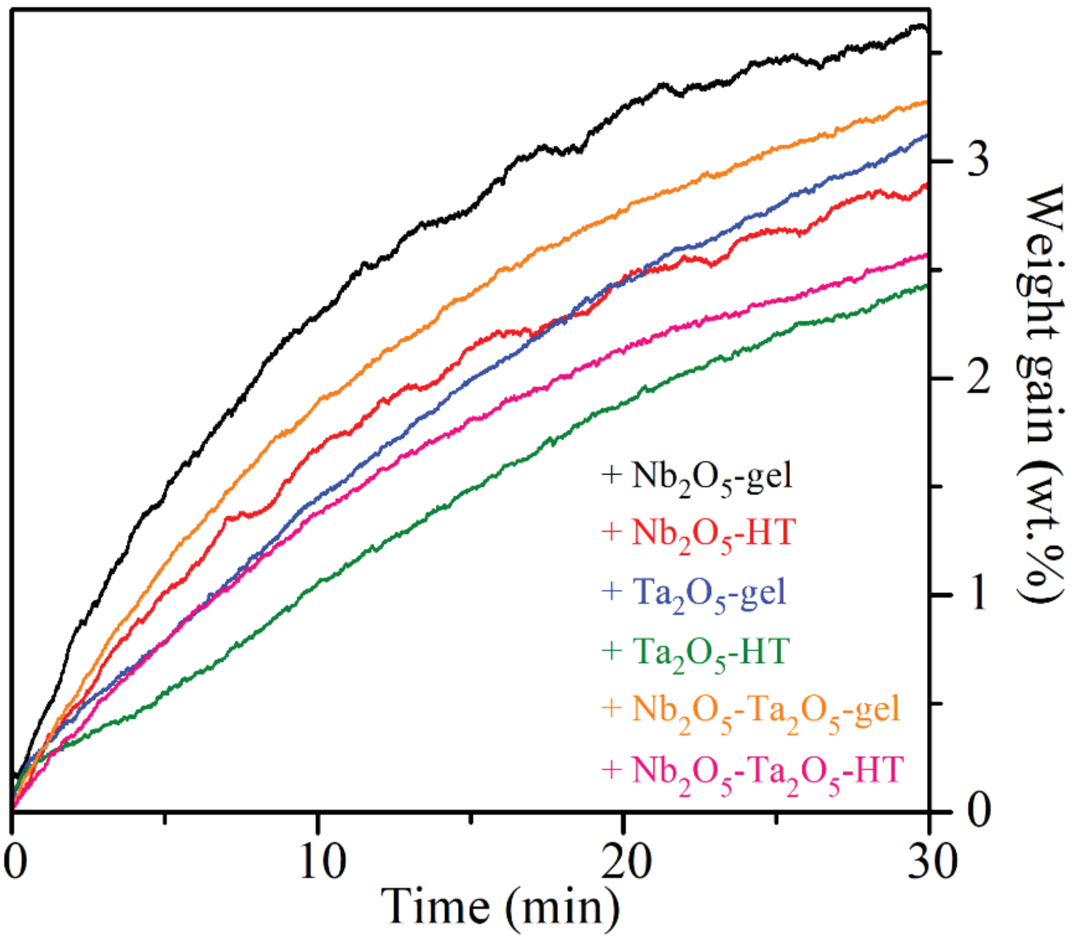

Figure 4.33 TG results for the hydrogen absorption of Mg with the prepared oxides

Figure 4.33 shows the isothermal hydrogen absorption profile performed at 40 °C under 0.1 MPa for all the catalyzed dehydrogenated samples. The starting point of experimental data was determined as the switching time of carrier gas from Ar to H_2. The hydrogen absorption reaction proceeded for all the samples, although the pristine Mg required thermal activation [4-9]. Among all the samples, the MgH_2 with Nb_2O_5-gel showed the highest hydrogen absorption rate, and the catalysis was better in order of Nb_2O_5 > Nb_2O_5-Ta_2O_5 mixtures > Ta_2O_5. The obtained tendency is the same as that of the hydrogen desorption experiments. Here, the formation of the MgH_2 phase and remaining Mg phase with the reasonable amount corresponding to the TG results were confirmed by XRD measurements as shown in Figure 4.44. The difference of catalysis for the hydrogen absorption process between the samples is significant compared with those observed in the desorption process because the hydrogen desorption reactions of MgH_2 are affected by the combined effects of the catalysts and thermal activation from the thermodynamic requirement. The gel oxides for all the series revealed were higher catalysis than the heat-treated oxides, indicating that the special reason exists for the gel oxide to be converted into a further activated state.

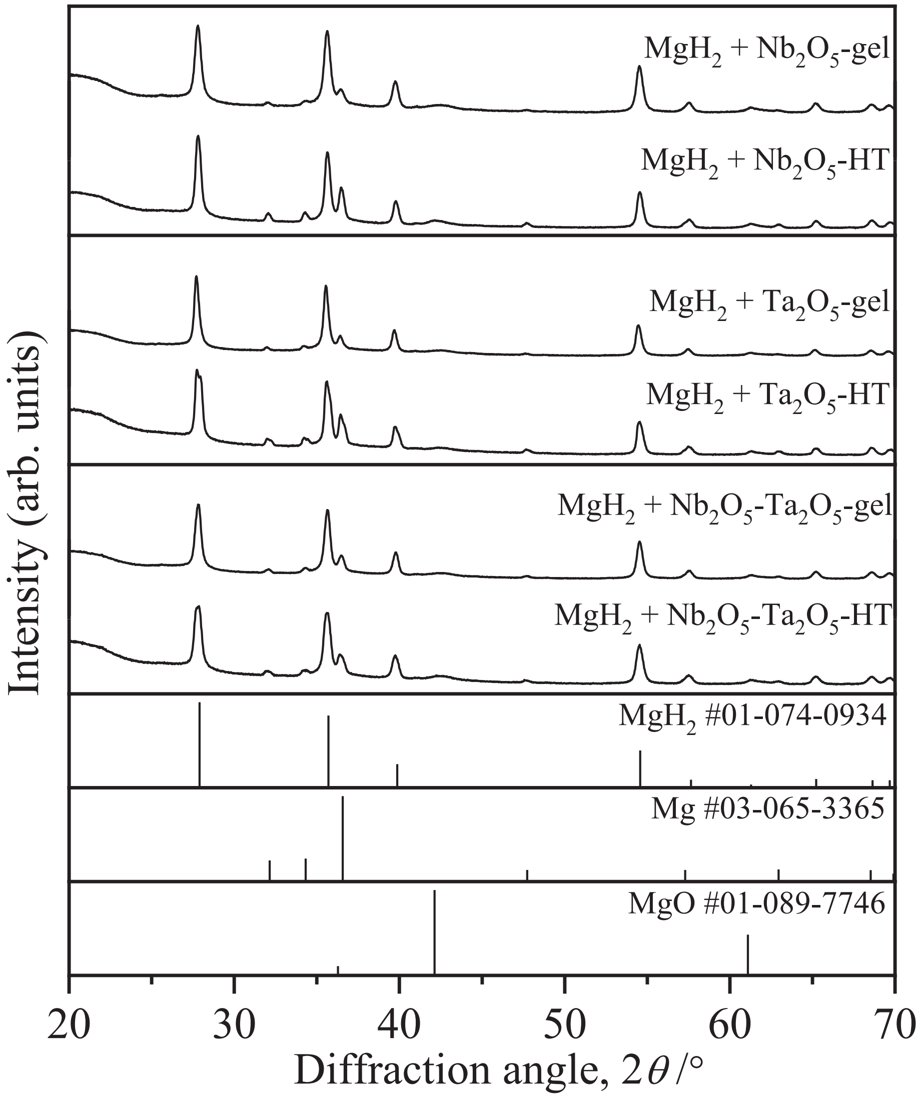

Figure 4.34 XRD patterns of the MgH_2 samples with oxide additives after the hydrogenation.

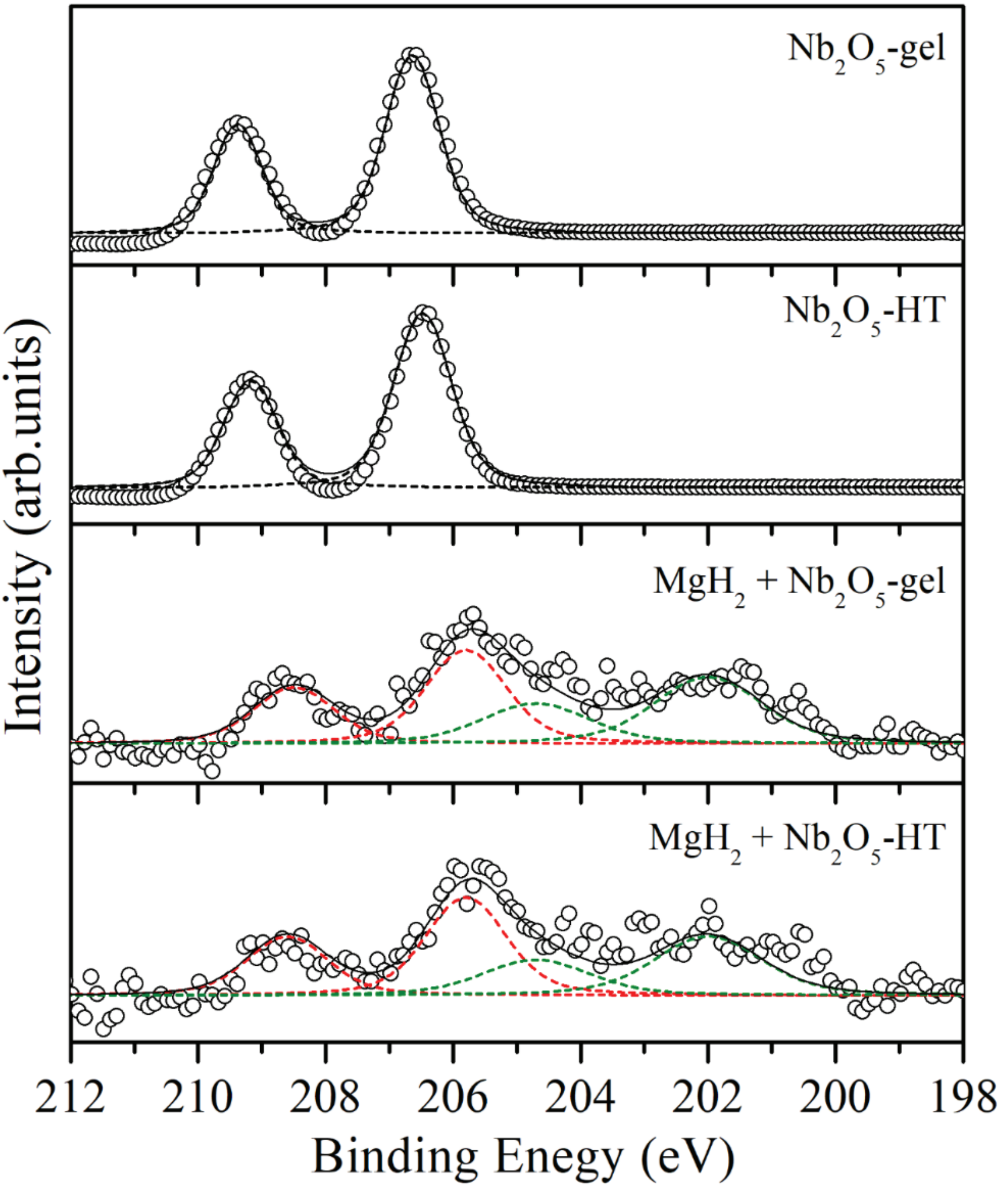

Figure 4.35 XPS spectra of Nb 3d for Nb_2O_5-gel, Nb_2O_5-HT, MgH_2+Nb_2O_5-gel and MgH_2+Nb_2O_5-HT. solid line: summation of fitting curves, broken line: fitting curves of Nb^{5+} (black), Nb^{4+} (red), and Nb^0 (green).

4.3.3 Chemical states of gel oxides

The XPS analysis was carried out for the Nb_2O_5 series as a represented system to understand catalytic active states, which shows higher catalytic effects among the evaluated oxides in this work. The XPS spectra of the samples are shown in Figure 4.35. The peaks of Nb 3d were examined to know the variation of chemical state by the ball-milling process with MgH_2. The Nb_2O_5-gel and Nb_2O_5-HT oxides were completely assigned to Nb^{5+} in their pristine form and then reduced to lower valence states after the ball-milling. The XPS spectra were expressed by fitting curves corresponding to Nb^{4+} and Nb^0 states, where the reduction of Nb during the ball-milling with MgH_2 is a similar phenomenon to the previous reports [4-7,10]. The peak area ratio of Nb^0/Nb^{4+} for $MgH_2+Nb_2O_5$-gel and $MgH_2+Nb_2O_5$-HT was estimated to be about 0.95 and 0.80, respectively, suggesting that the Nb_2O_5-gel without heat treatment is easily reduced compared with another one. Previous work reported that the more reduced state of Nb is more active as the catalyst and the catalytic activity of Nb^{4+} is not high [4-12]. In addition, Shirasu et al. reported that the multivalence state of transition metal is important for the catalytic effects for the reaction with H_2 in the case of Vanadium membrane [4-14]. On the analogy of this report, it is possible that the balance of existing valence states of Nb is effective to obtain the highly active state as the catalyst. It is clarified from the above results that reduction states are important to obtain the high catalysis on Nb oxide for the hydrogen absorption and desorption reaction of Mg.

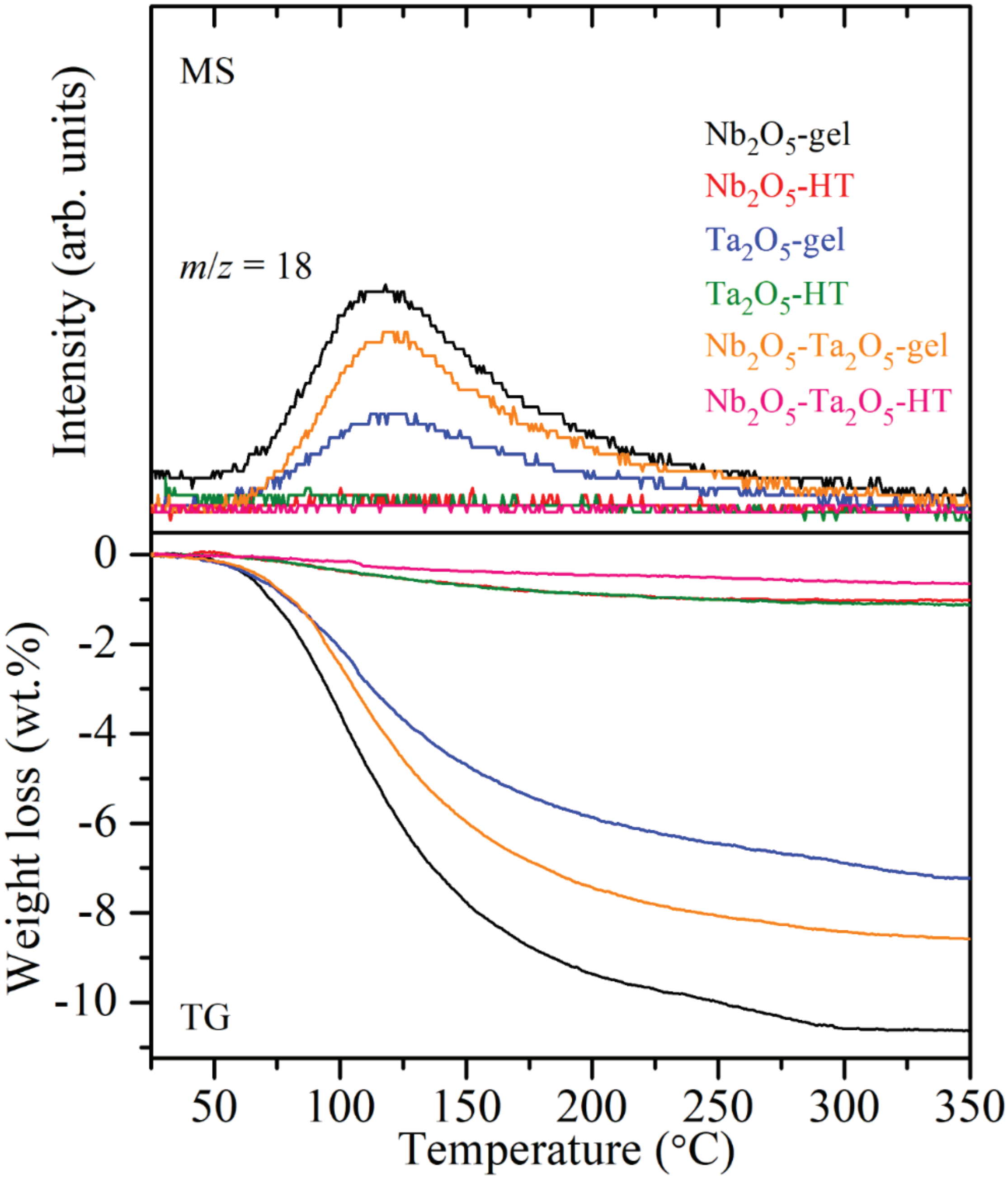

Figure 4.36 TG-MS results of the prepared oxides

4.3.4 H_2O desorption analysis of gel oxides

To understand the phenomena, thermal analyses of oxides were performed. Figure 4.36 is TG-MS profiles under Ar flow of the as-synthesized oxides. All the gel oxides emitted water (m/z = 18) in a wide temperature region from 50 to 300 °C, and the water emission was negligible after the heat treatment. The results suggest that only the drying process at 50 °C is not enough to eliminate the –OH groups included in the sample during the synthesis process by the sol-gel method. The gel oxides contain the –OH groups as a bridge-like role in the network of Nb and O atoms considering the synthesis process, namely it would be the precursor of Nb_2O_5 [4-15-16]. During the heat treatment, the –OH groups disappear by releasing as H_2O to form stable Nb and O bonds. Therefore, the Nb_2O_5-gel as intermediate is metastable state and easier form the reduced state, which is catalytic active for the reactions of Mg. By using the metastable Nb_2O_5-gel prepared by the simple sol-gel method without any heat treatments, the highly active Mg as hydrogen storage materials can be synthesized under milder conditions such as the only 2 h ball-milling than those of previous ones.

4.3.5 Stability of gel oxides compared with ternary oxide

In 4.2 study on catalysis tuning of oxides by synthesis of ternary oxide, we performed the catalytic tuning of MgH_2 using ternary oxide synthesized by ball milling followed by heat treatment. The synthesis itself took around 12h ball milling followed by 12h heat treatment at 1000 °C for around 12h respectively. When we performed the structural analysis of ternary oxide, we found some different hydrogen desorption peak temperatures compared to individual oxide. On the other hand, in 4.3 Study on synthesis technique of highly activated Mg, the same catalytic tuning is obtained using Nb_2O_5+Ta_2O_5 (gel and HT) mixed oxide prepared by solution gel method. In this case, also we observed some different dehydrogenation peak temperatures compared to individual oxide Nb_2O_5 and Ta_2O_5. The synthesis of ternary oxide using the ball milling method followed by heat treatment is a quite complicated process as well as expensive process, it needs more than one day to synthesize, whereas the solution gel process is quite easy to synthesize using just mixing, ultrasonication and heating.

4.4 Study on thermodynamic modification of MgH_2 using CaH_2

The hydrogen absorption and desorption reactions of Mg-MgH_2 and Ca-CaH_2 are given below:

$$MgH_2 \leftrightarrow Mg + H_2 \quad (34)$$

$$CaH_2 \leftrightarrow Ca + H_2 \quad (35)$$

The temperature required for the above reactions as calculated using HSC Chemistry 6.0 date base (Outotec, Oberursel, Germany) was found to be 290 ºC for reaction (34) and more than 1000 ºC for reaction (35) under 0.1 MPa hydrogen pressure. The hydrogen absorption-desorption temperature of the reaction (35) could be lowered by changing the experimental conditions such as hydrogen absorption at high hydrogen pressure (> 0.1Mpa) and hydrogen desorption under vacuum/ inert gas flow conditions. The hydrogen absorption desorption of the MgH_2-CaH_2 composite could be much lower if they can form intermetallic. The addition of a catalyst could also ease the hydrogen absorption desorption temperature.

4.4.1 Structural properties of MgH_2-CaH_2 composite

The SEM-EDS analysis of ball-milled MgH_2-CaH_2-$ZrCl_4$ composite is presented in Figure 4.37 (a-d). The scanning electron microscopic analysis indicates the homogeneous particle distribution of submicron size. However, these particles are appearing to be in agglomerated form. Spatial elemental distribution has also been present in the same figure. The homogeneous distribution of Zr indicates that proper mixing during ball milling occurs. The uniform distribution of catalyst seems to be favorable to improve the kinetics of hydrogenation-dehydrogenation of the composites.

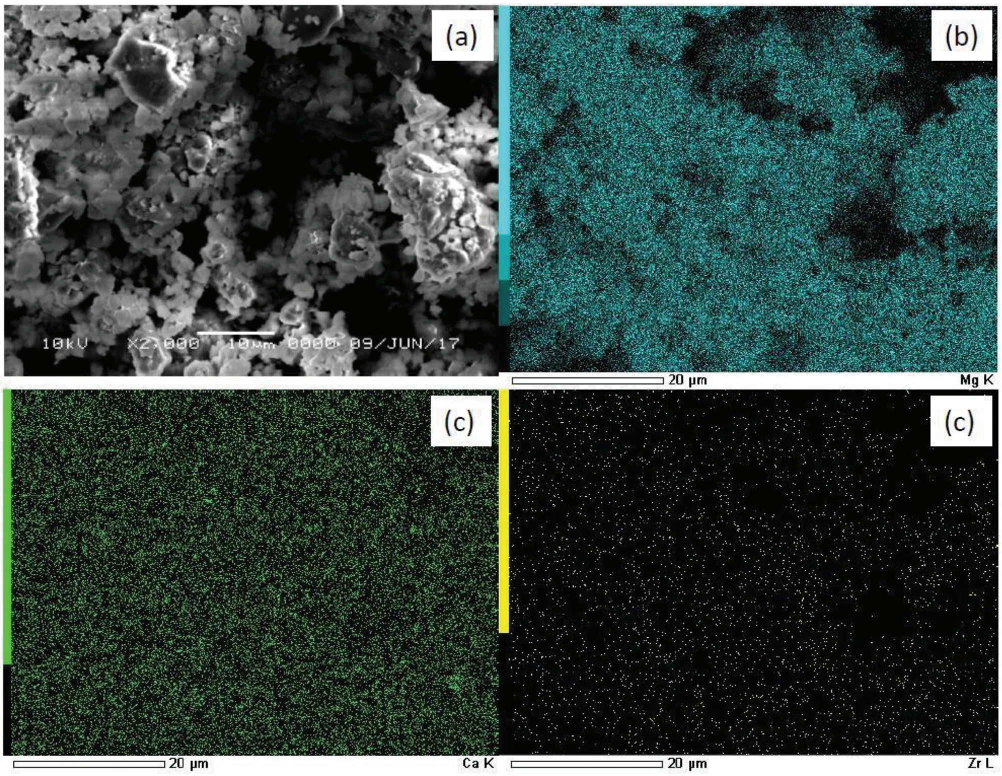

Figure 4.37 SEM-EDS analysis of the Ca-Mg-H_2 sample with catalyst. The figure shows the homogeneous distribution of the catalyst throughout the samples.

The phase changes and the evolution of the new phase during ball milling of MgH_2-CaH_2-$ZrCl_4$ composite were analyzed by XRD. The XRD result is presented in Figure 4.38 a-c. The ball-milled sample of MgH_2-CaH_2-$ZrCl_4$ composite has shown the retention of crystallinity even after ball milling. The presence of CaH_2 and MgH_2 indicated no interaction during the ball milling has happened. The result is obvious as the ball milling was done under the hydrogen atmosphere to prevent dehydrogenation during ball milling.

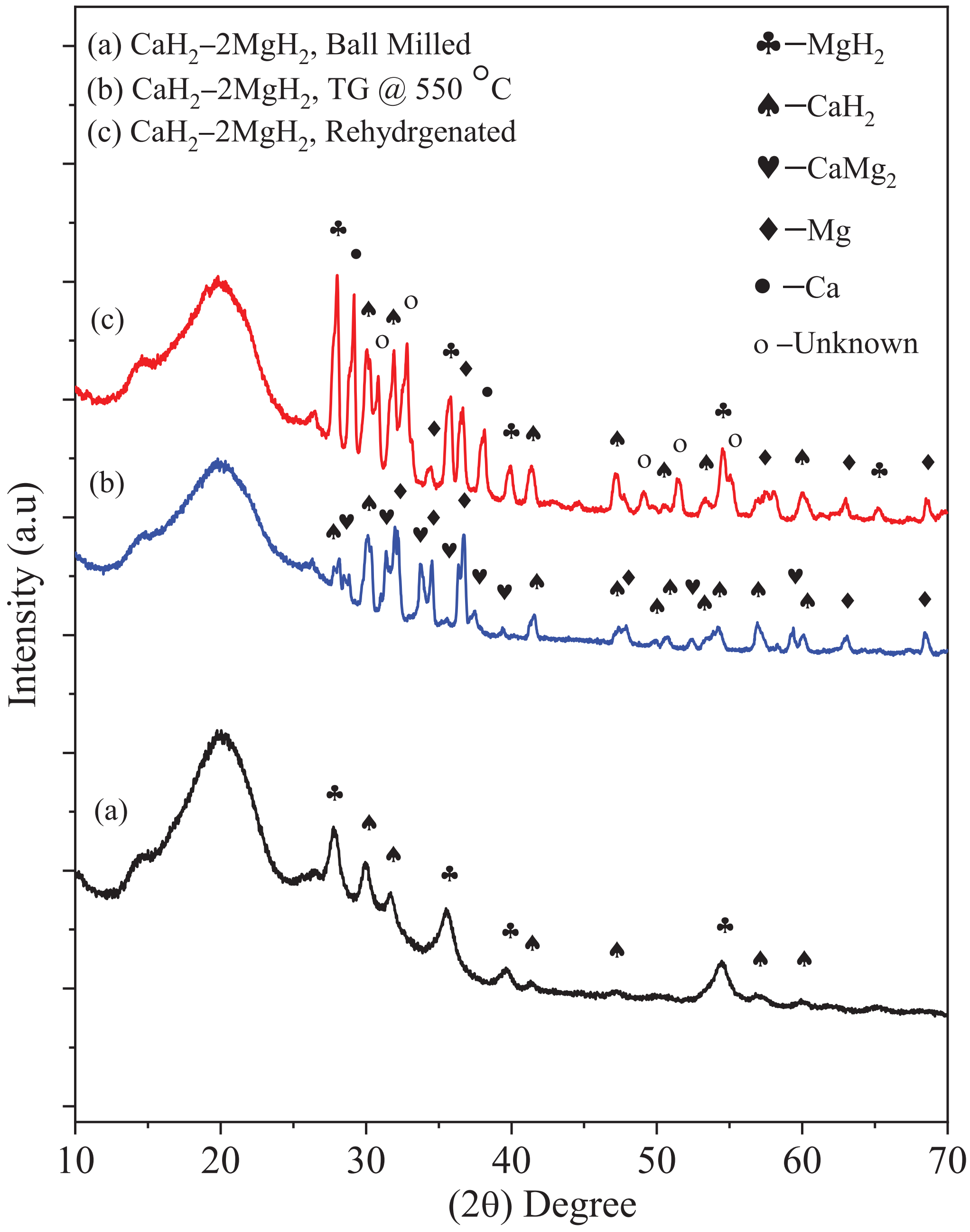

Figure 4.38 XRD analysis of the samples (a) ball-milled (b) Dehydrogenated CaH_2-MgH_2 in a TG-MS system up to 550 °C (c) Re-hydrogenated product of the sample.

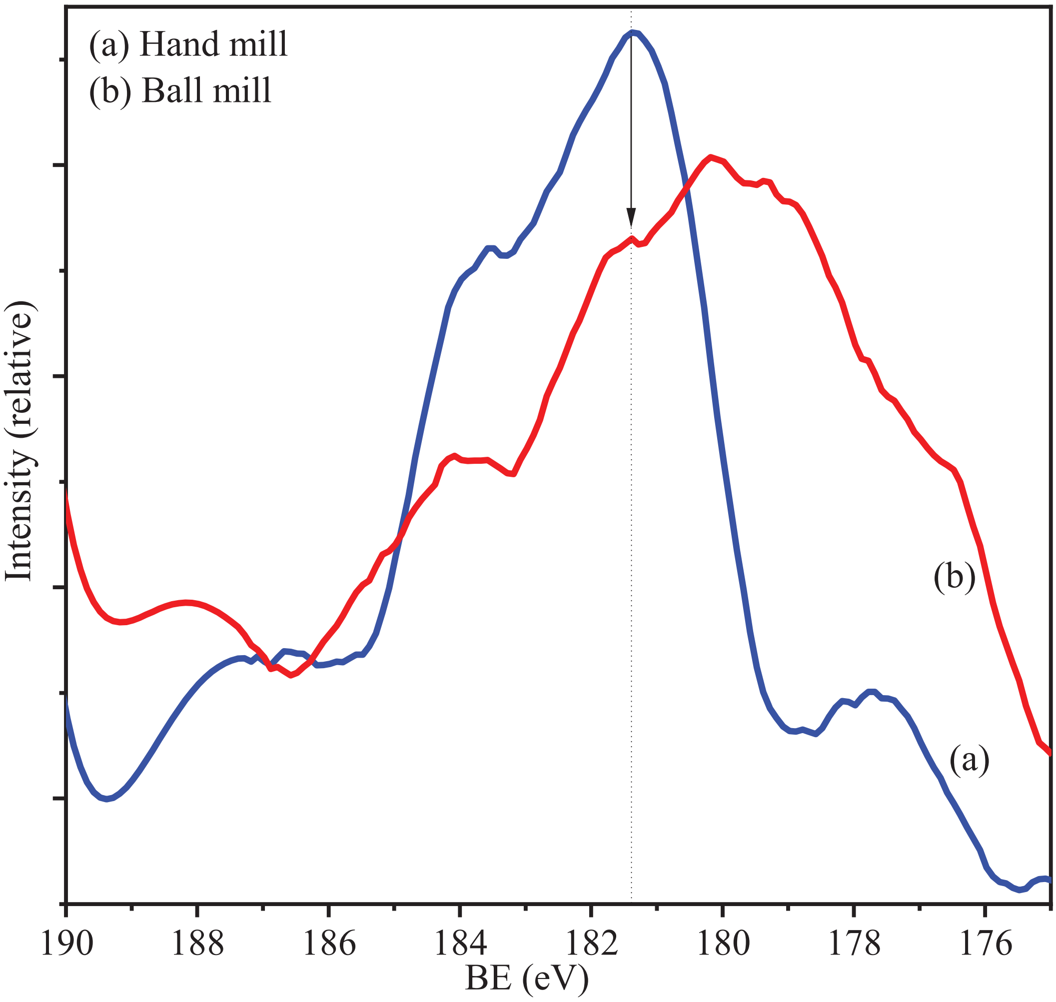

Figure 4.39 XPS analysis of the chemical state of the catalyst after ball milling with Ca-Mg-H_2 samples. A marginal peak shift indicates that the $ZrCl_4$ was reduced to nano Zr metal during ball milling.

The changes in the chemical states of the catalyst ($ZrCl_4$) during ball milling have been analyzed using XPS. The results were compared with the hand-milled MgH_2-CaH_2-$ZrCl_4$ samples as shown in Figure 4.39. The XPS of pristine $ZrCl_4$ under similar ball milling conditions reported somewhere else [20] has been taken as a reference for the pure $ZrCl_4$ sample. The binding energies peak of the Zr3d curve of pure ball-milled ZrCl4 was reported at 185.04 and 182.86 eV, respectively, indicating

Zr^{4+} oxidation state with marginal peaks shift [21]. In the case of MgH_2-CaH_2-$ZrCl_4$, the binding energy peaks of Zr3d curves were found to be at 184.28, 181.89, and 178.30 eV as illustrated in Figure 4.39 a-b. The peaks at 184.28 and 178.30 could be the first and second peaks of Zr^{3+} and Zr^0, respectively [21]. Very similar XPS results were obtained for hand-milled MgH_2-CaH_2-$ZrCl_4$. The XPS analysis reveals marginal peaks shift of Zr^{3+} and Zr^0 towards the lower energy side. The peak shift in the case of $ZrCl_4$ could be possible if $ZrCl_4$ is electrochemically interacting with MgH_2, and as consequence, the 3d electron is in the diffused state. On the other hand, the peak shift of Zr^0 could be due to the doping of zirconium over the MgH_2-CaH_2-$ZrCl_4$ sub-surface. Both the situations favor the de- and re-hydrogenation kinetics. Our labs already estimated experimentally that the Zr doped MgH_2 surface favors the de- & re-hydrogenation kinetics of MgH_2 [20]. In a conclusion, during ball milling and de-hydrogenation, $ZrCl_4$ seems to be reduced to metallic zirconium.

4.4.2 Hydrogen sorption properties of MgH_2-CaH_2 composite

In general, hydrogen desorption of MgH_2 and CaH_2 could be presented as per the equations (34) and (35) as shown below:

$$MgH_2 \leftrightarrow Mg + H_2 \qquad (34)$$

$$CaH_2 \leftrightarrow Ca + H_2 \qquad (35)$$

Figure 4.40 plotted using HSC Chemistry 6.0 date base and thermodynamics of hydrogen desorption can be understood using this. The reactions (34) occurred below 300 ºC, whereas reaction (35) occurred above 1000 ºC as discussed in the previous section. Simultaneous desorption of MgH_2-CaH_2 leads to the formation of Mg-Ca intermetallic or solid solution which could further reduce the decomposition temperature. A temperature higher than 500 ºC is not suitable for the practical application to extract the hydrogen from the MgH_2-CaH_2.

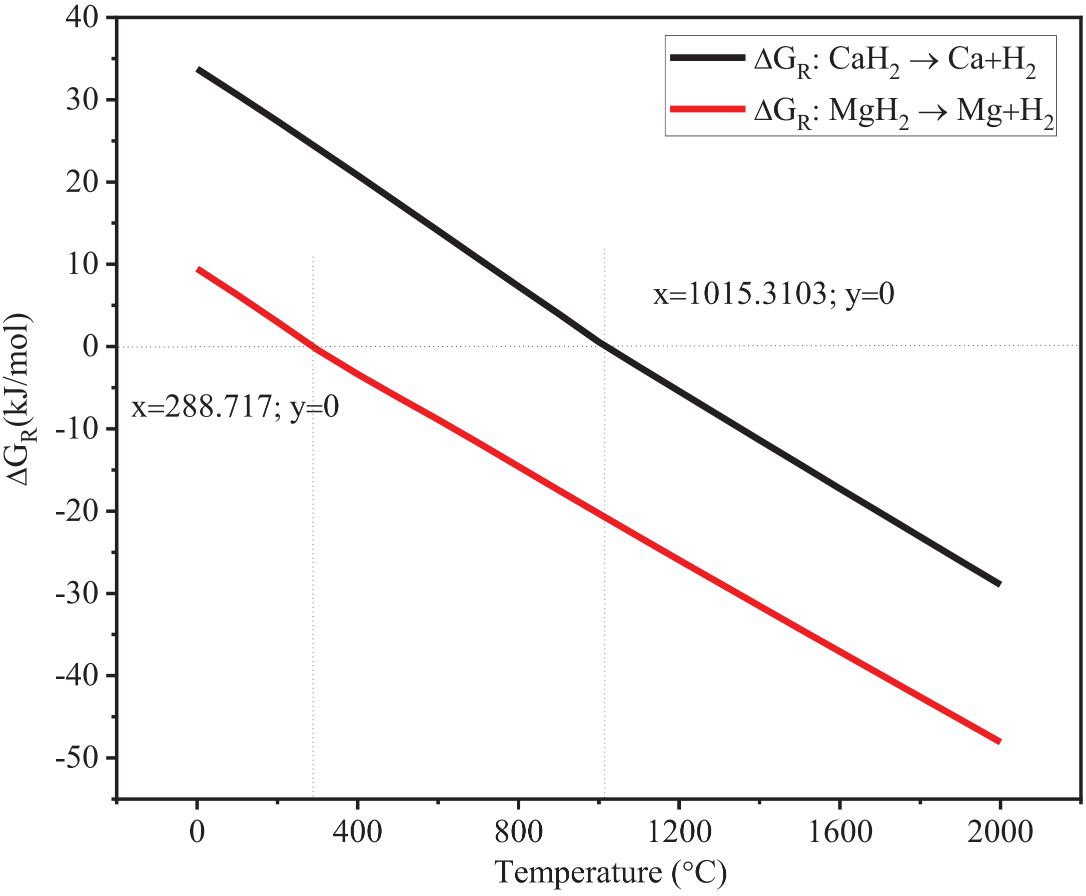

Figure 4.40 Thermodynamics calculation to understand the dehydrogenation temperature of MgH_2 and CaH_2.

A suitable catalyst could reduce the desorption temperature by modifying the reaction pathways. Zirconium tetrachloride ($ZrCl_4$) has appeared as a resilient catalyst for the deuterium-desorption reaction of many complex hydrides [22–24]. A similar effect could be expected for the MgH_2-CaH_2 system. Thus, the hydrogen desorption kinetics MgH_2-CaH_2 composite with and without catalyst has been investigated and compared. For all the explanations aMg-Ca stands for the composite without catalyst and cMg-Ca will be for the composite with catalyst.

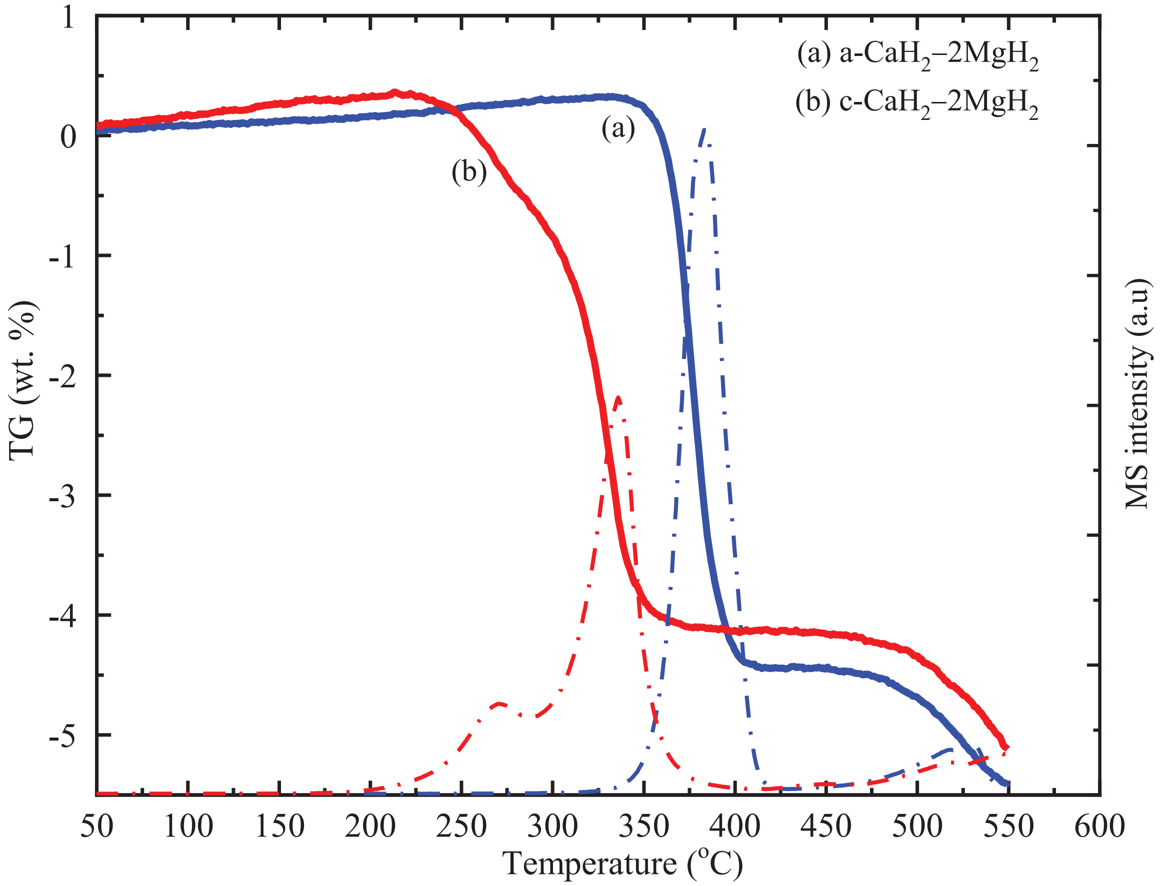

Figure 4.41 Thermogravimetric analysis of catalyzed and uncatalyzed CaH_2-MgH_2 up to 550 ºC to understand the catalytic effect on the dehydrogenation of the composite.

4.4.3 Thermogravimetric analysis of MgH_2-CaH_2 composite

Thermogravimetric-mass spectrometric (TG-MS) analysis of aMg-Ca hydrides and cMg-Ca hydrides were carried out at the heating rate of 5 ºC/min under the argon flow at the rate of 1.5 lit/hours and presented in Fig. 4.41a-b. The dehydrogenation of aMg-Ca as presented in Fig. 4.41a. The results indicate a substantial reduction of onset temperature of dehydrogenation of aMg-Ca hydrides as competed to theoretical estimated dehydrogenation temperature for individual components (MgH_2 and CaH_2). The dehydrogenated product has been analyzed by XRD and presented in Figure 4.38b. The dehydrogenation product has the formation of Mg-Ca intermetallic. The re-hydrogenation of the dehydrogenated aMg-Ca hydrides has been carried out at the 5 MPa hydrogen pressure and the XRD results are presented in Fig. 4.38c. The results indicate the separation of MgH_2 and CaH_2 with hydrogenation. The mechanism of hydrogenation dehydrogenation of aMg-Ca hydrides could be

$$2MgH_2+CaH_2 \longleftrightarrow Mg_2Ca+3H_2 \qquad (36)$$

The formation of Mg-Ca intermetallic during dehydrogenation lowered the dehydrogenation temperature. It has been found that the dehydrogenation temperature of aMg-Ca hydrides is still beyond 350 ºC. The temperature could be further reduced by the suitable catalyst. It has been reported earlier that $ZrCl_4$ is the better catalytic effect of the metal hydrogen system [20,23,24]. The dehydrogenation of MgH_2-CaH_2-$ZrCl_4$ (designated as cMg-Ca hydrides) has been carried out under identical experimental conditions in the same TG-MS unit. The results are presented in Fig 4.41b. The results indicated a substantial reduction in the onset temperature of the dehydrogenation process. The dehydrogenation temperature of 200 ºC indicates a resilient catalytic effect of $ZrCl_4$ on the MgH_2-CaH_2 system. The dehydrogenation process is like an uncatalyzed MgH_2-CaH_2 system.

4.4.4 Hydrogen desorption kinetics of MgH_2-CaH_2 composite

The dehydrogenation of the hydrogenated composites, aMg-Ca hydrides, and cMg-Ca hydrides has been studied to understand kinetics changes due to catalysts. The dehydrogenation experiments were conducted in the TG-MS unit at various heating rates (1, 2, 5, and 10 °C/min) under the flow of Ar gas at 18 liters/hours. The thermogravimetric analysis result is presented in Figure 4.42. The simultaneous MS analysis of hydrogen evolution of the same experiments is presented in Figure 4.42.

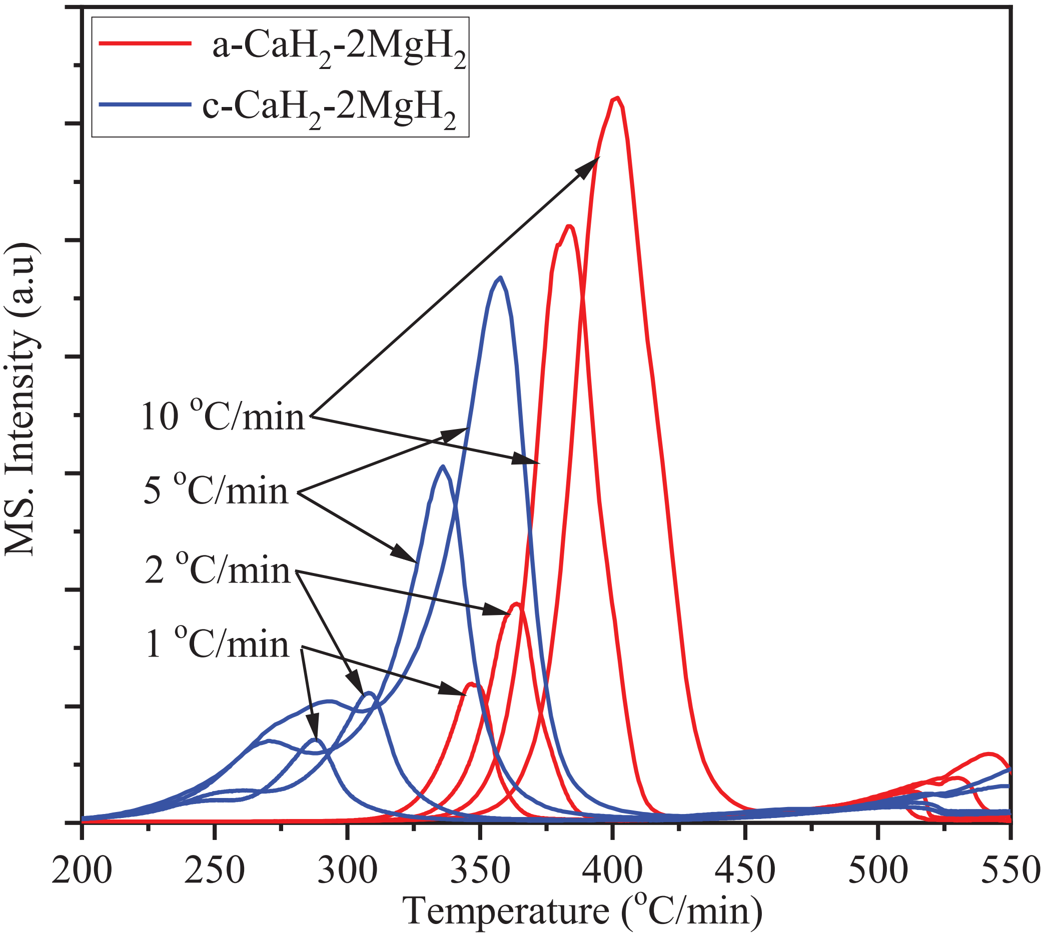

Figure 4.42 MS spectra of dehydrogenation of catalyzed and uncatalyzed CaH_2-MgH_2 to determine the Kissinger plot.

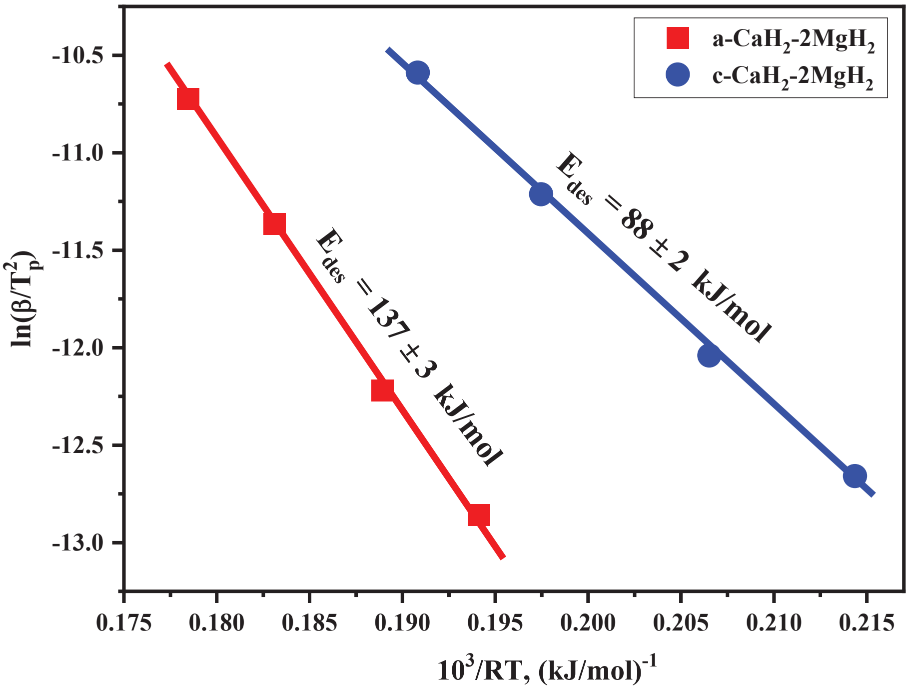

Figure 4.43 Kissinger plot of dehydrogenation of catalyzed and uncatalyzed CaH_2-MgH_2 to understand the change in activation energy due to catalyst

It is evident from figure 4.41 a-b that the catalyzed composite starts dehydrogenation even at 200 °C. The minimum dehydrogenation temperature of the uncatalyzed composite was found to be above 350 °C. The kinetic improvement of the dehydrogenation reaction of composite has been quantified by measuring the apparent activation energy.

$$\ln\frac{\beta}{T_p^2} = -\frac{E_a}{RT_p} + \ln\frac{RK_o}{E_a} \qquad (37)$$

The Kissinger equation (37) and peak temperatures (T_p) of H_2-MS analysis (m/z: 2) as shown in Figure 4.42 at a different heating rate, were used for the calculation. The linear plot of the Kissinger equation is presented in Figure 4.43. The apparent activation energy of dehydrogenation for uncatalyzed and catalyzed composites was calculated using the Kissinger equation. The activation energy of the uncatalyzed composites was found to be 137 ± 3 kJ/mol. Whereas the apparent activation energy of catalyzed composite was found to be 88 ± 2 kJ/mol.). A comparison for the activation energy of MgH_2, CaH_2, and MgH_2-CaH_2 composite has been made in Table 4.3 to understand the thermodynamic behavior of all these systems[20,25,26]. The remarkably reduced activation energy of dehydrogenation of catalyzed composite seems to be the possible reason for decreased dehydrogenation temperature.

Table 4.3 Activation energy of the MgH_2-CaH_2 composites and MgH_2, CaH_2 as a reference

Sample	Activation Energy for desorption
Uncatalyzed a-2MgH_2-CaH_2	E = 137±3 kJ/mol
Catalyzed c-2MgH_2-CaH_2	E = 88±2 kJ/mol
Uncatalyzed a-MgH_2	E = 143 kJ/mol
Catalyzed c-MgH_2	E = 92 kJ/mol
Uncatalyzed a-CaH_2	E = NA
Catalyzed c-CaH_2	E = NA

4.4.5 PCI analysis of MgH_2-CaH_2 composite

The thermodynamics of hydrogenation - dehydrogenation of the cMg-Ca composite have been studied by pressure-composition isotherm (PCT). The PCT curves were obtained at 350 ºC, 375 ºC, and 400 ºC respectively, and presented as an inset of Figure 4.44.

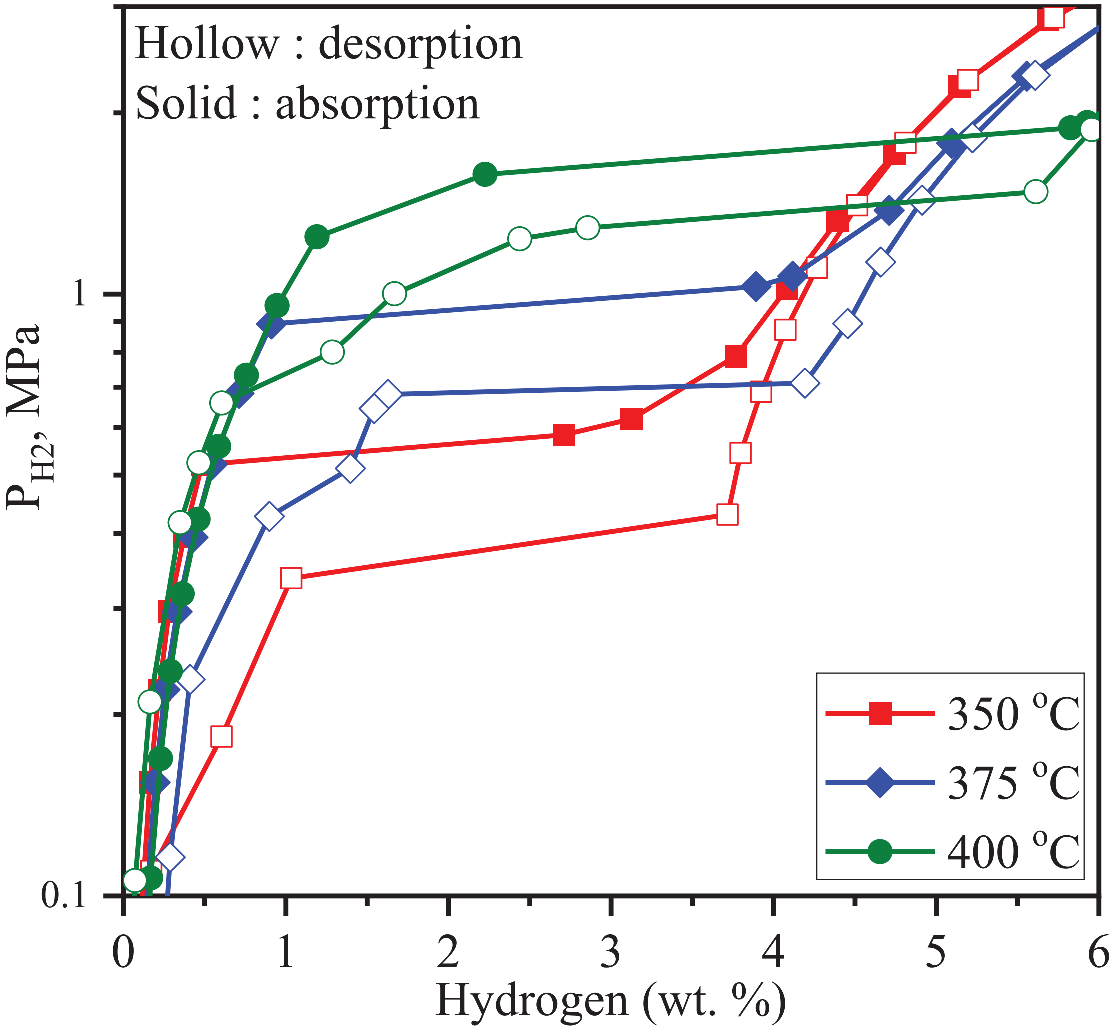

Figure 4.44 Pressure composition temperature plot of catalyzed MgH_2-CaH_2 composite

The mechanism of hydrogenation and dehydrogenation reaction in plateau region could be

$$2MgH_2 + CaH_2 \leftrightarrow Mg_2Ca + 3H_2 \qquad (36)$$

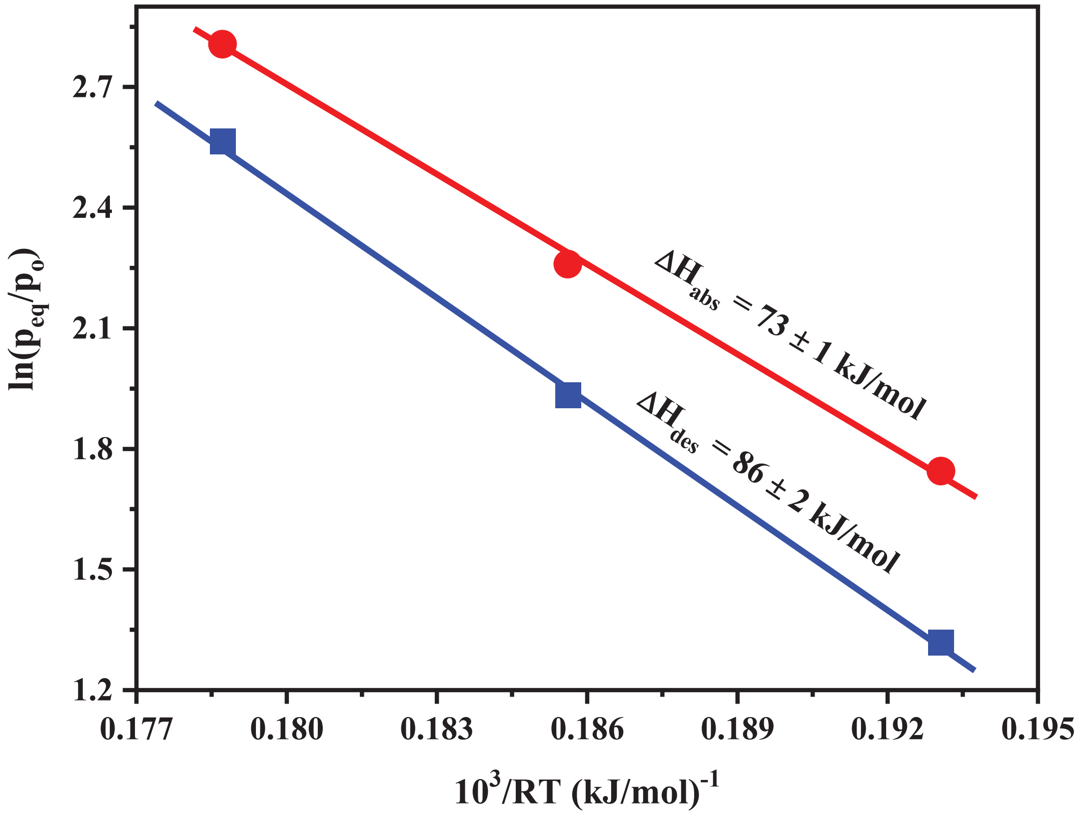

Figure 4.45 Van't Hoff plot of catalyzed MgH_2-CaH_2 composite obtained by pressure composition temperature (PCT) analysis.

The enthalpies of the hydrogenation-dehydrogenation reaction of the composite were calculated using equilibrium hydrogen pressure of PCT curves using Van't-Hoff equation (38))

$$\ln\frac{P_{eq}}{P_o} = \frac{\Delta Ho}{RT} - \frac{\Delta So}{R} \qquad (38)$$

Where P_{eq}: plateau pressure, P_o: standard pressure, ΔH^o: molar enthalpy, ΔS^o: molar entropy, R: universal gas constant, and T is the temperature in Kelvin. The hydrogenation enthalpy was found to be 73 ± 1 kJ/mol and the dehydrogenation enthalpy was found to be 86 ± 2 kJ/mol for catalyzed MgH_2-CaH_2 composite. A comparative study has been done using reaction enthalpy for both dehydrogenation and hydrogenation using previously reported theoretical and experimental values, summarised in Table 4.4 [20,25–27].

Table 4.4 Enthalpy change (ΔH) of dehydrogenation and rehydrogenation reactions for MgH_2-CaH_2 composites and MgH_2, CaH_2 as references

Sample	Enthalpy comparison for dehydrogenation	Enthalpy comparison for hydrogenation
Uncatalyzed a-$2MgH_2$-CaH_2	$\Delta H = 86\pm2$ kJ/mol	$\Delta H = 73\pm1$ kJ/mol
Catalyzed c-$2MgH_2$-CaH_2	$\Delta H = 86\pm2$ kJ/mol	$\Delta H = 73\pm1$ kJ/mol
Uncatalyzed a-MgH_2	$\Delta H = 77$ kJ/mol	$\Delta H = 74$ kJ/mol
Catalyzed c-MgH_2	$\Delta H = 77$ kJ/mol	$\Delta H = 74$ kJ/mol
Uncatalyzed a-CaH_2	$\Delta H = 181.5$ kJ/mol	ΔH = NA

Similar enthalpy has been investigated for uncatalyzed Mg-Ca composite and found to be similar. Thus it could be concluded that the $ZrCl_4$ is a resilient catalyst that merely altered the apparent activation energy whereas thermodynamics remains the same for the composite.

4.5 References

[4-1] O. Friedrichs, D. Martínez-Martínez, G. Guilera, JCS López, A. Fernández, J Phys Chem C, 2007; 111:10700–6.

[4-2] G. Barkhordarian, T. Klassen, R. Bormann, J Phys Chem B 2006; 110:11020–4.

[4-3] G. Barkhordarian, T. Klassen, R.U. Bormann, J Alloys Compd 2004; 364:242–6.

[4-4] G. Barkhordarian, T. Klassen, R. Bormann, Scr. Mater 2003; 49:213–7.

[4-5] T. Kimura, H. Miyaoka, N. Hanada, T. Ichikawa, J Japan Inst Met Mater, 2015; 79:107–11.

[4-6] S. Kumar, G.P. Tiwari, J Mater Sci, 2017:1–7.

[4-7] F. Friedrichs, F. Aguey-Zinsou, J.R.A. Fernández, J.C. Sánchez-López, A. Justo, T. Klassen, R. Bormann, and A. Fernández: Acta Mater. 54 (2006) 105-110.

[4-8] N. Hanada, T. Ichikawa and H. Fujii: J. Alloy. Compd. 404406, (2005), 716-719.

[4-9] T. Kimura, H. Miyaoka, T. Ichikawa and Y. Kojima: Int. J. Hydrogen Energy 38 (2013), 13728-13733.

[4-10] N. Hanada, T. Ichikawa, S. Isobe, T. Nakagawa, K. Tokoyoda, T. Honma, H. Fujii and Y. Kojima: J. Phys. Chem. C 113 (2009) 13450-13455.

[4-11] N. Hanada, T. Ichikawa, S. Hino and H. Fujii: J. Alloy. Compd. 420, (2006) 46-49.

[4-12] S. Isobe, K. Kudoh, S. Hino, K. Hara, N. Hashimoto, and S. Ohnuki: Appl. Phys. Lett. 107 (2015) 081602.

[4-13] D.D. Wagman, W.H. Evans, V.B. Parker, R.H. Schumm, Iva Halow, S. M. Bailey, K.L. Churney, R.L. Nuttall, Journal of Physical and Chemical Reference Data, 11, 1982, Supplement No. 2

[4-14] Y. Shirasu, T. Nambu, K. Omata, H. Yukawa and Y. Matsumoto: Mater. Trans. 60 (2019), 2174-2178.

[4-15] M. Ristić, S. Popović and S. Musić: Mater. Lett. 58 (2004) 2658-2663.

[4-16] K. Nakajima, Y. Baba, R. Noma, M. Kitano, J.N. Kondo, S. Hayashi and M. Hara: J. Am. Chem. Soc. 133 (2011) 4224-4227.

[4-17] H. Gi, K. Shinzato, R. Balgis, T. Ogi, M. Sadakane, Y. Wang, S. Isobe, H. Miyaoka and T. Ichikawa, ACS Omega, 2020, 5, 21906-21912.

[4-18] P. K. Singh, H. Gi, K. Shinzato, K. Katagiri, H. Miyaoka, T. Ichikawa, Y. Kojima, Materials Transactions, 62 (2), 284-289 (2021).

[4-19] K. Shinzato, H. Gi, T. Murayama, M. Sadakane, Y. Wang, S. Isobe, T. Ichikawa, and H. Miyaoka, ACS Omega, 2021, 6, 23564-23569.

[4-20] S. Kumar S, A. Jain A, S. Yamaguchi S, H. Miyaoka, T. Ichikawa, A. Mukherjee, Int J Hydrogen Energy 2017; 42:6152-9.

[4-21] NIST, https://srdata.nist.gov/xps/selEnergyType.aspx.

[4-22] S. Kumar, G.P. Tiwari, N. Krishnamurthy, Y. Kojima, J Nucl Mater, 2017; 492:183-8.

[4-23] S. Kumar, V. Kain, Y. Kojima, Int J Hydrogen Energy, 2017; 42:15299-307.

[4-24] S. Kumar, A Singh, P.K. Singh, H. Miyaoka, V. Kain, Y. Kojima, Int J Hydrogen Energy 2020; 45:14413-7.

[4-25] S.V. Alapati, J. Karl, D.S. Sholl, Phys Chem Chem Phys 2007:1438-52.

[4-26] M. Wang, W. Sun W, C. Sha, B. Hu, Y. Du, L. Sun L, J Phase Equil Diffus 2012; 33:89-96.

[4-27] J.J. Reed. J. Res.Digitizing, Natl Inst Stand Technol 2020;125.

5. Conclusion

I focus on the kinetic and thermodynamic modification of the Mg-H system. The results in this work are concluded as follows,

The catalytic behaviors of single phase of TiO_2, ZrO_2, HfO_2, V_2O_5, Nb_2O_5, Ta_2O_5, CrO_3, MoO_3, and WO_3 (Nb_2O_5 and its neighboring oxide) with the Mg-MgH_2 system were investigated. Finally, the samples are categorized into two group; group A: MgH_2 + TiO_2, MgH_2 + V_2O_5, MgH_2 + Nb_2O_5, MgH_2 + CrO_3, MgH_2 + ZrO_2, MgH_2 + MoO_3 (without initial oxide peaks) and group B: MgH_2 + HfO_2, MgH_2 + Ta_2O_5 and MgH_2 + WO_3 (with initial oxide peaks). The dispersion state expected from the XRD patterns is an important factor because almost the samples with no diffraction peaks of oxides showed high catalysis. On the other hand, the catalysis of MoO_3 cannot be explained by the dispersion state. The hydrogen desorption temperature for MgH_2 + TiO_2, MgH_2 + V_2O_5, MgH_2 + Nb_2O_5, MgH_2 + ZrO_2 and MgH_2+CrO_3, shifted around 200 °C compared to pristine MgH_2 (425 °C) categorized as Group A. The thermodynamics reduction route for each oxide was calculated and proposed using a possible equation. The thermodynamic estimation and XPS analyses clarified that the high catalytic activity was obtained when the intermediate oxidation states such as +2 and +3 can be formed. The study on effective factors of oxide catalysts for the Mg-H system reveals that the dispersion state of oxide is one of the important factors. Furthermore, the chemical state of oxide is also an important factor to realize a highly active state as catalysis, in which the intermediate oxidation state especially for +2 and +3 is responsible for the catalytic activity of oxides.

The low, as well as extremely high catalysis, was not suitable for practical application, former requires excess energy input and the latter is dangerous due to the high activity. The purpose to search the newest and best catalysts using tuning of catalysis of Mg-H system by single phase of ternary oxide formation using combining the different metal elements. Synthesis of ternary oxides ensued using single phases such as V_2O_5 (active) and Ta_2O_5 (inactive), likewise others. Catalytic tuning was achieved using the ternary oxides to control the catalysis as per our aim. The hydrogen desorption peak temperature for MgH_2 with synthesized $TaVO_5$ ternary oxide was found around 250 °C which is in the middle of MgH_2+V_2O_5 peak temperature 213 °C and Ta_2O_5 peak temperature 288 °C respectively. On the other hand, for Nb_9VO_{25} ternary oxide, the hydrogen desorption peak temperature for MgH_2 with synthesized Nb_9VO_{25} oxide was found around 250 °C which is comparatively higher compared to MgH_2+V_2O_5 peak temperature 220 °C and Nb_2O_5 peak temperature 225 °C, respectively. Similarly, for $Nb_{0.6}Cr_{0.4}O_2$ ternary oxide, the hydrogen desorption peak temperature for MgH_2 with synthesized $Nb_{0.6}Cr_{0.4}O_2$ oxide was found around 303 °C which is comparatively higher compared to MgH_2+Nb_2O_5 peak temperature 222 °C and MgH_2+CrO_3 peak temperature 206 °C respectively. Therefore, the synthesis of ternary oxide is useful to tune the catalysis of magnesium hydride.

In this work, various types of amorphous Nb and Ta oxides are synthesized by simple sol-gel methods. These oxides are dispersed on the MgH_2 surface by the ball-milling for 2 h, which is ten times shorter than that of the previous synthesis process using the ball-milling. All the oxides reveal catalysis for the hydrogen desorption and absorption reactions of Mg. Especially, the hydrogen absorption can proceed around room temperature, suggesting that the high activation of Mg can be achieved. The gel oxides include -OH groups, which would exist in the network between Nb and O, namely they are regarded as precursors of stable Nb_2O_5 state formed during the heat treatment at 500 °C. The metastable oxides are easily converted to the catalytic active state, which is a reduced state generated due to the mechanochemical reaction with MgH_2 during the ball-milling. Therefore, the gel oxides are recognized as a suitable precursor to produce the highly activated Mg by simple and mild conditions.

The purpose is to achieve the thermodynamic modification of MgH_2 using CaH_2 by composite formation. The thermodynamic properties of the $2MgH_2$-CaH_2 composite have been investigated with and without catalyst. The uniform distribution of catalyst pretended improvement in the kinetics of hydrogenation-dehydrogenation of the composites. Interestingly, the peak shift in the case of $ZrCl_4$ could be possible, if $ZrCl_4$ is electrochemically interacting with MgH_2 and as consequence, the 3d electron is in the diffused state. On the other hand, the peak shift of Zr^0 could be due to the doping of zirconium over the MgH_2-CaH_2-$ZrCl_4$ sub-surface. The dehydrogenated product has shown the formation of Mg_2Ca intermetallic which favored the hydrogenation - dehydrogenation process. Thermodynamic modification of MgH_2 was achieved by introducing CaH_2 in the ratio of 2:1 respectively by the formation of Mg_2Ca intermediate stage.

Acknowledge

It is a great honor for me to express the heartiest gratitude and thanks to my Ph.D. supervisor, Dr. Hiroki Miyaoka for kind guidance, support, enthusiastic interest, vital discussions, suggestions, and kind cooperation throughout the research work. Their timely help, constructive criticism, and conscientious effort made it possible to present this thesis. His cool and polite nature is a chapter for the coming generation and society.

I am also very much thankful to Prof. Takayuki Ichikawa for their valuable guidance, time, continuous support in conducting the experiments during my research work. His kind suggestions are fruitful for the in-depth knowledge of the research work.

A special thanks to my lovely Guru Prof. Sanjay Kumar (Senior Scientist, BARC, HBNI) who provided me with proper guidance and very much flexibility during my project work at BARC, Mumbai. He also taught me a lot of technical tricks and tips which are very useful in research. I am very much thankful and will always be for their love and for forcing me to learn more and more in life.

I am also very much thankful to Prof. Yoshitsugu Kojima for his continuous guidance, suggestions, kind help, and support throughout my research work. As a part of my research work, Dr. Yoshitsugu Kojima has provided me with this opportunity to work here in Japan at Hiroshima University. I am thankful and will always be for his kind love, support, and teaching.

I am sincerely obliged to Dr. Sanjib Majumdar (Prof. HBNI, Mumbai & Head, HTMS, MP & CED, BARC, Mumbai, India), Dr. Tammana S.R.Ch. Murthy (Senior Scientist, BARC, Mumbai), Dr. Bhaskar Paul (Senior Scientist, BARC, Mumbai) for their encouragement to learn and grow. I am sincerely obliged to and for his support in several ways, including opportunities to visit different facilities in BARC, Mumbai, India.

I am also very much thankful to Dr. Ankur Jain for his guidance during my Ph.D. work.

I also sincerely thank my colleague Dr. Keita Nakajima, Dr. Hiroki Uesato, Dr. Masakuni Yamaguchi for extending their help and technical support. I sincerely thank Mr. Hiroyuki Gi for his valuable cooperation and experimental support.

I am also thankful to Dr. Keita Shinzato, Dr. Fanquine Guo, and Dr. Khushboo Sharma for their kind suggestions at different places of research work. I immensely enjoyed their company and intellectual discussions.

I am also very much thankful to a few of my other friends, especially Dr. Shiv Kumar (HiSOR, Hiroshima University), who always supported me here during my stay in several ways.

I am also very much thankful to a few other Indians staying in Japan for their company Dr. Ajay Tiwari (Scientist, Micron, Japan), Dr. Yash Sharma (Scientist, Micron, Japan), and Mr. Gajendra Kumar.

I am deeply indebted to Dr. Anamika Singh and Mr. Shreyansh Singh, particularly for their encouragement in educational life.

I would like to thank group members Mrs. Saroi Inagaki San, Mr. Ichikawa San, Mr. Harada, Mr. Yao, Mr. Tsunematsu, and others for their kind cooperation and helping me at various stages.

I deeply acknowledge my respected and beloved parents and all my family members, my sisters Mrs. Shashi Singh & Mrs. Usha Singh, my Jeeja Mr. Subba Singh. A lot of love and blessings to my little champ Rohit, Shatrughan, Vandana, Vijay, Anjali, Priyanshu, Shudhanshu, Sheshnath. Without their love and encouragement, this work would not have evolved and been accomplished in its present form. I express my praise to all of them.

Last but not least, I express my deepest thanks to the Almighty, who have given me this wonderful life and whose blessings have paved my way ahead through all ordeals.

公表論文
(Articles)

(1) Synthesis of Highly Activated Magnesium by Niobium and Tantalum Gel Oxide Catalyst
P. K. Singh, H. Gi, K. Shinzato, K. Katagiri, H. Miyaoka, T. Ichikawa, Y. Kojima
Materials Transactions, 62 (2), 284-289 (2021).

(2) Development of Ca-Mg-H_2-$ZrCl_4$ composite for hydrogen storage applications
P. K. Singh, A. Singh, V. Kain, Y. Kojima, H. Miyaoka, S. Kumar
International Journal of Hydrogen Energy, 46, 34362-34368, (2021).

参 考 論 文
(Thesis Supplements）

(1) The catalytic effect of ZrCl4 on thermal dehydrogenation $LiAlD_4$
S. Kumar, A. Singh, P. K. Singh, H. Miyaoka, V. Kain, Y. Kojima
International Journal of Hydrogen Energy, 45, 14413-14417, (2020).

(2) Systematic Study on Nitrogen Dissociation and Ammonia Synthesis by Lithium and Group 14 Element Alloys,
K. Shinzato, K. Tagawa, K. Tsunematsu, H. Gi, P. K. Singh, T. Ichikawa, H. Miyaoka,
Submitted, Advanced Materials, Under Review